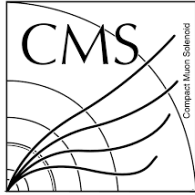
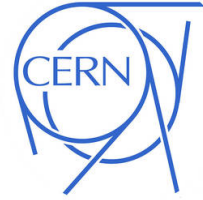


DOCTORAL THESIS

Search for a new light boson in exotic Higgs
boson decays and the CMS muon spectrometer
upgrade using GEM technology



THE CMS EXPERIMENT AT THE CERN LHC



Submitted in partial fulfillment of the requirements for the degree of
Doctor of Philosophy in Physics



Author

Aashaq Shah

Defended on February 10, 2020

DEPARTMENT OF PHYSICS AND ASTROPHYSICS
UNIVERSITY OF DELHI
DELHI-110 007, INDIA



Student Approval Form

Author	Aashaq Hussain Shah
Department	Department of Physics and Astrophysics
Degree	Doctor of Philosophy (Ph. D.)
University	University of Delhi
Supervisor	Dr. Ashok Kumar
Title	Search for a new light boson in exotic Higgs boson decays and the CMS muon spectrometer upgrade using GEM technology
Year of Award	2020

Agreement

1. I hereby certify that if appropriate, I have obtained and attached hereto a written permission/statement from the owner(s) of each third party copyrighted matter to be included in my thesis/dissertation, allowing distribution as specified below.
2. I hereby grant to the university and its agents the non-exclusive license to archive and make accessible, under the conditions specified below, my thesis/dissertation, in whole or in part in all forms of media, now or hereafter known. I retain all other ownership rights to the copyright of the thesis/dissertation. I also retain the right to use in future works (such as articles or books) all or part of this thesis, dissertation, or project report.

Conditions:

1. Release the entire work for access worldwide	
2. Release the entire work for 'My University'only for: 1 Year 2 Year 3 Year and after this time release the work for access worldwide.	

3. Release the entire work for 'My University' only while at the same time releasing the following parts of the work (e.g. because other parts relate to publications) for worldwide access:	
<ul style="list-style-type: none"> a) Bibliographic details and Synopsis only b) Bibliographic details, synopsis and the following chapters only c) Preview/Table of Contents/...page only 	
4. View Only (worldwide)	

.....
Signature of the Scholar

.....
Supervisor's Signature/Stamp

Place:

Date:

Acknowledgements

I was born in Bandipora, a small town in Jammu & Kashmir, and a remote place with limited access to quality education and a daily hub of violence between armed rebels and state forces. From a middle-class family with many financial constraints and with a little peace of mind, I never thought of working in the world's top laboratories such as CERN, Switzerland, and Fermilab, the United States with great minds scratching my head while seeking answers to the most fundamental questions of the modern physics.

Unending glory to God, The Exalted, Who granted me the stamina all along to complete this small piece of work which is only a drop of appreciation from His ocean of munificence. The work is a part of the big team and has been facilitated by many people. The part of the work in this thesis has been carried out at the University of Delhi while as the major part of it has been done at the Large Hadron Collider (LHC) at CERN, Switzerland.

Words are an inadequate medium to express concisely one's feelings of the heart, yet one has to invariably depend on them. It is a matter of pleasure for me to pen down the lines to express my sincere thanks to all those who pledged their support because of which I am able to stand where I am today, and I never thought of writing these acknowledgments as a part of my dissertation.

First and foremost, I would like to acknowledge my deep sense of gratitude to my supervisor Dr. Ashok Kumar for all the “pep talks” and cheerful cooperation throughout the tenure of this work. He is a marvelous human being and a great soul. Besides his professional guidance, he shared with me many lessons on moral and ethical education. I consider myself very fortunate of having him as my supervisor and I do not have words to thank him as it is very impossible to return his favors.

Additionally, I would like to extend my thanks to Dr. Md. Naimuddin, University of Delhi (DU) for his timely suggestions and reviewing part of the work presented in this thesis. I am indebted to Prof. Kirti Ranjan (DU), Prof. Brajesh Choudhary (DU), Dr. Ashutosh Bhardwaj (DU), Dr. Shashi Verma (DU) for their valuable suggestions and encouragement throughout this work. Despite being incredibly busy, the doors of their respective offices used to be always open for me. I am also grateful to Prof. Sanjay Jain, Head, Department of Physics and Astrophysics, University of Delhi for allowing me to utilize the departmental facilities whenever needed.

I am especially thankful to Prof. Archana Sharma (CERN, Switzerland) for allowing me to be part of the CMS muon upgrade project and for facilitating me to work in her lab.

My sincere thanks to Prof. Michael Tytgat (Ghent University, Belgium), Prof. Paul Edmund Karchin (Wayne State University, the United States), Prof. Stefano Bianco (INFN, Italy) and Prof. Kerstin Hoepfner (DESY, Germany) for reviewing some of my manuscripts and sharing their useful comments. I am also indebted to Prof. Marcus Hohlmann (FIT, the United States), and Luigi Bensui (INFN, Italy) for their valuable inputs during the CMS internal hardware meetings at CERN.

I am very thankful to my colleagues Dr. Jeremie Merlin (CERN, Switzerland), Dr. Brian Dorney (Universite Libre de Bruxelles, Belgium), and Dr. Michele Bianco (CERN,

Switzerland) for all the useful discussions on detector R&D and the CMS upgrade work. I am thankful to Mohsin Abbas (KIT, Germany), for assisting me in some of the technical drawings used in this work.

I am very thankful to Dr. Abida Jafari (CERN, Switzerland) and Dr. Hamed Bakhshiansohi (DESY, Germany) for all the discussions while helping me in physics data analysis. Of course, I can't move ahead without thanking Prof. Andrea Giammanco (UCL, Belgium) for allowing me to be part of his physics analysis group. Thanks to Dr. Maria Cepeda (CERN, Switzerland), and Dr. Mario Pelliccioni (INFN, Italy) who provided me a platform to start the physics analysis during the early years of my Ph.D. and introduced me to Abida and Hamed with whom I carried the rest of the physics analysis.

I extend thanks to my friends Arif Khan, Yasir Bhat, Dr. Sabzar, Waseem Bhat, Syed Shah, Zubair Dar, and Ilyas Lone with whom I spent the last few years of my Ph.D. My special thanks to Azeem Banday and Dr. Asif Iqbal who in addition to their precious help, made these years truly memorable.

I thank all my colleagues Ankit Gaur, Aman Phogat, Arjun Chettri, Asar Ahmad, Chekresh Jain, Daljeet Kaur, Francesco Fallavollita, Geetika Jain, Marek Gruchala, Mohit Gola, Prabjot Singh, Praveen Kumar, Priyanka Phogat, Ramkrishana Sharma, Shivali Malhotra, Sumit Khehri and Varun Sharma. I also extend my thanks to engineers Hemant Kumar, Md. Rafiq, Prajesh Sharma, Abhishek, and Rizwan Ahmad. I am also thankful to office staff Amir Hussain, Md. Yunus, Pradhan Ali, and Sanjay Kumar.

Further, I acknowledge the financial support during my Ph.D. from the University of Delhi, University Grants Commission (UGC) and Department of Atomic Energy (DAE), India, CERN (Switzerland), Fermilab (United States), and European network "Marie Curie Initial Training Network (MCnet)".

Of course, this dissertation remains incomplete without mentioning Aabid Shah, my late brother who became a victim of the Kashmir conflict between India and Pakistan. Although he disappeared from my life but could not disappear from my heart. I seek comfort in the memories of our time together and I am grateful for all the good things that happened. It is difficult to move past the pain, but memories keep my heart warm always.

I am also thankful to my elder brothers Arif Shah and Maroof Shah who have always supported my work and played a big role in shaping me. I very much remember their continuous support and encouragement with gratitude. I would like to thank also my maternal uncle Prof. Wali Mohd. Shah who has been my teacher and a source of inspiration.

Last but not least, I do not have words to express my obligation and gratitude to my parents who taught me never to settle for "good enough", and without their moral support, it was very difficult for me to complete this work. I believe there are people whose names slipped out from my mind but deserve to be mentioned in this thesis, my apologies for not mentioning their names specifically but I express my sincere gratitude to all of them.

Aashaq Shah

Abstract

The work presented in this thesis consists of a search for a new light boson in the exotic decays of Higgs boson into the final state with a pair of bottom quarks ($b\bar{b}$) and a pair of muons ($\mu^-\mu^+$), and muon endcap upgrade of the Compact Muon Solenoid (CMS) experiment using Gas Electron Multiplier (GEM) technology.

The Brout-Englert-Higgs mechanism of the Standard Model (SM) explains that all massive particles acquire their mass through interaction with the Higgs field. The existence of such a field could be proven through the experimental detection of the Higgs boson. A similar particle with a mass of 125 GeV and featuring properties as that of the Higgs boson was detected by the ATLAS and CMS experiments at the CERN Large Hadron Collider (LHC) in 2012. The measurements of the couplings and properties of this newly discovered particle show compatibility with SM within the experimental uncertainties. However, the existence of Beyond the Standard Model (BSM) exotic decays of the Higgs boson into light pseudoscalar particles which might have eluded our detection so far are not yet fully excluded. Therefore, the current work is carried out to explore the possibilities of such decays. The search considers exotic decay of newly discovered boson (h) into a new light pseudoscalar boson (a) via two different decay channels $h \rightarrow Za \rightarrow b\bar{b}\mu^-\mu^+$ and $h \rightarrow aa \rightarrow b\bar{b}\mu^-\mu^+$. The two two-Higgs-doublet model extended with extra singlet (2HDM+S) and the Next-to-Minimal Supersymmetric Model (NMSSM) are used for benchmarking the performance of the search. The search uses the proton-proton collision data collected by the CMS experiment during the year 2017 at the center-of-mass energy equal to 13 TeV corresponding to an integrated luminosity of 41.5 fb^{-1} . The analysis is performed by simulating private signal samples at the leading order in gluon-gluon and vector boson fusion processes. The event categorization technique is exercised to enhance search sensitivity. The dimuon mass distributions for the simulated signal events are parameterized with the combination of Voigtion and double-sided Crystal Ball functions. The background contribution from various processes is directly extracted from data and its shape is modeled with a set of analytical functions by employing discrete profiling. Various experimental and theoretical factors contributing to the uncertainties are taken into account and the search results are extracted from the unbinned fit to the reconstructed dimuon mass distribution.

Since a successful physics program can only be achieved with sufficient understanding and optimization of the detector performance, therefore part of the work is dedicated to the detector R&D and muon endcap upgrade of the CMS experiment. After the second Long Shutdown (LS2) of the LHC, the center-of-mass energy is expected to reach 14 TeV with the steady increase in the beam luminosity over the years to a peak value $7 \times 10^{34} \text{ cm}^{-2} \text{ s}^{-1}$. The corresponding increase in particle rates pushes the present CMS detection and trigger capabilities to their limits and strongly affect the muon system. Therefore, CMS collaboration has proposed to upgrade the muon system in the endcap using GEM detectors. These detectors are known to operate under high rates with excellent performance and are

considered ideal for the high luminosity phase of the LHC (HL-LHC). Such chambers, in turn, could offer enhanced tracking and triggering capabilities for the muon system and are suited for stable, long-term operation in high rate environments such as the HL-LHC. A total of 144 detectors are going to be installed in positive and negative endcaps of the CMS experiment. These chambers will be integrated with the CMS during LS2 of the LHC. The introduction of such technology into the CMS will increase the acceptance and the efficiency of reconstruction of muons and would be crucial in the future for the broad coverage of physics processes whose signatures are characterized by the presence of muons in the final state¹.

Currently, the forward endcap high- $|\eta|$ region $1.6 < |\eta| < 2.2$ of the CMS remains uninstrumented. The part of the work presented in this thesis aims at covering this region of the muon endcap with large size GEM GE1/1 chambers and presents their design layout and a novel construction technique. Several full-size prototype chambers built with the current design and newly developed assembly technique described in this thesis have been operated successfully in various beam tests at CERN. The work presents the performance measurements such as gain, efficiency, rate capability, discharge probability, spatial and timing resolutions, of these chambers estimated during the intensive R&D program and beam tests at CERN. The important recommendations based on such results for the performance of the GE1/1 chambers during their usage in the CMS experiment are provided to the CMS collaboration. Since these chambers use large size foils that are developed using a single mask technique. Such a technique results in asymmetrically bi-conical holes compared to symmetrically bi-conical holes obtained with the double mask technique, the characterizations of such foils are performed and some important conclusions regarding the impact of hole asymmetry on the detector performance that have proved very crucial to CMS collaboration are also presented.

Also, during the course of this work, the first commercial double mask GEM foils were successfully produced in India as a part of the Transfer of Technology (TOT) between CERN and Micropack, Indian Industry. However, before these foils could be declared fit for applications and technology as reliable, a series of quality control and assessment tests on these foils have been performed at the University of Delhi. The tests include optical and electrical measurements to check their reliability and usability, the results are also included in the current work.

¹This is the main motivation of considering a physics analysis in the current thesis having muons in the final state, though, the upgrade will be relevant only in future for all such processes.

CONTENTS

Contents	ix
List of Figures	xii
List of Tables	xxi
1 Prologue	1
1.1 General	1
1.2 Thesis layout	2
Bibliography	5
2 Theoretical background and overview of the LHC	7
2.1 The Standard Model (SM)	7
2.1.1 Fundamental interactions	8
2.1.2 The Higgs mechanism	11
2.1.3 SM Higgs field	13
2.2 Physics beyond the SM	15
2.2.1 Exotic decays of the Higgs boson	16
2.3 Overview of the LHC	17
2.3.1 The CMS experiment	18
Bibliography	21
3 The CMS muon endcap upgrade using GEM technology	23
3.1 Introduction	24
3.2 Impact of GE1/1 upgrade on the CMS experiment	25
3.3 The GE1/1 station	26
3.4 Chamber design	27
3.4.1 The drift board	28
3.4.2 The external frame	29

CONTENTS

3.4.3	The internal frame	29
3.4.4	The GEM foils	30
3.4.5	The readout board	31
3.4.6	On-chamber HV distribution	31
3.4.7	Gas distribution within the chamber	32
3.5	Assembly technique	33
3.5.1	Drift board preparation	33
3.5.2	GEM stack assembly	34
3.5.3	Foil stretching mechanism	35
3.5.4	Closing the chamber	37
3.6	Performance of GE1/1 chambers	38
3.6.1	Gain measurements	38
3.6.2	Efficiency and timing measurements	40
3.6.3	Rate capability	44
3.6.4	Discharge probability	44
3.7	Fits to data	46
3.8	Involvement of Delhi University in GE1/1 project	47
3.9	Current status of the GE1/1 project	48
3.10	Summary and conclusions	49
Bibliography		51
4 R&D on GEM foils		54
4.1	Introduction	55
4.2	Single-mask foil production	55
4.2.1	Polyimide etching	55
4.2.2	Copper etching	56
4.3	Performance studies	57
4.3.1	Effective gain measurements	58
4.3.2	Energy resolution	59
4.3.3	Charging-up behaviour	61
4.3.4	Impact of continuous irradiation on resolution	63
4.3.5	Rate capability	64
4.3.6	Gain and resolution uniformity	66
4.4	Production of first Indian GEM foils	68
4.4.1	Double-mask foil production	68
4.5	Qualification	69
4.5.1	Optical measurements	69
4.5.2	Leakage current measurements	73
4.6	Conclusions	76
Bibliography		77

5	Search for exotic Higgs boson decay in $h \rightarrow Za \rightarrow b\bar{b}\mu^-\mu^+$	80
5.1	Introduction	80
5.2	Simulated Samples	81
5.3	Object reconstruction	82
5.4	Selection optimization	83
5.4.1	Further optimization	86
5.5	Event Selection	88
5.6	Signal model	90
5.7	Background model	92
5.8	Systematic uncertainties	93
5.9	Results	94
5.10	Summary	95
	Bibliography	96
6	Search for exotic Higgs boson decay in $h \rightarrow aa \rightarrow b\bar{b}\mu^-\mu^+$	100
6.1	Introduction	100
6.2	Review of $h \rightarrow aa$ searches	103
6.2.1	4τ final state	103
6.2.2	4μ final state	104
6.2.3	$2\mu 2\tau$ final state	105
6.2.4	$2\mu 2b$ final state	106
6.2.5	Interpretation	106
6.3	Present analysis	109
6.4	Simulated samples	110
6.5	Event selection and optimization	110
6.6	Signal and background models	116
6.7	Systematic uncertainties	118
6.8	Results	119
6.9	Conclusions	120
	Bibliography	122
7	Epilogue	129
7.1	Summary and conclusion	129
A	Tables	135
A.1	GE1/1 operating conditions for Ar/CO ₂ gas	135
A.2	GE1/1 operating conditions for Ar/CO ₂ /CF ₄ gas	135

LIST OF FIGURES

2.1	Potential $V(\phi)$ as a function of field ϕ for: (left) $\mu^2 > 0$ with minimum at $\phi_0 = 0$ and (right) $\mu^2 < 0$ with minimum at $\phi_0 = \pm\nu$	11
2.2	Schematic layout of the CERN LHC accelerator complex [23].	17
2.3	A photograph of the CMS detector showing its different subdetectors including muon stations [23, 25].	18
2.4	A sliced view of the CMS detector showing the muon detectors such as CSC (highlighted in blue colour), DT (in green) and RPC (in red) in the barrel and endcap [26]. Two yellow colour stations GE1/1 and GE2/1 which be installed in the CMS during LS2 and LS3 are also highlighted.	19
3.1	A quadrant of the R-z cross-section of the CMS detector, highlighting (in red) the location of the GE1/1 station in the pseudo-rapidity region $1.6 < \eta < 2.2$ [4].	24
3.2	Trigger rate reduction with the deployment of muon direction measurement using GEM GE1/1 and CSC ME1/1 chambers [4].	25
3.3	The first CMS muon endcap station with the GE1/1 super-chambers in the inner ring [4]. The GE1/1 10° long and short superchamber strcutures are also shown.	26
3.4	Evolution [†] of GE1/1 detector since 2010 [4] from generation-I to generation-X (2018). (†) Picture courtesy: J. A. Merlin	27
3.5	GE1/1 layout [†] and its main components starting from bottom: drift board mounted all around with stainless steel pull-outs used for stretching of GEM foils, 3 mm frame (Spacer), first foil, 1 mm frame, second foil, 2 mm frame, third foil, 1 mm frame, first O-ring, external frame, second O-ring and the readout board [17]. (†) Picture courtesy: M. Abbas	28

3.6	(left) Design of GE1/1 drift board and (right) magnified view of the design of the wider side of the drift board, with the twelve HV pins and corresponding soldering pads for the resistive divider network. There are on-board HV circuit traces and pads for the spring-loaded pins that make the electrical connections to the GEM foils; the pads for a 10 M Ω SMD resistor, 100 k Ω and 330 pF capacitor; the holes to fix pull-outs against the board [17].	28
3.7	(left) The GE1/1 epoxy-glass external frame. (right) Close-up view of the section of the external frame showing the groove in the frame, O-ring in and out of the groove and notches in the inner side of the frame to accommodate the pull-outs [17].	29
3.8	(left) Design [†] of the GE1/1 internal frames, (middle) magnified view of a section of the Figure 3.8, and (right) shapes and mechanical structure of the different pieces of the frames (right). Ten pieces are joined together to form each frame. The stacked frames surround the GEM foils along their periphery [17]. ([†])Picture courtesy: M. Abbas	30
3.9	(left) Design of the GE1/1 GEM foils and (right) close-up view of a section of a foil. Small holes for alignment pins are used during assembly. Large holes allow the passage of screws used to attach a foil to the internal frame. "Plus"-shaped grooves are there to accommodate stretching nuts. The boundaries between the different HV sectors are visible [17].	30
3.10	(left) Design of the readout board with the gas plugs fixed at opposite edges, (middle left) outer side of GE1/1 readout board showing 24 (η , ϕ) readout sectors, each with a male Panasonic connector for signal readout. There are holes at opposite corners used to mount the two gas plugs; one serves as gas inlet and another as gas outlet. Holes on the periphery of the board allow the passage of screws that fix the board against the chamber structure. (middle right) Inner side of the drift board showing the readout strips and (right) close-up view showing readout strips on the inner side and a Panasonic connector on the outer side of the board [17].	31
3.11	(left) Sliced view of the chamber design [†] showing the mechanism to power the three GEM foils with twelve HV pins and (right) magnified sliced view of Figure 3.11 (left) showing various components such as the drift board, 3 GEM foils in a stack, 3 mm, 1 mm, 2 mm, 1 mm frames, second GEM foil powering pad, readout board and the single HV pin pressed against powering pad of the second GEM foil [17]. ([†])Picture courtesy: M. Abbas	32

LIST OF FIGURES

3.12	(left) Twelve spring-loaded pins soldered onto the drift board to make electrical HV connections to corresponding contact pads on the GEM foils; the three sets of pins have different heights so that they can properly reach the three GEM foils. (right) The resistive divider network used to power up the GE1/1 detector with a gap configuration of 3/1/2/1 mm using single channel power supply; the notation D, 1T, 1B, 2T, 2B, 3T and 3B corresponds to the drift board, the top and bottom electrodes of the first, second and third GEM foil respectively [17].	32
3.13	Exploded view of a GE1/1 chamber, including also the design of a gas plug fixed onto a GE1/1 readout board [17].	32
3.14	The 3 mm frame pieces placed on the Plexiglas plate forming the trapezoidal shape of the chamber [17].	33
3.15	(left) GEM foil cleaning using adhesive roller. (right) Leakage current measurement using a MIT 420 Megger [17].	34
3.16	(1) Shapes and mechanical structure of 4 different frame pieces, (2) 3 mm and 1 mm frame pieces are combined together with "+" shaped grove reserved for stretching nut, (3) placement of nut after stacking two frame pieces, (4) 3 mm, 1 mm, and 2 mm frame pieces combined in a specific order and (5) different frame pieces stacked together to maintain the gap configuration of 3/1/2/1 mm as demanded by GE1/1 geometry, similar frame pieces are combined to form four layers around the periphery of the GEM stack as depicted in Figure 3.8 [17].	34
3.17	(left) A GEM stack with a drift board and (right) the GEM stack structure from bottom to top [17].	35
3.18	(left) Placing the GEM stack onto the drift board. (right) The GEM stack on the drift board and fixation of the drift board with the assembly jig [17]. . .	36
3.19	Concept and mechanism employed to stretch the GEM foils in GE1/1 chambers [4].	36
3.20	(left) The implementation of the concept depicted in the Figure 3.19 by using various components to stretch the GEM stack against the pull-outs. Stretching screws are allowed to pass through the stainless steel pull-outs and are recieved by nuts embeded into the inner frame for tensioning the GEM foils in the stack. (right) The actual stretching is performed using a screw driver with an assembly jig mounted onto the drift board [17].	36
3.21	Close-up view of a section of a GE1/1 detector with the GEM foil stack tensioned against the pull-outs mounted onto the drift board and surrounded by the outer frame equipped with O-ringssections in its grooves. The active chamber volume is ready to be closed with the readout board [17].	37
3.22	(left) Closing the chamber with the readout board. (right) A completed, closed GE1/1 chamber [17].	37

LIST OF FIGURES

3.23	Design [†] of the setup used for gain measurements with X-ray tube and the GE1/1 detector inside the copper chamber. The copper chamber is completely closed when the detector is exposed to X-rays. (†) Picture courtesy: M. Abbas	38
3.24	(left) Map of the readout board showing 24 (η , ϕ) sectors of GE1/1 chambers, and (right) gain and rate measurements of sixth generation chamber (GE1/1-VI) while reading a particular (η , ϕ) = (5, 2) sector. The error bars on the measured rate are the Gaussian one sigma uncertainty which are very small and hence are multiplied by a factor of 25 so as to reflect their visibility on the rate plot.	39
3.25	(left) Gain of fourth generation GE1/1-IV detector for the gas mixtures Ar/CO ₂ (70/30) and Ar/CO ₂ /CF ₄ (45/15/40), and (right) Observed gain of fourth GE1/1-IV and sixth generation GE1/1-VI detectors for Ar/CO ₂ /CF ₄ (45/15/40). Points represent the data and the solid lines a fit to the observed data. The ratio plots have been calculated by fitting observed data and using the fit equations to interpolate into the regions of missing data points while taking the ratio between the gains corresponding to Ar/CO ₂ and Ar/CO ₂ /CF ₄	40
3.26	Schematic of the beam test set-up showing the direction of muon beam, triggering Scintillators (photo multiplier tubes (PMTs)) (in dark gray colour), 10 cm × 10 cm tracking GEMs (in yellow) and GE1/1 chambers (in green) [26].	40
3.27	(left) Design of the tracking telescope showing three triggering scintillators (in grey colour), 10 cm × 10 cm tracking GEMs (in yellow colour), (middle) a photograph of movable aluminum stand holding actual GE1/1 chamber in front of the tracking telescope during H4 beam test campaign, and (right) one of the earliest (December 2014) beam test setup at CERN SPS.	41
3.28	A photograph showing 24 VFAT chips mounted on the GE1/1 chamber.	42
3.29	(left) GE1/1 efficiency, and (right) timing resolution of GE11-IV detector for the gas compositions Ar/CO ₂ and Ar/CO ₂ /CF ₄ . Points represent the data and solide lines represent the logistic fits (details in Table 3.2). The error bars on data are the Gaussian one sigma uncertainty which are very small and are multiplied by a factor of 4 ($\sigma_{eff} \times 4$) so as to reflect their visibility on a given data point.	43
3.30	(left) The timing resolution for Ar/CO ₂ and Ar/CO ₂ /CF ₄ gases as a function of gain. The fit equations from Figure 3.29 (right) are used to obtain new data points by interpolation, the solid lines merely connect the points. The ratio plot is obtained by the division between the interpolated data points of Ar/CO ₂ /CF ₄ and Ar/CO ₂ , and (right) rate capability of a GE1/1-IV chamber, the Figure is also merged with a rate capability of a 10 cm × 10 cm test detector. The shaded portion ‘CMS Region’ is the expected particle flux region of the CMS during HL-LHC.	44
3.31	Discharge probability [†] for the gas composition Ar/CO ₂ . (†) Thanks to J. A. Merlin for sharing information/suggestions on this plot.	45

LIST OF FIGURES

3.32	A photograph of the shipment box containing six full-size GE1/1 chambers at Delhi University, waiting to be dispatced to CERN (August 2018).	45
3.33	Master plot of GE1/1 detectors showing the gain (pink), discharge probability (black), efficiency (red) and time resolution (blue) for the gas composition Ar/CO ₂ (70/30) as a function of drift voltage. The axes and corresponding data are represented by the unique color code in the plot. Also, the plot shows the shaded region which is the recommended operational region of the chambers during their use in CMS.	46
3.34	Master plot of GE1/1 detectors showing the gain (pink), discharge probability (black), efficiency (red) and time resolution (blue) for the gas composition Ar/CO ₂ /CF ₄ (45/15/40) as a function of drift voltage. The axes and corresponding data are represented by the unique color code in the plot. Also, the plot shows the shaded region which is the recommended operational region of the chambers during their use in CMS.	47
3.35	A photograph taken in December 2018 showing some of the large size GE1/1 chambers that have been constructed and stored in racks at CERN Preveessin building 904.	49
4.1	Schematic procedures for the fabrication of a single-mask GEM foil [5]. . . .	56
4.2	(left) Scanning Electron Microscope (SEM) image showing the asymmetric single hole structure in GEM produced by single-mask technique and (right) its schema.	57
4.3	(left) A 10 cm × 10 cm detector with a symmetric gap configuration of (2/2/2) mm and two windows, the one on the top and other on the bottom for irradiation purposes, and (right) design of the detector realized for the measurement purposes.	58
4.4	Gain measured in a triple GEM 10 cm × 10 cm detector when all the three foils either with ‘Orientation A’ or with ‘Orientation B’ are facing the incident source (Fe ⁵⁵). The ratio plot in the bottom shows that the gain is almost two times higher in ‘Orientation B’ compared to ‘Orientation A’.	59
4.5	Energy spectrum of the ⁵⁵ Fe source in Ar/CO ₂ (70: 30) showing the main photo and the Ar escape peaks: (left) ‘Orientation A’ and (right) ‘Orientation B’. The spectra are fitted with Gassian functions for the extraction of μ and σ . 60	
4.6	The GEM detector wrapped in a copper shield. The shield acts a Faraday cage for the detector.	61
4.7	Energy spectra taken at the start of the measurement, after 2 and 4 hours under continueous irradiation: (left) ‘Orientation A’ and (right) ‘Orientation B’.	62

LIST OF FIGURES

4.8	Normalized gain (charging-up curves) as a function of time for ‘Orientation A’ and ‘Orientation B’ when the detector is placed under continuous irradiation. Temperature is also plotted to demonstrate the stability under the ambient conditions. The humidity and pressure are recorded to be constant during the period of measurements.	62
4.9	Energy resolution determined as a function of time with the initial gain of 2.2×10^4 when ^{55}Fe source is continuously irradiated on the detector: (left) ‘Orientation A’ and (right) ‘Orientation B’	63
4.10	Profile plot of relative energy resolution measured as a function of relative gain with the initial gain of 2.2×10^4 when Fe^{55} source is continuously irradiated on the detector: (left) ‘Orientation A’ with the initial resolution of 24% and (right) ‘Orientation B’ with the initial resolution of 18%.	64
4.11	(left) The rate capability setup inside the copper box explicating detector being irradiated with the X-ray source and (right) Rate capability for single-mask with ‘Orientation A’ and ‘Orientation B’ configurations. The gain is normalized to average gain value 2.2×10^4	65
4.12	The active window divided into 7×7 sectors. Each sector have $1 \text{ cm} \times 1 \text{ cm}$ area.	66
4.13	Effective gain map at various sectors: (left) ‘Orientation A’ and (right) ‘Orientation B’. The bottom histograms in each Figure show the average gain at equal electric field setting in each orientation.	66
4.14	Gain ratios corresponding to each sector of ‘Orientation A’ and ‘Orientation B’. The bottom histogram shows that the gain is approximately 1.8 times higher in each sector in ‘Orientation B’ than the corresponding sector in ‘Orientation A’.	67
4.15	The energy resolution of each sector over the active area of the detector: (left) ‘Orientation A’ and (right) ‘Orientation B’. The bottom histogram in each Figure show that the resolution of 26 % and 22.8 % is obtained for ‘Orientation A’ and ‘Orientation B’, respectively.	67
4.16	(left) $10 \text{ cm} \times 10 \text{ cm}$ GEM foil encapsulated in a frame, (middle) Cross-sectional view of the foil showing the double cone structure of an engraved hole, and (right) Scanning Electron Microscope (SEM) image showing the topview of a hole with diameter $70 \mu\text{m}$ [31].	68
4.17	Sketch of the setup used for the optical measurements [31].	69
4.18	Observed imperfections in the foils: (extreme left) un-etched area, (left) under-size hole, (middle) over-size hole (right) missing hole, (extreme right) excess etching [31].	70
4.19	(left) Image formed in gray-scale and (right) Histogram of gray-scale image for the calculation of gray threshold [31].	70
4.20	Hole size distribution of (left) inner, and (right) outer holes for one sector.	70

LIST OF FIGURES

4.21	Mean diameter of (left) Inner holes of all the sectors (right) Outer holes of all the sectors. The hole distributions were fitted with Gaussian functions to extract values for mean and standard deviation as shown in Figure 4.22. . . .	71
4.22	Mean diameter for (left) Inner and (right) outer holes for each side of GEM foils. The error bars represent the 1 standard deviation error obtained from the statistical combination of the standard deviations of hole diameter distributions of each sub-sector.	71
4.23	(left) SEM image at μm level resolution showing the overall uniformity of the foil sample and (right) hole diameters and the pitch under SEM at μm level resolution.	72
4.24	Number of defects seen for one of the $10\text{ cm} \times 10\text{ cm}$ foil in (left) Insulator (Apical Type NP) and (right) Copper [31].	73
4.25	Sketch of the setup used for the measurement of leakage current [31].	73
4.26	Leakage current of (left) Micropack and (right) CERN foils at an average temperature of $T=27^\circ\text{C}$ and relative humidity equal to 20%.	74
4.27	Leakage current versus relative humidity taken at different voltages for (left) Micropack and (right) CERN foils.	74
4.28	QC Long: Leakage Current as a function of time in dry nitrogen environment at different voltage steps with an ambient average temperature of $T = 28^\circ\text{C}$ and ambient relative humidity of 17% for Micropack and CERN foils.	75
4.29	QC Long: Leakage Current as a function of time in a dry nitrogen environment at different voltage steps with an ambient average temperature of $T = 28^\circ\text{C}$ and relative humidity of 17% for Micropack (left) foil-02 and (right) foil-03. .	75
5.1	Predicted $\mathcal{B}(a \rightarrow \mu^- \mu^+)$ for $m_a = 20\text{ GeV}$ in the different models of 2HDM+S, for various of $\tan\beta$. The branching fractions for the signal $h \rightarrow Za \rightarrow b\bar{b}\mu^- \mu^+$ are computed following the prescription in references [15, 16].	81
5.2	Feynman diagram for signal topology $h \rightarrow Za \rightarrow b\bar{b}\mu^- \mu^+$	82
5.3	For $m_a < 11\text{ GeV}$, events fall in the region $\Delta R < 0.4$, implying the muon pair is not well separated and (right) for $m_a > 11\text{ GeV}$, events does not fall in the region $\Delta R < 0.4$, implying the muons are well separated.	84
5.4	(left) The significance as a function of leading jet p_T threshold and (right) the significance for different working point combinations of the selected b -tagged jet pair for CSV v 2 and DeepCSV taggers.	84
5.5	(left) The significance for different combinations of muon isolations (μ -Iso) and identifications (μ -ID), and (right) the comparison of significance for CSV v 2 versus DeepCSV taggers for different working point combinations of the selected b -tagged jets.	85
5.6	Data Monte Carlo (Data-MC) comparison for momentum distribution of leading jet (left) CSV v 2 and (right) DeepCSV tagger.	85

LIST OF FIGURES

5.7	The distribution of $\chi_{b\bar{b}}$ versus χ_h as defined in equation 5.2 for (left) background simulated and (right) for signal process with m_a GeV. The encircled area with $\chi^2 < 5$. In each plot, the scale on the right side represents the expected yields at 41.5 fb^{-1}	86
5.8	The reconstructed Z boson: (top left) mass and (top right) its momentum; and the reconstructed pseudo scalar a : (bottom left) mass and (bottom right) its momentum.	87
5.9	The reconstructed: (left) mass and (right) momentum of the Higgs boson (four object ($b\bar{b}\mu^-\mu^+$) system).	89
5.10	Results of the signal model $S(m_{\mu^-\mu^+} f, p_V, p_{CB})$, fitted independently to $m_{\mu^-\mu^+}$ distributions for $m_a = 12, 15, 20, 30$ GeV. Dotted lines in each distribution are the Crystal Ball and Voigtion components, and the solid line is the constructed model.	91
5.11	Various pdf's describing the background shape from the control region of the data (TL category).	92
5.12	Observed and expected upper limits at 95% CL on the (left) Higgs boson production times branching fraction ($\mathcal{B}(h \rightarrow Za \rightarrow b\bar{b}\mu^-\mu^+)$) and (right) the branching ratio as a function of pseudoscalar mass m_a . The green and yellow bands represent 68 and 98% confidence intervals, respectively, around the median for expected and observed distribution of limits.	95
6.1	Expected and observed 95% CL limits on $\frac{\sigma(h)}{\sigma_{SM}} \mathcal{B}(h \rightarrow aa)$ as a function of the mass of the light boson in 2HDM+S: (top left) type-1, (top right) type-2 with $\tan\beta = 2$, (bottom left) type-3 with $\tan\beta = 5$, and (bottom right) type-4 with $\tan\beta = 0.5$ [11].	108
6.2	Feynman diagram for signal topology $h \rightarrow aa \rightarrow b\bar{b}\mu^-\mu^+$	109
6.3	(left) The significance as a function of m_a for DeepCSV and CSVv2 taggers, and (right) the significance as a function of missing transverse energy (\cancel{E}_T).	111
6.4	(left) The distribution of $\chi_{b\bar{b}}$ versus χ_h as defined in equation 6.3 for simulated background processes and (right) the signal process with $m_a = 30$ GeV. The contours encircle the area with $\chi^2 < 5$. The scale on the right side of each plot represents the expected yields at 41.5 fb^{-1}	112
6.5	The reconstructed pseudo-scalar a boson from pair of b tagged jets: (top left) mass and (top right) its momentum; and the reconstructed pseudo scalar a from pair of muons: (bottom left) mass and (bottom right) its momentum.	113
6.6	The reconstructed: (left) mass and (right) momentum of the Higgs boson from four object ($b\bar{b}\mu^-\mu^+$) system).	114
6.7	The projected signal shape (dimuon invariant mass distribution) using the model presented in Equation 6.5. The shapes are normalized to unit area.	116

LIST OF FIGURES

6.8	Results of the signal model $S(m_{\mu^-\mu^+} \mid f, p_V, p_{CB})$, fitted independently to $m_{\mu^-\mu^+}$ distributions for $m_a = 20, 30, 40$ and 50 GeV. Dotted lines in each distribution are the Crystal-ball and Voigtion components, and the solid line is the constructed model.	117
6.9	The best fits to background model under background-only hypothesis for the (left) TL category (data fitted with different polynomial functions), (right) TM category (data fitted with different polynomial functions).	118
6.10	The best fits to background model to the data under background-only hypothesis for TT category.	118
6.11	Observed and expected upper limits at 95% CL on the (left) Higgs boson production times branching fraction ($\mathcal{B}(h \rightarrow aa \rightarrow b\bar{b}\mu^-\mu^+)$) and (right) the branching ratio as a function of pseudoscalar mass m_a . The green and yellow bands represent 68 and 95% confidence intervals around the median, respectively, for expected and observed distribution of limits.	119
6.12	The comparison of the expected upper limits at 95% CL on the Higgs boson production cross section times branching fraction for the analysis based on 2016 and 2017 data corresponding to $35.9 fb^{-1}$ and $41.5 fb^{-1}$, respectively. . .	120

LIST OF TABLES

3.1	Technical specifications of the GE1/1 Short and Long chambers.	27
3.2	The fit equations and the value of constants obtained by fitting gain, efficiency, timing resolution and discharge probability data for the gas compositions Ar/CO_2 and $Ar/CO_2/CF_4$	46
5.1	Event yields obtained by DeepCSV tagger for simulated processes and data after selecting two muons and two b jets (tight-loose). The expected number of simulated events are normalized to the integrated luminosity of 41.5 fb^{-1}	89
5.2	Event yields obtained by CSV v 2 tagger for simulated processes and data after selecting two muons and two b jets (tight-loose). The expected number of simulated events are normalized to the integrated luminosity of 41.5 fb^{-1}	89
5.3	Event yields obtained using DeepCSV tagger for simulated processes and data after final cuts.	90
5.4	The parameters for the signal model and their modeling with the mass: \hat{f} , $\hat{\gamma}$, $\hat{\alpha}$ and \hat{n} are fixed where σ and σ_{CB} are linearly modeled. Apart from the signal mass perturbative term, $\hat{m}_a = m_a + \epsilon_{m_a}$, the model also has two free parameters, a_1 and b_1	91
5.5	Trial functions with different orders are selected to model the background in TL category depending upon the outcome of the F-test. The pdf's marked with '+' sign are not selected as they are repeating in another polynomial category.	93
5.6	Trial functions with different orders are selected to model the background in TL category depending upon the outcome of the F-test. The pdf's marked with '+' sign are not selected as they are repeating in another polynomial category.	93
5.7	Systematic uncertainties considered in the present analysis.	94
6.1	Coupling of different types of fermions to doublets in different types of 2HDM without FCNC at the lowest order. [†] lepton specific [‡] flipped	101

LIST OF TABLES

6.2	The ratio of the Yukawa couplings of the 2HDM pseudoscalar a boson to those of the SM Higgs boson h , in the four types of 2HDM without FCNC at lowest order [11]. [†] lepton-specific [‡] flipped	101
6.3	Branching fractions [11], as a function of the mass of the pseudoscalar boson a to b quarks, τ leptons, and muons in the four different scenarios of 2HDM+S considered in Figure 6.1.	107
6.4	Event yields obtained for simulated processes and data after selecting two muons and two b jets (tight-loose). The expected number of simulated events are normalized to $\mathcal{L} = 41.5 \text{ fb}^{-1}$. ([†]) is for $b\bar{b}\mu^-\mu^+$ final state when only ggF is considered.	115
6.5	Event yields obtained for simulated processes in TL category. (*) is for $b\bar{b}\mu^-\mu^+$ final state when only VBF is considered, ([†]) is for $\mu^-\mu^+\tau^-\tau^+$ final state when only ggF is considered, and ([‡]) is for $b\bar{b}\tau^-\tau^+$ final state when only ggF is considered.	115
6.6	Event yields obtained after applying final cuts for simulated processes and data in tight-loose (TL) category. The expected number of simulated events are normalized to $\mathcal{L} = 41.5 \text{ fb}^{-1}$. ([†]) is for $b\bar{b}\mu^-\mu^+$ final state when only ggF is considered.	115
6.7	Event yields obtained for simulated processes in TL category after applying final cuts. (*) is for $b\bar{b}\mu^-\mu^+$ final state when only VBF is considered, ([†]) is for $\mu^-\mu^+\tau^-\tau^+$ final state when only ggF is considered, and ([‡]) is for $b\bar{b}\tau^-\tau^+$ final state when only ggF is considered.	115
A.1	The gain, efficiency, rate capability and discharge probability as a function of drift voltage for GE1/1 chambers corresponding to Ar/CO ₂ gas. The green region are the recommended working points while as light gray is under efficient region. The red region is merely an extrapolation and should be strongly avoided because of steep rise in discharge probability.	135
A.2	The gain, efficiency, rate capability and discharge probability as a function of drift voltage for GE1/1 chambers corresponding to Ar/CO ₂ /CF ₄ gas. The green region are the recommended working points while as light gray is under efficient region. The red region is merely an extrapolation and should be strongly avoided because of steep rise in discharge probability.	135

Prologue

*We Shall not cease from exploration
And the end of all our exploring
Will be to arrive where we started
And know the place for the first time.*

— T. S. Eliot

1.1 General

What triggered the Big Bang and what came before it? What is the origin of the universe, and what are its building blocks and how do they interact with each other? What is dark matter and dark energy? Why is gravity so different from other interactions? Why is matter abundant compared to antimatter? Are there any additional dimensions? Does supersymmetry exist and if so, does it stabilize at the electroweak scale? These are some of the questions particle physics tries to answer.

Gian F. Giudice, a theoretical physicist at CERN, begins his book “A Zeptospace Odyssey: A Journey into the Physics of the LHC”, with the quote of T. S. Eliot¹ with an invitation to explore and understand the universe and emphasizes that even in case of no discovery, the journey will extend our knowledge compared to where we started.

From the past few decades, particle physics has undergone a hurried development starting from the discovery of the electron to discoveries of quarks and gluons, W and Z bosons. Further explorations started after 2012 with the discovery of the Higgs boson by the ATLAS and CMS experiments at the CERN Large Hadron Collider (LHC), making the journey even more exciting. The questions like; is this boson really the scalar particle predicted by the SM of the particle physics and, are there any signs of new physics in its properties? have quickly shifted the attention towards measuring its properties to ascertain whether it is the SM Higgs boson or completely a new particle. Of particular interest is to search for exotic decays of this new particle into the Beyond Standard Model (BSM) particles. Several well-motivated theories predict such decays and are the motivation for the current work.

¹The lines are quoted on the top right corner of the current page. In fact, the quotes have been introduced at the beginning of each chapter to describe the essence of the corresponding chapter.

1.2 Thesis layout

The theoretical skeleton of the Standard Model (SM) has been primarily established. It has been significantly successful at explaining many physical phenomena observed at particle physics experiments and even predicting new particles before their discovery [1–3]. Numerous precision measurements and experimental results confirm what was predicted by the SM [4,5]. Despite all the successes of the SM, it has many limitations such as the strong CP problem, neutrino oscillations, matter-antimatter asymmetry, and the nature of dark matter and dark energy, etc. New models beyond SM have therefore been proposed to mitigate its limitations. In this context, the current work has been undertaken with the focus to search for a new light boson by considering the exotic decays of already discovered h (125 GeV) boson [6]. The search lies under the domain of BSM physics and considers the search for two decay channels $h \rightarrow Za$ and $h \rightarrow aa$ into the $b\bar{b}\mu^-\mu^+$ final state with ‘ a ’ being a new pseudoscalar boson. The analysis is performed using the proton-proton collision dataset corresponding to an integrated luminosity of 41.5 fb^{-1} recorded by the Compact Muon Solenoid (CMS) experiment [7] at the LHC during the year 2017.

The physics analysis project has been considered in the current work such that it has muons in the final state as the major part of it has been dedicated to the muon spectrometer upgrade of the CMS detector [7]. Ideally, all the decay products in the final should have been considered as muons, however, such a decay channel has a small branching fraction and would be more challenging to probe with the current LHC data. Therefore, instead of four muons, only a pair of muons and a pair of b -quark jets are considered, and the introduction of b -quark jets in the final state serves to improve the branching fraction of the decay channel and makes it more feasible to study at the LHC with the current data.

The upgrade component of the current work considers usage of new micro-pattern gaseous detectors named as GE1/1 chambers based on Gas Electron Multiplier (GEM) technology. The introduction of GEM technology into the CMS will increase the acceptance and the efficiency of reconstruction of muons, and would be crucial in the future for the broad coverage of physics analysis whose signatures are characterized by the presence of muons in the final state². The GEM detectors are known to operate at very high rates with good performance and are considered ideal during the high luminosity phase of the LHC (HL-LHC) starting after 2026. A total of 144 detectors are going to be installed in positive and negative endcaps of the CMS detector. These detectors will be constructed after years of R&D and installed in the CMS during 2019-2020, the period being known as the second Long Shutdown (LS2) of the LHC. Although, such an upgrade will not have an impact on the current work but will be very crucial in the future for the existing decay channels or decay modes having muons in the final state, especially after the upgrade of the LHC to center-of-mass energy of 14 TeV with the gradual increase of the instantaneous luminosity.

²Few examples include, search for lepton flavor violating decay $\tau \rightarrow 3\mu$, Higgs boson decays $h \rightarrow ZZ \rightarrow 4\mu$ and $h \rightarrow 4\mu$, B meson decay $B \rightarrow 2\mu$, and two-Higgs doublet model extended with a scalar singlet (2HDM + S) Higgs decay $h \rightarrow (Za) aa \rightarrow b\bar{b}\mu\mu$, the latter decay processes have been considered in the current work.

Therefore, including both detector upgrade and physics analysis components, the structure of the current thesis is as follows:

Chapter 1 is a prologue that provides a general overview and thesis layout.

Chapter 2 provides a brief review of the SM and introduces the models used for benchmarking the performance of the search. It also introduces the Large Hadron Collider (LHC) and Compact Muon Solenoid (CMS) experiment with the focus on its muon sub-detectors, since part of the work in this thesis is particularly dedicated to muon upgrade.

Chapter 3 describes the CMS muon endcap upgrade using GEM technology. It illustrates the design layout and assembly of the GEM GE1/1 chambers to be used for muon high- η endcap upgrade of the CMS [8,9]. It further describes the performance of the GE1/1 chambers in which different versions are tested for gain, efficiency, timing resolution, rate capability, and discharge probability in different gas compositions. Based on the R&D results, the recommended operating conditions of GEM chambers are provided for their proper usage in the CMS experiment. The chapter also provides a glimpse of contribution for the GE1/1 project from Delhi University (DU).

Chapter 4 provides the results of R&D on the single mask GEM foils which have been used to construct GE1/1 chambers. The GE1/1 detector employs single-mask foils having asymmetrically biconical holes. The impact of such asymmetry on the properties of GEM detectors has been evaluated by considering a small 10 cm \times 10 cm test detector, and by estimating gain, resolution, charging-up, and the rate capability. The results show that the hole asymmetry indeed has an impact on the properties of GEM detectors. Though the measurements are performed on a 10 cm \times 10 cm test detector but results are very much relevant to GE1/1 chambers as most of these properties are determined by the local phenomena taking place within the GEM holes that are independent of the size of the foils. The studies performed to understand the rate capability, demonstrate that the GEMs does not show any decrease in gain with the expected particle flux in the CMS and is, therefore, considered constant for the CMS operating region [10].

Further, this chapter provides an insight into the vital development of the first commercial double mask GEM foils produced in India [13,14]. The foils were produced as a part of the transfer of technology (TOT) between CERN and Micropack, an Indian Industry. However, before these foils could be declared fit for applications and technology as reliable, the desired quality control assessment and characterization of these foils have been performed. The quality control assessment included optical and electrical tests to check their reliability and usability. The measured optical and electrical properties of these foils reflect the desired parameters. The chapter concludes by stating that the foils are at par with the double mask GEM foils produced at CERN, and are declared fit for scientific and other applications.

Chapter 5 presents the first search results for the Higgs boson decay to an electroweak Z boson and a light pseudoscalar particle having pair of b quarks jets and pair of muons in the final state [15]. The decay channel ($h \rightarrow Za \rightarrow b\bar{b}\mu^-\mu^+$) is extremely motivated in many Beyond Standard Models (BSMs) and is expected to provide better sensitivity compared to other final states with either 4 b -quark jets or 4 leptons. The measurements at 8 TeV data leave room for such decays at 95% Confidence Limits (CLs) with a limit of 34% [11,12].

Despite its low branching fraction, the analysis profits from the excellent dimuon mass resolution of the CMS experiment, and with the current data, the channel is very promising to explore BSM physics. The search uses proton-proton collision data collected by the CMS experiment at center-of-mass energy equal to 13 TeV corresponding to an integrated luminosity of 41.5 fb^{-1} during the year 2017. The measurements performed so far are consistent with the exotic decays of the Higgs boson which are allowed in the BSM models.

Chapter 6 reports a search for the exotic decay to a pair of new pseudoscalar spin-0 light bosons in the decay channel $h \rightarrow aa \rightarrow b\bar{b}\mu^-\mu^+$. The search for a narrow dimuon resonance has been conducted using a dataset collected by the CMS during the year 2017 [16]. The data sample corresponds to an integrated luminosity of 41.5 fb^{-1} and has been collected at 13 TeV center-of-mass energy proton-proton collisions. The decay channel has also been probed during Run-I of the LHC. Compared to Run-I analysis, several improvements have been made in the search strategy. In addition to the gluon-gluon fusion (ggF) production mechanism, vector boson fusion (VBF) production process has been included. Apart from the new tagger, DeepCSV, new optimization techniques that include event categorization has been employed to enhance the search sensitivity. Contributions to the current final state due to hadronically decaying τ leptons being misidentified as b quark jets from the decays $h \rightarrow aa \rightarrow \mu^-\mu^+\tau^-\tau^+$ and $h \rightarrow aa \rightarrow b\bar{b}\tau^-\tau^+$ have also been studied.

Chapter 7 is an epilogue that summarizes the contributions of this Ph.D. project to the CMS muon upgrade. It also sums up the results of R&D and the outcome of physics analysis performed throughout the tenure of this work.

BIBLIOGRAPHY

- [1] F. Englert et al., “[Broken symmetry and the mass of gauge vector mesons](#)”, Phys. Rev. Lett. 13 (1964) 321.
- [2] P. W. Higgs, “[Broken symmetries, massless particles and gauge fields](#)”, Phys. Lett. 12 (1964) 132.
- [3] P. W. Higgs, “[Broken symmetries and the masses of gauge bosons](#)”, Phys. Rev. Lett. 13 (1964) 508.
- [4] ATLAS Collaboration, “[Observation of a new particle in the search for the Standard Model Higgs boson with the ATLAS detector at the LHC](#)”, Phys. Lett. B 716 (2012).
- [5] CMS Collaboration, “[Observation of a new boson at a mass of 125 GeV with the CMS experiment at the LHC](#)”, Phys. Lett. B 716 (2012).
- [6] D. Curtin et al., “[Exotic decays of the 125 GeV Higgs boson](#)”, Phys. Rev. D 90 (2014) 075004.
- [7] CMS Collaboration, “[The CMS experiment at the CERN LHC](#)”, JINST, 3 (2008) S08004.
- [8] D. Abbaneo, A. H. Shah et al., “[Layout and assembly technique of the GEM chambers for the upgrade of the CMS first muon endcap station](#)”, Nucl. Inst. Meth. A 918 (2019) 67.
- [9] A. Shah et al., “[A Novel Assembly Procedure of GE1/1 Detectors for CMS High Luminosity Phase of the LHC](#)”, Spring. Proc. in Phy., (2018) 203.
- [10] A. Shah, “[Impact of single-mask hole asymmetry on the properties of GEM detectors](#)” Submitted to Nucl. Inst. Meth. A, [arXiv:1811.04439](#).
- [11] ATLAS and CMS Collaborations, “[Measurements of the Higgs boson production and decay rates and constraints on its couplings from a combined ATLAS and CMS analysis of the LHC pp collision data at \$\sqrt{s} = 7\$ and 8 TeV](#)”, JHEP 08 (2016) 045.
- [12] ATLAS and CMS Collaborations, “[Combined measurement of the Higgs boson mass in pp collisions at \$\sqrt{s} = 7\$ and 8 TeV with the ATLAS and CMS experiments](#)”, Phys. Rev. Lett. 114 (2015) 191803.

- [13] A. Shah et al., “[Development, characterization and qualification of first GEM foils produced in India](#)”, Nucl. Inst. Meth. A 892, (2018) 10.
- [14] M. Gola. A. Shah et al., “[Performance of the triple GEM detector built using commercially manufactured GEM foils in India](#)”, Nucl. Inst. Meth. A, 951 (2020) 162967.
- [15] CMS Collaboration, “[Search for exotic Higgs boson decay into a \$Z\$ boson and a pseudoscalar boson with \$b\bar{b}\mu^-\mu^+\$ as a final state](#)”, CMS AN-2019/007, in CMS review.
- [16] CMS Collaboration, “[Search for \$h \rightarrow aa \rightarrow b\bar{b}\mu^-\mu^+\$: Combined Run-II results](#)”, CMS AN-2019/194, in CMS review.

Theoretical background and overview of the LHC

*I do present you with a man of mine
Cunning in music and the mathematics
To instruct her fully in those sciences.*

— William Shakespeare

The Higgs boson is the last prognosticated particle of the Standard Model (SM). Its existence was predicted back in the 1960s, and it has been the topic of several large physics experiments. The Higgs boson, as introduced within the SM is the manifestation of the Brout-Englert-Higgs (BEH) mechanism. Other types of the Higgs bosons are also predicted by theories that go beyond the Standard Model. In July 2012, physicists at the Large Hadron Collider (LHC) announced the discovery of a new particle with a mass of around 125 GeV. While the discovery of this new particle is encouraging, its exact identity is yet to be ascertained and it will take further work to ascertain whether or not it is the Higgs boson predicted by the SM and the work performed in this thesis is an effort in this regard.

The current chapter provides a brief introduction to the BEH mechanism followed by an overview of the exotic Higgs boson decays within the two-Higgs-doublet model extended with a complex scalar singlet (2HDM+S) which has been used to benchmark the performance of the searches carried out in this thesis. Also, an overview of the Large Hadron Collider (LHC) is provided with a special focus on the muon endcap of the Compact Muon Solenoid (CMS) experiment as part of the work is on its muon spectrometer upgrade.

2.1 The Standard Model (SM)

The SM of particle physics presents a description of the elementary particles and their interactions. It was mostly developed between 1960s and 1970s and has been most successful in explaining the outcome of the various physics experiments. The most important predictions of the SM that were experimentally confirmed are the existence of the Z and W^\pm bosons discovered at CERN [1], the top quark found at the Tevatron [2], and the most recent discovery of Higgs boson at the LHC [3, 4]. The SM postulates the existence of fermions classified into leptons and quarks that form the known matter. The interactions between fermions are described by fields mediated by the exchange of gauge bosons. The model provides a

description of the electromagnetic, weak, and strong force. However, it does not include the gravitational force. The theoretical description is given in the framework of quantum field theory (QFT) where the key assumption is the “gauge invariance”. The underlying symmetry is $SU(3)_C \times SU(2)_L \times U(1)_Y$ and the description follows to a large extent from the textbooks provided in references [5–7].

2.1.1 Fundamental interactions

The SM consists of different components, each representing specific interactions of the elementary particles. Historically, the first and very important part is Quantum Electrodynamics (QED) which describes the electromagnetic interactions, and the second part is Quantum Chromodynamics (QCD) which describes the strong interactions. The weak force is unified with QED in the Electroweak (EW) model [8–10], and describes the weak interactions. The latter is also called “GWS model”, after the names of physicists Glashow, Weinberg, and Salam.

Quantum electrodynamics (QED)

The QED is mathematically described by a Lagrangian or more precisely Lagrangian density, ‘ \mathcal{L} ’, which is derived by invoking symmetry arguments and the invariance under local phase transformation. For a free fermion (spin- $\frac{1}{2}$), it is written as

$$\mathcal{L} = i\bar{\psi}\gamma^\mu\partial_\mu\psi - m\bar{\psi}\psi \quad (2.1)$$

where ψ is the Dirac spinor of the fermion field and $\bar{\psi} = \psi^\dagger\gamma^0$ is its adjoint, γ^μ are the Dirac gamma matrices and $\partial_\mu = \frac{\partial}{\partial x^\mu}$ are the partial derivatives. The Dirac equation

$$(i\gamma^\mu\partial_\mu - m)\psi = 0 \quad (2.2)$$

is the corresponding equation of motion.

The Lagrangian in Equation 2.1 is required to be invariant under local phase transformations of the form

$$\psi(x) \rightarrow \psi'(x) = e^{i\alpha(x)}\psi(x) \quad (2.3)$$

where $\alpha(x)$ represents the local phase. The transformations form a $U(1)$ abelian unitary group as $e^{i\alpha(x)}$ can be written as a 1×1 U matrix with $U^\dagger U = 1$. It is found from the first term of the Equation 2.1, \mathcal{L} is not invariant under this transformation, since

$$\partial_\mu\psi \rightarrow \partial_\mu\psi' = e^{i\alpha(x)}\partial_\mu\psi + ie^{i\alpha(x)}\psi\partial_\mu\alpha(x) \quad (2.4)$$

The invariance is, however, established by introducing an additional field A_μ , transforming as

$$A_\mu \rightarrow A'_\mu = A_\mu + \frac{1}{e}\partial_\mu\alpha(x) \quad (2.5)$$

Replacing ∂_μ in Equation 2.5 with the covariant derivative D_μ as

$$D_\mu = \partial_\mu - ieA_\mu \quad (2.6)$$

we find

$$D_\mu \psi \rightarrow D'_\mu \psi' = e^{i\alpha(x)} D_\mu \psi \quad (2.7)$$

and the Lagrangian density becomes

$$\mathcal{L} = i\bar{\psi}\gamma^\mu D_\mu \psi - m\bar{\psi}\psi \quad (2.8)$$

$$= \bar{\psi}(i\gamma^\mu \partial_\mu - m)\psi + e\bar{\psi}\gamma^\mu \psi A_\mu \quad (2.9)$$

Therefore, by introducing the gauge field A_μ , the local phase invariance is re-established. Thus field couples to the fermionic field with the coupling constant e , the elementary electric charge. By introducing a kinetic term employing the field strength tensor $F_{\mu\nu} = \partial_\mu A_\nu - \partial_\nu A_\mu$, the gauge field A_μ is identified as the physical photon field and the complete Lagrangian of the QED takes the form as

$$\mathcal{L}_{QED} = i\bar{\psi}\gamma^\mu \partial_\mu \psi - m\bar{\psi}\psi + e\bar{\psi}\gamma^\mu \psi A_\mu - \frac{1}{4}F_{\mu\nu}F^{\mu\nu} \quad (2.10)$$

The specific terms are the kinetic energy and mass of the fermionic fields, the coupling between photonic and fermionic fields, and the last term is the kinetic energy of the photonic field. The local phase invariance prohibits the introduction of a mass term of the form $\frac{1}{2}m^2 A_\mu A^\mu$ for the photonic field. Hence this formalism requires photon to be massless, which is in line with known experimental findings.

Quantum chromodynamics (QCD)

The QCD describes the interaction of quarks and gluons. In QCD, quarks are treated as fermions with an additional degree of freedom: the color charge, which exists in the states red (r), green (g), and blue (b). The Lagrangian is derived by including eight gauge fields G_μ^a , $a = 1, \dots, 8$ corresponding to gluons and substituting three Dirac spinors by vectors of three spinors representing quarks as

$$\mathcal{L}_{QCD} = i\bar{\psi}\gamma^\mu \partial_\mu \psi - m\bar{\psi}\psi - g_s \left(\bar{\psi}\gamma^\mu \frac{\lambda_a}{2} \psi \right) G_\mu^a - \frac{1}{4}G_{\mu\nu}^a G_a^{\mu\nu} \quad (2.11)$$

where g_s denotes the strong coupling constant, λ_a are the eight Gell-mann-matrices. The three component ψ spinor and $G_{\mu\nu}^a$ field strength tensor are written as

$$\psi = \begin{pmatrix} \psi_r \\ \psi_g \\ \psi_b \end{pmatrix} \text{ and } G_{\mu\nu}^a = \partial_\mu G_\nu^a - \partial_\nu G_\mu^a - g_s f_{abc} G_\mu^b G_\nu^c$$

The Equation 2.11 is invariant under transformations of the non-abelian unitary group $SU(3)_C$, whose generators are $T_a = \lambda_a/2$. Since $SU(3)_C$ is non-abelian and does not have its equivalent in QED, it contributes an additional (last) term to the field strength tensor and enables the gluons to interact with themselves. Imposing the local phase invariance condition makes force carriers, here gluons, to be massless. The structure constants f_{abc} fulfill the condition $\left[\frac{\lambda_a}{2}, \frac{\lambda_b}{2} \right] = i f_{abc} \frac{\lambda_c}{2}$.

Electroweak (EW) model

In the EW model, all the fermions are subjected to the weak force and the interaction is carried out by the exchange of W^\pm and Z bosons, known as charged and neutral current interactions, respectively. While the exchange of W^\pm bosons allows changing the flavor of quarks, there are no flavor-changing neutral currents (FCNC) observed at the tree level. Experiments reveal that the charged weak current couples only to left-handed fermions.

In the EW model, conserving weak $SU(2)_L \times U(1)_Y$ symmetry, the left-handed fermions are described by $SU(2)_L$ doublets with the corresponding isospin of $I = \frac{1}{2}$ and gauge fields W_μ^a . The $U(1)_Y$ singlets describe the right-handed fermions with $I = 0$ and gauge field B_μ . Also, the hypercharge Y which has a relationship with the electric charge via $Q = I_3 + Y/2$ is introduced.

There are left-handed isospin doublets χ_L and right-handed singlets ψ_R which form $SU(2)_L \times U(1)_Y$ symmetry and under local phase transformation behaves as

$$\chi_L(x) \rightarrow \chi'_L(x) = e^{i\alpha_a(x)\tau_a} e^{i\beta(x)Y} \chi_L \quad (2.12)$$

$$\psi_R(x) \rightarrow \psi'_R(x) = e^{i\beta(x)Y} \psi_R \quad (2.13)$$

where, $\alpha(x)$ and $\beta(x)$ are the local phases, τ_a with $a = 1, 2, 3$ are the generators of $SU(2)_L$, and Y which is generating $U(1)_Y$ is the weak hypercharge operator.

The resulting electroweak Lagrangian is formed as

$$\mathcal{L}_{EW} = i\bar{\chi}_L^i \gamma^\mu D_\mu \chi_L^i + i\bar{\psi}_R^i \gamma^\mu D_\mu \psi_R^i - \frac{1}{4} W_{\mu\nu}^a W_a^{\mu\nu} - \frac{1}{4} B_{\mu\nu} B^{\mu\nu} \quad (2.14)$$

with the covariant derivative D_μ given by

$$D_\mu = \partial_\mu + ig W_\mu^a \frac{\tau_a}{2} + ig' B_\mu \frac{Y}{2} \quad (2.15)$$

where g and g' represents the coupling constants of the $SU(2)_L$ gauge field W_μ^a , and the $U(1)_Y$ gauge field B_μ , respectively.

The field tensors in Equation 2.14 are given by

$$W_{\mu\nu}^a = \partial_\mu W_\nu^a - \partial_\nu W_\mu^a - g\epsilon_{abc} W_\mu^b W_\nu^c \quad (2.16)$$

$$B_{\mu\nu} = \partial_\mu B_\nu - \partial_\nu B_\mu \quad (2.17)$$

The structure constants of $SU(2)_L$ in the Equation 2.16 denoted by ϵ_{abc} form a completely antisymmetric tensor enabling W_μ^a fields to interact with themselves, while the structure constant of $U(1)_Y$ is zero, meaning B_μ field has no self-interaction.

The physical fields are obtained by the linear combinations of W_μ^a and B_μ as

$$W_\mu^\pm = \frac{1}{\sqrt{2}} (W_\mu^1 \mp iW_\mu^2) \quad (2.18)$$

$$Z_\mu = \cos\theta_W W_\mu^3 - \sin\theta_W B_\mu \quad (2.19)$$

$$A_\mu = \sin\theta_W W_\mu^3 + \cos\theta_W B_\mu \quad (2.20)$$

where θ_W is the weak mixing angle and relates the coupling constants through $\cos\theta_W = g/\sqrt{g^2 + g'^2}$ and $\sin\theta_W = g'/\sqrt{g^2 + g'^2}$.

It is very clear that the local phase invariance in QED and QCD prohibits the introduction of mass terms for the bosons, and similarly, in the electroweak sector, mass term of the form $-m\bar{\psi}\psi$ is forbidden for the fermions. This is in contradiction with the experiments where the W^\pm and Z bosons, and the fermions are found to be massive. The problem is, however, solved by the Higgs mechanism described in the following section.

2.1.2 The Higgs mechanism

The predicted bosons by the SM¹, as described in Section 2.1.1, must be massless, otherwise, the $SU(2)_Y$ gauge invariance would be broken. However, the masses of the W^\pm and Z bosons must be non-zero to describe the short range of the weak force [9–11]. Therefore, the gauge theory that works for electromagnetism appears like a natural explication for the weak force as the experimental evidence pointed to a force mediated by more massive particles. Latter can be achieved by breaking the $SU(2)_L \times U(1)_Y$ symmetry of the electroweak sector, yielding the concept Brout-Englert-Higgs-Guralnik-Hagen-Kibble mechanism, now popularly known as the Higgs mechanism [12–15].

To illustrate this mechanism, consider a very simplified model consisting of a single complex field, the Higgs field $\phi = \phi_1 + i\phi_2$ having Lagrangian

$$\mathcal{L} = \frac{1}{2}(\partial^\mu \phi^\dagger)(\partial_\mu \phi) - V(\phi), \quad (2.21)$$

$$\text{with } V(\phi) = \frac{1}{2}\mu^2 |\phi^\dagger \phi| + \frac{1}{4}\lambda(|\phi^\dagger \phi|)^2 \quad (2.22)$$

Notice from the Equation 2.21 that if the mass term², μ^2 , takes a negative value, then the minimum of this potential occurs at a non-zero value of ϕ . Figure 2.1 shows this potential in a complex space for the arbitrary values of μ and λ , the minimum energy occurs for a continuous set of values on a circle of radius $\nu = \sqrt{\frac{-\mu^2}{\lambda}}$ and the Lagrangian is invariant with respect to the position on this circle.

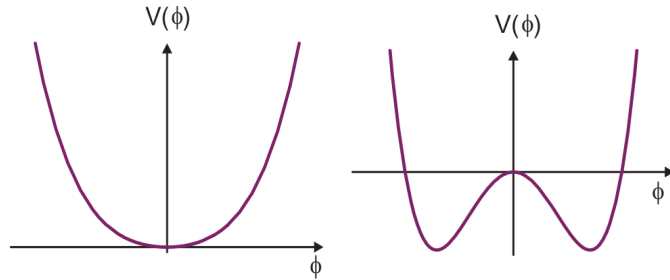


Figure 2.1: Potential $V(\phi)$ as a function of field ϕ for: (left) $\mu^2 > 0$ with minimum at $\phi_0 = 0$ and (right) $\mu^2 < 0$ with minimum at $\phi_0 = \pm\nu$.

¹The theory is explicitly referred to as Yang-Mills gauge theory.

²The mass is denoted here with μ so as to be consistent with the terminology used in most of the literature.

Expanding field $\phi = \frac{1}{\sqrt{2}}(\nu + \phi_1 + i\phi_2)$ around minimum ν (basically, around a circle of radius ν) in the potential, the effective Lagrangian for the Higgs sector becomes

$$\mathcal{L} = \frac{1}{2}\mu^2\phi_2^2 + \frac{\lambda}{4}|\phi_2|^4 \quad (2.23)$$

$$= \frac{1}{2}\mu^2(\phi_1^2 + \phi_2^2) + \frac{1}{4}\lambda(3\nu^2\phi_1^2 + 2\nu^2\phi_2^2 + \phi_1^4 + \phi_2^4 + 2\phi_1^2\phi_2^2 + 4\nu\phi_1^3 + 4\nu\phi_1\phi_2^2) \quad (2.24)$$

$$= -\mu^2\phi_1^2 + \frac{1}{4}\lambda\phi_1^4 + \frac{1}{4}\phi_2^4 + \frac{1}{2}\lambda\phi_1^2\phi_2^2 + \lambda\nu\phi_1^3 + \lambda\nu\phi_1\phi_2^2 \quad (2.25)$$

where the field ϕ_2 is massless, and if the exercise is repeated for a tuplet of ‘ n ’ fields, $\Phi = \phi_1, \phi_2, \dots, \phi_n$, with a same potential term, $\Phi^\dagger\Phi = \phi_1^2 + \phi_2^2 + \dots + \phi_n^2$, similar results can be obtained. The minimum of the potential would lie on hyperspace of radius ν , choosing an arbitrary direction on the sphere and expanding around this minimum, one massive and ‘ $n - 1$ ’ massless fields are found. This is a fundamental example of the Goldstone theorem, which states for every spontaneously broken continuous symmetry, a massless spin-0 boson known as the Goldstone boson is obtained [16].

Spontaneous symmetry breaking

Consider again the case of scalar electrodyanmics Lagrangian, as discussed in Section 2.1.1 with an additional quadratic coupling term as

$$\mathcal{L} = D_\mu\phi^\dagger D^\mu\phi - \frac{1}{2}\mu^2|\phi^\dagger\phi| + \frac{1}{4}\lambda(|\phi^\dagger\phi|)^2 + F_{\mu\nu}F^{\mu\nu} \quad (2.26)$$

Such a Lagrangian is invariant under local $U(1)_Y$ transformation, $\phi \rightarrow e^{ie\alpha(a)}\phi$, and if we expand the kinetic term in it, we obtain

$$D_\mu\phi^\dagger D^\mu\phi = \frac{1}{2}(\partial^\mu\phi_1)(\partial_\mu\phi_1) + \frac{1}{2}(\partial^\mu\phi_2)(\partial_\mu\phi_2) + \nu^2\lambda\phi_1^2 + \frac{1}{2}e^2\nu^2 A_\mu A^\mu + ie\phi_1\partial_\mu A^\mu + ie(\partial_\mu\phi_1)A^\mu + \dots \quad (2.27)$$

The previously massless gauge boson A_μ , now appears with a mass term. Here, the ϕ_1 has gained a mass term, and ϕ_2 represents the massless Goldstone boson predicted by Goldstone’s theorem. This demonstrates that in such a simplified model, it is indeed possible to generate mass for a gauge boson with the penalty of birth of a new massless particle, but no such a particle has ever been observed. Therefore, any theory attempting to use spontaneous symmetry breaking to generate mass must explain it.

Another problem with the above Lagrangian is that it has more degrees of freedom than it had at the time of beginning. Initially, complex scalar had two degrees and one massless vector boson, and now it has two scalar fields, plus a massive gauge boson resulting in three degrees of freedom. Also, there are unphysical bilinear terms in the Lagrangian. The Lagrangian, however, can be made more comprehensible by noting that the complex field, $\phi = \nu + \phi_1 + i\phi_2$, can equivalently be written as

$$\phi = e^{i\frac{\Gamma(x)}{\nu}}(\nu + \phi_1(x)) \quad (2.28)$$

A gauge term can be added to the vector field to form $A_\mu \rightarrow A_\mu + \frac{1}{e\nu} \partial_\mu \Gamma(x)$, as the original field is invariant under the gauge transformations of the form $e^{i\alpha(x)}$. By rotating the complex field ϕ by $e^{-i\Gamma(x)}$ eliminates the term $e^{i\Gamma(x)}$, but the new effective Lagrangian is not invariant under the gauge transformation. The kinetic term in the new Lagrangian after introducing modified scalar field $\phi = \nu + \phi_1(x)$ takes the form

$$D_\mu \phi^\dagger D^\mu \phi = \frac{1}{2}(\partial^\mu \phi_1)(\partial_\mu \phi_1) + \frac{1}{2}e^2\nu^2 A_\mu A^\mu + \nu^2 \lambda \phi_1^2 + \frac{1}{2}e^2\nu^2 A_\mu A^\mu + \dots \quad (2.29)$$

Now, the massless Goldstone boson, as well as bilinear terms, disappear from the Lagrangian, and only physical fields, a massive gauge boson and a massive scalar field remain [17]. Such a gauge is known as the unitary gauge. However, after this transformation, the Lagrangian no longer appears to be invariant under the $U(1)_Y$ gauge symmetry. Notice that the actual theory is still invariant under it but the theory evaluated around the vacuum state³ is not and it is stated that the $U(1)_Y$ gauge symmetry is spontaneously broken.

As remarked earlier, the electroweak symmetry must be broken because of the non-zero mass of the W^\pm and Z bosons. The special case considered here shows that it is possible. In the next section, it is considered for the SM as a whole and the Higgs mechanism is introduced to the $SU(2)_L \times U(1)_Y$ symmetry group, and expanding around the minimum of the Higgs potential, it is shown that gauge symmetry no longer manifests in the theory, and the W^\pm and Z bosons gain mass. Similar statements can be made to provide mass terms to fermions.

2.1.3 SM Higgs field

In the SM, a sophisticated mechanism is required to describe the masses of the three electroweak bosons. The existence of a complex scalar doublet [18], represented by Φ is postulated as

$$\Phi = \frac{1}{\sqrt{2}} \begin{pmatrix} \phi^\dagger \\ \phi^0 \end{pmatrix} = \frac{1}{\sqrt{2}} \begin{pmatrix} \phi_1 + i\phi_2 \\ \phi_3 + i\phi_4 \end{pmatrix} \quad (2.30)$$

adding following gauge invariant terms to the SM Lagrangian,

$$\mathcal{L} = (D^\mu \Phi^\dagger)(D_\mu \Phi) - V(\Phi) \quad (2.31)$$

$$V(\Phi) = \frac{1}{2}\mu^2 |\Phi^\dagger \Phi| + \frac{1}{4}\lambda(|\Phi^\dagger \Phi|)^2 \quad (2.32)$$

the doublet in Equation 2.30 couples to electroweak sector and the field Φ interacts with the B and W fields through the covariant derivative

$$D_\mu = \partial_\mu + i\frac{g}{2}\tau \cdot W_\mu - i\frac{g'}{2}B_\mu Y \quad (2.33)$$

³The vacuum energy state is the lowest energy state of the theory.

2.1. THE STANDARD MODEL (SM)

Since the Higgs field has four degrees of freedom and after expanding potential around some arbitrary minimum of the Higgs potential, the minimum lies on a four-dimensional hyperspace of radius $\nu = \sqrt{\frac{-\mu^2}{\lambda}}$.

Redefining fields as

$$W^\pm = \frac{1}{\sqrt{2}}(W_\mu^1 \mp iW_\mu^2) \quad (2.34)$$

$$Z^\mu = \frac{g_2 W_\mu^3 - g_1 B_\mu}{\sqrt{g_1^2 + g_2^2}} \quad (2.35)$$

$$A^\mu = \frac{g_2 W_\mu^3 + g_1 B_\mu}{\sqrt{g_1^2 + g_2^2}} \quad (2.36)$$

and using the gauge invariance to rotate the unitary gauge as

$$\Phi = e^{-i\theta(x)\tau} \begin{pmatrix} 0 \\ h(x) + \nu \end{pmatrix} \rightarrow \begin{pmatrix} 0 \\ h(x) + \nu \end{pmatrix}, \quad (2.37)$$

following mass terms are obtained with A^μ being massless

$$\left(\frac{\nu g_2}{2}\right)^2 W_\mu^+ W^{-\mu} + \left(\frac{\nu \sqrt{g_1^2 + g_2^2}}{2}\right)^2 Z_\mu Z^\mu \quad (2.38)$$

The fermion masses can also be obtained using Higgs fields as described above. The quarks and leptons could be coupled by adding gauge-invariant Yukawa interactions to the SM Lagrangian⁴

$$\mathcal{L}_f = \lambda_e \bar{L} \Phi_{e_R} + \lambda_d \bar{Q}_L \Phi_{d_R} + \lambda_u \bar{Q}_L \Phi^c u_R + h.c. \quad (2.39)$$

After subjecting Equation 2.39 to unitary gauge, it becomes

$$\mathcal{L}_f = \lambda_e e_L(\nu + h)e_R + \dots \quad (2.40)$$

which corresponds to a fermionic mass term, m_e and a Higgs coupling term, g_{hff} ,

$$m_e = \frac{\lambda_e \nu}{\sqrt{2}} \quad (2.41)$$

$$g_{hff} = \frac{\lambda_e}{\sqrt{2}} = \frac{m_e}{\nu} \quad (2.42)$$

The term g_{hff} defines the coupling in terms of mass and vacuum expectation value of the Higgs field, ν . In terms of the W mass and g_2 , the vacuum expectation value is written as

$$\nu = \frac{2m_W}{g_2} = 246 \text{ GeV} \quad (2.43)$$

⁴h.c. indicates the Hermitian conjugate of the preceding terms.

where, m_W is measureable and g_2 can be measured using couplings of W to fermions. The remaining terms in the Lagrangian involve the Higgs itself,

$$V_H = (D^\mu \Phi^\dagger)(D_\mu \Phi) - \frac{\mu^2}{2} \Phi^\dagger \Phi - \frac{\lambda}{4} (\Phi^\dagger \Phi)^2 \quad (2.44)$$

which can be expressed in unitary gauge as

$$V_H = (\partial^\mu \phi)(\partial_\mu \phi) - \frac{\mu^2}{2} (\eta + h)^2 - \frac{\lambda}{4} (\eta + h)^2 = (\partial^\mu \phi)(\partial_\mu \phi) - \lambda \nu^2 h^2 - \lambda \nu h^3 - \frac{\lambda}{4} h^4 \quad (2.45)$$

Finally, the Higgs mass can be presented as

$$m_h = 2\lambda \nu^2 \quad (2.46)$$

From the above discussion, it is clear that the Higgs couplings involve trilinear and quartic-coupling terms. The couplings to gauge bosons and fermions are ascertained by theory as a function of Higgs boson mass and hence reduces the search for the Higgs boson to only one parameter. Also, since the field has a non-zero vacuum expectation value, the proposed Higgs field must be a scalar as the non-scalar field would break the Lorentz invariance of the vacuum. Also, since the field is a scalar, the predicted Higgs boson by SM must be spin-zero with even CP. Further, as the couplings are determined by theory, measuring them accurately would confirm if the discovered boson is really SM boson. However, the precision obtained with the current LHC data is not yet enough to ascertain whether it is a SM or BSM boson.

2.2 Physics beyond the SM

Although the SM provides the best description of the subatomic world along with the prediction of a scalar with properties close to that of discovered boson, this theory has several limitations. It does not provide a complete description of nature, and there are many strong conceptual implications of the existence of BSM physics expected to manifest at TeV energies. Some of these include the existence of dark matter in the universe, the lack of explanation of the bosons which mediate gravitational interactions within the SM, the asymmetry between matter and antimatter, problem of naturalness and coupling unification.

The simple extensions of the SM are two-Higgs-doublet models (2HDM) [19], where two doublets of scalar fields are considered leading to five physical states after symmetry breaking. These include two neutral scalars h and H , one CP-odd pseudoscalar A and two charged scalars H^\pm . The minimal supersymmetric extension of the SM (MSSM) which addresses the coupling unification and the hierarchy problem is included in 2HDM models. Moreover, these models could explain the baryon asymmetry by permitting the existence of additional sources of CP-violation with respect to the SM. Further, these models are simple extensions of the SM in the scalar sector. The two-Higgs-doublet model with extra singlet (2HDM+S) obtained by adding a complex scalar singlet to already present scalar doublets in 2HDM

results into addition of two new bosons. There are four types of such models and a special case of the 2HDM+S type-2 model represents the next-to-minimal supersymmetric extension of the SM (NMSSM) [20–22].

2.2.1 Exotic decays of the Higgs boson

The 2HDM+S identifies already discovered 125 GeV boson as h boson and allows it to decay exotically to non-SM particles. Such decays are also allowed in 2HDM but have been extremely constrained so far by the LHC searches. The extension of 2HDM with a singlet does not have its own Yukawa couplings but couples to Φ_1 and Φ_2 in the potential in such a way that it inherits its couplings to SM fermions. The mixing of scalar h with singlet S should be very small to allow SM-like properties. The pseudoscalar a and the scalar s inherit from the imaginary and real parts of the singlet leading to the possibility of exotic decays of h .

In general, there are four types of 2HDM+S with different scenarios leading to various signatures for exotic h decays:

Type-1: Such type of model considers the branching fractions of the pseudoscalar proportional to those in SM with the coupling of all the fermions to Φ_1 . The branching fractions are further considered as independent of $\tan\beta$.

Type-2: It considers the coupling of down-type quarks and leptons to the same doublet as in the NMSSM. The branching fractions of the pseudoscalar to down-type quarks and leptons are enhanced for larger values of $\tan\beta$ (values greater than unity). This makes $h \rightarrow aa \rightarrow b\bar{b}b\bar{b}$, $h \rightarrow aa \rightarrow b\bar{b}\mu^-\mu^+$ and $h \rightarrow aa \rightarrow b\bar{b}\tau^-\tau^+$ interesting decay channels to look for exotic h decays.

Type-3: This type of model considers the coupling of leptons to the Φ_2 doublet enhancing the branching fractions of pseudoscalar decays to leptons for larger values of $\tan\beta$ making $h \rightarrow aa \rightarrow \mu^-\mu^+\tau^-\tau^+$ and $h \rightarrow aa \rightarrow \tau^-\tau^+\tau^-\tau^+$ decays favoured channels.

Type-4: This type of model enhances the pseudoscalar decays to up-type quarks and leptons for larger values of $\tan\beta$, making $h \rightarrow aa \rightarrow b\bar{b}\tau^-\tau^+$ and $h \rightarrow aa \rightarrow c\bar{c}\tau^-\tau^+$ interesting decay channels.

The exotic pseudoscalar decays are the simplest extension of the SM and are yet permitted after all the measurements made during Run-I of the LHC. Indeed an upper limit on the branching of the h (125 GeV) boson to BSM particles leaves a large room for its possible exotic decays. Specifically, the CMS measured at 95% CL using Run-I LHC data, the $\mathcal{B}(h \rightarrow \text{BSM})$ less than 30% [19]. Projections for future LHC runs provide precision on $\mathcal{B}(h \rightarrow \text{BSM})$ of the order of 10%, which nevertheless allows for non-negligible decays of the 125 GeV boson.

Out of the interesting decay channels, the $h \rightarrow Za$ and $h \rightarrow aa$ with $b\bar{b}\mu^-\mu^+$ as a final state are considered in Chapter 5 and Chapter 6 of the present thesis, respectively. The bound on $\mathcal{B}(h \rightarrow Za) \times \mathcal{B}(a \rightarrow \mu^-\mu^+)$ is $\leq 10^{-4}$ for considered mass range $11 \leq m_a \leq 34$ GeV, and for $\mathcal{B}(h \rightarrow aa) \times \mathcal{B}(a \rightarrow \mu^-\mu^+)$, it is higher by a factor of 10 in the mass range $20 \leq m_a \leq 62.5$ GeV compared to former decay mode. The possibility of the Higgs boson decaying to $b\bar{b}\mu^-\mu^+$ final state via BSM particles is intriguing as presence of a clean dimuon resonance makes it very attractive for discovering SM extensions with extra singlets. In context of

2HDM+S and NMSSM models, it represents a compromise between very difficult but often dominant $b\bar{b}b\bar{b}$ final state and the spectacular but rare $\mu^-\mu^+\mu^-\mu^+$ signature. Assuming SM Higgs production, a benchmark $\mathcal{B}(h \rightarrow aa) = 10\%$ leads to zero $h \rightarrow aa \rightarrow \mu^-\mu^+\mu^-\mu^+$ events from gluon fusion process at the LHC Run-I, while as about twenty $h \rightarrow aa \rightarrow b\bar{b}\mu^-\mu^+$ events are expected to occur. This is much less compared to few hundred expected events from $h \rightarrow aa \rightarrow b\bar{b}b\bar{b}$ including associated production mode. However, the backgrounds for the $b\bar{b}b\bar{b}$ search are so challenging that the $b\bar{b}\mu^-\mu^+$ final state may provide much better sensitivity in the long run [19]. Hence, current thesis considers the search study for a new light pseudoscalar boson ‘ a ’ in exotic decays of Higgs boson in the $b\bar{b}\mu^-\mu^+$ final state.

2.3 Overview of the LHC

The Large Hadron Collider (LHC) [23] is a proton-proton (and/or ion-ion) colliding machine operating at Conseil Européen pour la Recherche Nucléaire (CERN), in a deep 100 m underground tunnel having a circumference of 27 km covering Swiss and French border. The non-elementary particle such as proton is considered for collisions and such a choice with respect to electron or positron is made as the latter suffers energy losses due to the synchrotron radiation.

The LHC injection chain comprises of several accelerators with the proton beams starting from a small linear accelerator (LINAC) which is used to raise the energy of protons up to 50 MeV after stripping electrons by applying high electric fields to hydrogen atoms collected from the hydrogen cylinder. The beam is allowed to pass through a booster and then to Proton Synchrotron (PS) which raises its energy to 26 GeV. The beam is further allowed to pass through Super Proton Synchrotron (SPS) which raises its energy up to 450 GeV before beams are injected into the Large Hadron Collider (LHC) where it is accelerated up to 7 TeV with the center of mass energy equal to 13 TeV⁵. The LHC acceleration chain is sketched in Figure 2.2.

The magnetic field of 8.3 Tesla used to confine proton beams in the LHC ring is obtained by employing superconducting magnets maintained at 1.9 °K all along the ring. The radio frequency cavities are used to provide the accelerating power by providing an energy gain of 485 keV per revolution with 7 keV loss per rotation due to synchrotron radiation.

A typical proton beam at the LHC consists of bunches of protons having 10^{11} protons in each bunch. A total of 2808 bunches with a time separation of 25 ns are injected into

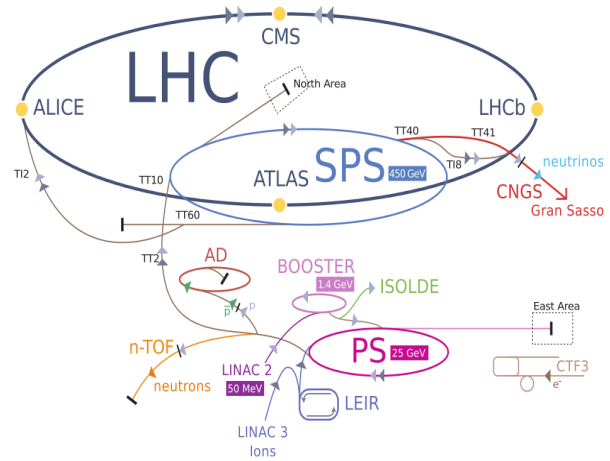


Figure 2.2: Schematic layout of the CERN LHC accelerator complex [23].

⁵The data taken during whole Run-II, a period from 2015 to 2018 were collected at 13 TeV.

synchrotrons in opposite directions and with acceleration up to 7 TeV per proton. The beams are allowed to collide at four different points which form the hearts of four experiments which include A Toroidal LHC Apparatus (ATLAS), Compact Muon Solenoid (CMS), Large Hadron Collider beauty experiment (LHCb), and A Large Ion Collider Experiment (ALICE). The ATLAS and CMS have been designed to provide sensitivity over a wide range of physics processes and are considered general-purpose detectors. On the other hand, ALICE and LHCb are specialized detectors and are used to study some particular processes such as quark-gluon plasma and matter-antimatter asymmetry, respectively. The present thesis is the part of the work carried with the CMS experiment, discussed in Section 2.3.1.

2.3.1 The CMS experiment

The CMS experiment is situated 100 m deep inside an underground LHC cavern at point 5 (P5), Cessy, France. The picture of the CMS detector is shown in Figure 2.3.

It has a cylindrical shape with a total length of around 28.7 m and a diameter of around 15.5 m. Its mechanical structure is defined by an iron yoke which is also used to collect the magnetic field from a large central solenoid. The iron yoke has a cylindrical shape and has a central region known as ‘barrel’ and two side regions around the barrel known as ‘end-caps’. Due to the large iron yoke, the CMS detector is very heavy and weighs around 14000 tons. However, in comparison to the ATLAS detector, it is very compact as it does not require an external magnetic field for the muon system. The barrel is segmented into

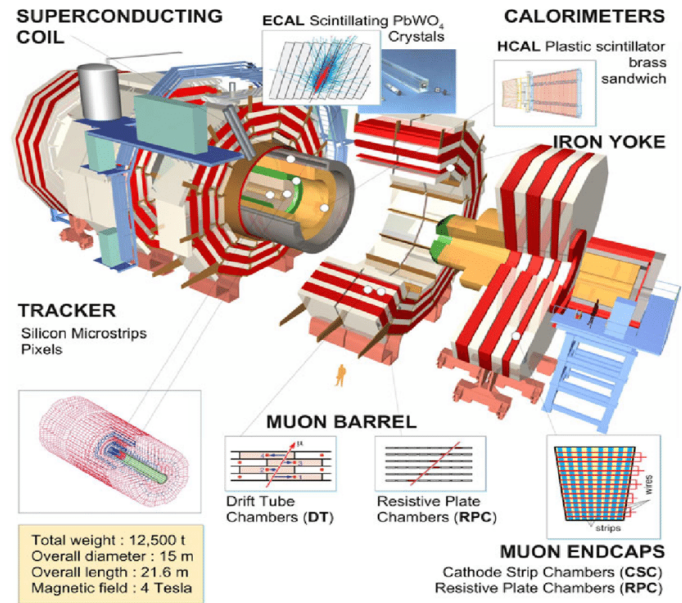


Figure 2.3: A photograph of the CMS detector showing its different subdetectors including muon stations [23, 25].

5 wheels and each endcap is segmented into three rings. The central region inside the iron yoke is delimited by a large superconducting solenoid. In the CMS barrel region and outside the solenoid, there are muon stations comprising of Cathode Strip Chambers (CSC), Drift Tubes (DT), and Resistive Plate Chambers (RPC). Inside the solenoid, there is a tracker made of silicon sensors, an electromagnetic calorimeter (ECAL) based upon lead tungstate (PbWO_4) scintillating-crystals [24] and hadron calorimeter (HCAL) mainly comprising of brass absorbers and plastic scintillators. In the endcaps, there are CSC and RPC inserted in the different rings of the yoke structure. Further details about the LHC, the CMS experiment and its subdetectors can be found in references [23, 24].

CMS muon spectrometer upgrade

The CMS muon spectrometer has important functions of muon triggering, identification, and their momentum measurement. It is very important as muon detection and recognition over the high background rates are central importance for recognizing signatures of many SM and interesting rare physics processes. Such rare signatures, include the decay of B -meson $B \rightarrow 2\mu$, tau lepton decay $\tau \rightarrow 3\mu$ and the Higgs boson decay $h \rightarrow 4\mu$. The muon system was designed to provide the measurement of charge and momentum of the muons precisely over a large kinematical range. To maintain the performance of the muon system during the high luminosity phase of the LHC (HL-LHC), it is important to mitigate the loss of efficiency due to the radiation-induced aging phenomena.

Currently, muon spectrometer of the CMS has three different detector technologies CSC, DT and RPC (Figure 2.4). The DT and RPC are present in the barrel region while as CSC and RPC are in the end cap region. The CSC and DT provide triggering and tracking while RPC provides triggering and coarse position resolution. During HL-LHC, high particle rates are expected in the forward region $1.6 < |\eta| < 2.4$ in the forward region $1.6 < |\eta| < 2.4$ of the CMS. However, CSCs are expected to suffer aging which may result in the loss of efficiency.

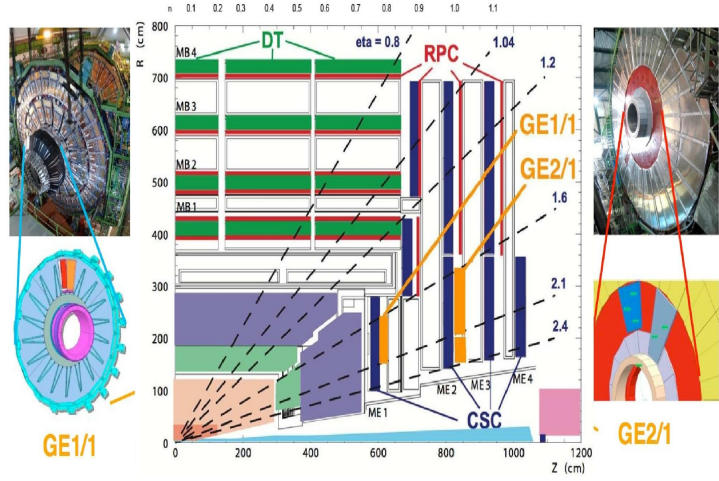


Figure 2.4: A sliced view of the CMS detector showing the muon detectors such as CSC (highlighted in blue colour), DT (in green) and RPC (in red) in the barrel and endcap [26]. Two yellow colour stations GE1/1 and GE2/1 which be installed in the CMS during LS2 and LS3 are also highlighted.

The CMS forward region has currently four stations of CSC designated as⁶ ME_x/y . The forward region $1.6 < |\eta| < 2.4$ has challenging backgrounds for muons and also lack redundancy. Therefore, to maintain the performance of the CMS detector, additional muon chambers are going to be deployed in this region. These chambers are gaseous chambers and are based on Gas Electron Multiplier (GEM) technology. This detector technology can withstand the high particle rates with an efficiency of over 98%. Additionally, these detectors have spatial and timing resolutions of the order of $100 \mu\text{m}$ and 5 ns , respectively, and would, therefore, provide precise tracking and fast triggering. Further, the gain of such detectors is stable up to 10^5 kHz/cm^2 of the incoming particle flux demonstrating that these detectors are suitable for the CMS forward endcap region.

⁶Here “M” stands for muon and “E” for endcap, and “x” for the name of the station whereas “y” the name of the ring. For example, ME1/1, where “M” stands for the muon and “E” for the endcap. The first “1” for station one and second “1” for ring one. Other notations also follow the same terminology except in the barrel region where “MB” stands for muon barrel.

The use of GEM detectors to upgrade the CMS endcap region has been approved after an intensive R&D program. The upgrade will be in the form of two GEM stations GE1/1 and GE2/1. These GE1/1 chambers⁷ will be instrumented into the CMS during second Long Shutdown (LS2) and third Long Shutdown (LS3)⁸, respectively. Both the GE1/1 and GE2/1 are trapezoidal super-chambers which are formed after combining two detectors back to back. These detectors will cover slightly more than 10° and 20° in GE1/1 and GE2/1 to provide an overlapping in azimuthal angle ϕ . In total, 36 super-chambers will be installed in the GE1/1 station and 18 in GE2/1 to provide full azimuthal coverage. Further details about the CMS muon endcap upgrade can be found in references [27, 28].

⁷In “GE1/1”, the “G” stands for GEM and the “E” for Endcap; the first “1” corresponds to the first muon station and the second “1” to the first, innermost ring of the station.

⁸The LS2 starts from the beginning of 2019 and will last till December 2020 while as LS3 will start from the beginning of 2025 and will last till the end of 2026.

BIBLIOGRAPHY

- [1] G. Taubes, “[Carlo Rubbia and the discovery of the W and the Z](#)”, Phys. World 16 (2003) 23-28.
- [2] CDF Collaboration, “[Observation of Top Quark Production in \$p\bar{p}\$ Collisions with the Collider Detector at Fermilab](#)”, Phy. Rev. Lett. 74 (1995) 2626-2631.
- [3] ATLAS Collaboration, “[Observation of a new particle in the search for the Standard Model Higgs boson with the ATLAS detector at the LHC](#)”, Phys. Lett. B 716 (2012) 1-29.
- [4] CMS Collaboration, “[Observation of a new boson at a mass of 125 GeV with the CMS experiment at the LHC](#)”, Phys. Lett. B 716 (2012) 30-61.
- [5] F. Halzen and A. D. Martin, “[Quarks and Leptons: An Introductory Course in Modern Particle Physics](#)”, Wiley, 1984.
- [6] D. Griffith, “[Introduction to Elementary Particles](#)”, Wiley-VCH, 2. ed., 2008.
- [7] M. E. Peskin and D. V. Schroeder, “[An Introduction to Quantum Field Theory](#)”, Westview Press, 1995.
- [8] S. Glashow, “[Partial Symmetries of Weak Interactions](#)”, Nucl. Phys. 22 (1961) 579.
- [9] A. Salam, “[Electromagnetic and weak interactions](#)”, Phys. Lett. 13 (1964).
- [10] S. Weinberg, “[A Model of Leptons](#)”, Phys. Rev. Lett. 19 (1967) 1264.
- [11] J. Schwinger, “[Non-abelian gauge fields. relativistic invariance](#)”, Phys. Rev. 127 (1964) 324.
- [12] P. W. Higgs, “[Broken symmetries and the masses of gauge bosons](#)”, Phys. Lett. 13 (1964) 508.
- [13] F. Englert et al., “[Broken Symmetry and the Mass of Gauge Vector Mesons](#)”, Phys. Rev. Lett. 13 (1964) 321.
- [14] G. S. Guralnik et al., “[Global Conservation Laws and Massless Particles](#)”, Phys. Lett. 13 (1964) 585.

- [15] T. W. B. Kibble, “[Symmetry Breaking in Non-Abelian Gauge Theories](#)”, Phys. Rev. Lett. 155 (1967) 1554.
- [16] J. Goldstone, “[Field theories with superconductor solutions](#)”, Nuovo Cim. 19 (1961) 154.
- [17] A. Djouadi, “[The anatomy of electroweak symmetry breaking Tome II: The Higgs bosons in the Minimal Supersymmetric Model](#)”, Phy. Rep. Vol. 459 (2008) Issues 1-6.
- [18] A. Djouadi, “[The anatomy of electroweak symmetry breaking: Tome I: The Higgs boson in the Standard Model](#)”, Phy. Rep. Vol. 459 (2008) Issues 1-216.
- [19] D. Curtin et al., “[Exotic Decays of the 125 GeV Higgs Boson](#)”, Phys. Rev. D 90 (2014) 075004.
- [20] J. M. Frere et al., “[Fermion masses and induction of the weak scale by supergravity](#)”, Nucl. Phys. B222 (1983) 11-19.
- [21] E. Cremmer, “[Gravity induced supersymmetry breaking and low-energy mass spectrum](#)”, Phys. Lett. B 122 (1983) 41.
- [22] U. Ellwanger et al., “[The Next-to-Minimal Supersymmetric Standard Model](#)”, Phys. Rept., 496 (2010) 1.
- [23] L. Evans et al., “[LHC Machine](#)”, JINST, 3 (2008) S08001.
- [24] CMS Collaboration, “[The CMS Experiment at the CERN LHC](#)”, JINST, 3 (2008) S08004.
- [25] CMS Collaboration public web, “[CMS Detector Design](#)”, <http://cms.web.cern.ch/news/cms-detector-design>.
- [26] CMS Collaboration, “[CMS Technical Design Report for the Muon Endcap GEM Upgrade](#)”, CMS TDR, CERN-LHCC-2015-012 (2015).
- [27] CMS Collaboration, “[The Phase-2 Upgrade of the CMS Muon Detectors](#)”, CERN-LHCC-2017-012, CMS-TDR-016, (2017).
- [28] D. Contardo, “[Technical proposal for the phase II upgrade of the Compact Muon Solenoid](#)”, CERN-LHCC-2015-10, CMS-TDR-15-02 (2015).

The CMS muon endcap upgrade using GEM technology

The experiment should be set up to open as many windows as possible on the unforeseen.

— Frederic J. Curie

The high-luminosity phase of the Large Hadron Collider (HL-LHC) will result in particle backgrounds ten times higher than its current value. To fully exploit the highly-demanding operating conditions during HL-LHC, the Compact Muon Solenoid (CMS) Collaboration has proposed the use of Gas Electron Multiplier (GEM) detector technology. The technology will be integrated into the innermost region of the forward muon spectrometer of the CMS as an additional station to cover pseudo-rapidity region $1.6 < |\eta| < 2.2$. The primary purpose of this auxiliary station is to help in muon reconstruction and to control level-1 muon trigger rates. The new chambers will add redundancy to the muon system in the eta region where the background rates are high, and the bending of the muon trajectories due to the CMS magnetic field is small. The new station will be embellished with specific trapezoidal-shaped GEM detectors known as GE1/1 chambers (detectors) and will provide stable operation in the high radiation environment expected during the future HL-LHC.

The design of GE1/1 chambers is finalized, and the installation is foreseen during the second Long Shutdown phase (LS2) currently underway¹. A novel construction technique for such chambers has been developed in such a way that the foils are mounted onto a single stack and then uniformly stretched mechanically avoiding the use of spacers and glue inside the active gas volume. Several full-size prototypes have been built using this technique and operated successfully in various beam tests at CERN.

The current chapter describes the layout, final design of GE1/1 chambers, and the technique employed to assemble these detectors. Also, the performance studies such as gain, efficiency, timing resolution, rate capability, and discharge probability of these chambers are provided. The chapter concludes by recommending operating conditions for GE1/1 chamber during their use in the CMS experiment.

¹The period from January 2019 till December 2020.

3.1 Introduction

The upgrade of the LHC to center-of-mass energy of 14 TeV and increasing the instantaneous luminosity (\mathcal{L}) up to or above $5 \times 10^{34} \text{ cm}^{-2}\text{s}^{-1}$ will result in High Luminosity LHC (HL-LHC). The increase in the collision rate will affect the operational conditions due to the increase in pileup and radiation background. It will also pose a challenge to maintain an efficient and reliable trigger particularly in the region $|\eta| > 1.6$. Additionally, the high-radiation background may speed-up the aging of the current muon system and may cause performance losses, dead regions, and the degradation of the efficient online event selection due to bandwidth limitations.

During the HL-LHC period, the CMS experiment [1] will continue its present physics program and, therefore, needs to maintain its sensitivity for electroweak and TeV energy scale searches. As such, the CMS Collaboration is planning several detector upgrades to maintain its high level of performance particularly in the region $1.6 < |\eta| < 2.4$ of the CMS. This, in turn, will increase the redundancy of the muon system and enhance its trigger and reconstruction capabilities [2, 4].

The CMS Collaboration is, therefore, preparing for the upgrade of the current muon system scheduled in 2019. The current schedule of the LHC includes several long shutdown periods to allow for upgrades of the accelerator complex as well as the experiments. The ultimate upgrade of the LHC will enable its operation at proton-proton collisions with a center-of-mass energy of 14 TeV and a gradual increase in instantaneous luminosity up to $5\text{--}7 \times 10^{34} \text{ cm}^{-2}\text{s}^{-1}$. Therefore, after LS2, the instantaneous luminosity will exceed $2 \times 10^{34} \text{ cm}^{-2} \text{ s}^{-1}$, while the third Long Shutdown (LS3) scheduled for 2025-2026 will bring the LHC luminosity to its ultimate level of about 5 to 7 times its design value. The HL-LHC (or Phase-II of the LHC) period starting after LS3 and currently foreseen up to the year 2035 is expected to yield a total integrated luminosity of about 3000 fb^{-1} .

A quadrant of the CMS muon system where both present detectors and the proposed extensions is shown in Figure 3.1. In the $1.6 < |\eta| < 2.4$ forward end-cap region, currently only Cathode Strip Chambers (CSC) are installed. To enhance muon trigger and reconstruction capabilities, the large-size GEM detectors known as GE1/1 [4] would be installed in this region. The GE1/1 chambers will employ Gas Electron Multiplier (GEM) technology [5].

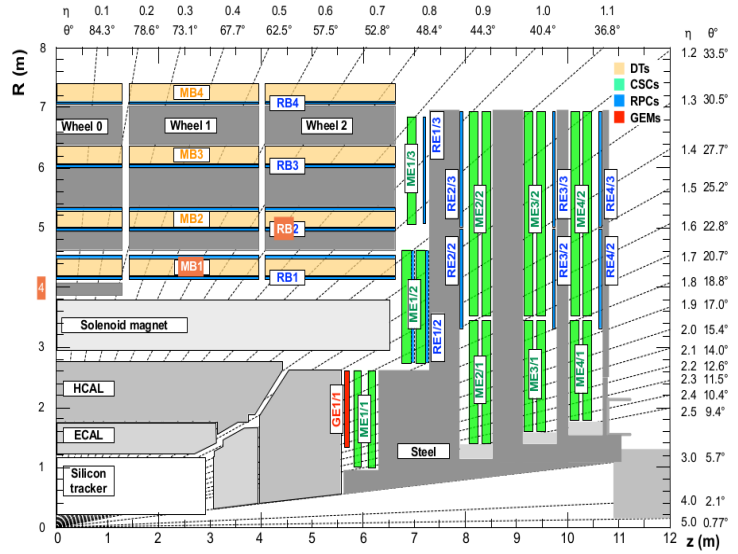


Figure 3.1: A quadrant of the R-z cross-section of the CMS detector, highlighting (in red) the location of the GE1/1 station in the pseudo-rapidity region $1.6 < |\eta| < 2.2$ [4].

Such a detector technology is playing a significant role in the instrumentation of particle physics experiments and is known to have very high performances such as spatial resolution better than $70 \mu\text{m}$, rate capability of the order of MHz/cm^2 and high tolerance to radiation in strong radiation backgrounds. The integration of these new detectors together with the existing CSC system would profoundly improve the muon trigger momentum resolution due to an increase in the lever arm for the measurement of the muon bending angle.

3.2 Impact of GE1/1 upgrade on the CMS experiment

The introduction of new station known as GE1/1 covering the pseudo-rapidity region $1.6 < |\eta| < 2.2$ of the CMS [4] is to complement the current CSC system. The station will extend the path length and will provide additional hits that will help to refine the stub reconstruction and improve the momentum resolution. With the new station installed, muon direction will be measured using hit positions in the adjacent GEM GE1/1 and CSC ME1/1 chambers. The good position resolution of both the detectors and an increased lever arm formed by the two detectors will allow excellent directional measurement.

FLUKA simulation studies at $\mathcal{L} = 5 \times 10^{34} \text{ cm}^{-2}\text{s}^{-1}$, are used to assess the capability of this new technology to cope with background fluxes expected in the high- η region [4]. The background rate is estimated by convoluting the fluxes mentioned above with the chamber sensitivities to background computed through standalone Geant4 simulations. The resulting rate is found to be of the order of $1 \text{ kHz}/\text{cm}^2$, orders of magnitude below the rate capability of the chambers, whose gain is stable up to $100 \text{ MHz}/\text{cm}^2$. Therefore, introducing the GE1/1 muon station will help to reduce the level-1 (L1) muon trigger rates as shown in Figure 3.2. The distance between adjacent

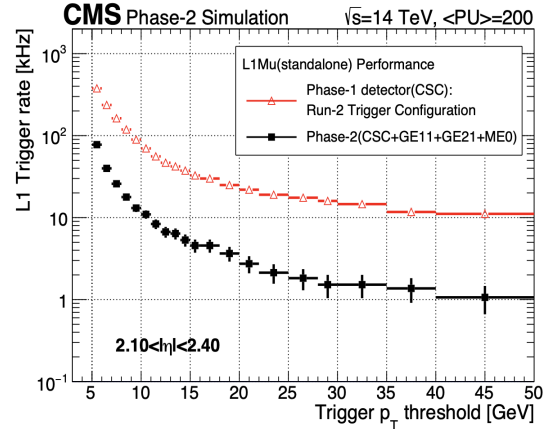


Figure 3.2: Trigger rate reduction with the deployment of muon direction measurement using GEM GE1/1 and CSC ME1/1 chambers [4].

CSCs and GEMs will allow determination of the muon p_T by measuring the bending angle due to the magnetic field in the first muon station alone. This p_T measurement, independent from the one based on the muon bending through the rest of the detector, will allow the maintenance of a low momentum threshold. It will be crucial for a broad spectrum of physics processes whose signatures are characterized by the presence of low p_T muons in the final state. A few examples include the search for the lepton flavor violating decay $\tau \rightarrow 3\mu$, Higgs boson decays $h \rightarrow ZZ \rightarrow 4\mu$ and $h \rightarrow 4\mu$, B meson decay $B \rightarrow 2\mu$, and two-Higgs doublet model extended with a scalar singlet (2HDM + S) (Higgs) decay² $h \rightarrow aa \rightarrow b\bar{b}\mu^-\mu^+$ [4].

²This analysis is considered in the current thesis and is discussed in Chapter 6.

3.3 The GE1/1 station

GEM detectors exploit the electron amplification that occurs within a gas medium inside narrow holes that perforate a thin polyimide foil in a triangular pattern. The polyimide foil is clad on both sides with a thin conductive copper layer. With a voltage, up to about 400 volts applied across the two copper-clad surfaces of a foil, a strong electric field (60-100 kV/cm) is produced inside the GEM holes.

The primary electrons produced due to ionization of the gas by a charged particle passing through the chamber drift towards the holes and once they start experiencing the very intense electric field inside the holes, they acquire enough kinetic energy to produce secondary ionization in the gas. This process eventually leads to the formation of an electron avalanche. An arrangement of three cascaded GEM foils, commonly known as a “triple-GEM detector”, allows a high charge amplification factor up to several 10^5 for modest applied high voltage, which limits the probability of electrical breakdown. The amplified charge induces a measurable signal on a readout electrode that can be segmented to provide positional information.

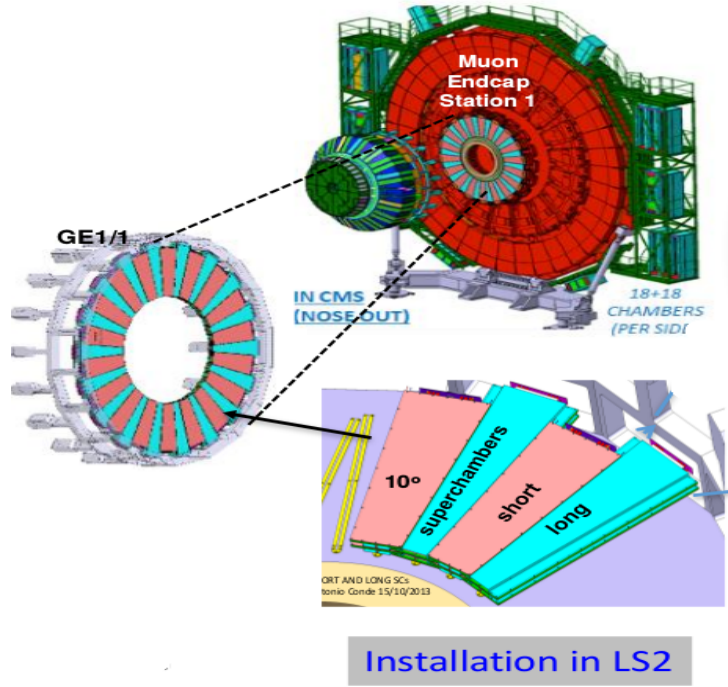


Figure 3.3: The first CMS muon endcap station with the GE1/1 super-chambers in the inner ring [4]. The GE1/1 10° long and short superchamber structures are also shown.

The GE1/1 detectors are trapezoidal shaped and consist of a gas volume containing a stack of three large-area GEM foils, i.e., a triple-GEM detector, embedded between a drift electrode and a readout board, with an induction/transfer-1/transfer-2/induction gap configuration of 3/1/2/1 mm. The first transfer gap has been set to minimize the charge released after the first GEM. The induction gap has been set to achieve the induction field up to 5 kV/cm without too much increase in the potential across the entire structure. The baseline gas mixture for operating the CMS triple-GEMs is Ar/CO₂ in 70:30 proportion.

In the GE1/1 stations, a pair of triple-GEM detectors are combined to form a “super-chamber” that provides two measurement planes to maximize detection efficiency. Each super-chamber covers a 10.15° sector so that 36 super-chambers are required to form a ring that gives full azimuthal coverage as can be seen in Figure 3.3. To instrument both endcap disks i.e. two GE1/1 stations, a total of 72 super-chambers or 144 basic chamber units are required. The super-chambers will alternate in ϕ between long and short versions as dictated

by the mechanical envelope of the existing endcap disk, i.e. each endcap disk will hold 18 long and 18 short super-chambers.

Over the past years, the performance of several generations of GE1/1 prototypes have been studied in a series of beam tests at CERN and Fermilab [7, 8]. With 98.0% chamber efficiency, a GE1/1 super-chamber will have efficiency above 99.9% when the logical OR of the signals from the two basic units are taken.

3.4 Chamber design

After several years of R&D program, many versions of GE1/1 chambers have been built so far by improving their design in each release.

Figure 3.4 shows a development of the GE1/1 chambers since 2010 when the CMS collaboration proposed their use in the muon end-cap region of the CMS detector. The latest version is Generation-X with its final design shown in Figure 3.5. The structure consists of a trapezoidal-shaped drift board, three GEM foils stacked together within frames, a readout board, and an external gas frame.

Three trapezoidal GEM foils are sandwiched in between drift and readout boards in a particular triple-GEM module with a gap configuration of 3/1/2/1 mm to ensure the best timing resolution. However, the mechanical constraints in the GE1/1 station, allow the use of two versions of chambers to have maximum detection coverage, the long GE1/1-L with a length of 128.5 cm and the short GE1/1-S of 113.5 cm. The main technical specifications of the GE1/1 detectors for both the Long and Short versions are listed in Table 3.1 [17].

Further, the two identical GE1/1 detectors are combined to form a ‘super-chamber’ to obtain two detection planes and thus maximize the detection efficiency and the redundancy of the GE1/1 layer. The large-size GEM foils needed for CMS are in trapezoidal-shape and are produced at the CERN printed circuit board (PCB) workshop using a single-mask production technique [9]. The drift and readout boards are trapezoidal-shaped PCB. The design of the drift board, the external and internal

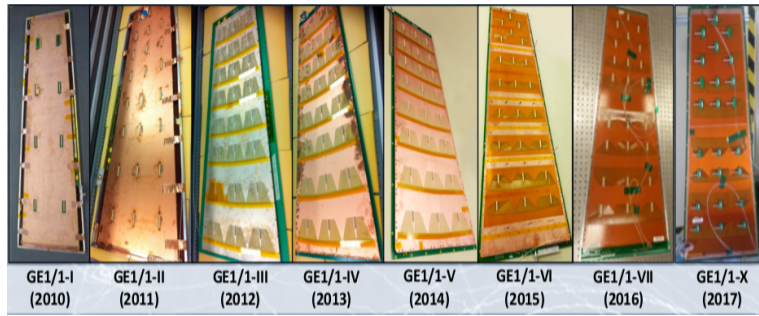


Figure 3.4: Evolution[†] of GE1/1 detector since 2010 [4] from generation-I to generation-X (2018).

([†]) Picture courtesy: J. A. Merlin

GE1/1 detector		
Specification	Short	Long
Shape	Trapezoidal	Trapezoidal
Chamber Length	113.5 cm	128.5 cm
Chamber Width	(28.5-48.4) cm	(28.6-51.2) cm
Chamber thickness	1.42 cm	1.42 cm
Active readout area	3787 cm ² (app.)	4550 cm ² (app.)
Active chamber volume	2.6 liters	3 liters
Geometric acceptance in η	1.61-2.18	1.55-2.18

Table 3.1: Technical specifications of the GE1/1 Short and Long chambers.

frames, the GEM foils, the readout board, and the gas distribution system are described in the following subsections.

3.4.1 The drift board

The GE1/1 drift board is a trapezoidal-shaped printed circuit board holding the drift electrode. The actual board and the magnified view of its wider side is shown in Figure 3.6.

The board has an active area coated with a copper layer, i.e. the drift electrode, that is contained in the active gas volume. GEM foils are electrically connected to the HV power supply using spring-loaded pins. As shown in Figure 3.6 (right), these HV pins are mounted on the drift board, at positions corresponding to the HV pads located on the GEM foils. Four pins are foreseen for each foil, i.e. a bottom and top side contact plus two spare pins. Pins for a given GEM foil, i.e. at a given height in the stack, have an identical height. The drift board has several holes around the periphery to accommodate mechanical stainless steel pieces called pull-outs, that are used to stretch the foils as will be explained in Section 3.5.3. Other onboard elements are outside the gas volume. There are pads for a 10 M Ω protection resistor that is used to limit the current from the HV power supply.

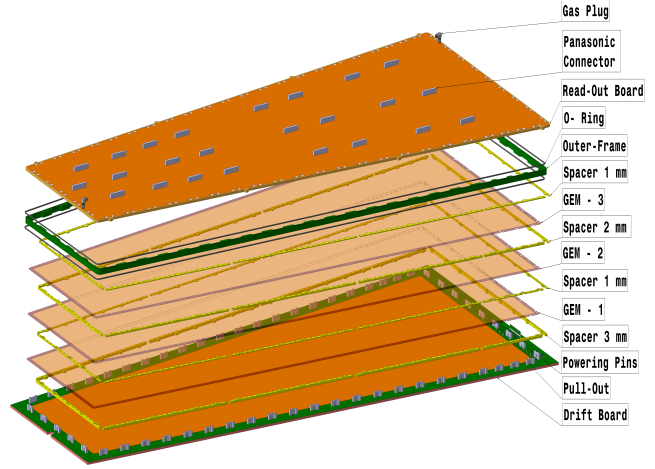


Figure 3.5: GE1/1 layout[†] and its main components starting from bottom: drift board mounted all around with stainless steel pull-outs used for stretching of GEM foils, 3 mm frame (Spacer), first foil, 1 mm frame, second foil, 2 mm frame, third foil, 1 mm frame, first O-ring, external frame, second O-ring and the readout board [17].

([†]) Picture courtesy: M. Abbas

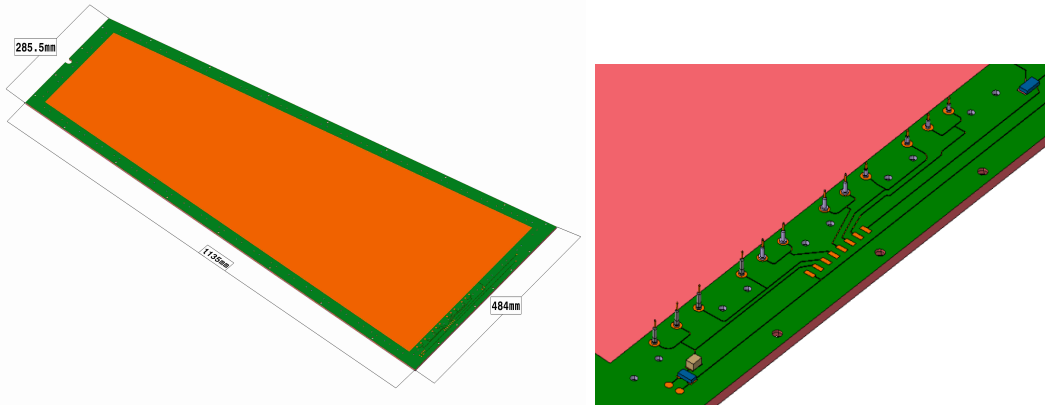


Figure 3.6: (left) Design of GE1/1 drift board and (right) magnified view of the design of the wider side of the drift board, with the twelve HV pins and corresponding soldering pads for the resistive divider network. There are on-board HV circuit traces and pads for the spring-loaded pins that make the electrical connections to the GEM foils; the pads for a 10 M Ω SMD resistor, 100 k Ω and 330 pF capacitor; the holes to fix pull-outs against the board [17].

There are pads for a 100 k Ω resistor and a 330 pF capacitor used to decouple the signal from the HV when during the post-assembly chamber quality control procedure a detector signal is extracted from the bottom of the third GEM foil. Finally, there are HV traces as shown in Figure 3.6.

3.4.2 The external frame

The GE1/1 external frame is shown in Figure 3.7. It is made up of halogen-free glass-epoxy material, machined from a single piece. The frame is used to close the active gas volume between the drift and readout boards. It has a trapezoidal shape and has numerous wide notches to accommodate the stainless steel pull-outs. It is coated with Nuvovern polyurethane varnish before assembly to seal in particulates. Narrow grooves are machined on both sides in order to accommodate a Viton O-ring.

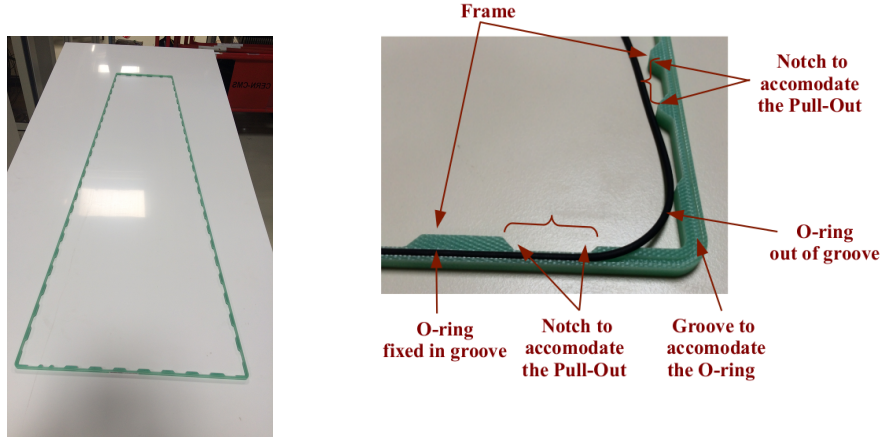


Figure 3.7: (left) The GE1/1 epoxy-glass external frame. (right) Close-up view of the section of the external frame showing the groove in the frame, O-ring in and out of the groove and notches in the inner side of the frame to accommodate the pull-outs [17].

3.4.3 The internal frame

The design of the internal frames is shown in Figure 3.8. There are four layers of internal frames made from halogen-free glass epoxy with a thickness of 3 mm, 1 mm, 2 mm, and 1 mm. Each frame is composed of 10 individual pieces per layer. The pieces are coated with Nuvovern polyurethane varnish before assembly which ensures that no glass epoxy particulates get detached from the frames during the chamber assembly as any dust falling onto the GEM foils could produce electrical shorts in the holes. Small threaded M2 brass inserts are fixed within the 3 mm frame to avoid loosening of macroscopic and microscopic glass epoxy particulates from the frames when screws pass through the frame. The frame layers are stacked and define the 3/1/2/1 mm spacings between the drift board, the triple-GEM structure, and the readout board.

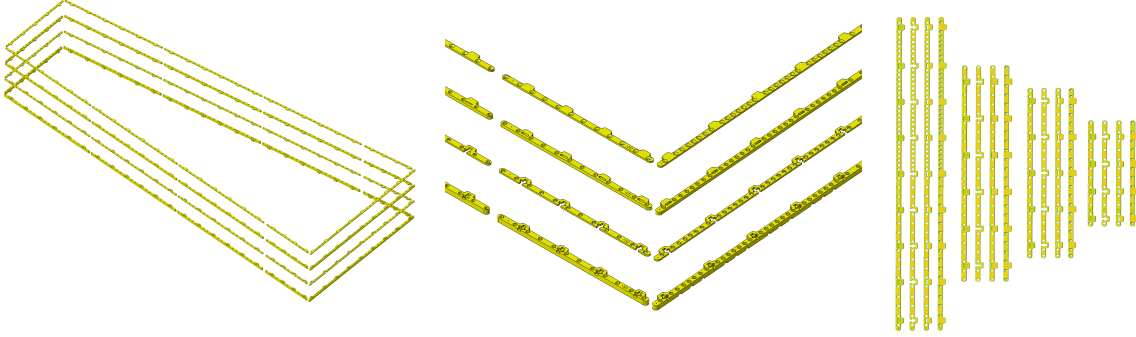


Figure 3.8: (left) Design[†] of the GE1/1 internal frames, (middle) magnified view of a section of the Figure 3.8, and (right) shapes and mechanical structure of the different pieces of the frames (right). Ten pieces are joined together to form each frame. The stacked frames surround the GEM foils along their periphery [17].

([†])Picture courtesy: M. Abbas

3.4.4 The GEM foils

The GE1/1 detector uses three identical trapezoidal-shaped GEM foils as shown in Figure 3.9. The foils are produced at the CERN PCB workshop using a single-mask production technique [9].

The GEM foil surfaces oriented towards the readout board are a single continuous conductor whereas the GEM foil surfaces oriented towards the drift board are segmented into sectors. The sectors run across the trapezoid in the same direction as the parallel ends. The sector width (in the radial direction) is largest at the short end of the trapezoid and smallest at the wide

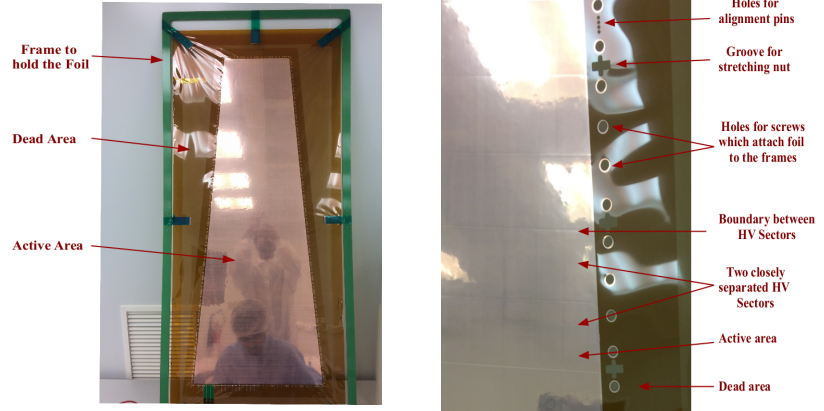


Figure 3.9: (left) Design of the GE1/1 GEM foils and (right) close-up view of a section of a foil. Small holes for alignment pins are used during assembly. Large holes allow the passage of screws used to attach a foil to the internal frame. "Plus"-shaped grooves are there to accommodate stretching nuts. The boundaries between the different HV sectors are visible [17].

end so that the area of each sector is approximately the same, about 100 cm^2 . This segmentation limits the charge and energy in case of a discharge. In an extreme case, if a discharge large enough to generate a short were to occur in a particular HV segment, it would render unusable only that particular HV segment and not the entire foil. Therefore, each segment has a separate connection to the HV supply via a trace around the edge of the GEM foil to a common connection point at the wide end. Each trace is connected through a $10 \text{ M}\Omega$ surface-mounted protection resistor that limits the current from the HV supply, decouples the capacitance from other HV sectors, and quenches a discharge. The voltage for the other

side of the foil is connected at two points located at the wide end of the foil, where the two points provide redundancy.

3.4.5 The readout board

The readout board is a trapezoidal-shaped printed circuit board with a mechanical design as shown in Figure 3.10. The inner side of the board features 3072 trapezoidal readout strips oriented radially along the longer sides of the chamber. The active area covered by the strips subtends an azimuthal angle of 10.15° which allows for an overlap of 0.15° (equivalent to 5.67 strips) between the active areas of adjacent chambers. All the readout strips are connected through metalized vias to the outer side of the board where traces are routed from the vias to readout pads in 8×3 partitions in (η, ϕ) . Each η -partition has 384 strips comprised of three 128-strip sectors in ϕ . The strip pitch varies between 0.6 mm at the shorter end of the chamber and 1.2 mm at the wider end. The readout board has two holes at diagonally opposed corners, in which gas plugs are mounted that serve as inlet and outlet explained in Section 3.4.7.

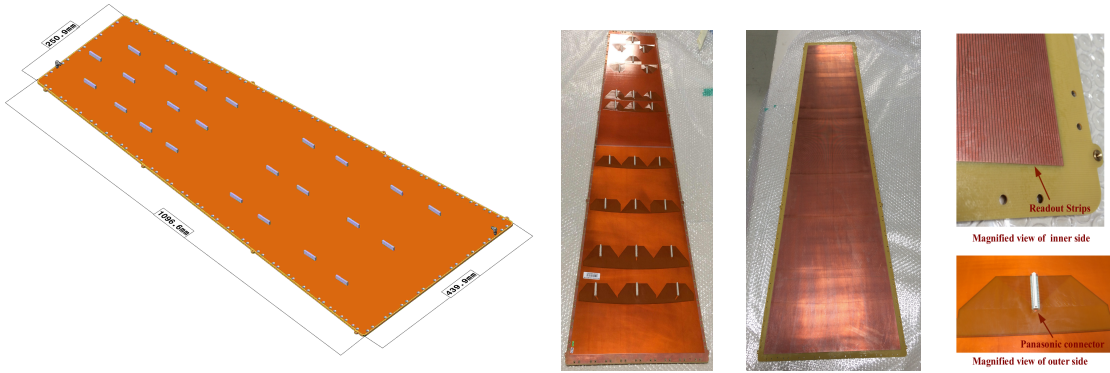


Figure 3.10: (left) Design of the readout board with the gas plugs fixed at opposite edges, (middle left) outer side of GE1/1 readout board showing 24 (η, ϕ) readout sectors, each with a male Panasonic connector for signal readout. There are holes at opposite corners used to mount the two gas plugs; one serves as gas inlet and another as gas outlet. Holes on the periphery of the board allow the passage of screws that fix the board against the chamber structure. (middle right) Inner side of the drift board showing the readout strips and (right) close-up view showing readout strips on the inner side and a Panasonic connector on the outer side of the board [17].

3.4.6 On-chamber HV distribution

As described in Section 3.4.1, the GEM foils are powered through high voltage pins soldered onto the drift board within the gas volume, the design of which is shown in Figure 3.11, while an actual photograph is shown in Figure 3.12. These pins get pushed against their corresponding connection pads on the GEM foils which are at different heights as shown in Figure 3.11. The HV pins are connected with pads outside the gas volume. These pads are designed to allow powering GEM chambers either using multi-channel or single channel power supply. In the latter case, the pads will be used to fix a special resistive divider network which allows a correct voltage distribution to the GEM foils. The circuit diagram for the 3/1/2/1 mm chamber gap configuration is shown in Figure 3.12.

3.4. CHAMBER DESIGN

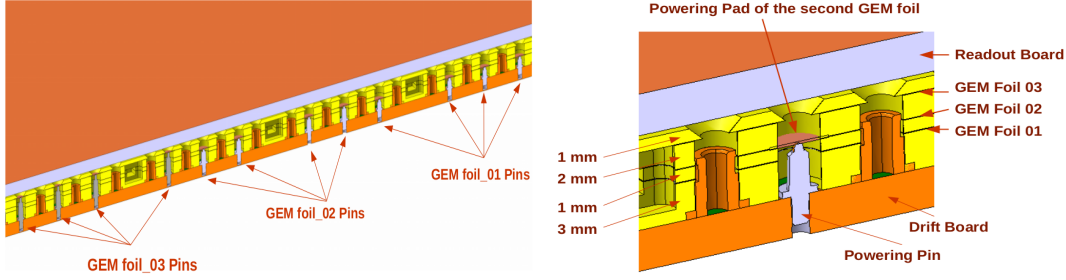


Figure 3.11: (left) Sliced view of the chamber design[†] showing the mechanism to power the three GEM foils with twelve HV pins and (right) magnified sliced view of Figure 3.11 (left) showing various components such as the drift board, 3 GEM foils in a stack, 3 mm, 1 mm, 2 mm, 1 mm frames, second GEM foil powering pad, readout board and the single HV pin pressed against powering pad of the second GEM foil [17].

([†])Picture courtesy: M. Abbas

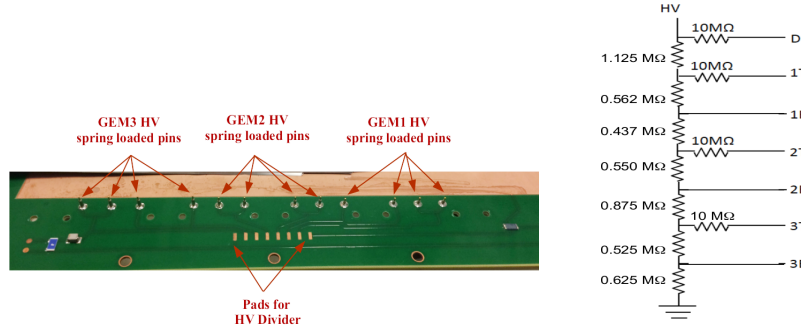


Figure 3.12: (left) Twelve spring-loaded pins soldered onto the drift board to make electrical HV connections to corresponding contact pads on the GEM foils; the three sets of pins have different heights so that they can properly reach the three GEM foils. (right) The resistive divider network used to power up the GE1/1 detector with a gap configuration of 3/1/2/1 mm using single channel power supply; the notation D, 1T, 1B, 2T, 2B, 3T and 3B corresponds to the drift board, the top and bottom electrodes of the first, second and third GEM foil respectively [17].

3.4.7 Gas distribution within the chamber

Gas connections to each GE1/1 chamber are made with a single inlet and a single outlet located on diagonally opposite corners of the readout board.

The design of a gas plug fixed on the readout board is shown in Figure 3.13. The gas mixture flows diagonally through the chamber and the presence of the GEM stack in the gas volume (i.e., between the Readout, external frame, and Drift boards) directs the gas flow towards the other corners and makes the flow laminar. The gas distribution inside the GEM stack (i.e. between GEM foils) is made possible by diffusion through the gaps between the inner frames and the GEM holes.

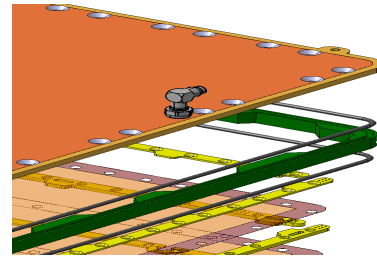


Figure 3.13: Exploded view of a GE1/1 chamber, including also the design of a gas plug fixed onto a GE1/1 readout board [17].

3.5 Assembly technique

Any kind of contamination can make a GE1/1 detector fail as particles going inside the 50-micron diameters holes of the GEM foils can cause electrical shorts. Therefore, the assembly of such detectors takes place in a cleanroom environment of the International Standards Organization (ISO) class 6. The use of tools with lubricated shafts, soldering equipment that requires heating of volatile fluxes, motors, and vacuum pipes with out-gassing oils, hair, and fingernail cosmetics are sources which can contaminate the detector and are forbidden in the assembly area.

For the construction of the very first GE1/1 prototype, the GEM foils were initially thermally stretched for 24 hours at 37° in a special oven [10]. Fiberglass spacer frames were then glued onto the foils to fix and keep them separated at the correct distance in the triple-GEM configuration. This procedure was however prone to possible glue contamination, very time-consuming and labor-intensive, and therefore not well suited for mass production. This gluing assembly procedure was eventually abandoned after the construction of the first two generations of GE1/1 chambers.

Alternative methods were tested to stretch GEM foils including stretching due to infrared heating lamps [4]. However, a major development in the GE1/1 chamber assembly procedure was introduced in 2011 with a new technique [7, 11] in which the GEM foils are mechanically stretched and the chamber is constructed without the use of any glue. The technique has been initially tested on small $30 \times 30 \text{ cm}^2$ prototypes [12] and later used to construct actual GE1/1 chambers [14, 15]. Since no glue is needed during the assembly this technique reduces the chamber assembly time from several days to a few hours only, and also allows for a chamber to be reopened in case of problems.

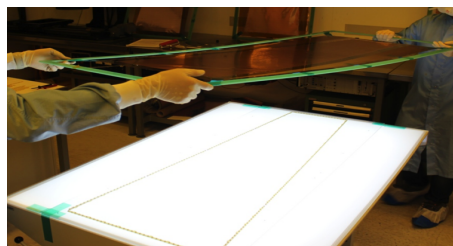


Figure 3.14: The 3 mm frame pieces placed on the Plexiglas plate forming the trapezoidal shape of the chamber [17].

The important steps performed during the assembly of a GE1/1 chamber are discussed in the forthcoming sections. The procedure starts with the preparation of the drift board, followed by the assembly of the GEM stack. Next, the GEM foils are mechanically stretched using the above-mentioned new technique after which the chamber is closed by the readout board.

3.5.1 Drift board preparation

The drift board is prepared outside the cleanroom to avoid the contamination of the cleanroom due to the soldering of different components which must be mounted on the board. Twelve pins are mounted on the drift board for making HV connections to the corresponding GEM foils. The three sets of pins have different heights to properly reach the three GEM foils in the stack. Pull-outs are bolted onto the perimeter of the drift PCB with two A2 stainless steel $M 3 \times 6/8$ screws that are sealed with polyamide washers against the drift board to prevent gas leakage. As described already in Section 3.4.1, a surface mounted (SMD) 10 M Ω Resistor, a 330 pF Capacitor, and a 100 k Ω resistor are also soldered to the

drift board.

3.5.2 GEM stack assembly

The most critical part of the chamber construction is the preparation of the GEM foil stack, which is realized with the help of a Plexiglas base plate that includes alignment pins at desired positions to keep the entire structure aligned during the assembly procedure. These alignment pins are fixed into the Plexiglas sheet following the trapezoidal geometry demanded by the mechanical layout of the detector.

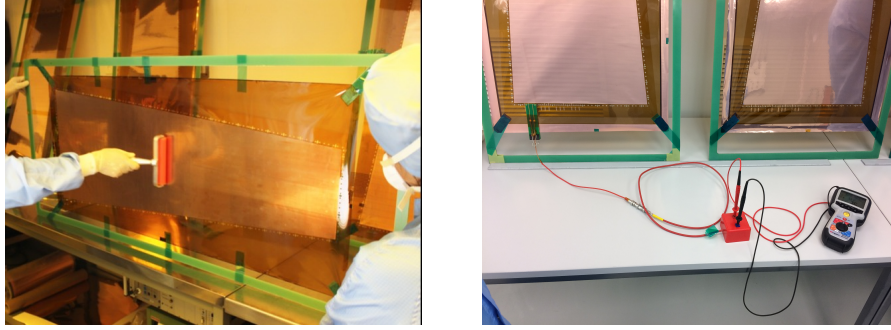


Figure 3.15: (left) GEM foil cleaning using adhesive roller. (right) Leakage current measurement using a MIT 420 Megger [17].

In the stack, the internal frame pieces fabricated in Fire Retardant 4 (FR4) material are alternated with the GEM foils to define the different gaps.

The 10 pieces of the 3 mm frames are inserted first over the alignment pins before placing the first GEM foil as shown in Figure 3.14. Before placing a GEM foil on the stack, it is first cleaned using an antistatic adhesive roller, which removes dust particles at the micron level by its strong sticking capacity as shown in Figure 3.15 (left). This is followed by a leakage current measurement in which a potential difference of 550 V is applied across the foil using an insulation tester as shown in Figure 3.15 (right).

The applied potential produces a very high electric field, typically of the order of 70-100 kV/cm, within the GEM holes and may lead to initial sparks due to the burning of any dust particles within the

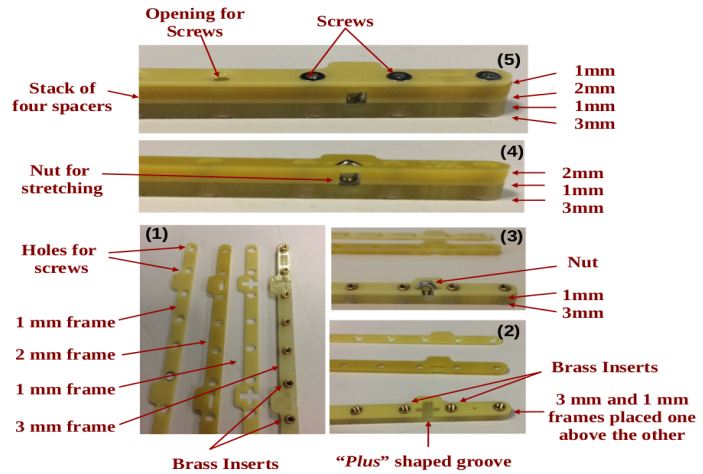


Figure 3.16: (1) Shapes and mechanical structure of 4 different frame pieces, (2) 3 mm and 1 mm frame pieces are combined together with "+" shaped groove reserved for stretching nut, (3) placement of nut after stacking two frame pieces, (4) 3 mm, 1 mm, and 2 mm frame pieces combined in a specific order and (5) different frame pieces stacked together to maintain the gap configuration of 3/1/2/1 mm as demanded by GE1/1 geometry, similar frame pieces are combined to form four layers around the periphery of the GEM stack as depicted in Figure 3.8 [17].

GEM holes. As such, this test may effectively help to clean the foils from leftover impurities. In an environment with 30% of relative humidity (RH) or less, the maximum allowed value of the leakage current when a potential difference of 550V is applied across the foils is 35 nA. However, above 30% of RH, the leakage current can drastically rise above that level. During this test, electrostatic charge is accumulated inside the GEM holes making them more likely to catch any remaining dust particles. Moreover, during the mounting of the stack, the GEM foils are not yet perfectly stretched, and if two adjacent foils in the stack come in contact, the whole energy accumulated on the foils can be released in a single point which may lead to a damaged GEM foil. For this reason, at the end of the leakage current test, the GEM foils must be fully discharged by shorting the top and bottom electrodes.

As shown already in Figure 3.9, the edges of the GEM foils have a pattern of holes, which are used to attach the foils to internal frames. The stack of three GEM foils is formed by sandwiching foils at their edges between the four layers of internal frames described in Section 3.4.3.

A detailed view of these frames is shown in Figure 3.16. The stack is held together by numerous small M 2 × 6 non-magnetic stainless steel screws, spaced about every centimeter along the frame, and penetrating all the frame layers and foils. These screws are tightened against small threaded M2 brass inserts. After the second GEM foil is placed on the stack followed by the 2 mm frame, stainless steel nuts are embedded into the frames (at specifically designed "+" shaped grooves) every few centimeters around the periphery of the stack, with the axes of their threaded holes oriented parallel to the plane of the inner frame. These nuts together with the pull-outs mounted on the drift board and the corresponding screws are used in the stretching mechanism as will be explained in Section 3.5.3. The GEM stack consisting of three foils with the 3/1/2/1 mm frames is finished by removing the dead area surrounding the active area of the foils as shown in Figure 3.17.

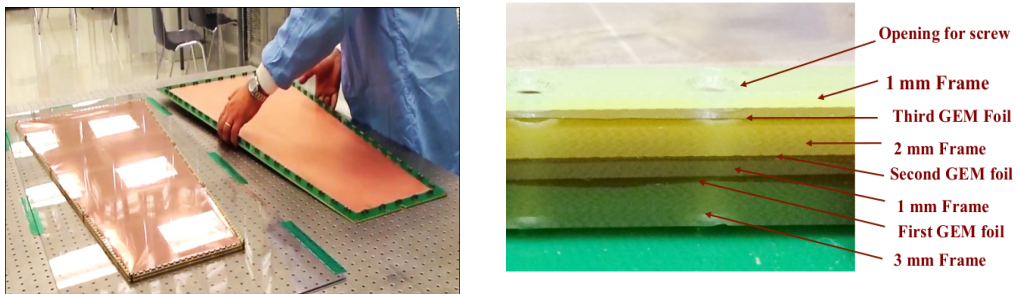


Figure 3.17: (left) A GEM stack with a drift board and (right) the GEM stack structure from bottom to top [17].

3.5.3 Foil stretching mechanism

After the preparation of the three-layered GEM stack as described in Section 3.5.2, this stack is then placed over the drift board as shown in Figure 3.18 (left). The drift board is fixed against a special assembly jig made of aluminum bars which are tightened with the help of fixation bolts as shown in Figure 3.18 (right). The jig is used to keep the drift board flat by preventing deformations during the stretching of the GEM stack or during the fixation of

3.5. ASSEMBLY TECHNIQUE

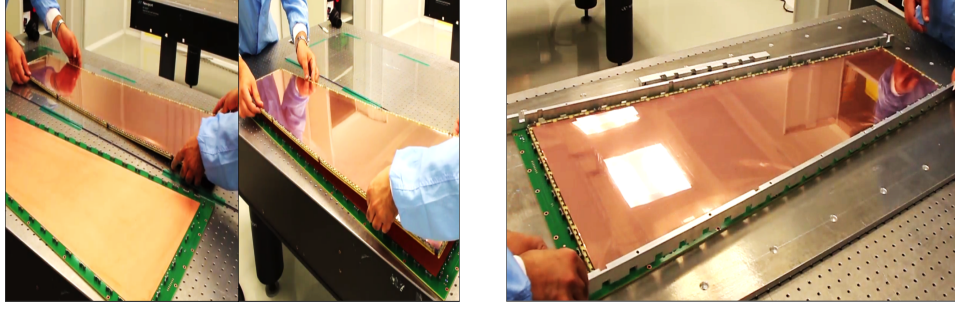


Figure 3.18: (left) Placing the GEM stack onto the drift board. (right) The GEM stack on the drift board and fixation of the drift board with the assembly jig [17].

the readout board against it when closing the chamber at the end of the assembly procedure. Next, the entire GEM stack is mechanically stretched, i.e. all three foils at once, following the technique that is conceptually visualized in Figure 3.19.

The nuts inserted after the second GEM foil is put on the stack as explained in Section 3.5.2 receives M 2.5×8/×8 stainless steel screws that are inserted laterally into the pull-outs located within the gas volume on the drift board as shown in Figure 3.20 (left). The stack is then uniformly stretched against the pull-outs by manually applying a controlled torque of about 8-10 cNm on the lateral screws, pulling the inner frame outwards towards the pull-outs as shown in Figure 3.20 (bottom). To lower the risk of forming “waves” in the GEM foils during the stretching of the stack, a specific order is followed in the tightening of the screws. Pairs of corresponding screws on opposite sides of the chamber are tightened simultaneously by two people.

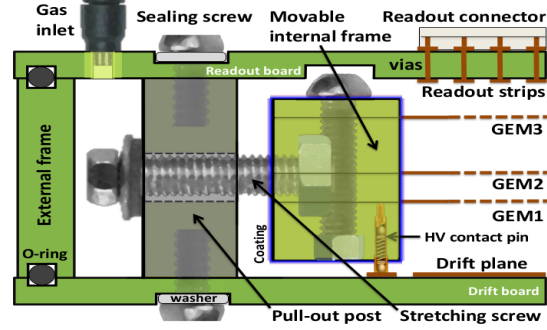


Figure 3.19: Concept and mechanism employed to stretch the GEM foils in GE1/1 chambers [4].

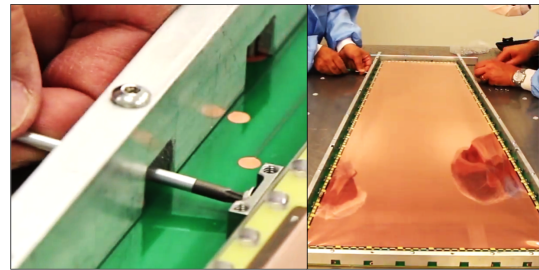
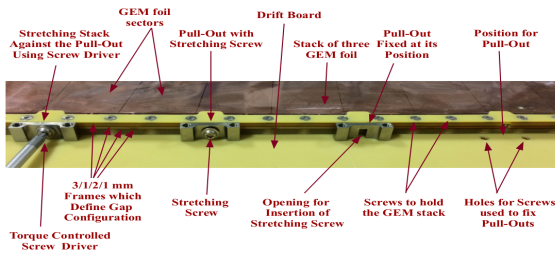


Figure 3.20: (left) The implementation of the concept depicted in the Figure 3.19 by using various components to stretch the GEM stack against the pull-outs. Stretching screws are allowed to pass through the stainless steel pull-outs and are received by nuts embedded into the inner frame for tensioning the GEM foils in the stack. (right) The actual stretching is performed using a screw driver with an assembly jig mounted onto the drift board [17].

Tolerances inherent in the stretching mechanism of the GEM foils and their relative positioning can have an impact on the uniformity of the gas gain and the detector timing

response. It is, therefore, crucial to ensure uniform stretching during assembly in order to achieve a uniform response across the detector surface. This uniform stretching is ensured by setting specifications on the torques applied to the pull-out screws during assembly. To determine and validate the optimal mechanical tension applied to the GEM foils, a procedure involving Fiber Bragg Grating (FBG) sensors were used [13].

3.5.4 Closing the chamber

After the foil stretching, a connectivity test between the gaps and across the foils is performed by measuring the impedance using a Mega-Ohm insulation tester. This is done by applying a potential difference of 550 V across the GEM foils and in between different gaps through the HV traces outside of the gas volume on the drift board.

An impedance of more than $100\text{ G}\Omega$ and $15\text{ G}\Omega$ is expected between the gaps and across each GEM foil, respectively, for RH of 30% or less. The impedance may have lower values at higher values of humidity. At the end of the assembly procedure, the external frame is placed around the tensioned GEM stack. It defines the limits of the gas volume as shown in Figure 3.21. The anode read-out board is placed on top of this outer frame and is attached to the stainless steel pull-outs with A2 stainless steel $M3 \times 6/ \times 8$ screws which are sealed with polyamide washers against the readout board as shown in Figure 3.22. This sandwiches the outer frame tightly between the drift and readout boards and provides a solid gas barrier. The final detector is shown in Figure 3.22.

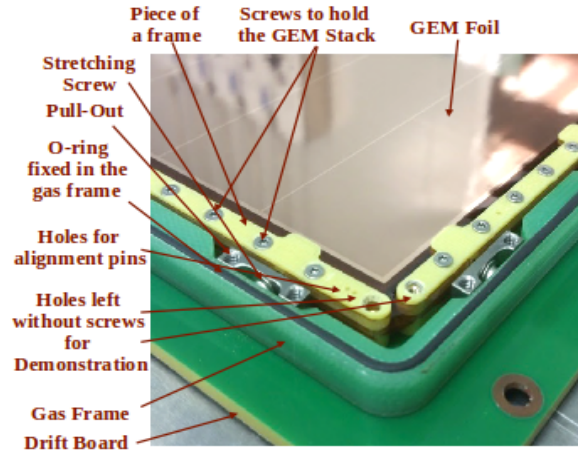


Figure 3.21: Close-up view of a section of a GE1/1 detector with the GEM foil stack tensioned against the pull-outs mounted onto the drift board and surrounded by the outer frame equipped with O-rings sections in its grooves. The active chamber volume is ready to be closed with the readout board [17].

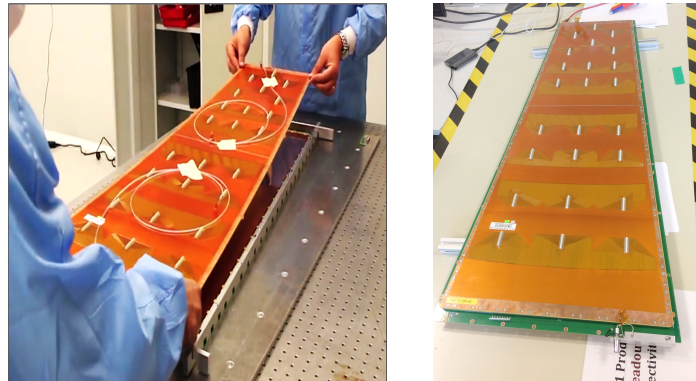


Figure 3.22: (left) Closing the chamber with the readout board. (right) A completed, closed GE1/1 chamber [17].

3.6 Performance of GE1/1 chambers

The current section describes the performance studies such as gain, efficiency, timing resolution, rate capability, and discharge probability of GE1/1 chambers. These studies are discussed in the following subsections.

3.6.1 Gain measurements

Test setup

The detector under test is powered using a programmable high voltage (HV) power supply (CAEN N1470) that allows controllable current limit (I_{set}), voltage ramping up and down in steps, maximum voltage, and trip time. The power supply delivers a current up to 1 mA with a monitoring resolution of about 50 nA which allows identification of unusual current fluctuations. Measurements are performed by irradiating the detector using a mini AMPTEK X-ray Silver (Ag) target source. The detector is irradiated within a closed copper chamber, the design of which is shown in Figure 3.23, which prevents radiation exposure to human beings.

The detector output (from a sector $(\eta, \phi) = (5, 2)$ as in Figure 3.24) is read out by using a charge sensitive pre-amplifier (ORTEC 142PC) whose output is sent to an amplifier plus shaper (ORTEC 474) unit followed by a discriminator. The resulting digital pulses from the discriminator (Lecroy 623A) are fed to a scaler unit, and the rate plateau is obtained by ramping up the detector slowly using the HV source.

Even though X-ray photons interaction rate is of the

order of the kHz ; the primary current is very small and is very challenging to measure it directly from the drift electrode usually powered at high voltage and is prone to noise. The primary current produced in the drift gap by the X-ray source is, therefore, obtained by multiplying rate count (R) with the number of primary electrons (n_{e^-}) per X-ray photon and by charge (e^-). The output current is measured using a pico-ammeter connected to Keithley Electrometer Model 6487, and the data is recorded with a Labview program via a General Purpose Interface Bus (GPIB).

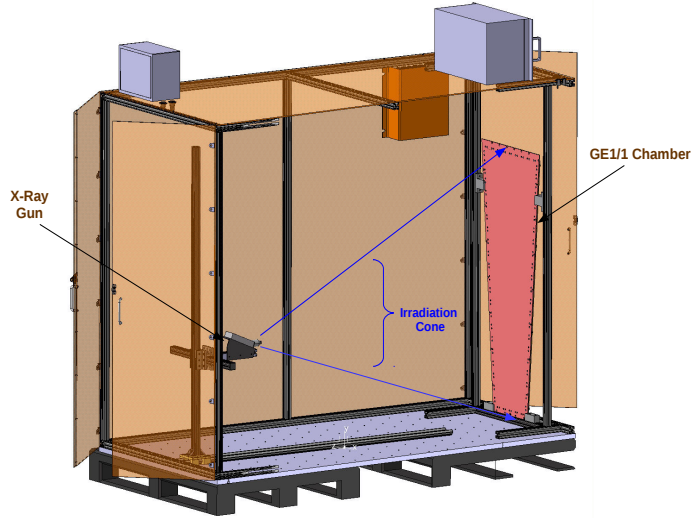


Figure 3.23: Design[†] of the setup used for gain measurements with X-ray tube and the GE1/1 detector inside the copper chamber. The copper chamber is completely closed when the detector is exposed to X-rays.

([†]) Picture courtesy: M. Abbas

Results

The chamber is connected to the gas system and flushed with the standard gas mixtures at the flow rate of 5 liters per hour, and left to flush for at least 5 hours before taking the actual measurement. Two test gas mixtures, Ar/CO₂ and Ar/CO₂/CF₄ in proportion 70/30 and of 45/15/40, respectively, are used. The choice of using CF₄ quencher in the latter case is driven by its good timing characteristics [21] and the fact that it is non-flammable, non-corrosive for metals, and is safer with respect to other hydrocarbons like methane.

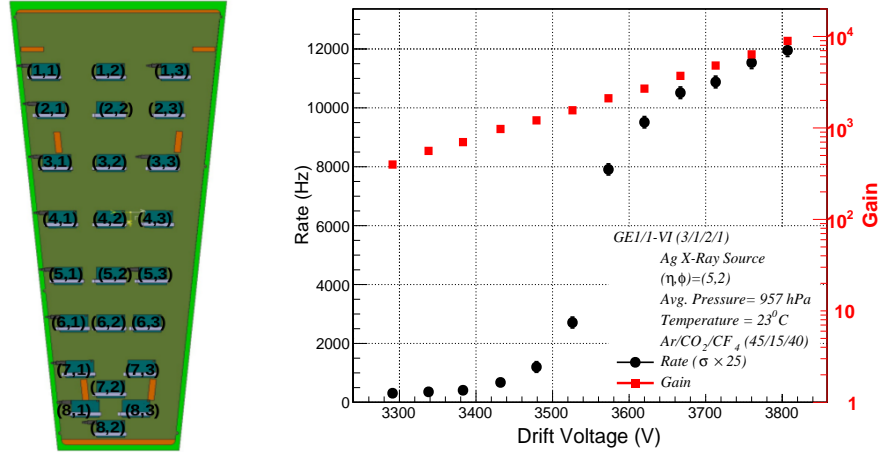


Figure 3.24: (left) Map of the readout board showing 24 (η , ϕ) sectors of GE1/1 chambers, and (right) gain and rate measurements of sixth generation chamber (GE1/1-VI) while reading a particular (η , ϕ) = (5, 2) sector. The error bars on the measured rate are the Gaussian one sigma uncertainty which are very small and hence are multiplied by a factor of 25 so as to reflect their visibility on the rate plot.

The effective gas gain is measured by exposing the detector to an X-ray source with a silver target for generating X-rays. The incident X-rays consist of silver K_α and K_β peaks (centered around the energy of 22 and 25 keV) over an electron bremsstrahlung continuum background. The X-ray photons are absorbed by the copper atoms of the drift electrode which in turn, emits copper X-ray photons of 8 keV energy while returning to the ground state. The X-ray photons emitted by the copper are then converted by the photoelectric effect in the active gas volume. The resulting spectrum is thus a convolution of the energies of the incident X-rays photons interacting in the active gas volume of the detector, the bremsstrahlung continuum background, and a small fraction of unconverted silver K_α and K_β lines. The gain is then measured in each gas composition by comparing the primary current I_p induced in the drift gap by the X-ray source, and the amplified output current (I_o) induced on the readout board.

One such measurement of rate and gain for the sixth generation GE1/1-VI detector is shown in Figure 3.24 for the gas mixture of Ar/CO₂/CF₄. The gain of various other chambers are also estimated, the result of one such case where a fourth-generation GE1/1-IV has been considered is presented in Figure 3.25 for the gas mixtures Ar/CO₂ and Ar/CO₂/CF₄. It is observed that the gain for GE1/1-IV is higher in Ar/CO₂ compared to Ar/CO₂/CF₄, and is due to electron absorption by CF₄ quencher.

3.6. PERFORMANCE OF GE1/1 CHAMBERS

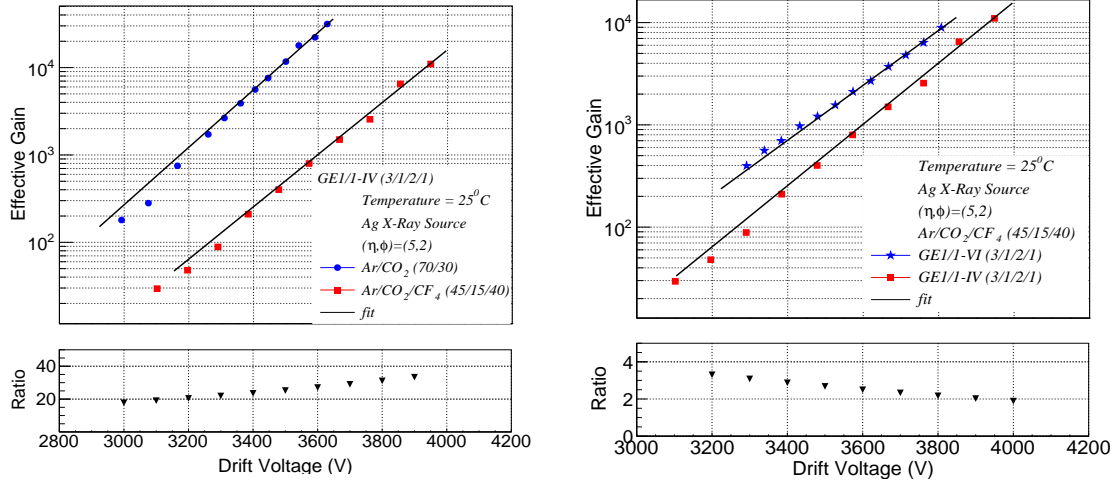


Figure 3.25: (left) Gain of fourth generation GE1/1-IV detector for the gas mixtures Ar/CO₂ (70/30) and Ar/CO₂/CF₄ (45/15/40), and (right) Observed gain of fourth GE1/1-IV and sixth generation GE1/1-VI detectors for Ar/CO₂/CF₄ (45/15/40). Points represent the data and the solid lines a fit to the observed data. The ratio plots have been calculated by fitting observed data and using the fit equations to interpolate into the regions of missing data points while taking the ratio between the gains corresponding to Ar/CO₂ and Ar/CO₂/CF₄.

Further, the gain measurements are also performed on fourth and sixth generation detectors (GE1/1-IV and GE1/1-VI) for the gas composition of Ar/CO₂/CF₄. The results are compared and are presented in Figure 3.25. The results show that the gain is higher for sixth-generation GE1/1-VI compared to the fourth generation GE1/1-IV and is attributed to GEM foil orientation. The GE1/1 detector uses single-mask GEM foils, which are asymmetrically bi-conical in shape compared to symmetrically bi-conical holes in double-mask foils. The holes with the narrow opening facing the incident radiation (source), which is also now preferred orientation of the CMS, show a higher gain compared to the case when a wider opening of the holes face the incident radiation [19, 20].

3.6.2 Efficiency and timing measurements

Beam facility

The CERN's Northern Area Experimental Halls (EHs), located at Preveessin site host Super Proton Synchrotron (SPS), a circular particle accelerator and a multi-purpose facility designed to deliver primary ion and attenuated proton beams.

This facility is also meant to provide a wide spectrum of secondary and tertiary particle beams of varying and flexible composition (hadrons and leptons) to fixed-target experiments. Before being injected into the LHC main accelerator, the protons beams with 115 billion protons are bunched together (up to 2,808 bunches). These protons are

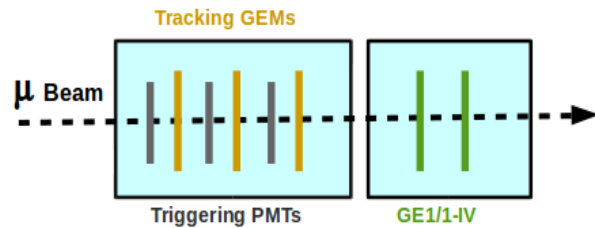


Figure 3.26: Schematic of the beam test set-up showing the direction of muon beam, triggering Scintillators (photo multiplier tubes (PMTs)) (in dark gray colour), 10 cm × 10 cm tracking GEMs (in yellow) and GE1/1 chambers (in green) [26].

then passed through a series of accelerator systems that successively increase their energy. The 50 MeV protons from the linear particle accelerator are generated, which feeds the Proton Synchrotron Booster (PSB). The PSB accelerates these protons up to 1.4 GeV before they are injected into the Proton Synchrotron (PS). The PS accelerates these protons up to an energy of 26 GeV and injects them into the Super Proton Synchrotron (SPS), the latter increases their energy further to 450 GeV before they are at last injected into the LHC ring. For testing a prototype detector, the beam is extracted from the SPS and split into several channels called H2, H4, H6, H8, etc. to feed more than one test facility simultaneously.

Tracking telescope

The conceived experimental beam-test setup used a similar tracking telescope as developed by RD51 Collaboration [8]. The tracker consists of three organic plastic scintillators S1, S2 and S3, three 10 cm \times 10 cm GEM detectors and a movable aluminum structure (Figure 3.27). The scintillators are used to provide the trigger and, the GEM detectors featuring a strip-



Figure 3.27: (left) Design of the tracking telescope showing three triggering scintillators (in grey colour), 10 cm \times 10 cm tracking GEMs (in yellow colour), (middle) a photograph of movable aluminum stand holding actual GE1/1 chamber in front of the tracking telescope during H4 beam test campaign, and (right) one of the earliest (December 2014) beam test setup at CERN SPS.

based two-dimensional readout plane acts as a tracking system. The movable structure provides support to the entire tracking as well as to triggering system and also enables the translations in ϕ and η directions to allow the beam alignment with different GE1/1 readout sectors. The test beam setups used in various earlier test campaigns can be found in references [7, 12, 14].

Readout electronics

The GE1/1 chamber has 3072 readout strips which are organized in groups of 128 to form 8×3 partitions. Application Specific Integrated Chip (ASIC) VFAT2 [22, 23], a digital front end chip (Figure 3.28) originally developed by TOTEM Collaboration [24] is used to read the signal from the GEM chambers. The chip has 128 readout channels, each being connected to a pre-amplifier, a shaper, and a constant fraction discriminator. The chip is controlled

by TURBO cards, a stand-alone portable control and data acquisition (DAQ) platform developed by TOTEM Test Platforms (TTP) [25] for front-end VFAT2. Each TURBO card can accommodate up to 8 VFAT chips, and each VFAT2 chip provides a binary output with a variable latency for the position information and a fixed latency output, called SBIT, for the timing information. The TURBO boards are controlled through Labview.

Results

H4 beamline has been used for the measurements of efficiency and timing resolution of GE1/1 detectors. A secondary beam consisting of pions and their decay products is produced after striking the primary beam on the existing Beryllium target. Muon beams of 150 GeV energy are then selected by closing the collimators as they represent minimum ionizing particles (MIPs) at this energy and pass through the collimators while pions are stopped.

The GE1/1 chambers are aligned perpendicular to the direction of the muon beam and placed in front of the tracking telescope as shown in Figure 3.26 (also in Figure 3.27). Further, chambers are shielded with aluminum and copper-clad foils to reduce the noise level below the expected signals. The beam particles are selected by analog pulses from three scintillators S1, S2, and S3 placed in coincidence and are converted into digital form by using discriminators. The digitized signals are sent to three comparators connected to AND port, the output of which is used as a trigger to master TURBO card. The output from the master TURBO card acts as an input to the slave TURBO card and both the cards receive additional inputs from the VFAT2 chips connected to the tracker and GE1/1 chambers. Out of the 24 (η , ϕ) sectors in GE1/1 chamber, the output from the particular test sector (η , ϕ) = (5, 2) has been sent to the shaper of the VFAT2 and then compared to a customizable threshold used to optimize the process of data acquisition in noisy environments. The beam trajectories are reconstructed from the hit information from the tracking telescope. The beam profile from GE1/1 is obtained from the information collected from TURBO controlled VFAT2 chips and using the track reconstruction algorithm.

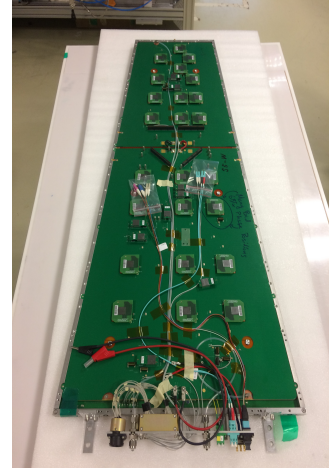


Figure 3.28: A photograph showing 24 VFAT chips mounted on the GE1/1 chamber.

Efficiency: The efficiency represents the probability to record an event when a particle crosses the detector. It has been estimated by recording the number N which is the total number of triggers obtained from the coincidence of the three scintillators and N_1 which are the hits from a detector test region. However, due to the possible misalignment of the test region and particle scattering, the number of hits ' N_2 ' is also observed from neighboring regions. The efficiency is, therefore, calculated by removing these additional hits from the total number of triggers using equation 3.1

$$\varepsilon = \frac{N_1}{N - N_2} \quad (3.1)$$

3.6. PERFORMANCE OF GE1/1 CHAMBERS

The efficiency of the chambers is measured in Ar/CO₂ and separately Ar/CO₂/CF₄ as a function of drift bias. An average efficiency plateau of over 98% is reached at lower voltages for Ar/CO₂ gas mixture compared to Ar/CO₂/CF₄ corresponding to effective gains of $\sim 10^4$ as shown in Figure 3.29.

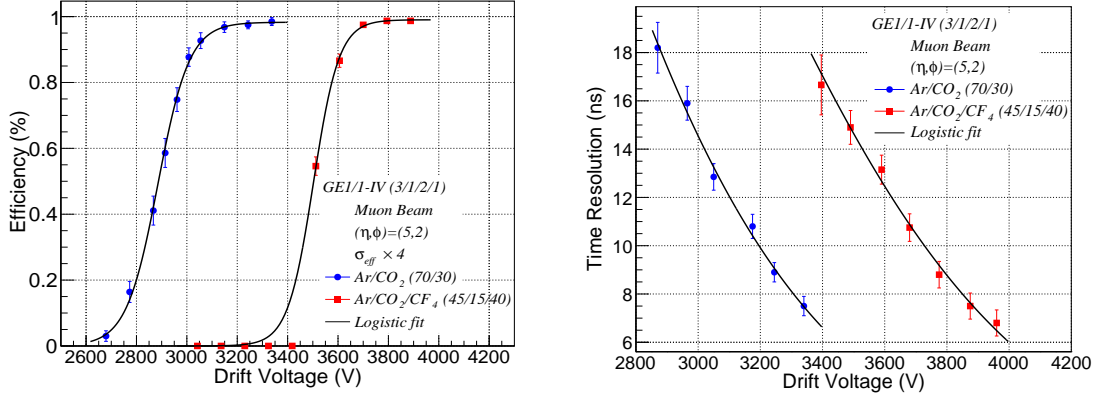


Figure 3.29: (left) GE1/1 efficiency, and (right) timing resolution of GE11-IV detector for the gas compositions Ar/CO₂ and Ar/CO₂/CF₄. Points represent the data and solid lines represent the logistic fits (details in Table 3.2). The error bars on data are the Gaussian one sigma uncertainty which are very small and are multiplied by a factor of 4 ($\sigma_{eff} \times 4$) so as to reflect their visibility on a given data point.

Timing: Timing resolution of GE1/1 detector is an essential parameter as it ensures that it can act as a fast triggering system in CMS and hence can identify correct bunch crossing. It has been estimated as the standard deviation of time distribution obtained by recording the events with a reference time being the particular instance when the particle crosses the drift region of the chamber. The trigger signals from the coincidence of the three scintillators are sent to the common stop input of a Time to Digital Converter (TDC) unit (CAEN V775), and the latency output from the detector under test is also sent to one of the inputs of the same TDC. For each event, the time difference between the two digital signals is determined. The timing resolution is then obtained from the width of the resulting distribution.

However, there are fluctuations in the period between a reference time and the detection of the signal due to the variations in the distance between the primary cluster formed in the drift region and the first GEM from one event to another. After crossing the first GEM foil, the charges follow the same path length till they are detected at the readout board. The timing resolution is degraded by the diffusion of the charges in the gaps between the GEM foils and this degradation, however, is improved by the addition of component gas with a low diffusion coefficient such as CF₄. The estimated results are depicted in Figure 3.29 and correspond to GE1/1-IV for gas compositions Ar/CO₂ and Ar/CO₂/CF₄. The timing resolution primarily depends upon the drift voltage at a constant value of transfer and induction fields. However, GE1/1 chambers are powered using a divider chain [17] allowing all the fields to vary simultaneously. Therefore, it is very difficult to make any conclusive statement for the timing improvement of Ar/CO₂/CF₄ with respect to Ar/CO₂ mixture in the present case. Therefore, results are expressed as a function of gain (Figure 3.30) by

fitting timing data in Figure 3.29 (right). The plot shows that there is an improvement of $\sim 24\%$ by adding CF_4 component in Ar/CO_2 . The CMS Region in the plot, defines the timing resolution of GE1/1 detectors when they will be operating in the CMS.

3.6.3 Rate capability

The flux in the CMS end-caps is not expected to exceed $10 \text{ kHz}/\text{cm}^2$. Therefore, rate capability of GE1/1 chambers is measured by varying the flux of X-ray photons at the starting gain equal to the expected CMS operational gain of the chambers ($\sim 7 \times 10^3$) [4].

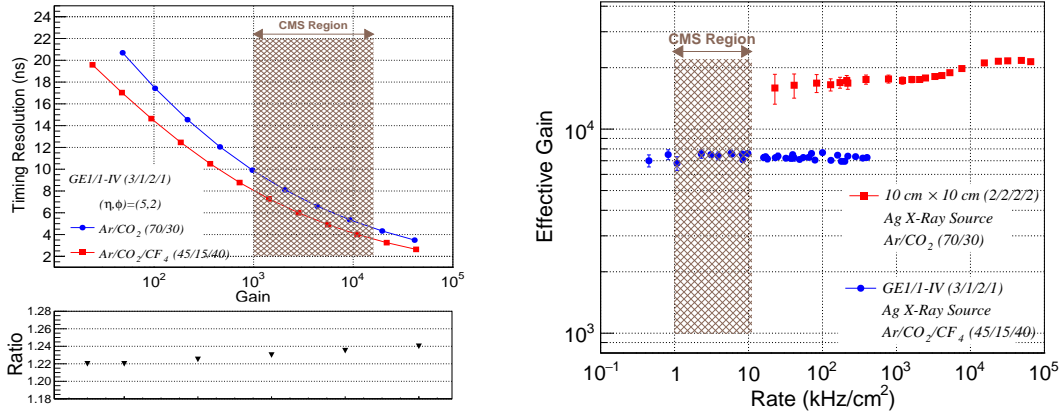


Figure 3.30: (left) The timing resolution for Ar/CO_2 and $\text{Ar}/\text{CO}_2/\text{CF}_4$ gases as a function of gain. The fit equations from Figure 3.29 (right) are used to obtain new data points by interpolation, the solid lines merely connect the points. The ratio plot is obtained by the division between the interpolated data points of $\text{Ar}/\text{CO}_2/\text{CF}_4$ and Ar/CO_2 , and (right) rate capability of a GE1/1-IV chamber, the Figure is also merged with a rate capability of a $10 \text{ cm} \times 10 \text{ cm}$ test detector. The shaded portion ‘CMS Region’ is the expected particle flux region of the CMS during HL-LHC.

In a separate campaign, rate capability is measured for a $10 \text{ cm} \times 10 \text{ cm}$ test detector with 2/2/2/2 mm gap configuration at a starting gain of $\sim 1.5 \times 10^4$ in Ar/CO_2 (70/30) [19, 27]. In each case, the chambers are irradiated with a very intense X-ray source, and the amplified current is measured using a pico-ammeter connected to the anode of the detector. The incident particle flux is varied by using copper attenuators, and the effective gain is measured (Figure 3.30 (right)). It is found that the effective gain remains stable up to $10^5 \text{ kHz}/\text{cm}^2$. Therefore, rate capability has been considered constant with a value of $10^5 \text{ kHz}/\text{cm}^2$.

3.6.4 Discharge probability

The GE1/1 detectors are to be operated at sufficiently high gains ($\sim 10^4$) to ensure the maximum detection efficiency while maintaining the timing performance. However, in case of intense particle fluxes or densely ionizing trails, operating a detector at high gains could increase the probability of producing discharges which might damage the detectors. Discharges start when the charge exceeds Raether limit [29], resulting in the variations in the local electric field. The local perturbation of the electric field can afterward transform the avalanche into a streamer which propagates through both the directions of GEM electrodes and hence provokes the electrical breakdown of the gas. The three amplification stages, however, in GE1/1 chamber are slightly set to different gains by applying different voltages across the foils.

The voltage across the first GEM foil is 3% higher than on the second GEM foil which itself is 5% higher than the third foil. This configuration reduces the probability of discharge significantly because of the gain sharing between three amplification stages, and also because these layers are independent of the readout plane which considerably diminishes the propagation of a streamer before further amplification. The particular design, in turn, reduces their probability of inducing large signals on the readout board and reduces the chances of possible damage to the detector and electronics.

Furthermore, the design of GEM foils is such that the electrodes facing the drift plane are divided into several sectors with each sector having an area nearly equal to 100 cm^2 . Each sector is mounted with a $10 \text{ M}\Omega$ protection resistor, and in the extreme and rare case of a discharge, a voltage drop is induced when current flow through the resistance. This design, in turn, will limit the available charge, and the maximum energy of the discharges and hence helps to reduce the propagation of the discharges. CMS has adopted the sectorization of the GEM foils, the use of protection resistors to limit the energy available in case of a discharge, and the asymmetric distribution of charge-amplifying electric fields over the three GEM foils after following the recommendations in [28].

The discharge probability is estimated for third-generation GE1/1 [4] and separately for a $10 \text{ cm} \times 10 \text{ cm}$ test detector with the similar gap configuration as GE1/1 [27]. In each case, gain is set to extremely high values ranging from 4 to 6×10^5 (Figure 3.31) and the detector is irradiated by densely ionizing α -particles from ^{241}Am source. The actual discharge probability is then calculated by extrapolating its behavior against the drift potential (V). However, the alpha particle from the ^{241}Am source produces nearly a hundred times more primaries than a MIP and hence, the discharge probability is divided by this factor and is observed to be less than 10^{-11} for MIPs in standard CMS operating conditions (Figure 3.33) as shown in Figure 3.31.

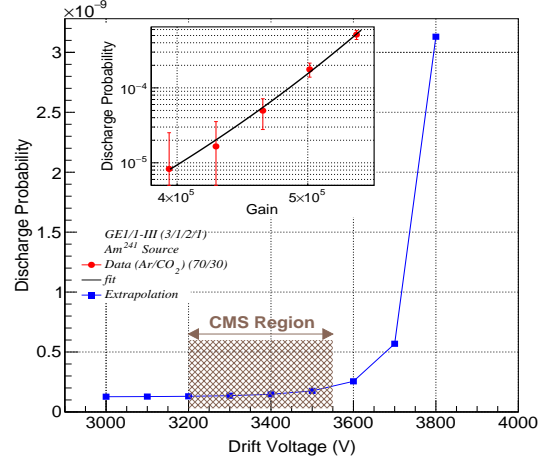


Figure 3.31: Discharge probability[†] for the gas composition Ar/CO₂.

([†]) Thanks to J. A. Merlin for sharing information/suggestions on this plot.



Figure 3.32: A photograph of the shipment box containing six full-size GE1/1 chambers at Delhi University, waiting to be dispatched to CERN (August 2018).

3.7 Fits to data

After several years of R&D that started in 2009, the design of these CMS GE1/1 chambers has been finalized. Before reaching the final design, several full-size prototype chambers have been produced and operated successfully in beam tests [7, 8, 14, 18].

Gas	Parameter	a	b	c	Fit Equation
Ar/CO ₂	Gain	270.85	-22.72	0.007	$G = a * \exp(b + cV)$
	Efficiency	0.983	2885.12	62.59	$\varepsilon = a/1 + \exp - (V - b)/c$
	Timing Resolution	78.48	2346.92	441.1	$R = a/1 + \exp(V - b)/c$
	Discharge Probability	1.002×10^{-31}	0	0.013	$DP = a * \exp(b + cV)$
Ar/CO ₂ /CF ₄	Gain	4336.03	-26.27	0.0068	$G = a * \exp(b + cV)$
	Efficiency	0.99	3502.37	50.78	$\varepsilon = a/1 + \exp - (V - b)/c$
	Timing Resolution	39.21	3126.77	428.09	$R = a/1 + \exp(V - b)/c$
	Discharge Probability	1.79×10^{-28}	0	0.009	$DP = a * \exp(b + cV)$

Table 3.2: The fit equations and the value of constants obtained by fitting gain, efficiency, timing resolution and discharge probability data for the gas compositions Ar/CO₂ and Ar/CO₂/CF₄.

During the process of R&D, different GE1/1 generations have been tested for gain, efficiency, timing resolution, and discharge probability for the gas composition Ar/CO₂ and Ar/CO₂/CF₄. Gain measurements show that the detector can be operated smoothly up to a gain of about 10^5 with a discharge probability of less than 10^{-11} under CMS operating conditions and with a rate capability up to 10^5 kHz/cm². The performance of the chamber in beam tests show the efficiency of 98% or better obtained across the active area and timing resolution nearly equal to 5 ns.

To characterize the performance of a GE1/1 chamber for any drift voltage, the data for gain, discharge probability, efficiency, and time resolution are fit with parametric equations as shown in Table 3.2. The fits provide a good description of the data and allow interpolation to any desired value of drift voltage. Interpolated data points are obtained for the measured quantities and are displayed in the master plots of Figures 3.33 and 3.34 for Ar/CO₂ and Ar/CO₂/CF₄ gases, respectively. The parameters have been optimized and accordingly under efficient, standard CMS, and extrapolated regions are defined. The ‘CMS Region’, shown as a shaded area in the figures, corresponds to the operational regime for the CMS experiment.

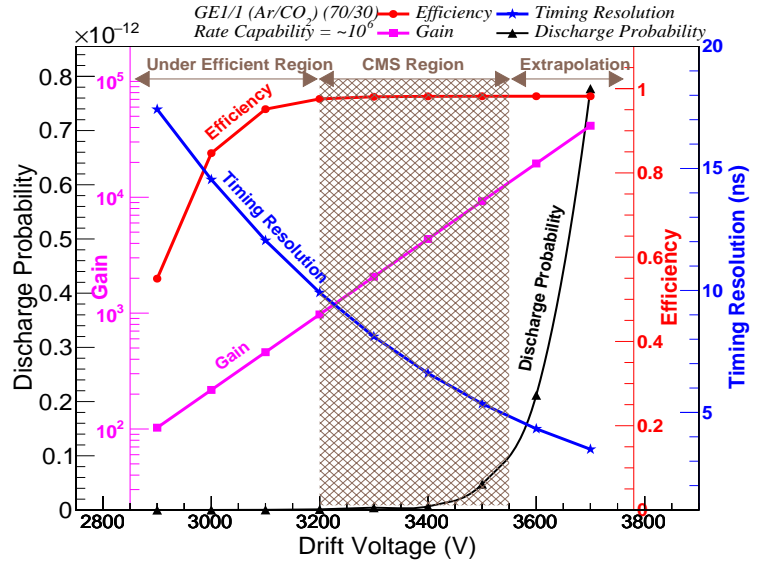


Figure 3.33: Master plot of GE1/1 detectors showing the gain (pink), discharge probability (black), efficiency (red) and time resolution (blue) for the gas composition Ar/CO₂ (70/30) as a function of drift voltage. The axes and corresponding data are represented by the unique color code in the plot. Also, the plot shows the shaded region which is the recommended operational region of the chambers during their use in CMS.

3.8 Involvement of Delhi University in GE1/1 project

Given the complexity of the GE1/1 chamber production and the quantity needed to instrument it in the CMS muon endcap station, several assembly lines have been established in parallel to perform mass production. These include production sites like FIT from the United States, INFN from Italy, DESY from Germany, Delhi University from India, etc. The read-out and drift boards are manufactured by Micropack, an Indian Industry based in Bengaluru, India. Micropack ships these boards to CERN. Apart from producing large area GEM foils needed for GE1/1 size detectors, CERN as a coordinating site performs some tests on these boards and deals with the detector raw materials and their specifications.

The assembly sites receive only components within the required specifications. CERN is the final recipient of the manufactured detectors from assembly sites, additional quality control (QC) procedures have been implemented to verify and test the performance of these chambers. After the final check and all the tests, chambers are eligible to be equipped with the electronics and ready to be installed in the CMS experiment. Delhi University has been involved in the GE1/1 upgrade project at all the fronts. This includes chamber production, quality control and validation, and R&D

both at CERN and Delhi. The following are the quality control tests implemented and recommended by CERN, and each production site is obliged to follow them. The tests performed are briefly discussed below, and the detailed explanation can be found in reference [3].

1. **Quality Control 1 (QC1):**

Visual inspections are performed to discard visibly faulty components. This is done explicitly at CERN.

2. **Quality Control 2 (QC2):**

The measurement of leakage current across a GEM foil is done to validate its performance. The test is divided into two parts QC2 fast and QC2 long. QC2 fast test is performed at 550 V in the air while measuring the impedance of the foil with Gigaohmmeter which supplies a voltage across the faces of the foil, and the number of sparks

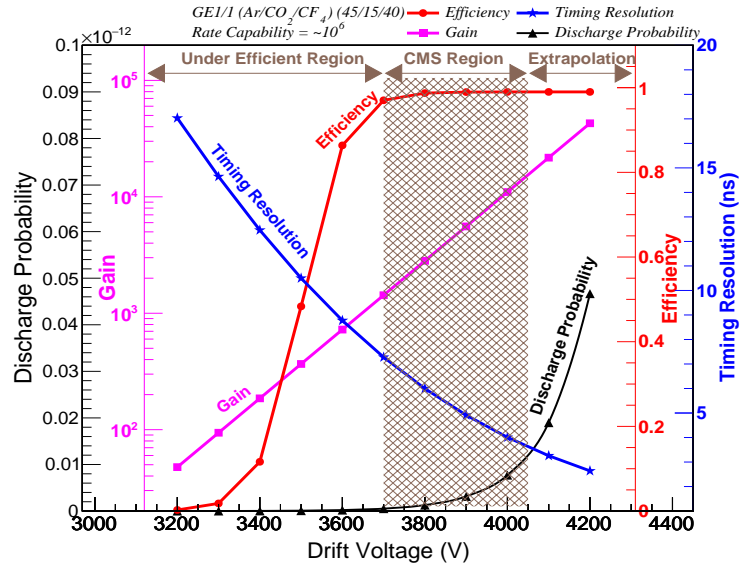


Figure 3.34: Master plot of GE1/1 detectors showing the gain (pink), discharge probability (black), efficiency (red) and time resolution (blue) for the gas composition Ar/CO₂/CF₄ (45/15/40) as a function of drift voltage. The axes and corresponding data are represented by the unique color code in the plot. Also, the plot shows the shaded region which is the recommended operational region of the chambers during their use in CMS.

per minute in 5 minutes are counted. A GEM foil passes the test if its impedance is above $10\text{ G}\Omega$ and the spark rate is lower than 2 Hz after 5 minutes. On the other hand, QC2 long is performed only at CERN, and the experimental setup includes a support frame (usually made up of FR4 material) to which a GEM foil is fastened, and a custom made clip is used to connect GEM foil HV pads to Keithley electrometer which supplies potential difference across the foils. LabVIEW software is used to record the current measurements, and depending upon the number of sparks and leakage current, foils are accepted.

3. **Quality Control 3 (QC3):**

This test is performed on a newly assembled chamber to check if it is adequately sealed after its assembly, and it ensures that it can run without affecting other detectors present in the CMS experiment. The test aims to measure the gas leakage rate by pressurizing the chamber to 25 mbar above ambient (atmospheric) pressure while recording the pressure inside the chamber with a pressure transducer, along with other environmental variables like temperature.

4. **Quality Control 4 (QC4):**

This test aims to ensure a safe and reliable powering system. The I-V characteristics of the detector are obtained in pure CO_2 under high voltage, and also, the spurious counts are monitored. A linear I-V curve is expected when a potential up to 5 kV is applied across the detector. To measure the spurious count rate, a charge sensitive pre-amplifier, amplifier, discriminator, and a scalar are connected to the bottom of the third GEM foil that faces the readout board; the RC circuit is used to decouple the DC component from the foil. The rate of spurious pulses should not exceed $\sim 30\text{ Hz}$.

5. **Quality Control 5 (QC5):**

This test consists of two parts, first part is the measurement of the effective gain of the chamber as a function of the drift voltage in one of the readout sector (e.g., $(\eta, \phi) = (4, 2)$). The second part consists of measuring the response uniformity of the detector strip-by-strip by employing the Scalable Readout System (SRS) and APV25 front-end chips. The variation in the response uniformity of the detector is expected to be less than 15 to 20%.

The QC5 is the last test performed at assembly sites before shipping a chamber to CERN. Specifically, following the assembly technique described in earlier sections of the current chapter, eight full-size GE1/1 chambers have been assembled alone at Delhi University (DU) in 2018. After assembly, chambers have been subjected to a series of quality control tests (QC2 through QC5 as described above) to validate them. The chambers have passed all the tests. Further, another eight chambers assembled at Panjab University were also validated at DU. All the sixteen chambers were finally shipped to CERN (Figure 3.32).

3.9 Current status of the GE1/1 project

The CMS Collaboration proposed the use of GEM technology in the muon endcap of the CMS experiment in 2009. In a first step, 144 new triple GEM GE1/1 chambers will be added

to the first muon endcap stations during the second LHC Long Shutdown (LS2) starting at the beginning of 2019. The shutdown period will last until December 2020.

After, several years of R&D, various generations of GE1/1 chambers have been produced, optimizing the design and performance in each release. The generation-X produced in 2017 is the latest one and is the final design. Ten such chambers have been installed inside the CMS experiment during the 2017 Extended Year End Technical Stop (EYETS). These chambers are providing the first operational experience with GEM detectors inside the CMS. In the first week of December 2018, CMS collaboration achieved a milestone of constructing and validating all the 144 chambers (Figure 3.35) needed for its positive and negative endcaps. The installation and integration of these chambers with the CMS experiment system are scheduled during LS2 (2019-2020).



Figure 3.35: A photograph taken in December 2018 showing some of the large size GE1/1 chambers that have been constructed and stored in racks at CERN Preveessin building 904.

3.10 Summary and conclusions

As part of the High Luminosity LHC project, the CMS collaboration approved the use of GEM technology to extend its muon system coverage in the forward region. Due to the geometrical constraints, the CMS will employ a specific GEM GE1/1 chamber, the design of which has been finalized. These chambers are constructed using a novel mechanical stretching technique presented in the current chapter that requires no spacers inside the active area and no gluing during detector assembly. The technique reduces the chamber construction time from several days to only a few hours. In the first step, ten chambers were produced with the current assembly technique and installed inside the CMS experiment during the 2017 Extended Year End Technical Stop (EYETS) [3, 16, 17]. These chambers are providing the first operational experience with GEM detectors inside the CMS cavern. Further, a total of 144 new full-size GE1/1 chambers have been produced using this technique. All these chambers needed for the CMS high eta upgrade have been validated successfully after subjecting them to a series of quality control (QC) tests. Out of 144, sixteen full-size GE1/1 chambers have been constructed at Delhi University (DU) and Panjab University (PU) in 2018. After assembly, all these chambers were validated at DU after a series of QC tests and shipped to CERN. The integration of these chambers with the CMS muon endcap is being prepared and is on schedule. The installation will take place during LS2 currently underway.

During the process of R&D, different GE1/1 generations have been tested for gain, efficiency, spatial and time resolutions, and discharge probability for the gas composition Ar/CO₂ and Ar/CO₂/CF₄. Measurements show that the detector can be operated smoothly up to a gain of about 10^5 with a discharge probability of less than 10^{-11} under CMS operat-

ing conditions which are being considered safe during HL-LHC. Since the expected particle rates in the CMS endcap are 10 kHz/cm^2 , and the rate capability tests performed in the current work on GE1/1 chambers demonstrated that these detectors can be operated up to 10^5 kHz/cm^2 without any loss in performance. Further, the performance of the chambers in beam tests shows an efficiency of 98% or better obtained across the active area, and time resolution close to 5 ns. The obtained results for different gas compositions such as Ar/CO₂ and Ar/CO₂/CF₄ with different mixtures have been compared. For a given value of gain, resolution for Ar/CO₂/CF₄ appears to be $\sim 23\%$ better than the corresponding value for Ar/CO₂. In other words, by adding CF₄ to Ar/CO₂, the timing performance of the detector improves. It also allows the detector to operate at the lower gains, hence reducing the discharge probability. However, since the CF₄ is a potential global warming gas and the CMS has followed not to continue working with the gas mixture with CF₄ as a part.

Further, to characterize the performance of a GE1/1 chamber for any drift voltage, the data for gain, discharge probability, efficiency, and time resolution are fit with parametric equations. The fits provide a good description of the data and allow interpolation to any desired value of drift voltage. Interpolated data points are obtained for the measured quantities for different gas compositions and the ‘CMS Region’, has been defined which corresponds to the operational regime for the CMS experiment.

BIBLIOGRAPHY

- [1] CMS Collaboration, “[The CMS experiment at the CERN LHC](#)”, JINST, 3 (2008) S08004.
- [2] CMS Collaboration, “[Performance of the CMS muon detector and muon reconstruction with proton-proton collisions at \$\sqrt{s}=13\$ TeV](#)”, JINST, 13 (2008) P06015.
- [3] D. Abbaneo et al., “[Operational experience with the GEM detector assembly lines for the CMS forward muon upgrade](#)”, IEEE Trans. Nucl. Sci. 65 (11) (2018) 2808-2816.
- [4] CMS Collaboration, “[CMS Technical Design Report for the Muon Endcap GEM Upgrade](#)”, CMS TDR, CERN-LHCC-2015-012 (2015), RD51-Note-004.
- [5] F. Sauli, “[GEM: A new concept for electron amplification in gas detectors](#)”, NIMA. A386 (1997) 531.
- [6] M. Alfonsi et al., “[Operation of triple-GEM detectors with fast gas mixtures](#)”, Nucl. Instrum. Meth. A 488 (2002) 493.
- [7] D. Abbaneo et al., “[Beam test results for new full-scale GEM prototypes for a future upgrade of the CMS high- \$\eta\$ Muon System](#)”, IEEE Nucl. Sci. Symp. Conf. (2012) N14-137.
- [8] D. Abbaneo et al., “[Test beam results of the GE1/1 prototype for a future upgrade of the CMS high- \$\eta\$ muon system](#)”, IEEE Nucl. Sci. Symp. Conf., (2011) 1806-1810, and RD51-Note-2011-013..
- [9] S. D. Pinto et al., “[Progress on large area GEMs](#)”, JINST 4 P12009 (2009).
- [10] D. Abbaneo, et al., “[Construction of the first full-size GEM-based prototype for the CMS high- \$\eta\$ muon system](#)”, IEEE Nucl. Sci. Symp. Conf., (2011) 1909.
- [11] D. Abbaneo et al., “[Status of the Triple-GEM project for the upgrade of the CMS Muon System](#)”, JINST 8 (2013) C12031.
- [12] M. Tytgat et al., “[Construction and performance of large-area triple-GEM prototypes for future upgrades of the CMS forward muon system](#)”, IEEE Nucl. Sci. Symp. Conf. (2011) 1019.

- [13] D. Abbaneo et al., “[A novel application of Fiber Bragg Grating \(FBG\) sensors in MPGD](#)”, 4th Int. Conf. on MPGD 174 (2018) 03002.
- [14] D. Abbaneo et al., “[Performance of a large-area GEM detector prototype for the upgrade of the CMS muon endcap system](#)”, IEEE Nucl. Sci. Symp. Conf. (2014) 1-8.
- [15] D. Abbaneo et al., “[GEM based detector for future upgrade of the CMS forward muon system](#)”, NIMA 718 (2013) 383-386.
- [16] A. Shah et al., “[A Novel Assembly Procedure of GE1/1 Detectors for CMS High Luminosity Phase of the LHC](#)”, Spring. Proc. in Phy., (2018) 203.
- [17] D. Abbaneo, A. H. Shah et al., “[Layout and assembly technique of the GEM chambers for the upgrade of the CMS first muon endcap station](#)”, Nucl. Inst. Meth. A 918 (2019) 67.
- [18] D. Abbaneo et al., “[Characterization of GEM Detectors for Application in the CMS Muon Detection System](#)”, RD51-NOTE (2010) 005.
- [19] A. Shah et al., “[Impact of Single-Mask Hole Asymmetry on the properties of GEM Detectors](#)”, submitted to Nucl. Inst. Meth. A, doi.org/10.1016/j.nima.2018.11.017.
- [20] J. A. Merlin, “[GEM single-mask characterization and influence of GEM foil orientation](#)”, MPGD (2017).
- [21] M. Alfonsi et al., “[Operation of triple-gem detectors with fast gas mixtures](#)”, Nucl. Inst. Meth. A 488 (2002), 493.
- [22] P. Aspell et al., “[VFAT2: A front-end system on chip providing fast trigger information, digitized data storage and formatting for the charge sensitive readout of multi-channel silicon and gas particle detectors.](#)” page 5 p, 2007.
- [23] D. Abbaneo et al., “[The status of the GEM project for CMS high- \$\eta\$ muon system](#)”, Nucl. Inst. Meth. A 732 (2013) 203-207.
- [24] G. Anelli et al., “[The TOTEM experiment at the CERN Large Hadron Collider](#)”, JINST 3 S08007 (2008).
- [25] P. Aspella et al., “[The VFAT Production Test Platform for the TOTEM Experiment](#)”, Topical Workshop on Electronics for Particle Physics, CERN, (2009).
- [26] D. Abbaneo et al., “[Charged Particle Detection Performance of Gas Electron Multiplier \(GEM\) Detectors for the Upgrade of CMS Endcap Muon System at the CERN LHC](#)”, IEEE Nucl. Sci. Symp. (2015) 04.
- [27] J. A. Merlin, “[Study of long-term sustained operation of gaseous detectors for the high rate environment in CMS](#)”, CERN-THESIS-2016-041, (2016).

BIBLIOGRAPHY

- [28] S. Bachmann et al., “[Discharge Studies and Prevention in the Gas Electron Multiplier \(GEM\)](#)”, Nucl. Inst. Meth. A 479 (2000) 294.
- [29] H. Raether, “[Electron avalanches and breakdown in gases](#)”, CERN CDS 191 (1964).
- [30] D. Abbaneo, A. H. Shah et al., “[Performance of GE1/1 Chambers for the CMS Muon Endcap Upgrade](#)”, submitted to Nucl. Inst. Meth. A, [arXiv:1903.02186](#).

R&D on GEM foils

*Measure what can be measured,
and make measureable what cannot be measured.*

— Galileo Galilei

The large size GEM-foils (as considered for the GE1/1 chamber production in Chapter 3) are produced by the “single-mask foil” production technique. This technique, unlike double mask foil production, does not require any alignment of masks as only one mask is employed and hence allows the production of foils with very large size as required for the CMS high eta upgrade. However, the holes obtained with refinements in the single-mask technique are asymmetrically bi-conical in shape compared to symmetrically bi-conical holes of the conventional double-mask technology. Since the hole geometry and their uniformity define the performance of the detectors constructed using such GEM-foils, the detailed effect is evaluated using a GEM prototype in which three foils are stacked on top of each other. The structure has the flexibility of changing the orientation of foils. The detector is tested with large holes openings (from top) as well as small holes openings (from bottom), and the results that include the study of measurements on the effective gain and its uniformity, energy resolution and its uniformity, charging up behavior, and rate capability for the two hole orientations are included in this chapter.

Further, the increasing demands for GEM foils have been driven by their applications in many current and proposed high-energy physics experiments. Micropack, a Bengaluru-based company in India along with other Indian research institutions, for the first time established and commercialized GEM foils under the transfer of technology (TOT) agreement with CERN and produced successfully 10 cm × 10 cm GEM foils using the double-mask etching technique. The chapter further documents foil development and detailed characterizations that were performed at the University of Delhi to validate these foils. The tests include geometrical hole size uniformity and measurement of leakage currents including discharge studies.

4.1 Introduction

The instantaneous luminosity at the Large Hadron Collider (LHC) will exceed $2 \times 10^{34} \text{ cm}^{-2}\text{s}^{-1}$ after the second Long Shutdown (LS2) upgrade. An additional set of muon detectors known as GE1/1 will be installed during LS2 in the first end-cap muon station in the region $1.6 < |\eta| < 2.2$ of the CMS experiment [1,2] to enhance the muon trigger and reconstruction capabilities. The proposed GE1/1 station uses Gas Electron Multiplier (GEM) technology [3] which has a high rate capability and works as an excellent choice for muon detector in the high eta (high- $|\eta|$) region of the CMS experiment [4]. The GE1/1 upgrade paves the way for further CMS muon system upgrades with GEM detectors for the High-Luminosity LHC. The GE1/1, however, uses large-size GEM foils which are produced using the single-mask technique [5]. In this chapter, a brief description of their production and detailed characterization study like effective gas gain, energy resolution, and stability under continuous irradiation is provided. The measurements are performed with $10 \text{ cm} \times 10 \text{ cm}$ prototype triple-GEM detector for convenience but are still valid for large size GE1/1 detector as local phenomena within the GEM holes govern most of these parameters.

4.2 Single-mask foil production

The double mask foil production is based on common photolithography processes used in the PCB industry where hole structure is created by exposing the polyimide foil laminated in photoresistive material to UV-radiation. Foils are then etched in an acid bath for copper removal from the holes. Photoresistive material prevents copper from being etched. For the etching of the polyimide substrate, copper holes act as a mask. The alignment between top and bottom films is usually within $5 - 10 \text{ }\mu\text{m}$ to obtain the uniform holes. However, due to the flexibility of the base material, the alignment between the top and bottom films is far from trivial. The method is, however, hardly feasible for large size foils exceeding dimensions half a meter and a way to defeat this hurdle is by using a single-mask technique as shown in Figure 4.1. By employing one mask over the top copper layer, no alignment is needed. Utilizing the polyimide holes as a mask, the bottom layer is etched. The polyimide etching controls the homogeneity and the geometry of the holes. The two critical steps in the production of GEM foils are polyimide and copper etching as described in the following subsections.

4.2.1 Polyimide etching

The polyimide etching of GEM foils is performed in an aqueous solution comprising of potassium hydroxide (KOH) and ethylenediamine. The material in touch with potassium hydroxide is removed isotropically in all directions. Contrary to it, ethylenediamine etches materials anisotropically in contact with it resulting in wide conical holes. The isotropic etching occurs in holes which are at least twice wider than their depth with the removal of the polyimide until far under the electrode. Generally, etching under the copper results low aspect ratio¹ and prevents the use of isotropic etching for a single-mask technique. Though

¹Aspect ratio is the ratio of depth over the width of a hole.

the material is not removed under copper, the edges are not steeply adequate to arrive at a high aspect ratio while using only ethylenediamine solution for etching. On the other hand, the steepness of the individual holes can be adjusted using a solution of ethylenediamine and KOH by controlling its composition.

The increase in temperature enhances the etching rate of KOH higher than that of ethylenediamine, and hence, the temperature must be kept control. When these parameters are optimized, holes of diameter $\sim 85 \mu\text{m}$ on top and $\sim 50 \mu\text{m}$ on the bottom are obtained as illustrated in Figure 4.2. Such a profile is used for the large size prototype. The technique has been further improved by adding ethanol to the etching liquid leading steeper holes. The solutions having constituents water, ethanol, ethylenediamine, and potassium hydroxide are normally used.

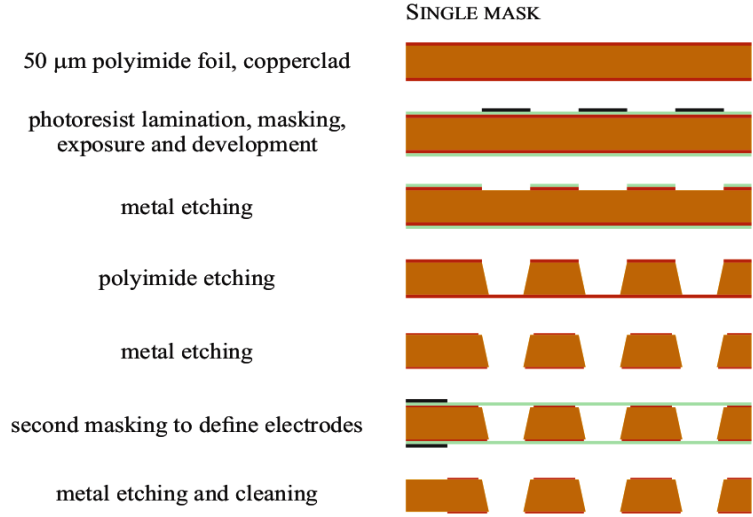


Figure 4.1: Schematic procedures for the fabrication of a single-mask GEM foil [5].

4.2.2 Copper etching

The top electrode etching is pretty much similar in single and double mask techniques but the bottom electrode etching varies. The bottom electrode is etched by immersing foil in acidic etchant both from the polyimide and the unprotected outer face of the copper. If the electrodes are not protected, they get etched at the same rate and at the same time. Therefore, the electrodes get trimmed nearly to half of their original thickness. Also, clearance arises around the edge of the hole in the polyimide due to the isotropic copper etching technique. The clearance customarily referred to as the rim is known to deteriorate time stability of the gain due to surface charging of dielectric surface charging, an effect called as charging up (discussed in the later sections of the present chapter). The electrode thickness is decreased before etching holes so as to minimize rim width. The material budget is reduced significantly by slimming down GEM electrodes using a microetch liquid based on ammonium persulfate, leaving the properties of the detector undeteriorated. The liquid etches more efficiently at grain boundaries furnishing the copper surface a matte appearance. The resulting copper thickness can be varied by a few microns across the foil using this surface etchant at large areas [5]. This, in turn, causes variations in the hole diameter of the bottom electrodes giving rise to non-uniformities in performance such as in gain. Additionally, the enhancement in surface roughness is responsible for the degradation of the holes in the bottom leading to coarse copper edges around them, which in turn may increase

the discharge probability of GEM-based detectors while in operation. The issues of surface roughness and inhomogeneity are overcome by using chromic acid as a surface etchant instead of a microetch, leaving a shiny surface. Further, to avoid producing the rim in electrodes (top), the metal is protected by galvanic and electrochemical protection when etching the bottom electrode. The top electrode is hermetically shielded with galvanic protection which does not allow etchant to reach it. It is very complicated to obtain a uniform hermeticity as slight delamination between polyimide and copper leads a leakage which finally attacks the copper. Electrochemical protection, on the other hand, proves to be more successful in bypassing a rim in the top electrode.

The GEM foils made following the above prescription have gain almost consistent with standard double-mask foils. However, their chances of damage due to discharges are found to be more than standard GEM-foils.

4.3 Performance studies

The single-mask production technique gives rise foils with asymmetric holes. Due to the refinements in the production technique, foils with lesser hole asymmetry has been produced as compared to the batch of foils considered for the present study. The foils have asymmetric holes with a wide hole opening ($85\ \mu\text{m}$) on one side (top) and slightly a narrow hole opening ($70\ \mu\text{m}$) on the other side (bottom) as depicted in Figure 4.2. The impact of the hole asymmetry on the detector properties such as gain, response uniformity and the rate is evaluated in detail.

Both these openings are irradiated independently, in one case wide opening faces the source and in the other case narrow opening facing the source. For the measurement purpose, the first orientation is termed as ‘Orientation A’ and the second orientation as ‘Orientation B’, respectively. Therefore, to study the effect due to this asymmetry, a special detector is constructed with stack accommodat-

ing three single-mask GEM foils having an active area of $10\ \text{cm} \times 10\ \text{cm}$ with a symmetric gap configuration of (2/2/2/2) mm for drift, transfer-1, transfer-2, and induction gap as shown in Figure 4.3.

The detector is assembled by placing two single pieces of copper plates on the top and bottom of the GEM stack which acts as the drift electrodes. To ensure gas tightness, the gas volume is closed by employing Viton O-rings between the lateral epoxy frames and the PCB. The detector has two windows, one on the top and the other on the bottom facilitating irradiation of the GEM foils with either ‘Orientation A’ or with ‘Orientation B’ without opening the detector. The configuration minimizes the scientific errors and human interference that may occur due to the repeated opening of the detector. In one set of measurements with ‘Orientation A’ on the top (facing the incident source), one copper plate serves as a drift cathode, and the other is merely connected to the ground. The



Figure 4.2: (left) Scanning Electron Microscope (SEM) image showing the asymmetric single hole structure in GEM produced by single-mask technique and (right) its schema.

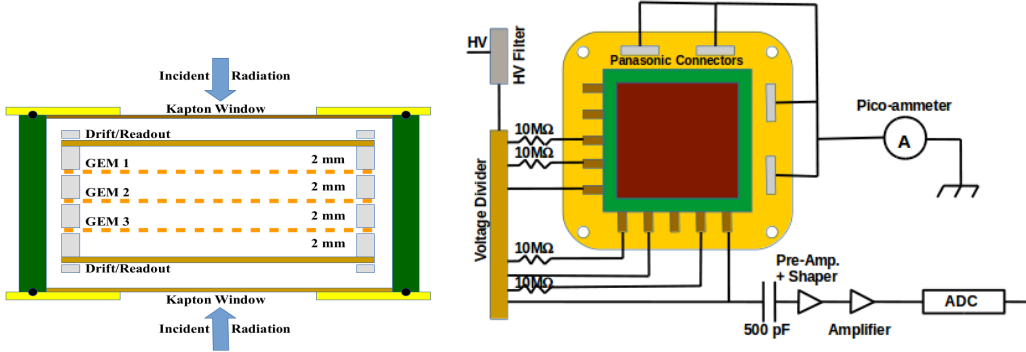


Figure 4.3: (left) A 10 cm \times 10 cm detector with a symmetric gap configuration of (2/2/2/2) mm and two windows, the one on the top and other on the bottom for irradiation purposes, and (right) design of the detector realized for the measurement purposes.

output is taken from the bottom of the third GEM via a decoupling capacitor. In the other test campaign with ‘Orientation B’ on the top (obtained after flipping the detector), the powering circuit is flipped, and the copper plate (previously connected to the ground) acts as a drift cathode, and the bottom of the third GEM is considered for reading the signal. The electrodes are powered with a high voltage (HV) divider that provides the appropriate electric fields for the efficient operation of the detector [7]. Additionally, GEM top electrodes are preceded by using 1 M Ω protection resistances (Figure 4.3) to limit the current flowing through the foils in the exceptional and rare case of discharge. Even though, the configuration (2/2/2/2) mm differs from the CMS gap configuration (3/1/2/1) mm, it facilitates the measurements. Since the behavior of GEM detectors is determined by the local phenomena occurring within and across the holes, therefore, measurements do not affect the comparative study significantly.

4.3.1 Effective gain measurements

The chamber is connected to the gas system and flushed with the standard gas mixtures at the flow rate of 2 to 3 liters per hour, and left to flush for at least 5 hours before taking the actual measurement.

The detector is irradiated with ^{55}Fe source on both the directions, i.e., from the top and the bottom side with the appropriate applied fields by inverting the external resistive divider used to provide different potential across three foils. The source produces photons with average energies of 5.9 keV which are fully converted into electron-ion pairs in the drift gap via the photoelectric effect in the gas of the drift region. The amplified current I_a induced on the bottom of the last GEM foil is measured and the effective gain ‘G’ is estimated by comparing the output with the input current. The output current is measured efficiently using a Keithley 6487 pico-ammeter connected to the anode and is expected to be of several tens of pico-amperes with a strong dependence upon the applied voltage. It is very challenging to measure the primary current in the drift region which is very small (nearly a few tens of femtoamperes). This is due to the reason that the current to be collected from the electrode (bottom of the third GEM) is placed HV and is susceptible to inherent noise.

Hence, the primary current is measured indirectly by estimating the interaction rate ‘R’ by counting the number of pulses induced by the particles and then multiplying by the charge of the ions.

The rate is measured using the bottom of the last GEM foil to an ORTEC pre-amplifier through a 500 pF (decoupling capacitor) to de-couple the HV. The digital pulses are obtained by allowing analogue pulses to pass through it. Finally, the gain is calculated by using the relationship (4.1) between various parameters as

$$G = \frac{I_\alpha}{R \times n_{e^-} \times e^-} \quad (4.1)$$

where ‘R’ is the incoming particle rate of the source, ‘ n_{e^-} ’ are number of primary electrons produced per incoming particle² which are approximately 212 for the gas composition Ar/CO₂ (70/30) and ‘ e^- ’ is the charge of the electron. The effective gain determined for ‘Orientation A’ and ‘Orientation B’ is shown in Figure 4.4. It clearly shows the extraction efficiency plays an important role in the effective gain measurement as the gain is observed to be higher in ‘Orientation B’ compared to ‘Orientation A’ configuration by a factor of ~ 2 . The effect could be attributed to the complex processes like electric field variations inside the hole etc. and their consequent impact on the amplification. The gain variation between the two single mask orientations is especially interesting for the GE1/1 applications as for a given applied voltage, ‘Orientation B’ provides better detection performance. On the other hand, ‘Orientation A’ would demand higher voltages to reach a similar performance.

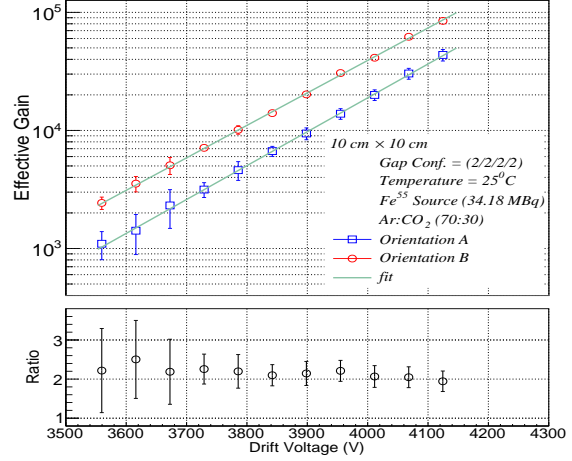


Figure 4.4: Gain measured in a triple GEM 10 cm \times 10 cm detector when all the three foils either with ‘Orientation A’ or with ‘Orientation B’ are facing the incident source (Fe^{55}). The ratio plot in the bottom shows that the gain is almost two times higher in ‘Orientation B’ compared to ‘Orientation A’.

4.3.2 Energy resolution

The energy resolution³ is an indicator of the quality of the GEM-foils. The good energy resolution demands good uniformity of the foils. Any defects in holes such as missing copper,

²The number of primary electrons n_{e^-} for Ar/CO₂ (70/30) gas mixture per incoming 5.9 keV photon from ^{55}Fe source are given by

$$n_{e^-} = E_\gamma \times \left(\frac{\%Ar}{W_i(Ar)} + \frac{\%CO_2}{W_i(CO_2)} \right) = 5900 \times \left(\frac{0.7}{26} + \frac{0.3}{33} \right) \approx 212 \quad (4.2)$$

where $E_\gamma \approx 5.9$ keV is the energy of the incident gamma-ray photons, %Ar and %CO₂ are the percentages of the gases in the mixture, $W_i(\text{Ar})$ and $W_i(\text{CO}_2)$ are the work functions of the gases. Using $E_\gamma \approx 8.03$ keV for copper (Cu) X-rays, n_{e^-} of 289 is obtained.

³Energy resolution is defined as the ratio of the Full Width at Half Maximum (FWHM) over the mean of the photopeak.

cracks in the Kapton, or overhanging copper cladding change the amplification properties resulting in the loss of energy resolution.

The energy resolution of the detector in Ar/CO₂ (70:30) gas composition is determined by measuring the pulse height spectrum of Iron-55 (⁵⁵Fe). The ⁵⁵Fe decays to excited Manganese (⁵⁵Mn) via electron capture (EC) and latter emits a photon while returning to the ground state. Depending on the inner rearrangement of the electrons, the photons with two different energy (E_γ) lines K_α or K_β are emitted depending on whether the transition of an electron is from the L to K or M to K shell. The former carries an energy of 5.90 keV and the latter 6.50 keV with the line intensity proportional to 24.4% and 2.86% for K_α and K_β lines, respectively. The K_α process dominates over K_β by, approximately, a factor of 10.

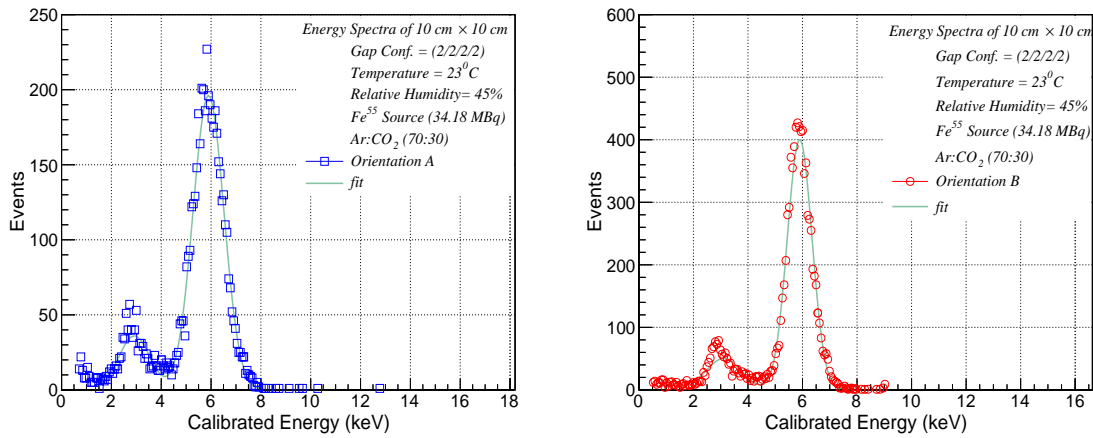


Figure 4.5: Energy spectrum of the ⁵⁵Fe source in Ar/CO₂ (70: 30) showing the main photo and the Ar escape peaks: (left) ‘Orientation A’ and (right) ‘Orientation B’. The spectra are fitted with Gaussian functions for the extraction of μ and σ .

The process of detection in GEM detectors begins with the ionization of the gas. The photons interact with the innermost shells of Ar/CO₂ gas and produce ionization. Since the K_α photon energy is higher than the binding energy of the Ar K shell electron ($E_K = 3.22$ keV), the electron can detach with residual kinetic energy of 2.68 keV. The excited Ar atom then returns to its ground state by emitting one or more photons which may leave the volume (without being detected). If this Ar- K_α photon escapes from the detector, an amount of energy equal to the energy of the escaped Ar X-ray (around 2.9 KeV) is lost from the detector. There is a non-negligible probability ($\sim 15\%$) that this de-excited photon escapes through the detector resulting in a loss of energy equal to photon energy. Therefore, the typical energy spectrum shows two peaks, the first one appears at the total energy deposited by the source (5.9 KeV for ⁵⁵Fe), and the second one, the Ar escape peak appearing at an energy 3.2 KeV less (around 6 KeV for Cu and 3 KeV for Fe) than the main peak. The main peak position in the energy spectrum is proportional to the energy deposited by the source. Recording such a spectrum with the triple GEM detector is used to affirm the energy resolution of the detector. The source is placed over the active area of the detector and the signal is readout via the bottom of the third GEM. The spectrum is recorded using a multichannel analyzer (MCA) and is illustrated in Figure 4.5. For affirming quantitatively

the energy resolution, Gaussian function

$$G(x, \mu, \sigma) = \frac{1}{\sqrt{\sigma}2\pi} \times \exp \frac{-(x - \mu)^2}{2\sigma^2} \quad (4.3)$$

is fitted to the histogram and the variable σ is extracted. The μ in above equation is recognized as the mean and σ as the standard deviation of the distribution. The energy resolution $\Delta E/E$ is then estimated by transferring σ into FWHM and employing the equation

$$\Delta E/E = \frac{FWHM}{E} = 2\sigma \frac{\sqrt{2\ln 2}}{E} = 2.35 \frac{\sigma}{E} \quad (4.4)$$

Equation 4.4 yields the best value of resolutions of 24% and 18% for ‘Orientation A’ and ‘Orientation B’, respectively.

4.3.3 Charging-up behaviour

The durability of the detector’s gain over time is essential for reaching a stable detector performance. This is also manifested in energy resolution and detector efficiency. The gain variation is connected directly to the charging-up behavior of the detector’s insulating surfaces (Kapton) which modifies the electric field in the charge-multiplication region.

When the detector is under continuous irradiation, effective gain (with dependence on time) is measured for both the orientations. The measurements are performed in Ar and CO₂ to ensure no charge losses from the detector’s insulator (by electro-negative gas molecules) and to evade possible neutralization of the charged electrodes (by the gas molecules). On the other hand, the use of electro-negative gas (hybrids) can partially attach charges accumulating on the insulating surfaces introducing an additional dependency of the gain-stabilization process. To avoid potential discharge-induced effects, the measured gain values are recorded below the discharge limit.

The setup used for the charging-up measurement is shown in Figure 4.6. The voltages are set a few hours before irradiating the detector to ensure that the insulator is fully polarized. The ⁵⁵Fe source is fixed on the top of the active transparent window. The snapshots of gain, each lasting for a short duration of approximately 30 seconds are taken and the variation over time in steps of 60 seconds while continuously irradiating the detector is recorded with the multichannel analyzer (MCA). At each step, the measured pulse-height spectra are fitted with a Gaussian function, and the values of mean and the standard deviation are extracted. The mean is recognized as the gain.

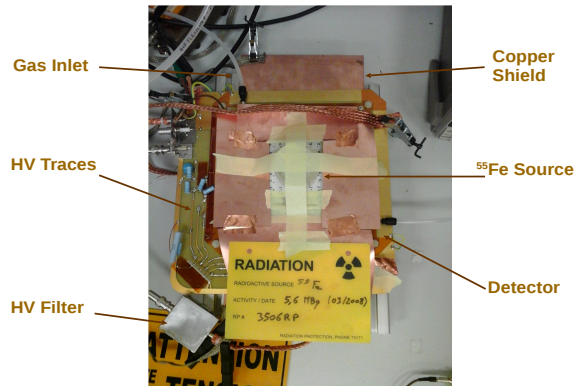


Figure 4.6: The GEM detector wrapped in a copper shield. The shield acts a Faraday cage for the detector.

4.3. PERFORMANCE STUDIES

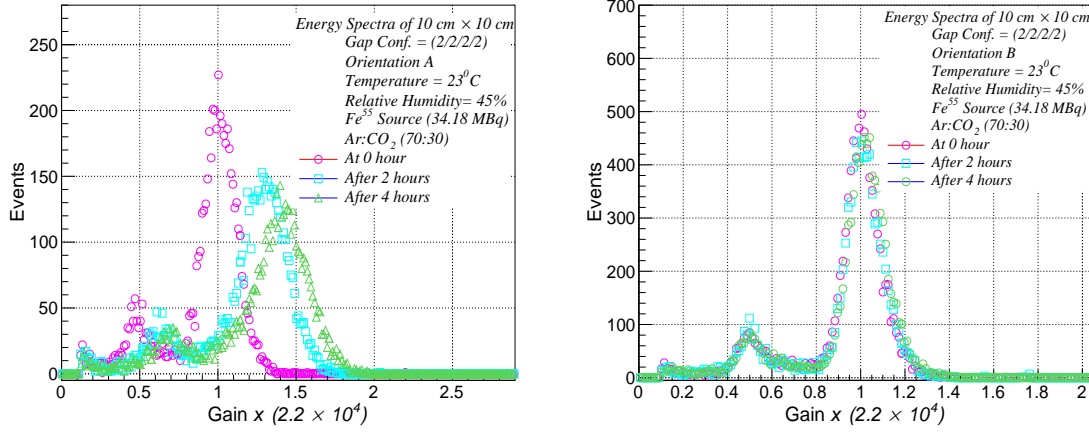


Figure 4.7: Energy spectra taken at the start of the measurement, after 2 and 4 hours under continuous irradiation: (left) ‘Orientation A’ and (right) ‘Orientation B’.

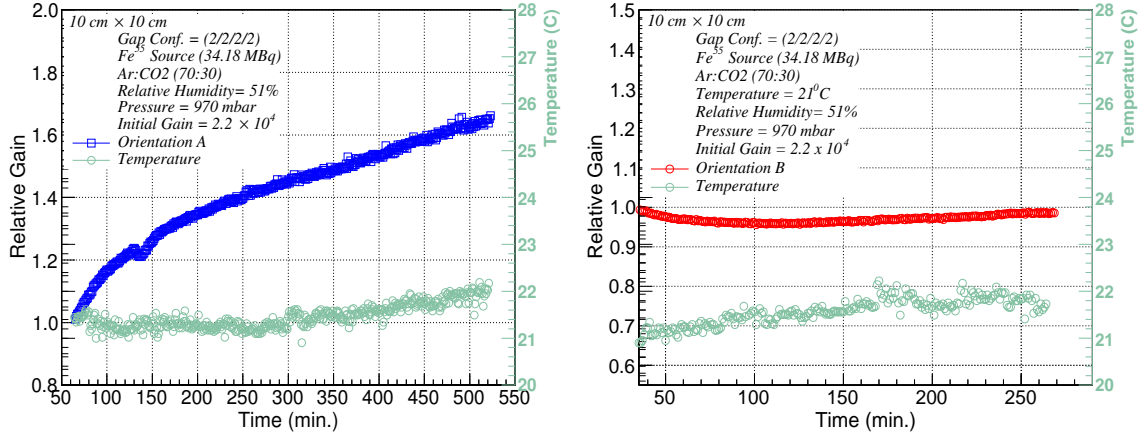


Figure 4.8: Normalized gain (charging-up curves) as a function of time for ‘Orientation A’ and ‘Orientation B’ when the detector is placed under continuous irradiation. Temperature is also plotted to demonstrate the stability under the ambient conditions. The humidity and pressure are recorded to be constant during the period of measurements.

The Figure 4.7 shows the back-to-back spectra taken for ‘Orientation A’ and ‘Orientation B’ at fixed intervals of time when the detector is under continuous irradiation. For ‘Orientation A’, the mean of the spectra shifts to the right due to the charging up effect while as no such an effect is observed for ‘Orientation B’. Further, recording gain continuously over a period of time reveals that the gain increases steadily in ‘Orientation A’ up to 1.6 times the initial gain of 2.2×10^4 during the period of measurement as shown in Figure 4.8. While in ‘Orientation B’, the gain is observed to be almost flat with respect to the initial value. The observed differences in gain (Section 4.3.1) and the charging up behavior are attributed to avalanche multiplication within the GEM holes in which charge deposits on the insulator surface and consequently modifies the electric field. The effective electric field map is, therefore, the sum of the initial electric field superimposed with the field induced by accumulated charges. The resulting effect modifies the gain. The gain clearly increases with radiation exposure with time. This can be qualitatively due to the increase of the electric field within the hole

induced by accumulating charges (on the side walls). After a certain duration of time, gain stabilizes due to the deposition of the charges on the surface of the dielectric consequently opposing an additional deposition of the charges [6].

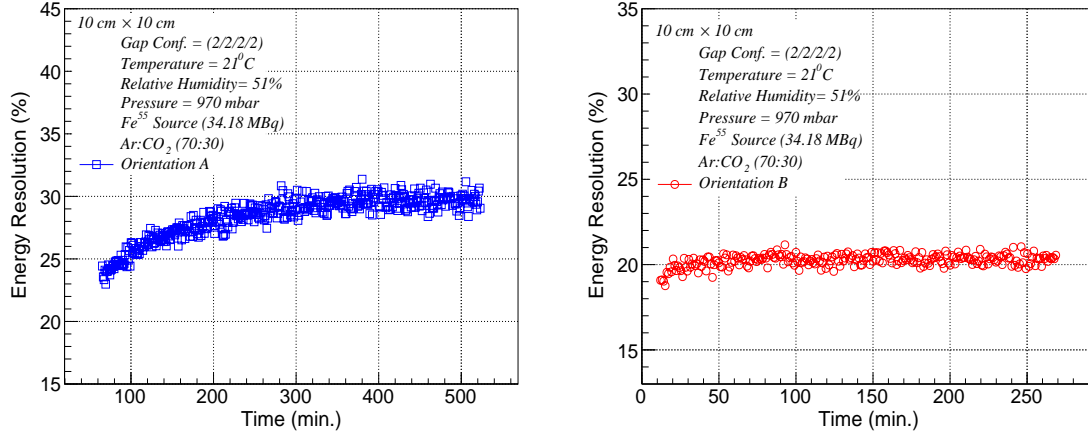


Figure 4.9: Energy resolution determined as a function of time with the initial gain of 2.2×10^4 when ^{55}Fe source is continuously irradiated on the detector: (left) ‘Orientation A’ and (right) ‘Orientation B’

The polarization and radiation effects affect the stability of detector gain. The transfer of charges inside the polyimide layer is characterized by polarization. This effect is independent of the charge deposition by particles on the outer surface. It becomes stable after a few hours of operation. On the other hand, the radiation effects occur during the amplification and are due to the appendage of charges to the inner polyimide surface. Due to the very high polyimide resistivity, charges accumulate on the surface till equilibrium is attained. This effect has a dependence on the hole geometry and the amount of charge crossing it per unit time. The stabilization time has a dependence on interaction rate, detector gain, and the primaries. Further, the time required to drain the attached charges is driven by the conductivity of the polyimide surface which in turn is humidity (of gas) dependent. Due to these reasons, the charging-up measurements are performed in a controlled environment where ambient pressure, temperature, and relative humidity are maintained constant throughout the measurement. The chambers are also wrapped with copper shields to minimize the electronic noise as shown in Figure 4.6. The chambers and electronic modules are switched ON for several hours before the start of the actual test. This is done to avoid possible instability of the modules and to avoid polarization fluctuations.

After comparing the measurements for ‘Orientation A’ and ‘Orientation B’ under identical operating conditions, ‘Orientation B’ appears to be more suited for the GE1/1 operation than ‘Orientation A’.

4.3.4 Impact of continuous irradiation on resolution

The energy resolutions are determined using ^{55}Fe source at an equal initial gain of 2.2×10^4 and the best-obtained values are $\sim 23.71\% \pm 0.02$ and $\sim 18.06\% \pm 0.01$ for ‘Orientation A’ and ‘Orientation B’, respectively (as explained in Section 4.3.2). Further, the resolutions

are determined after irradiating the detector continuously by ^{55}Fe source over a long period of time. The resolution in ‘Orientation A’ worsens with respect to the initial value of 24% and becomes nearly flat at 30% as shown in Figure 4.9, the effect might be attributed to the charging up behavior as noted in Section 4.3.3. On the other hand, the initial value of the resolution in ‘Orientation B’ is observed to be 18% and stabilizes at around 20%. Similar conclusions are drawn from Figure 4.10, where relative energy resolutions are plotted against the relative gain.

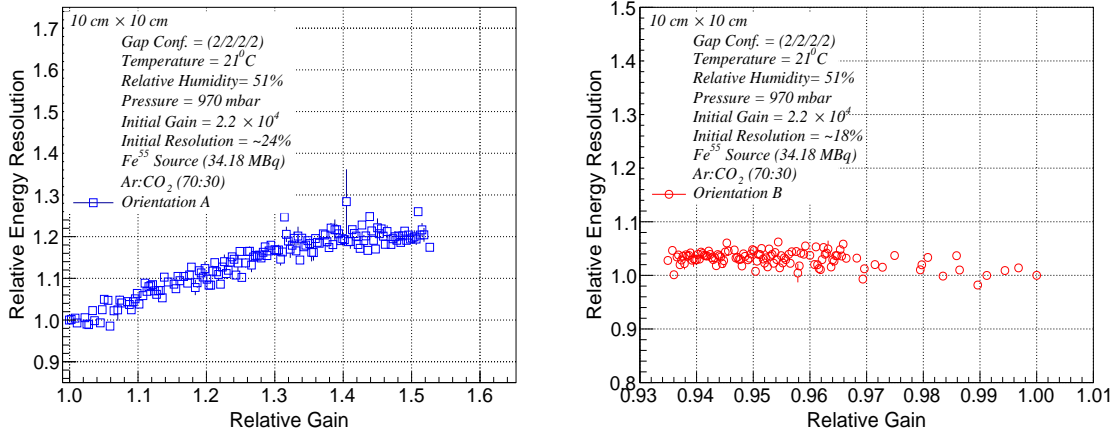


Figure 4.10: Profile plot of relative energy resolution measured as a function of relative gain with the initial gain of 2.2×10^4 when Fe^{55} source is continuously irradiated on the detector: (left) ‘Orientation A’ with the initial resolution of 24% and (right) ‘Orientation B’ with the initial resolution of 18%.

4.3.5 Rate capability

The problem with traditional detectors such as Resistive Plate Chamber (RPC) is the limited response at high interaction fluxes. At several Hz/mm^2 , the space-charge evokes a local electric field perturbation leading to a drop in gas gain. Such an effect can, however, be minimized by reducing the design of the amplifying structure to a microscopic scale. This, in turn, can help in reducing the time taken by the ions to deplete from an avalanche, thereby, minimizing space-charge effects. All such issues are well-taken care of in the design and working principle of GEM detectors.

High rate capability⁴ is crucial for in High Energy Physics (HEP) applications. It is measured by irradiating the test detector with a 22 keV (Ag target) intense X-ray source by increasing fluxes up to $10^5 \text{ kHz}/\text{cm}^2$. The dependence of effective gain on particle flux is estimated by measuring the amplified current at different operating conditions of the X-ray source. The current is measured at the anode of the detector by using Keithley pico-ammeter. At rates higher than 30 kHz, it is very tricky to measure the primary current and interaction rate due to the overlap of signal pulses in time after their passage through the pre-amplifying stage. The interaction rate is, therefore, varied with copper attenuators and the attenuation factor is calculated. The expected rate is then calculated by dividing it with the irradiated

⁴The rate capability is defined as the maximum flux before the performance (gain) drops.

4.3. PERFORMANCE STUDIES

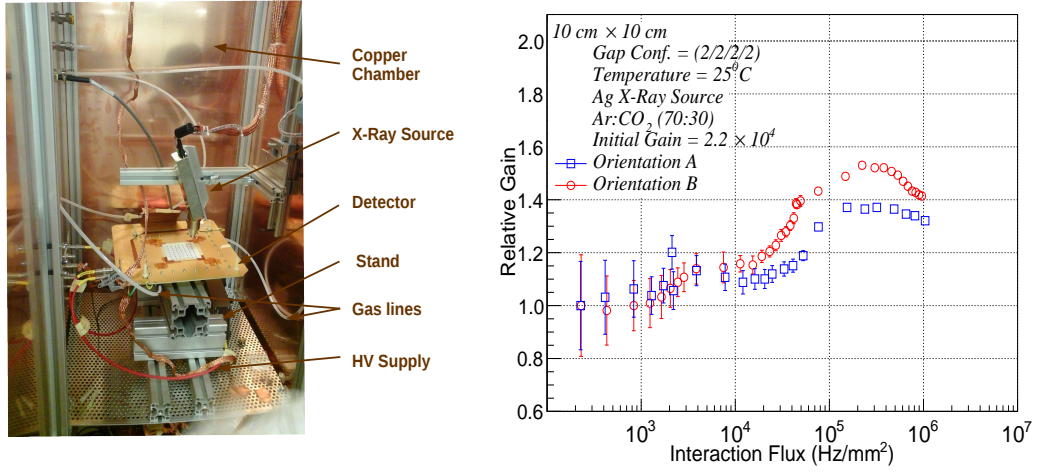


Figure 4.11: (left) The rate capability setup inside the copper box explicating detector being irradiated with the X-ray source and (right) Rate capability for single-mask with ‘Orientation A’ and ‘Orientation B’ configurations. The gain is normalized to average gain value 2.2×10^4 .

area and extrapolating it to the region having no attenuators. The effective gain is calculated as a function of interaction rate and is shown in Figure 4.11. Three different regions can be identified depending on the incoming flux of particles. The first region has the constant effective gain up to the particle fluxes of 10^4 Hz/mm². In this region, the space-charge neither affects the electric field in transfer regions nor in holes. The next region is from the particle fluxes from 10^4 to 10^5 Hz/mm². In this region, the space-charges in the transfer regions conduces which in turn diminishes the electric field nearly the top of the holes and increases it near the bottom of the holes resulting in the increase in overall collection and extraction efficiency of electrons. This, in turn, leads to an increase in gain. The third consists of higher fluxes $10^5 - 10^6$ where the ion extraction decreases resulting in the charge accumulation of ions in front of the holes. This phenomena results drop in effective gain due to the increase in the probability of electron-ion recombination and modification in the amplification field.

Further, the results are compared and interpreted in the context of double-mask foils [8]. It is found that the increase of gain in the ‘Orientation A’ is similar to the double mask configuration and is interpreted as the negligible rise in the collection efficiency due to space-charge and the gain is considered to be dominated by the increase in the electron extraction efficiency. While the ‘Orientation B’ has extraction efficiency close to the highest value because of the large exit holes and the incremental enhancement in the effective gain due to the reduction in space-charge. The drop of the effective gain occurs at fluxes around $2-6 \times 10^5$ Hz/mm² for both the configurations due to the electron-ion annihilation and the decrease in the amplification field.

The studies performed to understand rate capability, demonstrate that the GEM detectors do not show any decrease in gain up to 10^6 Hz/mm². In particular, the maximum flux in the CMS endcaps is not expected to exceed 100 Hz/mm² (10 kHz/cm²), which is below the region where the effective gain of GEM detectors starts decreasing. The effective gain is, therefore, expected to be constant throughout the CMS operating conditions, and hence, two orientations become irrelevant.

4.3.6 Gain and resolution uniformity

The estimation of gain and energy resolution, key parameters, has been described in Section 4.3.1 and Section 4.3.2, respectively.

In this section, uniformity over the active area $10\text{ cm} \times 10\text{ cm}$ of the detector is studied in detail. The intent is not to identify the reasons for the gain variations but to provide the information regarding its fluctuations which could be attributed to the gas composition, local contamination, non-uniformity of the hole geometry, the quality of the drift and readout boards, and poor stretching of GEM-foils.

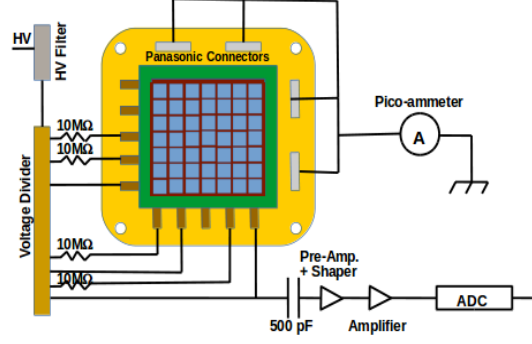


Figure 4.12: The active window divided into 7×7 sectors. Each sector have $1\text{ cm} \times 1\text{ cm}$ area.

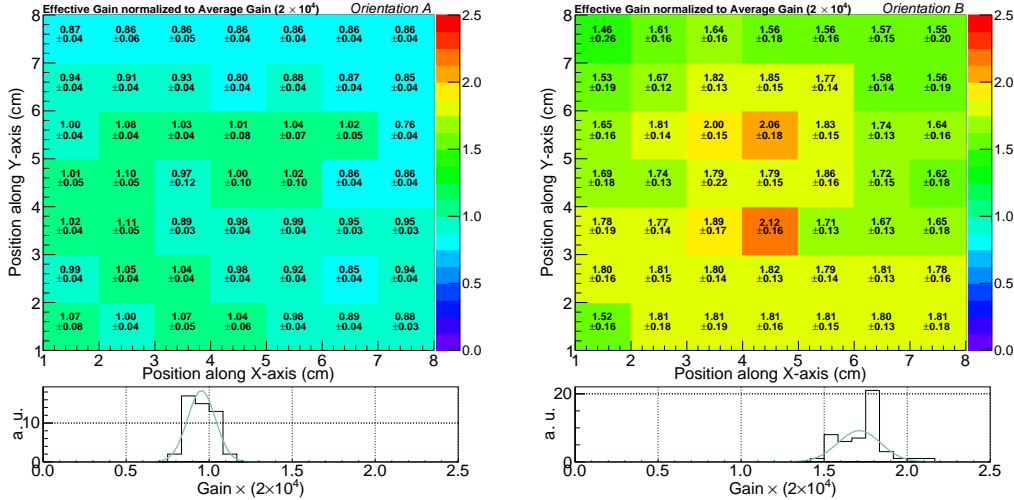


Figure 4.13: Effective gain map at various sectors: (left) ‘Orientation A’ and (right) ‘Orientation B’. The bottom histograms in each Figure show the average gain at equal electric field setting in each orientation.

These variations can be attributed to the change in ambient conditions such as temperature and pressure. All these variations modify the electric field inside and between the amplification layers leading to alterations in gain and resolution. The various attributes and the detection performance of GEMs such as charging up, discharge probability, efficiency, spatial, and time resolutions strongly depend upon gain. Therefore, the gain variations over the active surface of the detector are important and crucial in the quality control qualification of small as well as large size detectors.

The uniformity in gain and resolution are measured by considering 49 points on the active window $10\text{ cm} \times 10\text{ cm}$ of the detector. These points are treated as sectors each having $1\text{ cm} \times 1\text{ cm}$ area as illustrated in Figure 4.12. Each of these sectors is irradiated with

4.3. PERFORMANCE STUDIES

the ^{55}Fe source and the energy spectra are recorded. The spectrum corresponding to each sector is fitted with Gaussian function with mean and width being recognized as gain and resolution, respectively. The obtained mean in ADC channels is translated to the effective gain and is normalized to average gain 2.2×10^4 . The measurements are performed for both the orientations with similar electric field settings and ambient conditions. The results are summarized in Figure 4.13.

Further, the ratio of the gain for ‘Orientation B’ and ‘Orientation A’ (for each sector) is presented in Figure 4.14. The gain variations over the active area are about 25%. The variation reduces down to 20% when excluding the problematic sectors, such as central and boundary sectors. The fluctuations in the center could be related to foil stretching. The foils usually tend to be wavy in the center as compared to boundaries and is pronounced more in large size GEM detectors. Figure 4.15 shows the uniformity of energy resolution at a gain of 2.2×10^4 . The energy resolution over the active area varies from 18% to 22% in ‘Orientation A’ and 24% to 28% in ‘Orientation B’.

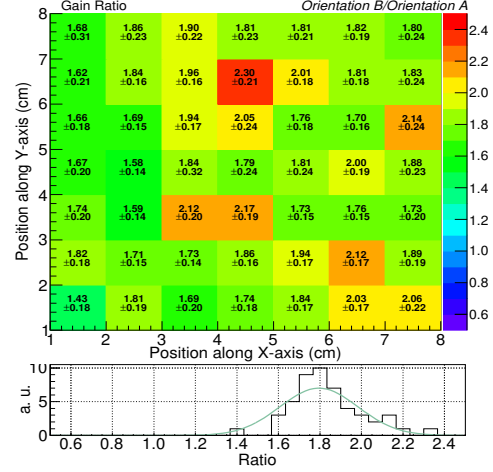


Figure 4.14: Gain ratios corresponding to each sector of ‘Orientation A’ and ‘Orientation B’. The bottom histogram shows that the gain is approximately 1.8 times higher in each sector in ‘Orientation B’ than the corresponding sector in ‘Orientation A’.

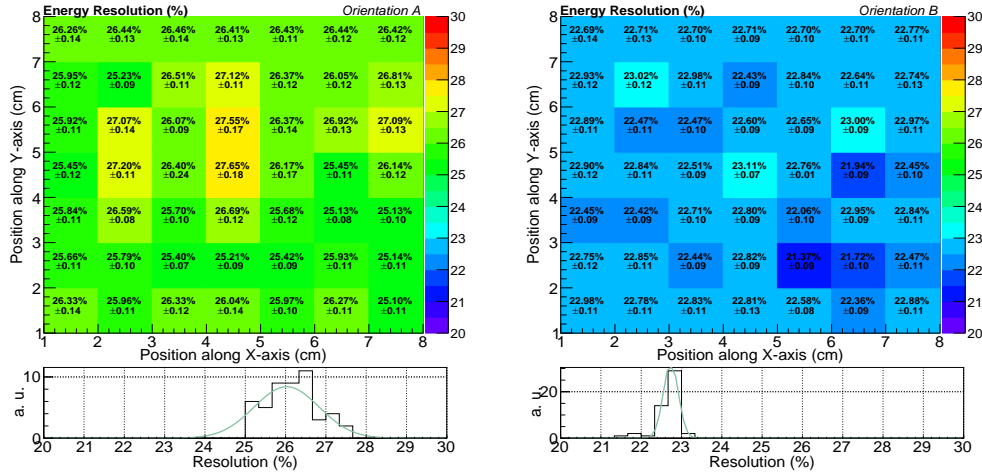


Figure 4.15: The energy resolution of each sector over the active area of the detector: (left) ‘Orientation A’ and (right) ‘Orientation B’. The bottom histogram in each Figure show that the resolution of 26 % and 22 % is obtained for ‘Orientation A’ and ‘Orientation B’, respectively.

4.4 Production of first Indian GEM foils

GEM foils have attracted significant interest from the nuclear and particle physics communities, as they are excellent candidates to be used in tracking detectors. This detector technology has been used successfully as a tracking detector in many experiments, such as STAR [10], TOTEM [11], LHCb [12], COMPASS [13] and ALICE [14], and is expected to be used in many future experiments and their upgrades [15]. Presently, CERN is the main distributor of small as well as large size GEM foils. It is quite difficult for such a production site to meet the growing demands. To meet the future requisites, Micropack Pvt. Ltd. [16] India has acquired a license from CERN to manufacture and commercialize GEM foils [5]. Currently, Micropack has successfully produced double-mask GEM foils of $10\text{ cm} \times 10\text{ cm}$ size. Such foils consist of a $50\text{ }\mu\text{m}$ thin polyimide (PI) foil coated with a thin layer of copper on both sides. Bi-conical holes with $50\text{ }\mu\text{m}$ inner and $70\text{ }\mu\text{m}$ outer diameters are chemically etched in the foil at a pitch of about $140\text{ }\mu\text{m}$ by using either a double mask [3] or single mask [5] technique. In this section, a description of the technique used for the foil production, details of the quality control tests, and various characterization studies performed to validate these foils in order to be used for various applications is provided.

4.4.1 Double-mask foil production

Several Indian CMS institutions, including the University of Delhi, are part of the muon detector upgrade project of the CMS experiment [2]. Indian groups are planning to contribute approximately 20% of the total GEM detectors required for the CMS GE1/1, GE2/1 and ME0 muon upgrade [17, 18]. As a result, an intensive R&D program on GEM detectors has been initiated at these institutions. Micropack Pvt. Ltd. in collaboration with these institutions have started the development of GEM foils in India.

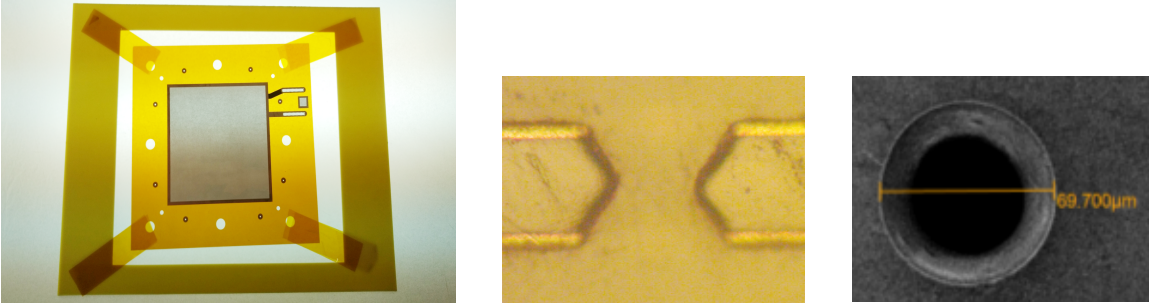


Figure 4.16: (left) $10\text{ cm} \times 10\text{ cm}$ GEM foil encapsulated in a frame, (middle) Cross-sectional view of the foil showing the double cone structure of an engraved hole, and (right) Scanning Electron Microscope (SEM) image showing the topview of a hole with diameter $70\text{ }\mu\text{m}$ [31].

In the latter part of 2013, Micropack signed a Transfer of Technology (TOT) agreement with CERN for the development of GEM foils in India. After continuous efforts, refining of processes, and repeated trials, Micropack has successfully produced $10\text{ cm} \times 10\text{ cm}$ GEM foils. The foil production at Micropack was initiated with the single-mask process. However, after several attempts, it was realized that copper removal through the reverse plating method was challenging. By contrast, the double-mask process succeeded and gave results very quickly. The double-mask GEM foils are produced in a similar fashion as produced at the

CERN PCB workshop [19] using photo-lithographic techniques in which hole geometries are transferred to the polyimide coated with copper using microscopic masks placed on both sides of the substrate. The foil used is a $50\text{ }\mu\text{m}$ PI (Apical Type NP) film with $5\text{ }\mu\text{m}$ copper foil on both sides. Several solvents and acid baths are used to etch the copper layer to form the holes. The Figure 4.16 (left) shows a newly produced $10\text{ cm} \times 10\text{ cm}$ GEM foil, and Figure 4.16 (right) shows its cross-sectional view displaying double cone structure of the engraved holes. The realization of the foils has been achieved primarily through accurate lithographic and controlled chemical processes with a double cone hole structure to enhance the end gain.

4.5 Qualification

In order to qualify these GEM foils as commercially and scientifically reliable, a number of quality control tests needed to be performed. Therefore, the foils have been characterized by studying their optical and electrical properties to render them usable for further applications.

4.5.1 Optical measurements

The GEM foil performance depends heavily upon the hole geometry and their pattern. A $10\text{ cm} \times 10\text{ cm}$ GEM foil with a $140\text{ }\mu\text{m}$ pitch using a hexagonal hole pattern contains approximately 600,000 holes. Any irregularity or defect in the hole pattern and its geometry can profoundly affect their performance.

It becomes, therefore, very important to study the geometry of the hole structure of the foil and to locate every glitch and piece of debris that could lead to foil failure. Though the qualitative estimate of hole density and diameters can manually be studied using an optical microscope, however, such a technique can become labor intensive especially when there are a large number of holes to be analyzed. To overcome this problem, various techniques have been developed [20, 21] to study the optical properties, where geometrical properties of the foils have been measured using an automated 2D CCD scanner.

However, in the current study, a slightly different approach exploring geometrical properties of the GEM foils has been used. Each of the foils is scanned using the Microlensing technique with an AF-S Micro Nikon 40 mm 1:2.8G lens where multiple images of micrometer resolution per pixel are captured. A softbox ($1\text{ m} \times 1\text{ m}$) light source is used to provide uniform illumination to the GEM foils. A sketch of the optical measurement setup is shown in Figure 4.17. The quantities that have been optically measured are the inner and outer

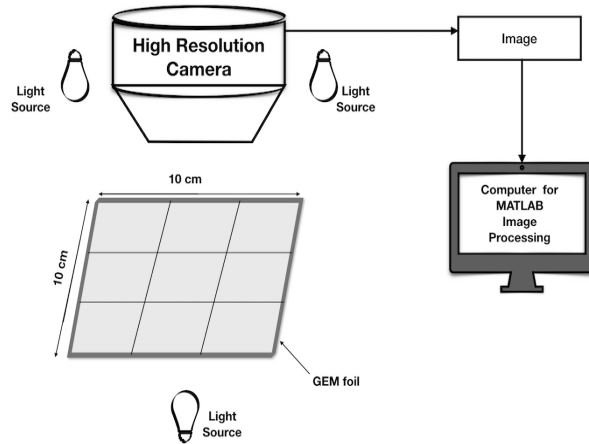


Figure 4.17: Sketch of the setup used for the optical measurements [31].

4.5. QUALIFICATION

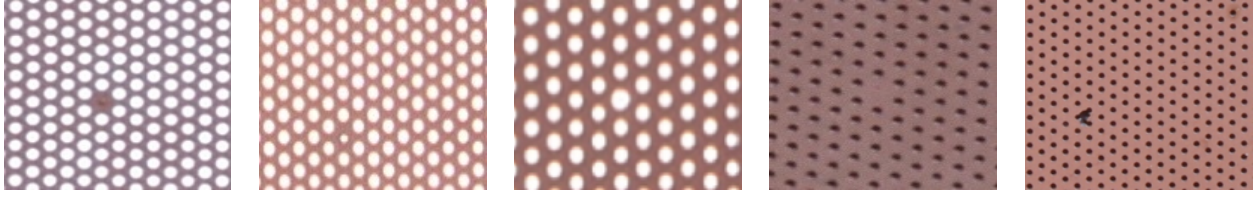


Figure 4.18: Observed imperfections in the foils: (extreme left) un-etched area, (left) under-size hole, (middle) over-size hole (right) missing hole, (extreme right) excess etching [31].

hole diameters. The various kinds of possible imperfections that have been observed are un-etched areas, under-size holes, oversize holes, without hole areas, excess etching, and burnt holes. All these imperfections are shown in Figure 4.18. Also, the scan with the front light ON and the backlight OFF has been performed to make the scan sensitive to the outer holes. For the inner holes of the foil, the scan has been performed with the front light OFF and backlight ON.

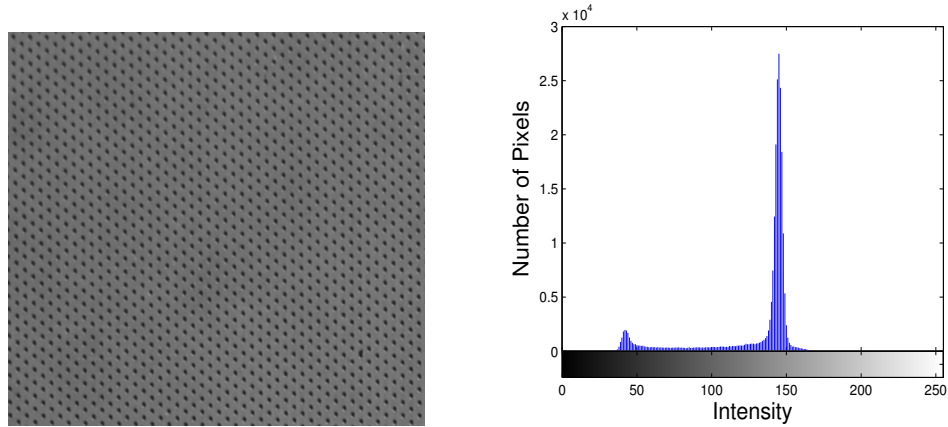


Figure 4.19: (left) Image formed in gray-scale and (right) Histogram of gray-scale image for the calculation of gray threshold [31].

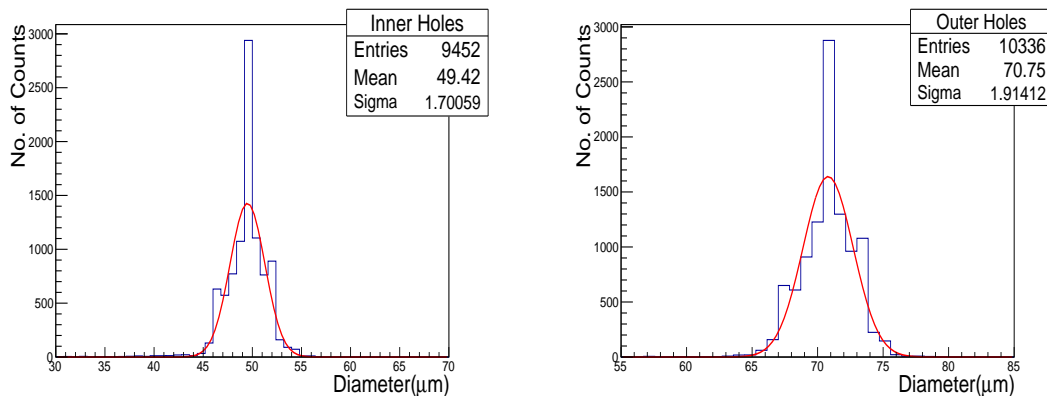


Figure 4.20: Hole size distribution of (left) inner, and (right) outer holes for one sector.

To assess the entire area of the foil, each of the foil is divided into several sub-sectors. While capturing inner holes, the foil is divided into 54 (9×6) sub-sectors, whereas to capture

4.5. QUALIFICATION

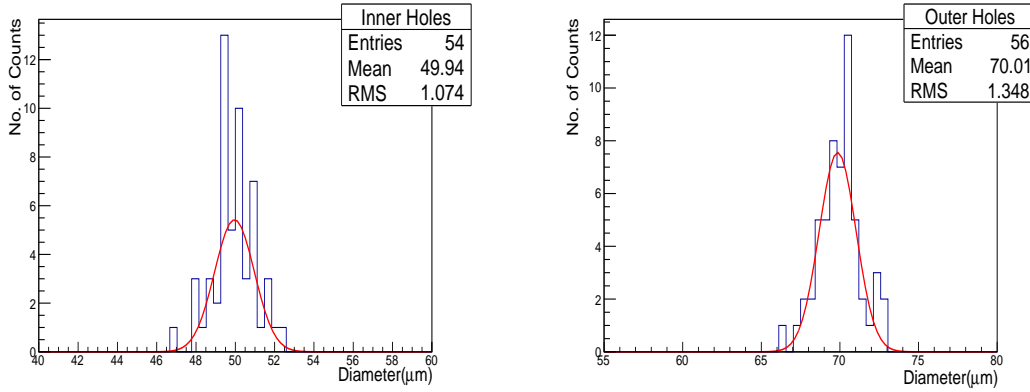


Figure 4.21: Mean diameter of (left) Inner holes of all the sectors (right) Outer holes of all the sectors. The hole distributions were fitted with Gaussian functions to extract values for mean and standard deviation as shown in Figure 4.22.

outer holes the foil is divided into 56 (8×7) sub-sectors. Images are captured in such a way that each image corresponds to a sub-sector. Each captured image is then processed using an Image Processing Toolkit within MATLAB [22], which contains built-in functions specifically designed to convert the pixel information obtained from images into numerical measurements. Therefore, the toolkit is used to convert the primary image acquired by the camera into a gray-scale image as shown in Figure 4.19 (left). In order to obtain the binary threshold to separate the holes from the background, the grayscale image is converted into the intensity histogram as shown in Figure 4.19 (right). The left peak in the figure represents the light reflected back from the edges of holes and screen behind the foil while the right peak represents the light from the copper surface. Each of the holes is labeled for each sub-sector. The hole diameter in pixels is calculated for each side of the GEM foils. The

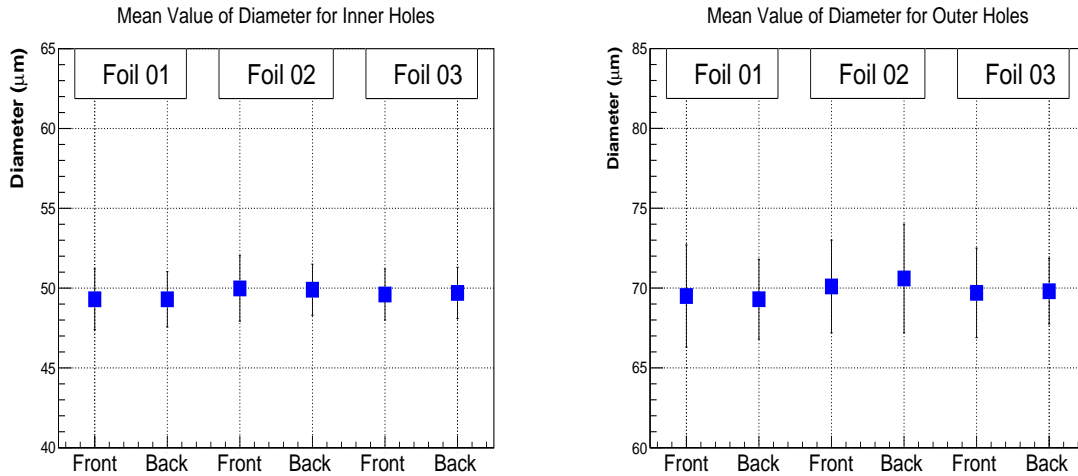
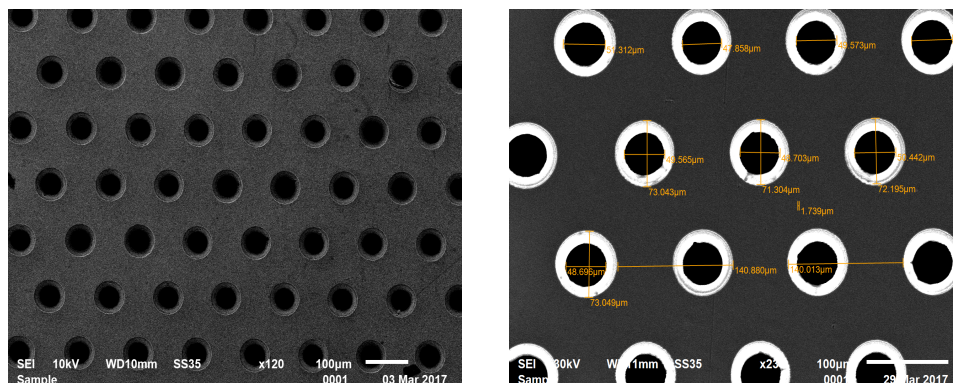


Figure 4.22: Mean diameter for (left) Inner and (right) outer holes for each side of GEM foils. The error bars represent the 1 standard deviation error obtained from the statistical combination of the standard deviations of hole diameter distributions of each sub-sector.

data generated from MATLAB is processed further using ROOT [23] to estimate the mean diameter in pixels of inner and outer holes for each sub-sector and finally for the entire foil.

4.5. QUALIFICATION



From the fit to the distribution of holes diameter for each sub-sector, the mean diameter and standard deviation values for all the sub-sectors are obtained. As a result, 54 values of mean and sigma are obtained corresponding to 54 sub-sectors for inner holes and 56 values of mean and sigma corresponding to 56 sub-sectors for the outer holes. These individual means and sigmas of each sub-sector are then statistically combined to estimate the mean diameter and standard deviation for inner and outer holes for the entire GEM foil. The distribution of mean diameters of all the sub-sectors for inner and outer holes of one GEM foil is shown in Figure 4.21. The mean hole diameter for the entire foils estimated from the Gaussian fit of this distribution gives a value of $49.9 \mu\text{m}$ and $70.01 \mu\text{m}$ for inner and outer holes, respectively. The standard deviation obtained from each sub-sector has been statistically combined to extract the value over the entire foil and is found to be $1.6 \mu\text{m}$ and $2.02 \mu\text{m}$ for inner and outer holes, respectively. The pitch obtained from the optical measurement is $140.0 \pm 2.4 \mu\text{m}$. The mean diameter of inner and outer holes for all the three foils are shown in Figure 4.22. The error bars on the mean diameters show the value of standard deviation. The findings are consistent with the double mask GEM foils produced elsewhere and in use, as can be found in the references [21, 24]. Further, in Figure 4.23 (left), scanning electron microscope (SEM) images of one of the GEM foil are shown, and Figure 4.23 (right) shows the average inner and outer hole diameters of $49.51 \mu\text{m}$ and $72.55 \mu\text{m}$, respectively with an average pitch of $140.44 \mu\text{m}$. This measurement of hole diameters from SEM measurement is in fair agreement with the values obtained from the optical assessment.

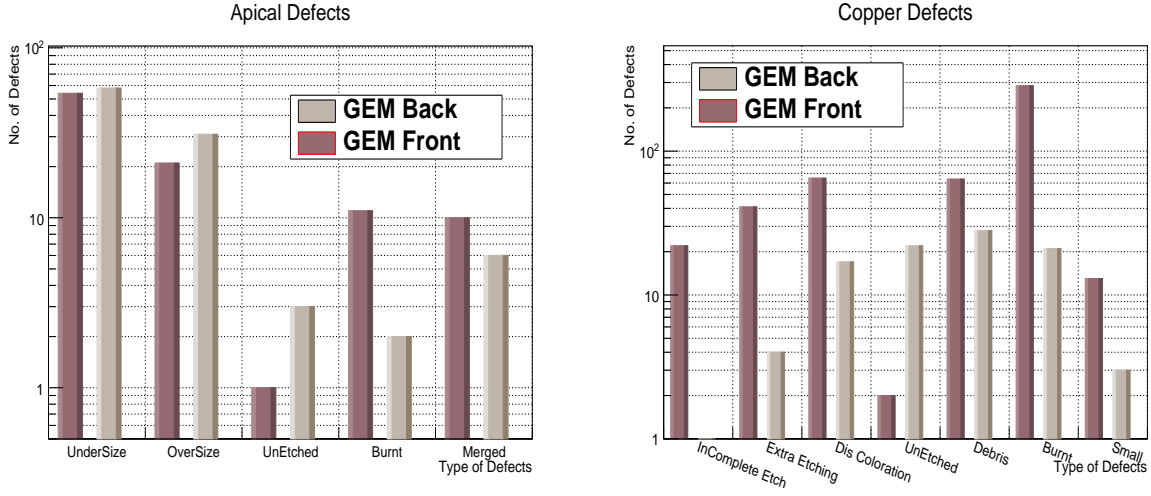


Figure 4.24: Number of defects seen for one of the 10 cm × 10 cm foil in (left) Insulator (Apical Type NP) and (right) Copper [31].

4.5.2 Leakage current measurements

The production quality of GEM foils can be quantified through optical and leakage current measurements.

The optical measurement provides the information regarding the hole geometry and pitch related information whereas leakage current measurements provide the parameters about the efficacy of the foils and hence are important in determining the quality of GEM foils. The leakage current measurements of the GEM foils have been discerned by measuring its leakage current extended over a period of time after proper cleaning using an adhesive roller and are mainly divided into two types: quality control short or fast (QC fast) and quality control long (QC long) as per the CERN standards of quality control procedure [27] that requires these two tests to be done in order to qualify these foils.

The difference between QC fast and QC long lies in applying voltage for shorter or longer periods of time, respectively, and monitoring the current in both the phases. The other difference being that the QC fast gives the preliminary idea of leakage current or electrical connectivity of the foil but for more detailed study, QC long provides the behavior of the foil at high voltages in terms of the actual leakage current and the number of discharges for the

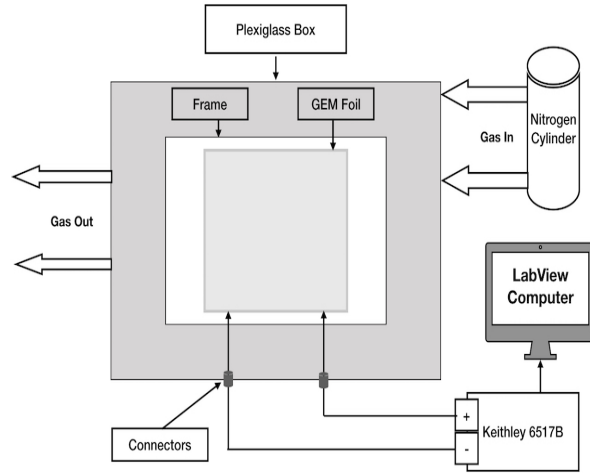


Figure 4.25: Sketch of the setup used for the measurement of leakage current [31].

4.5. QUALIFICATION

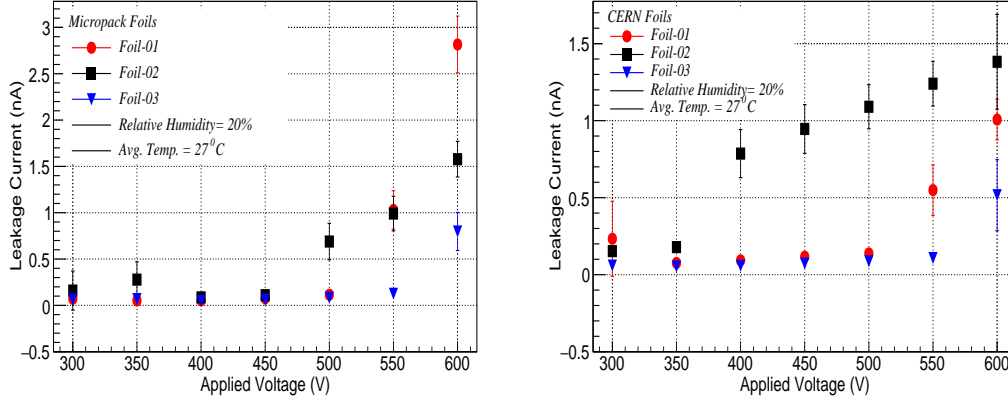


Figure 4.26: Leakage current of (left) Micropack and (right) CERN foils at an average temperature of $T=27^{\circ}\text{C}$ and relative humidity equal to 20%.

reasonably longer duration of time. In this study, both the tests have been performed. The electrical connectivity of the foils by QC fast method has been performed using insulation tester MIT Megger 420 [28]. Using this test, It is established that the foils have good electrical connectivity.

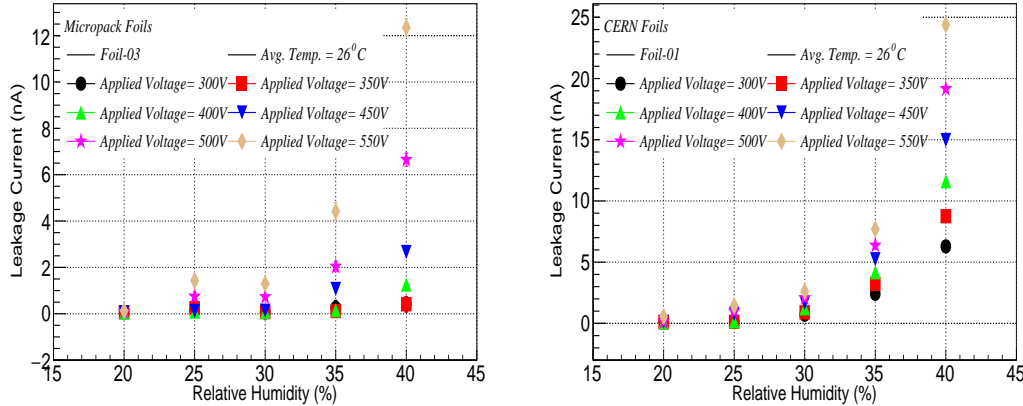


Figure 4.27: Leakage current versus relative humidity taken at different voltages for (left) Micropack and (right) CERN foils.

For the better precision, Keithley Electrometer 6517B [29] has been used for the current measurement. The measurement setup consists of a bare GEM foil connected to Keithley 6517B pico-ammeter interfaced with a computer via a GPIB interface and the Labview program is used to record the measurements as shown in the Figure 4.25. The current measurement range is set from 0 to 200 nA with an accuracy of $\pm 0.2\%$. The leakage current thus measured as a function of applied voltage is shown in Figure 4.26 (left) for the Micropack foils. The similar measurement were also performed for foils procured from CERN and the results are shown in the Figure 4.26 (right).

The Micropack and the CERN foils are found to show similar results under similar ambient conditions. However, as the humidity escalates, the leakage current in CERN foils increases more rapidly compared to the Micropack foils. The maximum current of 12 nA and 25 nA at an applied voltage of 550V corresponding to the humidity of 40% has been

4.5. QUALIFICATION

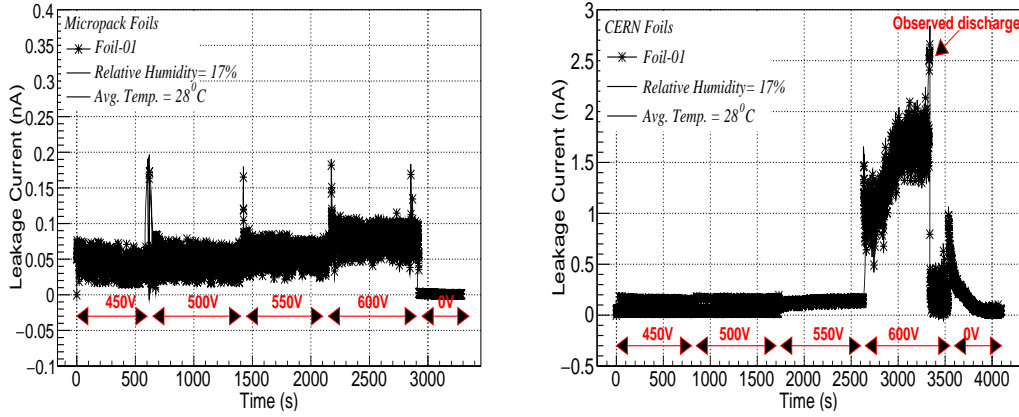


Figure 4.28: QC Long: Leakage Current as a function of time in dry nitrogen environment at different voltage steps with an ambient average temperature of $T = 28^{\circ}\text{C}$ and ambient relative humidity of 17% for Micropack and CERN foils.

observed in Micropack and CERN foils, respectively.

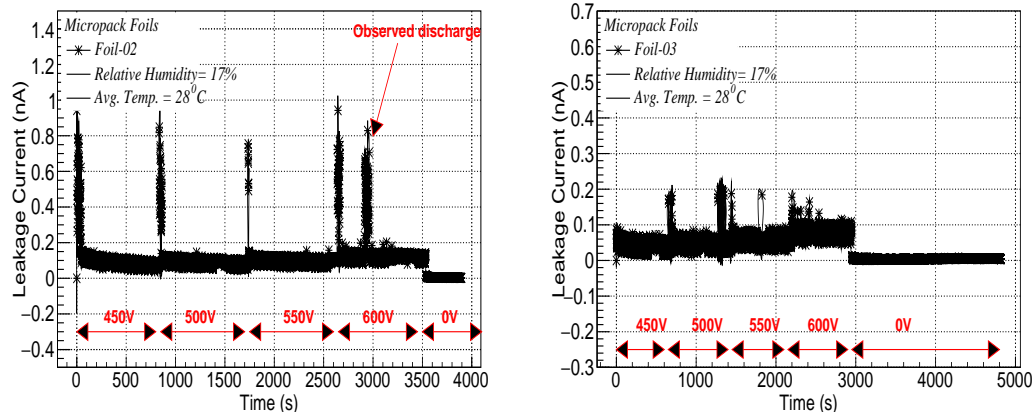


Figure 4.29: QC Long: Leakage Current as a function of time in a dry nitrogen environment at different voltage steps with an ambient average temperature of $T = 28^{\circ}\text{C}$ and relative humidity of 17% for Micropack (left) foil-02 and (right) foil-03.

Figure 4.27 shows the leakage current for various applied voltages under different ambient conditions. From Figure 4.27, it can be fairly concluded that humidity does have drastic effects on the leakage current measurement. Therefore, the current has been measured in a nitrogen environment. Since pure nitrogen is the contamination-free standard medium that does not react with the stored materials and does not carry moisture. By slowly percolating it into the gas-tight Plexiglass enclosure, moisture-laden air is purged out and the current is then measured. All the foils show a leakage current of less than 1 nA at 550 V.

All the measurements have been carried out in the cleanroom of class 100 installed with a KANOMAX dust particle counter Model 3887 [30] which monitors the particle count. The QC long test of the GEM foils is performed by placing foils in a Plexiglass enclosure. After flowing nitrogen continuously for more than two hours, the leakage current is measured at different voltages (in steps of 50V) starting from 450V to 600V for nearly 10 minutes.

At 600V, at most a single discharge is observed during this time interval. The results are presented in Figure 4.28 and similar results are obtained for other foils as shown in Figure 4.29.

4.6 Conclusions

The single-mask foil production technique introduces geometrical asymmetries in the shapes of holes and is expected to affect the operation of the GEM detectors conceived from these foils. By tagging GEM foil hole orientations as ‘Orientation A’ and ‘Orientation B’, the impact of such asymmetry has been evaluated by measuring gain, resolution, charging-up, and the rate capability. Further, the uniformity in gain and resolution over the active area of the triple-GEM detector has been studied numerically, and overall less than 10% fluctuations are observed. The CMS Muon group also reported some similar results on gain and rate capability measurement in different test campaign which can be found in reference [8]. Hence, it is concluded that the hole asymmetry strongly affects the properties of the detector, and the ‘Orientation B’ facing the incident radiation performs better compared to the ‘Orientation A’ [9]. The results acted as very important inputs and were accepted as recommendations by CMS collaboration.

The second part of the study considered the production and qualification of Indian GEM foils. The foils have been produced for the first time in India under the TOT agreement between Micropack Pvt. Ltd., Indian industry, and CERN. Micropack started preparations for the production of GEM foils in India since 2014. The first few attempts saw many deviations from the required quality. With further improvements in etching technology and several rounds of iterations, Micropack finally produced a batch of foils that appeared good from visual inspection and preliminary checks. However, before these foils could be declared fit for scientific and other applications, the desired quality control assessment which includes optical and leakage current measurements have been performed. Optical measurements reveal that the holes are quite uniform with inner and outer diameters of $49.9 \pm 1.6 \mu\text{m}$ and $70.01 \pm 2.02 \mu\text{m}$, respectively. The quoted errors are the Gaussian one sigma uncertainty on diameter distributions. A current of less than 1 nA at 550 V has been observed which is comparable to CERN foils [31].

A small size 10 cm \times 10 cm detector has been constructed from the double-mask Micropack GEM foils [32] and its performance measurement such as gain and relevant parameters have also been evaluated. With the successful production of 10 cm \times 10 cm double-mask GEM foils, Micropack has already extended its infrastructure to handle single-mask technology so that larger foils can be produced in order to ease the commercialization of large area GEM-foils. Indian CMS groups are planning to use these large size foils in the next upgrade (The CMS GEM GE2/1 and ME0 upgrade projects⁵) of the CMS. The first batch of large area foils has been produced and a detector has been constructed from these foils by Delhi University CMS group. The quality control tests on the constructed large size detector (GE2/1 size) from such foils are currently underway at CERN’s Gamma Irradiation Facility (GIF++).

⁵The details about the GE2/1 upgrade can be found in reference [17].

BIBLIOGRAPHY

- [1] CMS Collaboration, “[Performance of the CMS muon detector and muon reconstruction with proton-proton collisions at \$\sqrt{s}=13\$ TeV](#)” JINST 13 (2018) no.06, P06015.
- [2] CMS Collaboration, “[The CMS experiment at the CERN LHC](#)” JINST 3 (2008) S08004.
- [3] F. Sauli, “[GEM: A new concept for electron amplification in gas detectors](#)”, Nucl. Inst. Meth. A386 (1997) 531-534 1.
- [4] CMS Collaboration, “[The Phase-2 Upgrade of the CMS Muon Detectors](#)” CERN-LHCC-2017-012, CMS-TDR-016.
- [5] S.D. Pinto et al., “[Progress on large area GEMs](#)”, JINST 4 P12009 (2009).
- [6] F. Sauli, RD51-NOTE-2012-007, REVISED on 18.09.2012.
- [7] S. Bachmann et al., “[Charge amplification and transfer processes in the gas electron multiplier](#)”, Nucl. Inst. Meth. A 438 (1999) 376.
- [8] J. A. Merlin, “[GEM single-mask characterization and influence of GEM foil orientation](#)” MPGD (2017).
<https://indico.cern.ch/event/581417/contributions/2556690/>
- [9] A. Shah, “[Impact of single-mask hole asymmetry on the properties of GEM detectors](#)” submitted to Nucl. Inst. Meth. A, [arXiv:1811.04439](#).
- [10] B. Surrow et al., “[Beam Performance of Tracking Detectors with Industrially Produced GEM Foils](#)”, Nucl. Inst. Meth. A 617 (2010) 196.
- [11] M. Alfonsi et al., “[High-rate particle triggering with triple-GEM detector](#)”, Nucl. Inst. Meth. A 518 (2004) 106.
- [12] S. Lami et al., “[A triple-GEM telescope for the TOTEM experiment](#)”, Nucl. Phys. B Proc. Suppl. 172 (2007) 231.
- [13] C. Altunbas et al., “[Construction, test and commissioning of the triple-gem tracking detector for compass](#)”, Nucl. Inst. Meth. A 490 (2002) 177.
- [14] P. Gasik, “[Development of GEM-based Read-Out Chambers for the upgrade of the ALICE TPC](#)”, JINST 9 (2014) C04035.

- [15] D. Abbaneo et al., “[A study of film and foil materials for the GEM detector proposed for the CMS muon system upgrade](#)”, JINST 9 (2014) C10036.
- [16] Micropack Limited, “[Jigani Industrial Area, Anekal Taluk, Bangalore-560105](#)”.
<http://www.micro-pack.com>
- [17] A Colaleo et al., “[CMS Technical Design Report for the Muon Endcap GEM Upgrade](#)”, CERN-LHCC-2015-012 CMS-TDR-013 (2015).
- [18] D. Abbaneo et al., “[Technical Proposal for the Phase-II Upgrade of the CMS Detector](#)”, CERN-LHCC-2015-010/LHCC-P-008 (2015).
- [19] S. Duarte Pinto et al., “[A method of manufacturing a gas electron multiplier](#)”, Patent Wipo WO/2009127220.
- [20] M. Posik et al., “[Optical and electrical performance of commercially manufactured large GEM foils](#)”, Nucl. Inst. Meth. A 802 (2015) 10.
- [21] U. Becker et al., “[Test and evaluation of new GEMs with an automatic scanner](#)”, Nucl. Inst. Meth. A 556, (2006) 527.
- [22] URL: <http://hdl.handle.net/1721.1/32905>.
- [23] URL: <https://root.cern.ch>.
- [24] F. Simon et al., “[Development of Tracking Detectors With Industrially Produced GEM Foils](#)”, IEEE Trans. Nucl. Sci. NS 54 (2007) 2646.
- [25] ALICE collaboration, “[TDR for the Upgrade of the ALICE TPC](#)”, CERN/LHCC, (2014).
- [26] M. Ball et al., “[Quality assurance of GEM foils for the upgrade of the ALICE TPC](#)”, JINST 12 (2017) C01081.
- [27] D. Abbaneo et al., “[Quality control and beam test of GEM detectors for future upgrades of the CMS muon high rate region at the LHC](#)”, JINST 10 C03039 (2015).
- [28] [Megger MIT420 Insulation Tester](#),
<https://www.instrumart.com/products/35023/megger-mit420-insulation-tester>
- [29] [Keithley Electrometers for Ultra-High Resistance/Ultra-Low Current Measurements](#),
<http://www.tek.com/keithley-low-level-sensitive-and-specialty-instruments/keithley-high-resistance-low-current-electrom>
- [30] [Handheld Particle Counters](#),
<https://www.kanomax-usa.com/product/hpc-models-3888-3889>

BIBLIOGRAPHY

- [31] A. Shah et al., “[Development, characterization and qualification of first GEM foils produced in India](#)”, Nucl. Inst. Meth. A 892, (2018) 10.
- [32] M. Gola, A. H. Shah et al., “[Performance of the triple GEM detector built using commercially manufactured GEM foils in India](#)”, submitted to Nucl. Inst. Meth. A, [arXiv:1806.05016](#).

Search for exotic Higgs boson decay in $h \rightarrow Za \rightarrow b\bar{b}\mu^-\mu^+$

Physics is really nothing more than a search for ultimate simplicity, but so far all we have is a kind of elegant messiness.

— Bill Bryson

This chapter presents the results of a search performed for an exotic decay of h (125 GeV) boson to an electroweak ‘ Z ’ boson and a light pseudoscalar ‘ a ’ boson. The Z boson decays to a pair of b quark jets and a boson to a pair of μ leptons. The motivation lies in the models that lie Beyond the Standard Models (BSM) such as the two-Higgs doublet model augmented with a scalar singlet including the Next-to-Minimal Supersymmetric Standard Model (NMSSM). The results correspond to an integrated luminosity of 41.5 fb^{-1} collected by the CMS experiment during the year 2017 at 13 TeV center-of-mass energy. The mass of a boson between 11 and 34 GeV is probed.

5.1 Introduction

The Brout-Englert-Higgs (BEH) mechanism [1–4, 6] within the SM is responsible for electroweak symmetry breaking and predicts the existence of the Higgs boson. The ATLAS and CMS Collaborations at the CERN discovered a new particle compatible with the Higgs boson [7–9]. Measurements leave room for exotic decays with a limit of 34% on the branching fraction of the Higgs boson to BSM particles which are allowed in many models.

Over the past half-century, searches for narrow resonances in the dimuon invariant mass spectrum has become an important part of the physics program at the LHC. Though Minimal Supersymmetric SM (MSSM) cannot accommodate such decays with the physics analysis performed at the LHC [17–23], but such searches are well motivated within many classes of BSM theories such as two-Higgs-doublet model extended with a scalar singlet (2HDM+S) [12–15] which predict new resonances with significant couplings to muons. This is partly due to the reason that the width of the Higgs boson in the SM is so narrow that a small coupling could lead its branching fractions to the light states of the order of several percent. Additionally, the scalar sector can theoretically easily be an egress that allows matter from a hidden sector to interact with SM particles.

The decay channels with 4μ events in the final state are cleaner but have low statistics. On the other hand, $4b$ final state is expected to occur with more events but has challenging backgrounds. These channels are, therefore, very difficult to probe. The $b\bar{b}\mu^-\mu^+$ final state is considered a golden channel for discovering SM extensions with extra singlets [16]. The discovery potential of decay channels with $b\bar{b}\mu^-\mu^+$ final state has been estimated in reference [15]. An interesting exotic decay channel with such a final state consists of Higgs boson decaying to electroweak ‘ Z ’ boson and a light pseudoscalar ‘ a ’ boson. The Z boson is subsequently expected to decay into a pair of bottom quarks ($Z \rightarrow b\bar{b}$), and a boson to a pair of muons ($a \rightarrow \mu^-\mu^+$). Despite a low branching fraction, the analysis profits from the excellent dimuon mass resolution of the CMS detector with the current data, the channel is very promising to explore BSM physics. Such a decay channel ($h \rightarrow Za \rightarrow b\bar{b}\mu^-\mu^+$) is highly motivated in the theory [15] especially in 2HDM+S model. In the 2HDM+S model, seven scalar and pseudoscalar particles are predicted. One of them could be h a scalar compatible with the already discovered particle with a mass of 125 GeV and another could be a pseudoscalar a light enough that allows $h \rightarrow Za$ decays. There are four such model types that forbid flavor changing neutral currents (FCNC) at tree level [24]. One such a model 2HDM+S type-3 with $\tan\beta \sim 2$ allows $\mathcal{B}(a \rightarrow \mu^-\mu^+)$ up to $\sim 3 \times 10^{-3}$ (Figure 5.1) and a benchmark $\mathcal{B}(h \rightarrow Za)$ as 10%, $\mathcal{B}(Z \rightarrow b\bar{b})$ as 15% is considered in the current data analysis.

Therefore, an attempt is made to search for a new light boson by considering the exotic decay of Higgs boson (125) into ‘ Z ’ boson and one pseudo scalar light boson ‘ a ’ in the decay channel $h \rightarrow Za \rightarrow b\bar{b}\mu^-\mu^+$. The Feynman diagram of such a decay channel is shown in Figure 5.2 where a pair of gluons fuse together to form h , which then decays into a Z boson and a light pseudoscalar a . The Z and a bosons further decay to bottom quarks and muons, respectively. The decay channel has never been probed so far and the first results are reported with the dataset corresponding to an integrated luminosity of 41.5 fb^{-1} recorded by the CMS during the year 2017.

5.2 Simulated Samples

The signal samples with mass of boson ‘ a ’ equal to 12, 15, 20, 25, and 30 GeV are simulated for $h \rightarrow Za \rightarrow b\bar{b}\mu^-\mu^+$ at the leading order by importing NMSSMHET model [15] in Monte Carlo (MC) generator MADGRAPH_aMC@NLO [25] in gluon-gluon fusion (ggF) process. The parton distribution functions (PDF) used are NNPDF31_lo_as_0130 and NNPDF31_nlo_hessian_pdfas [26] for leading order (LO) and next-to-leading order (NLO) simulations, respectively.

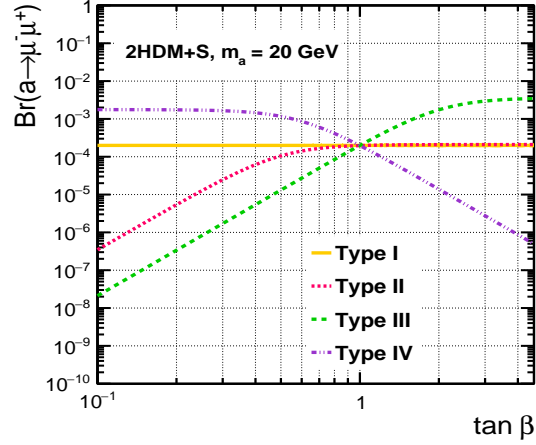


Figure 5.1: Predicted $\mathcal{B}(a \rightarrow \mu^-\mu^+)$ for $m_a = 20 \text{ GeV}$ in the different models of 2HDM+S, for various of $\tan\beta$. The branching fractions for the signal $h \rightarrow Za \rightarrow b\bar{b}\mu^-\mu^+$ are computed following the prescription in references [15, 16].

The background process Drell-Yan ($Z/\gamma^* \rightarrow ll$) + jets is generated with MRAPH5_aMC@NLO at LO and the cross section is computed using FEWZ 3.1 [27] at NLO. The top-antitop ($t\bar{t}$) and single top quark background processes are produced with POWHEG 2.0 [28–31] at next-to-leading order. Background contributions from diboson (WW, WZ, ZZ) is generated at NLO (except WW sample which is generated at LO) with the same program and inputs as that of Z/γ^* sample are used.

The LO NNPDF3.0 is used as a set of parton distribution functions (PDFs) for LO samples and NLO NNPDF3.0 for NLO samples [32]. PYTHIA 8.212 [33] with tune CUTE8M1 [34, 35] is used for modeling of the parton showering and fragmentation for all the samples with full CMS detector simulations using GEANT4 code [36]. Minimum bias events are generated and added to the simulated samples to account for the effect of additional interactions per bunch crossing. These additional interactions are reweighted in such a way to have the same pileup¹ distribution as in data [37]. Background processes Z/γ^* production in association with additional b jets and $t\bar{t}$ are observed to be dominant contributions in the dimuon final state. Event selections are optimized (Section 5.4) by using dominant background processes and only those selection steps that yield reasonable statistical precision are considered. The simulated samples are only used for optimization purposes and the actual background contribution from various processes to the selected signal samples is directly extracted with no reference to simulation.

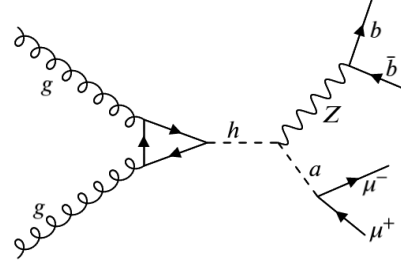


Figure 5.2: Feynman diagram for signal topology $h \rightarrow Za \rightarrow b\bar{b}\mu^-\mu^+$.

5.3 Object reconstruction

The event reconstruction relies on the particle-flow algorithm [38], which employs the information from the CMS sub-detectors including tracker, calorimeter, and muon systems to identify charged and neutral hadrons, photons, electrons, muons, etc. emerging from proton-proton (pp) collisions in an event. Muons in an event are reconstructed by combining tracks in the silicon tracker with those in the muon spectrometer with a cluster of energy in the electromagnetic calorimeter [44]. The quality of the reconstructed tracks is identified from variables related to the number of measurements in the tracker and muon systems. The relative isolation discriminant between the muons is calculated as

$$I^\mu \equiv \frac{\sum_{charged} p_T + \max\left(0, \sum_{neutral} p_T - \frac{1}{2} \sum_{charged} p_T\right)}{p_T^\mu} \quad (5.1)$$

where p_T^μ is the transverse momentum of the muons, $\sum_{charged} p_T$ is the scalar sum of transverse momenta of the charged particles (PF objects) associated to the primary vertex within

¹The number of simultaneous pp interactions occurring in the same bunch crossing.

a cone of radius² $\Delta R \geq 0.4$ centered in the direction of the muon. The $\sum_{neutral} p_T$ is a similar quantity for neutral particles. From simulations, the p_T of neutral particles from pileup vertices is considered to be half of the charged hadrons associated with pileup vertices, $\sum_{charged,PU} p_T$. Further, the scalar sum excludes the contribution from charged particles that are not associated with the event vertex, and corrections are applied to account for the neutral particle contamination arising from the pileup.

The anti- k_T clustering algorithm implemented in the FASTJET library [39, 40] is used for Jet reconstruction from PF objects using a distance parameter of 0.4 and are required to be separated from the selected muons by $\Delta R \geq 0.5$. Jet energy is corrected as a function of jet p_T and η , and further identification criteria are used to reject jets from pileup events or inherent detector noise [41, 45]. Jets that originate from b quarks known as b jets are identified with Deep Combined Secondary Vertex (DeepCSV) tagger which is based on the Deep Neural Network machine learning algorithm for flavor tagging and separately with Combined Secondary Vertex version 2 (CSVv2) algorithm [42]. These algorithms build a discriminator from the track-based lifetime information and the variables related to potential secondary vertices associated with a jet. The DeepCSV tagger which is a new version of CSVv2 that provides around 10 to 15% better efficiency with the same misidentification rate than the latter, which was used by the CMS in previous data analysis.

The other physics objects such as missing transverse momentum (p_T) and Higgs candidates are reconstructed by the combinations of these PF objects by a jet finding algorithm applied to all the tracks associated with the vertex and the corresponding missing transverse energy associated with it [39, 40]. The reconstructed vertex with the highest value of summed physics-object p_T^2 is taken to be the primary interaction vertex.

5.4 Selection optimization

One of the experimental cuts in this study requires a spatial separation between the muons greater than 0.4 ($\Delta R > 0.4$). However, for the smaller a boson mass, the kinematics may force muon pair from a pseudoscalar a to be produced with large p_T values such that they emerge as collimated within a cone of radius $\Delta R < 0.4$. In such a scenario, special search strategies are necessary for these collimated objects to be treated as a single special entity so that they may be distinguished from a single QCD jet, or be realized as a pair of objects with special isolation criteria such that they do not ruin the isolation criteria of the other. Therefore, parton level information is used to explore the isolation between the pair of muons as illustrated in Figure 5.3. For the pair of muons from pseudoscalar a , it is observed that the isolation criteria is ruined for mass $m_a < 11$ when $\Delta R < 0.4$. Therefore, the isolation cut of $\Delta R > 0.4$ is chosen for the lower bound on the a mass.

Further, the optimization is performed using the variable $S/\sqrt{S + (\Delta B)^2}$, where ΔB is the statistical uncertainty on the background for each simulated mass point with the major backgrounds Drell-Yan and $t\bar{t}$ processes in the final dileptonic state. The other variables³

² $\Delta R = \sqrt{(\Delta\eta)^2 + (\Delta\phi)^2}$

³The other variables used are S/\sqrt{B} and $\sqrt{2((S+B)\ln(1+S/B) - s)}$.

5.4. SELECTION OPTIMIZATION

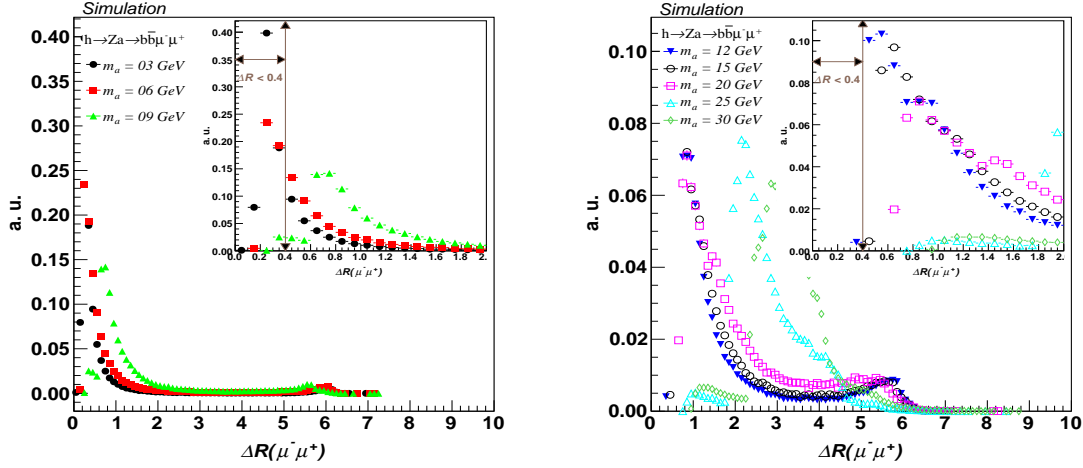


Figure 5.3: For $m_a < 11$ GeV, events fall in the region $\Delta R < 0.4$, implying the muon pair is not well separated and (right) for $m_a > 11$ GeV, events does not fall in the region $\Delta R < 0.4$, implying the muons are well separated.

are also used and yield similar result as that of the former [54].

Mass points with $m_a = 12, 20, 30$ GeV are considered for the optimization purposes. Events are selected at trigger level with two isolated muons having p_T greater than 17 GeV and 8 GeV, and two jets with $p_T > 15$ GeV. All the four objects are required to be within absolute pseudorapidity $|\eta| < 2.4$ region of the detector. The mass of the dimuon system is considered to lie within 10 and 40 GeV. The range is wider than the search interval 11 and 34 GeV to allow for the full coverage at the boundaries during optimization. The jets with a given discriminator are required to pass the different working points of the CSV $v2$ and DeepCSV algorithms.

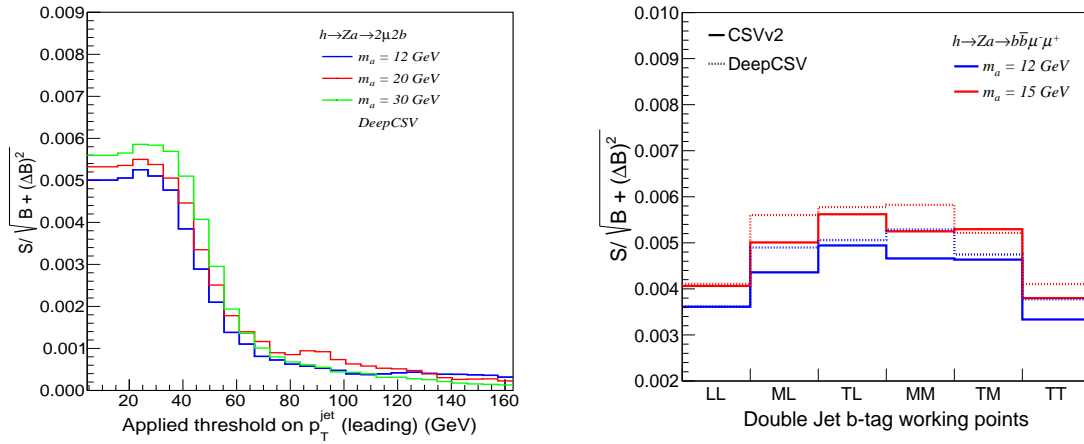


Figure 5.4: (left) The significance as a function of leading jet p_T threshold and (right) the significance for different working point combinations of the selected b -tagged jet pair for CSV $v2$ and DeepCSV taggers.

The optimization starts by calculating the variable $S/\sqrt{S + (\Delta B)^2}$ as a function of applied cuts on p_T of the leading and sub-leading muons, the p_T cut values of 20 GeV and 9

5.4. SELECTION OPTIMIZATION

GeV sound optimal, respectively. The p_T of the sub-leading objects are optimized after optimizing leading ones. Similarly, the optimized p_T threshold for the leading and sub-leading jets are 20 GeV and 15 GeV, respectively, which are obtained after optimizing the cuts for muon objects (Figure 5.4).

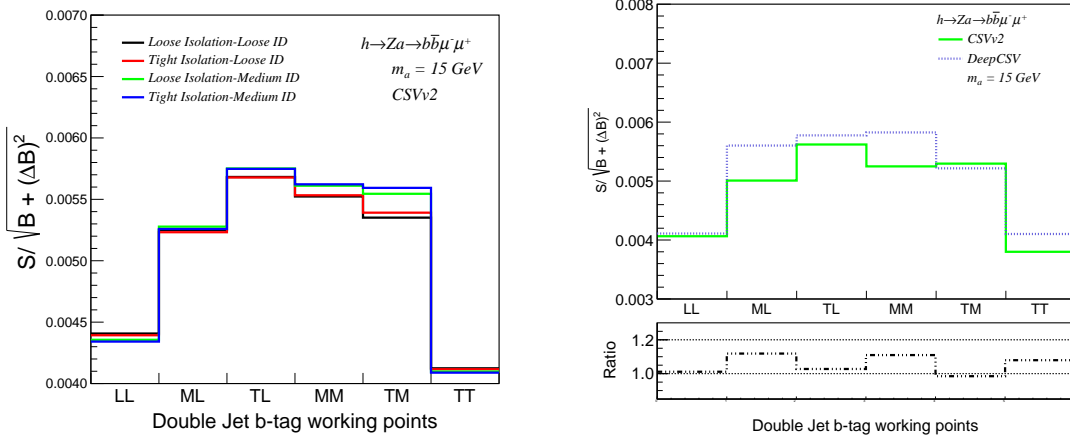


Figure 5.5: (left) The significance for different combinations of muon isolations (μ -Iso) and identifications (μ -ID), and (right) the comparison of significance for CSVv2 versus DeepCSV taggers for different working point combinations of the selected b -tagged jets.

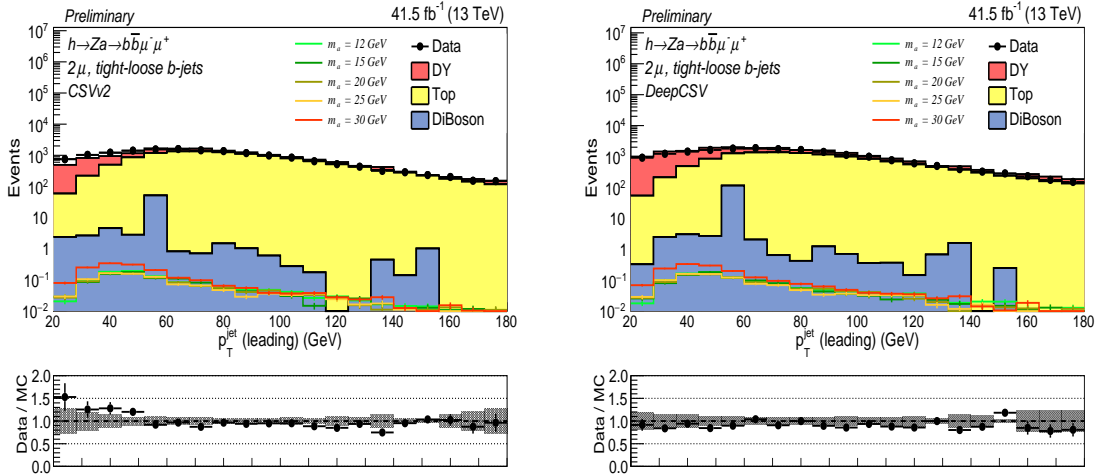


Figure 5.6: Data Monte Carlo (Data-MC) comparison for momentum distribution of leading jet (left) CSVv2 and (right) DeepCSV tagger.

The jets expected from the bottom quarks are identified with a DeepCSV (as well as CSVv2) algorithm which employs the information regarding the secondary vertices within the jet for the identification of a b jet [42]. Different working points “tight (T)”, “medium (M)” and the “loose (L)” are defined. These working points correspond to the threshold on the discriminator of a given tagger for which the misidentification probability is around

0.1%, 1%, 10%, respectively, for the jets that originate from gluons and light quarks. On the other hand probability of misidentification for jets that originate from charm (c) flavor quarks are 2% for T, 10% for M, and 30% for L. The b -jet identification efficiency for L is around 40%, for M is 60% and for the T is 80%.

The b jets with different combinations for the b jet identification working points are made to pass the working points L, M, and T, and accordingly, various permutations LL, ML, TL, MM, TM, TT are formed depending on whether or not the final jet pair passes discriminator thresholds. The events passing with many b jets, the two are considered having the highest transverse momentum (p_T). The significance is calculated in each case for the signal process for different mass points. It is observed that the combination in which one of the jets with a given discriminator value passes the tight working point and the second jet passes the loose working point (TL combination) of the algorithm shows higher significance (Figure 5.4). The simulated events for the identification of b jets are corrected after applying correction factors to obtain the agreement with data. Also, depending upon the available muon isolations and identification working points, the significance is observed to be slightly higher (Figure 5.5) in the Tight isolation-Medium ID [56] combination, which is selected for the current analysis. Further, the significance of the DeepCSV tagger is perceived to be higher than CSV $v2$ as shown in Figure 5.5 and the reason for it is explained in reference [42]. Therefore, in the present analysis, only a few data Monte-Carlo plots for CSV $v2$ tagger are shown (Figure 5.6) for comparison, and for the interpretation of final results, only DeepCSV tagger is considered.

5.4.1 Further optimization

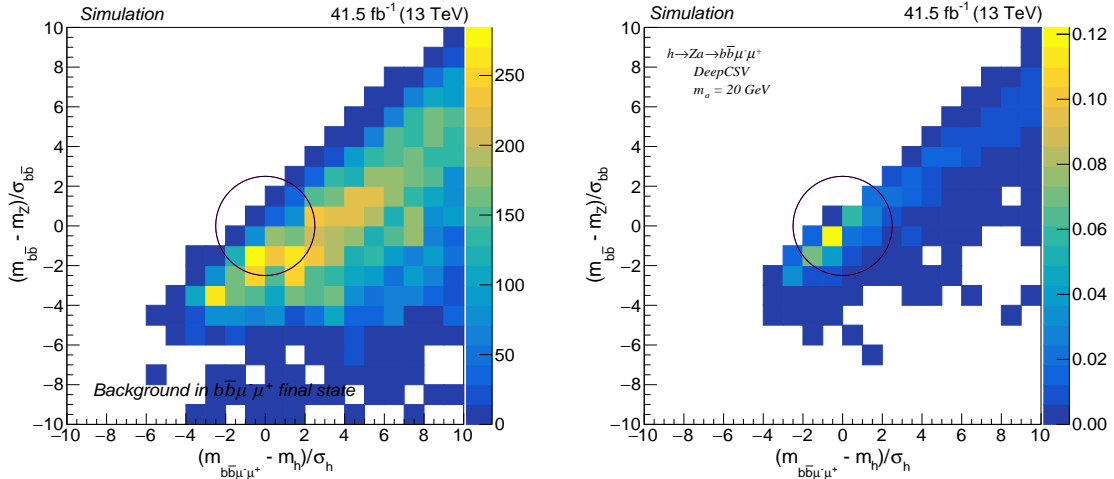


Figure 5.7: The distribution of $\chi_{b\bar{b}}$ versus χ_h as defined in equation 5.2 for (left) background simulated and (right) for signal process with m_a GeV. The encircled area with $\chi^2 < 5$. In each plot, the scale on the right side represents the expected yields at 41.5 fb^{-1} .

Since there are no semileptonic processes the final state of the current channel, therefore neutrino contribution is not expected and hence imbalance in the transverse momentum⁴

⁴ \vec{p}_T is the notational form to represent missing transverse momentum in the event.

5.4. SELECTION OPTIMIZATION

(\vec{p}_T) defined as the magnitude of the negative vector sum of the transverse momenta of all reconstructed particles in signal events is not expected to be large. The events are required to have missing transverse energy⁵ $\cancel{E}_T < 60$ GeV [55].

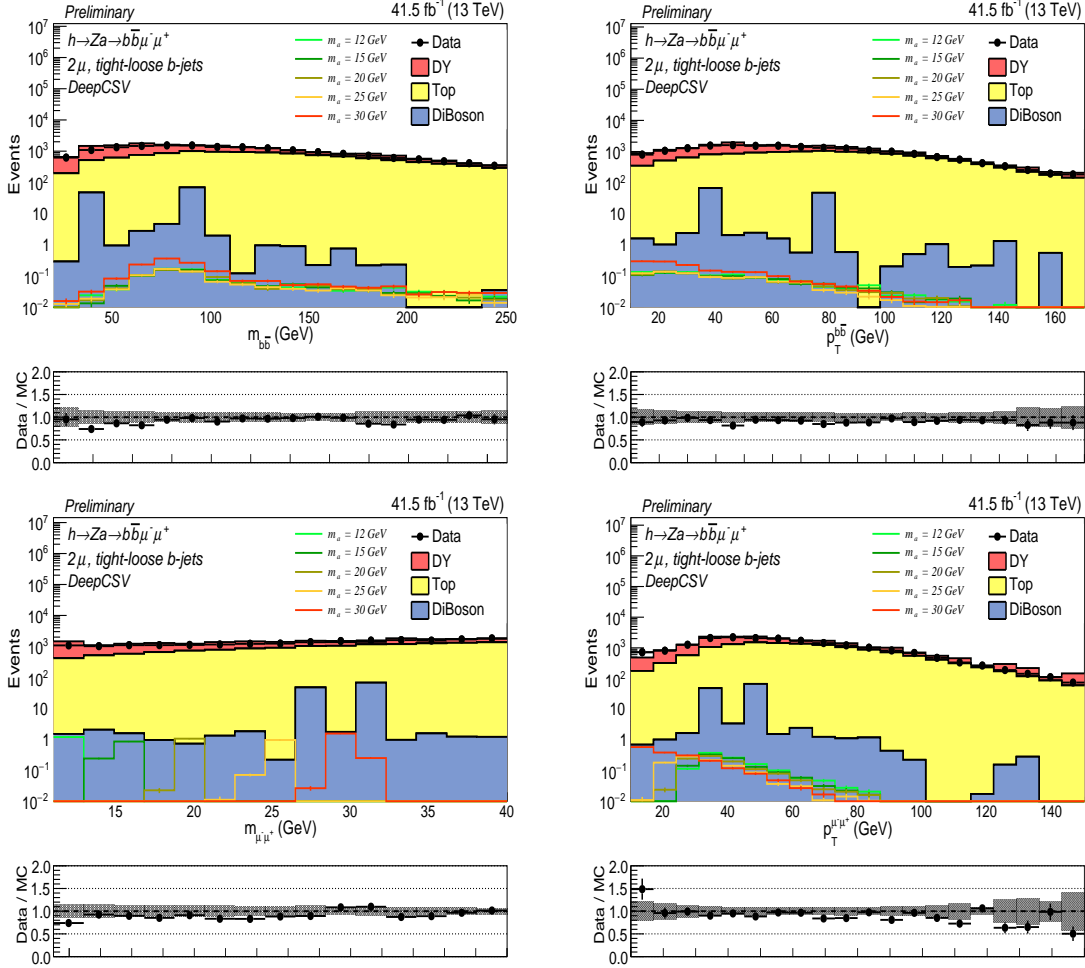


Figure 5.8: The reconstructed Z boson: (top left) mass and (top right) its momentum; and the reconstructed pseudo scalar a : (bottom left) mass and (bottom right) its momentum.

Assuming muons (μ^- , μ^+) and the jets from a pair of b quarks (b , \bar{b}) are coming from the parent particles a and Z boson, respectively, it is expected to have $m_{\mu^-\mu^+} \approx m_a$, $m_{b\bar{b}} \approx m_Z \approx 91$ GeV and $m_{\mu^-\mu^+b\bar{b}} \approx m_h \approx 125$ GeV in signal events. Therefore, a new variable χ^2 is introduced as

$$\chi^2 = \chi_{b\bar{b}}^2 + \chi_h^2 \quad (5.2)$$

where

$$\chi_{b\bar{b}} = \frac{(m_{b\bar{b}} - m_Z)}{\sigma_{b\bar{b}}} \quad \text{and} \quad \chi_h = \frac{(m_{b\bar{b}\mu^-\mu^+} - m_h)}{\sigma_h} \quad (5.3)$$

⁵The missing transverse energy (MET), denoted as \vec{p}_T is defined as the modulus of p_T and is the negative vector sum of all the reconstructed particles.

and $\sigma_{b\bar{b}}$ and σ_h are the mass resolutions derived from simulation of the di-b-quark jet system and the Higgs boson candidate, respectively. The mass resolution of $m_{\mu^-\mu^+}$ is assumed to be equal to m_a with a linear dependence. Also, the mass resolution of the di-b-quark system is evaluated on event-by-event basis and increase linearly with m_a . The χ^2 components i.e., $\chi_{b\bar{b}}^2$ and χ_h^2 for the signal with $m_a = 20$ GeV and backgrounds are shown in 2D histograms in Figure 5.7. The events are selected with $\chi^2 < 5$ and are represented with a contour⁶ of radius less than 5 (i.e., $\chi^2 < 5$). This region defines the signal region and has an efficiency up to $\approx 65\%$ for signal while rejecting over 95% of the background events. Recalling, events having $m_{\mu^-\mu^+}$ values outside the mass range [11, 40] GeV are discarded.

5.5 Event Selection

The data used for the current analysis is collected using asymmetric dimuon trigger. The optimized p_T thresholds used for the leading and the subleading muons are 20 GeV and 9 GeV, respectively. Oppositely charged and isolated muons with relative isolation and separation of less than 15% and ΔR greater than 0.4, respectively, are selected within the pseudorapidity region of $|\eta| < 2.4$ to reject events with muons from non-prompt decays [43]. The separation and isolation requirements make this search inefficient to signals with very low mass ($1 < m_a < 11$ GeV), which is characterized by semi-collimated muons from pseudoscalar boson. Additionally, to avoid the effect of interferences from quarkonium states, this region is not probed.

The leading b tagged jet pair with p_T greater than 20 GeV and 15 GeV, respectively, in a given event is identified as the Z ($Z \rightarrow b\bar{b}$) candidate and the leading muon pair invariant mass window between 10 GeV and 40 GeV is identified as a ($a \rightarrow \mu^-\mu^+$) candidate. Each signal event is, therefore, required to consist of Z and a candidates. The dimuon invariant mass window for a candidate is considered between 10 GeV and 40 GeV and the invariant mass of selected b jets and muons within the window of $100 < m_{b\bar{b}\mu^-\mu^+} < 250$ GeV is used to form the Higgs candidate.

Simulated background samples are used to optimize the selection, while as a method that relies on data, as described in Section 5.7, is used to estimate the background. Figure 5.8 shows invariant mass p_T distribution of di-b-jet system in simulation and data for events passing the selection requirements except those of \cancel{E}_T and χ^2 . The expected number of simulated events are normalized to the integrated luminosity of 41.5 fb^{-1} . Data and simulations are compared for the p_T of the di-b-jet system and the dimuon system. Figure 5.9 also illustrates the distribution of the invariant mass $m_{b\bar{b}\mu^-\mu^+}$ and the transverse momentum $p_T^{b\bar{b}\mu^-\mu^+}$ of the four-body system using selected jets and muons. Within the statistical uncertainties, the distributions for simulated events follow a reasonable agreement with data. The event yields in simulation and data are also in a reasonable agreement and are summarized in Table 5.1. The background from top quark ($t\bar{t}$) is dominant, contributing $\approx 62\%$, Drell-Yan is sub-dominant contributing $\approx 36.9\%$ and the other backgrounds contribute less than 0.1%

⁶The number 5 has been obtained by optimization studies.

5.5. EVENT SELECTION

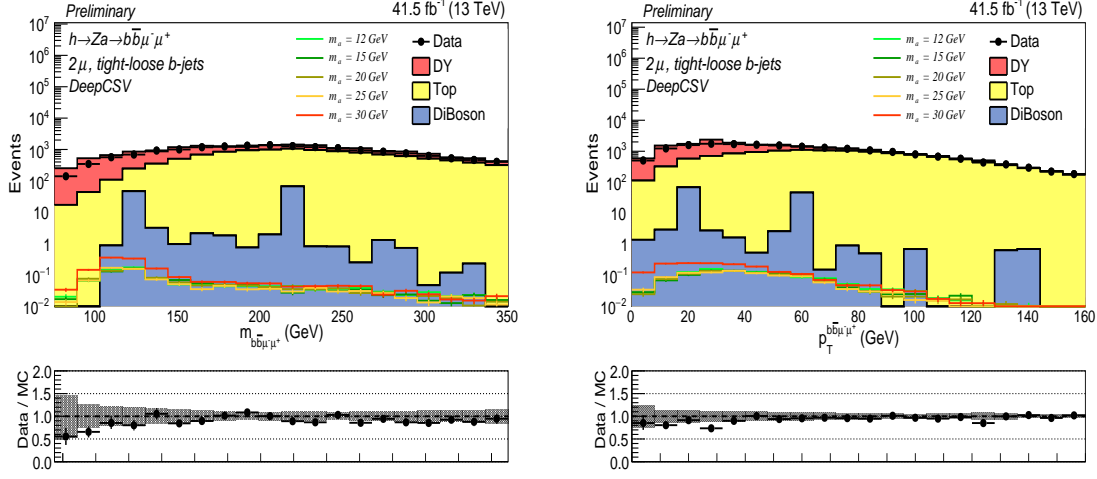


Figure 5.9: The reconstructed: (left) mass and (right) momentum of the Higgs boson (four object ($b\bar{b}\mu^-\mu^+$) system).

when DeepCSV tagger is used. However, the corresponding figures for CSV $v2$ are $\approx 76.9\%$, $\approx 23\%$ and 0.1% , respectively. The event yields in simulation and data after applying final cuts are in a reasonable agreement as shown in Table 5.3.

Process	Yield \pm Error	Signal (GeV)	Yield \pm Error
Top	13636.12 ± 30.71	$m_a = 12$	1.19 ± 0.03
Drell-Yan	8138.05 ± 399.34	$m_a = 15$	1.11 ± 0.03
Diboson	131.22 ± 80.26	$m_a = 20$	1.09 ± 0.03
Total	21905.39 ± 408.48	$m_a = 25$	1.04 ± 0.03
Data	20012.00 ± 141.46	$m_a = 30$	1.82 ± 0.04

Table 5.1: Event yields obtained by DeepCSV tagger for simulated processes and data after selecting two muons and two b jets (tight-loose). The expected number of simulated events are normalized to the integrated luminosity of 41.5 fb^{-1} .

Process	Yield \pm Error	Signal (GeV)	Yield \pm Error
Top	13040.71 ± 31.86	$m_a = 12$	1.17 ± 0.03
Drell-Yan	3860.19 ± 282.32	$m_a = 15$	1.11 ± 0.03
Diboson	71.74 ± 50.74	$m_a = 20$	1.07 ± 0.03
Total	16972.64 ± 411.92	$m_a = 25$	1.03 ± 0.03
Data	17061.00 ± 130.62	$m_a = 30$	1.81 ± 0.04

Table 5.2: Event yields obtained by CSV $v2$ tagger for simulated processes and data after selecting two muons and two b jets (tight-loose). The expected number of simulated events are normalized to the integrated luminosity of 41.5 fb^{-1} .

5.6. SIGNAL MODEL

Process	Yield \pm Error	Signal (GeV)	Yield \pm Error
Top	129.00 ± 3.27	$m_a = 12$	0.36 ± 0.03
Drell-Yan	692.94 ± 131.87	$m_a = 15$	0.33 ± 0.03
Diboson	3.40 ± 1.05	$m_a = 20$	0.34 ± 0.03
Total	825.34 ± 131.91	$m_a = 25$	0.35 ± 0.03
Data	887.00 ± 29.61	$m_a = 30$	0.77 ± 0.04

Table 5.3: Event yields obtained using DeepCSV tagger for simulated processes and data after final cuts.

5.6 Signal model

The signal samples are simulated for various mass points as described in Section 5.2 and the results are extracted by fitting the reconstructed dimuon mass distribution. The dimuon mass distributions of the simulated $h \rightarrow Za \rightarrow b\bar{b}\mu^-\mu^+$ signal events passing all selection criteria are parametrized with the combination of Voigtion (V) and double-sided Crystal Ball (CB) functions as

$$S(m_{\mu^-\mu^+} | f, p_V, p_{CB}) \equiv f \cdot V(m_{\mu^-\mu^+} | p_V) + (1 - f) \cdot CB(m_{\mu^-\mu^+} | p_{CB}) \quad (5.4)$$

where p_V corresponds to set of parameters for Voigtion with its relative contribution f , and p_{CB} is the parameter set for the Crystal ball function.

The Voigtion profile function is a convolution of Gaussian and Lorentz profiles as

$$\begin{aligned} V(m_{\mu^-\mu^+} | p_V) &\equiv V(m_{\mu^-\mu^+}, \sigma, \gamma, m_a) = G(m_{\mu^-\mu^+}, \sigma, m_a) * L(m_{\mu^-\mu^+}, \gamma, m_a) \\ &= \left(\frac{e^{-(m_{\mu^-\mu^+} - m_a)^2 / 2\sigma^2}}{\sigma\sqrt{2\pi}} \right) * \left(\frac{\gamma}{\pi((m_{\mu^-\mu^+} - m_a)^2 + \gamma^2)} \right) \end{aligned} \quad (5.5)$$

with σ and γ being the width of the respective functions, both centered at the common mean m_a .

The Crystal Ball function, on the other hand, has a Gaussian core with a power-law low-end tail below a certain threshold, α . The mean and width of the Crystal Ball profile are assumed to be proportional to m_a ,

$$CB(m_{\mu^-\mu^+}, n, \sigma_{CB}, \alpha, m_a) = N \cdot \begin{cases} e^{-(m_{\mu^-\mu^+} - m_a)^2 / 2\sigma_{CB}^2}, & \text{for } \frac{m_{\mu^-\mu^+} - m_a}{\sigma_{CB}} > -\alpha \\ A \cdot \left(B - \frac{(m_{\mu^-\mu^+} - m_a)}{\sigma_{CB}} \right)^{-n} & \text{for } \frac{m_{\mu^-\mu^+} - m_a}{\sigma_{CB}} \leq -\alpha \end{cases} \quad (5.6)$$

where the parameters A , B and N are functions of n , σ_{CB} and α with $CB(m_{\mu^-\mu^+} | p_{CB}) \equiv CB(m_{\mu^-\mu^+}, n, \sigma_{CB}, \alpha, m_a)$.

The model is simplest and robust enough to describe the shape of the simulated resonances very well. Figure 5.10 shows simulated signal distributions together with fitted functions where the constructed model obtains a reasonable signal description.

In the signal model $S(m_{\mu^-\mu^+} | f, p_V, p_{CB})$, there is a possibility of correlations amongst the various parameters f , p_V and p_{CB} etc., which could change with m_a . To account for such correlations and preserve the mass dependencies, the number of parameters of the signal

5.6. SIGNAL MODEL

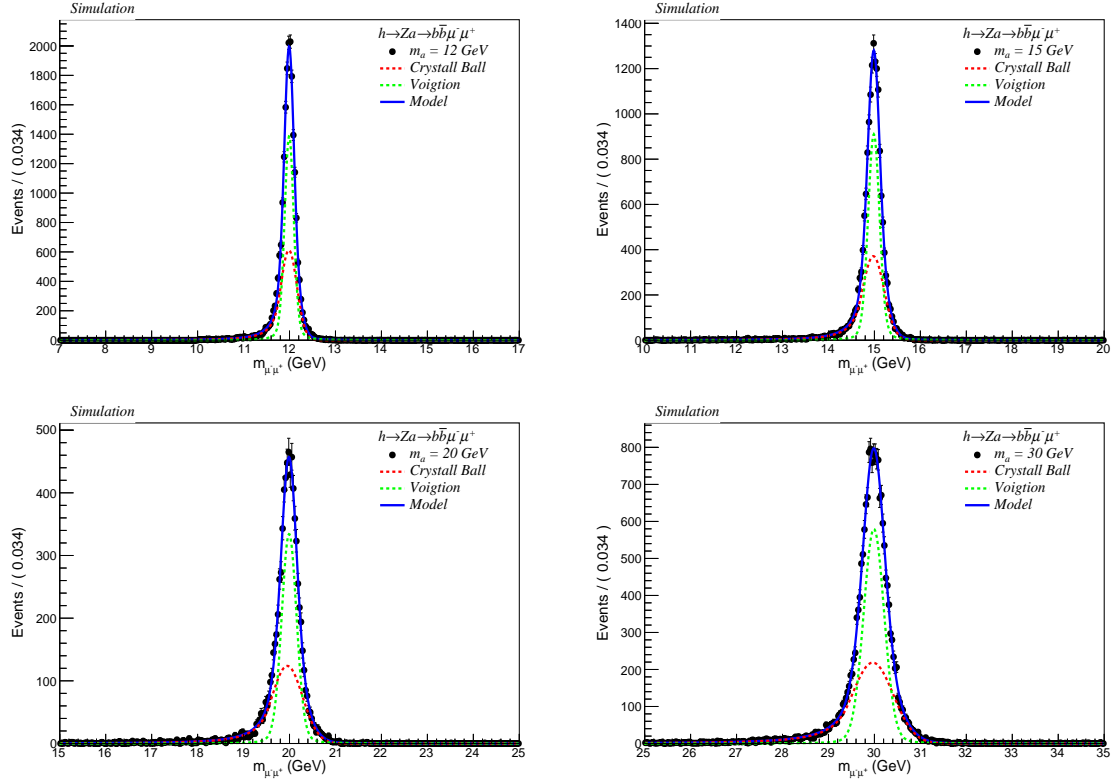


Figure 5.10: Results of the signal model $S(m_{\mu^-\mu^+} | f, p_V, p_{CB})$, fitted independently to $m_{\mu^-\mu^+}$ distributions for $m_a = 12, 15, 20, 30$ GeV. Dotted lines in each distribution are the Crystal Ball and Voigtion components, and the solid line is the constructed model.

model are reduced to three free parameters; one is a perturbation to the mass of the hypothetical signal, $\tilde{m}_a = m_a + \epsilon_{m_a}$, and the other two, a_1 and b_1 , are used to linearly model the resolutions, σ and σ_{CB} , with mass (Table 5.4). A simultaneous fit to all signal hypotheses is performed to establish the 3-parameter model as well as to extract the initial values of the fixed and free parameters. With this parameterization, it is possible to interpolate the signal shape into regions for which the simulated samples are not available.

$S(m_{\mu^-\mu^+} f, p_V, p_{CB}) _{f=\hat{f}}$	$\hat{f} \cdot V(m_{\mu^-\mu^+} \tilde{m}_a, \sigma, \gamma)$	$\sigma = \hat{\sigma} + b_1 \cdot m_{\mu^-\mu^+}$
		$\gamma = \hat{\gamma}$
	$(1 - \hat{f}) \cdot CB(m_{\mu^-\mu^+} \tilde{m}_a, n, \sigma_{CB}, \alpha)$	$\sigma = \hat{\sigma} + a_1 \cdot m_{\mu^-\mu^+}$
		$\alpha = \hat{\alpha}$
		$n = \hat{n}$

Table 5.4: The parameters for the signal model and their modeling with the mass: \hat{f} , $\hat{\gamma}$, $\hat{\alpha}$ and \hat{n} are fixed where σ and σ_{CB} are linearly modeled. Apart from the signal mass perturbative term, $\tilde{m}_a = m_a + \epsilon_{m_a}$, the model also has two free parameters, a_1 and b_1 .

5.7 Background model

A data-driven approach is employed to evaluate the background by performing a fit to $m_{\mu^-\mu^+}$ distribution.

The associated uncertainties due to the particular choice of a background model are treated similar to other uncertainties for which there are nuisance parameters in the fit. The likelihood function for the signal-plus-background fit has the form

$$\mathcal{L}(\text{data} \mid s(p, m_{\mu^-\mu^+}) + b(m_{\mu^-\mu^+})) \quad (5.7)$$

where $s(p, m_{\mu^-\mu^+})$ is the parameters signal shape with a set of parameters represented by p , and $b(m_{\mu^-\mu^+})$ is the background model.

The background shape is modeled with a set of analytical functions, using the discrete profiling method [45–47]. The approach treats background shape as a discrete nuisance parameter in the fit where its phase contains multiple models, each including their own parameters.

Therefore, input background models are provided to the profiling method by modeling background data with the different parameterization of polynomials. These include Polynomials ($P_n(x)$), Inverse Polynomials, Chebychev and Bernstein, where $P_n(x) \equiv \sum_i^n \alpha_i x^i$ are the n th order polynomials. To avoid the overfitting of the data, the degree of background models in each category are determined by F -test to ensure the sufficiency of the number of parameters. In each category, models with the lowest number of parameters are tried first and are considered justified based on the closure of the fit to the data ($\chi^2/\text{ndf} \sim 1$). Also, the cross-check of different selected categories is performed to make sure that no pdf is repeated in the final pool of background models.

The input background functions are tried in the minimization of the negative logarithm of the likelihood. The free parameters in the background model are accounted for by adding a penalty term. The likelihood ratio for the penalized likelihood function is written as

$$-2 \ln \frac{\tilde{\mathcal{L}}(\text{data} \mid \kappa, \hat{\theta}_\kappa, \hat{b}_\kappa)}{\tilde{\mathcal{L}}(\text{data} \mid \hat{\kappa}, \hat{\theta}, \hat{b})} \quad (5.8)$$

where κ is the measured quantity. The numerator is the maximized likelihood for a given κ , at the best-fit values of nuisance parameters, $\hat{\theta}_\kappa$ and \hat{b}_κ . The denominator is the global maximum for $\tilde{\mathcal{L}}$ achieved at $\kappa = \hat{\kappa}$, $\theta = \hat{\theta}$ and $b = \hat{b}$. A confidence interval on κ is obtained with the background function maximizing $\tilde{\mathcal{L}}$ for any value of κ . This interval is always wider than those evaluated with the fixed functional from the global best-fit, $b = \hat{b}$ [46]. Table 5.5

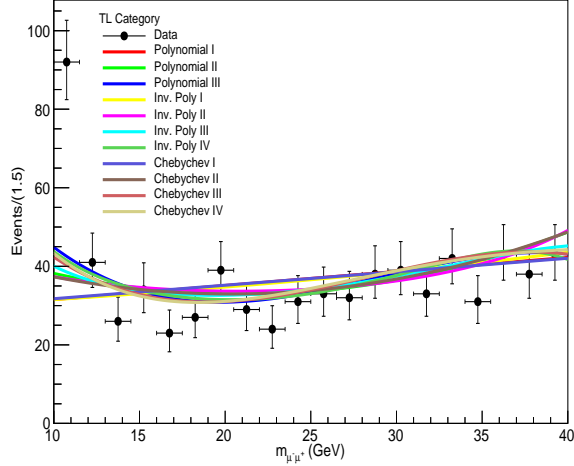


Figure 5.11: Various pdf's describing the background shape from the control region of the data (TL category).

5.8. SYSTEMATIC UNCERTAINTIES

Tight-Loose (TL) category			
Model	χ^2/ndf	F-test probability (> 0.05)	Decision
Polynomial I	0.94	-	✓
Polynomial II	0.73	0.06	✓
Polynomial III	0.61	0.13	✓
Polynomial IV	0.58	0.01	×
Polynomial V	0.57	0.00	×
Inv. Poly I [†]	0.94	-	✓
Inv. Poly II	0.76	0.12	✓
Inv. Poly III	0.65	0.20	✓
Inv. Poly IV	0.62	0.53	✓
Inv. Poly V	0.59	0.00	×

Table 5.5: Trial functions with different orders are selected to model the background in TL category depending upon the outcome of the F-test. The pdf's marked with '†' sign are not selected as they are repeating in another polynomial category.

Tight-Loose (TL) category			
Model	χ^2/ndf	F-test probability (> 0.05)	Decision
Bernstein I	1.2	-	×
Bernstein II	0.91	0.03	×
Bernstein III	-	0.00	×
Bernstein IV	0.55	0.00	×
Bernstein V	0.54	0.80	×
Chebyshev I [†]	0.99	-	×
Chebyshev II	0.73	0.051	✓
Chebyshev III	0.62	0.17	✓
Chebyshev IV	0.60	0.82	✓
Chebyshev V	0.55	0.83	✓

Table 5.6: Trial functions with different orders are selected to model the background in TL category depending upon the outcome of the F-test. The pdf's marked with '†' sign are not selected as they are repeating in another polynomial category.

and Table 5.6 summarize various functions in different categories with their corresponding statistical F-test results to each parameterization, and Figure 5.11 illustrates the summary of suitable background models used to describe the data.

5.8 Systematic uncertainties

The statistical interpretation of the final results takes into account various sources of uncertainties for simulations and data. Theoretical uncertainties that affect the signal include uncertainties from the choice of PDF sets which are determined by setting Higgs boson production cross section to the SM prediction with an uncertainty of 3.6% [49]. The simulations are reweighted to match the distribution in the number of pileup collisions per event in data and uncertainty is estimated by varying the total inelastic pp cross section by $\pm 4.6\%$ [50].

For the data collected by the CMS in the year 2017, the uncertainty 2.3% is assigned

5.9. RESULTS

Source	Type	Remarks
Integrated luminosity	rate	Signal and all backgrounds
PDF (gg)	"	Uncertainty for gg initiated processes
Lepton identification/isolation	shape	Signal and all backgrounds
Trigger efficiency	"	"
Pileup	"	"
Jet energy scale	"	"
Jet energy resolution	"	"
b tag hf fraction	"	"
b tag hf stats (linear)	"	"
b tag hf stats (quadratic)	"	"
b tag lf fraction	"	"
b tag lf stats (linear)	"	"
b tag lf stats (quadratic)	"	"
b tag charm (linear)	"	"
b tag charm (quadratic)	"	"

Table 5.7: Systematic uncertainties considered in the present analysis.

to the integrated luminosity [52]. The simulation-to-data correction factors for the selection and trigger efficiencies and muon reconstruction are estimated by using the ‘tag-and-probe’ method [51] in Drell-Yan data and simulated samples. These uncertainties include the pileup dependence of the correction factors. The variations on the jet energy scale (JES) are made according to the p_T and η dependent uncertainties which are propagated to p_T^{miss} of the event. For the jet energy resolution (JER), the smearing corrections are varied within their uncertainties [45]. Systematic uncertainty sources that affect the simulation-to-data corrections of the b tagging discriminator are JES, the statistical fluctuations from heavy flavor (HF) jets in the light-flavor jet sample, the contaminations from light flavor (LF) jets in the b jet sample, and the statistical fluctuations in MC and data. The uncertainties due to light-flavor jet contamination in b jet samples are found to be uncertainties have a negligible effect on the signal shape, their impact on the yield is taken into account by introducing nuisance parameters with log-normal distribution in the fit. Some of the leading sources of uncertainties are listed in Table 5.7.

5.9 Results

The results of the search are obtained from dimuon invariant mass distribution, The observed and expected upper limits at 95% confidence level (CL) using asymptotic CL_s method are set on $\sigma \times \mathcal{B}(h \rightarrow Za \rightarrow b\bar{b}\mu^-\mu^+)$ as a function of pseudoscalar mass m_a excluding the region $m_a \leq 11$. Interpolated mass points are obtained as described in Section 5.6. The upper limits on the branching fraction are also set with respect to theory expectations from type-3 2HDM+S at $\tan\beta = 2$, the theory uncertainty on $\sigma_{gg} \rightarrow h$ is taken into account. The results are presented in Figure 5.12.

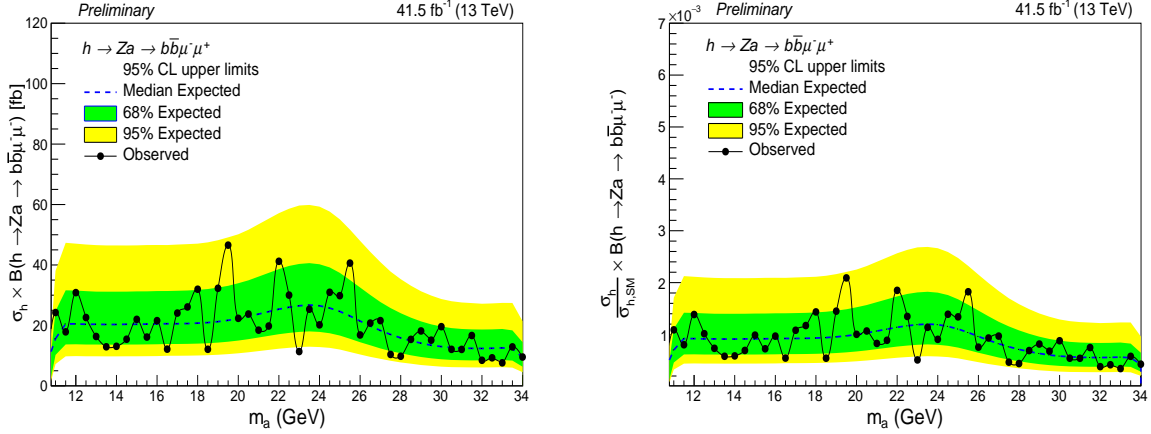


Figure 5.12: Observed and expected upper limits at 95% CL on the (left) Higgs boson production times branching fraction ($\mathcal{B}(h \rightarrow Za \rightarrow b\bar{b}\mu^-\mu^+)$) and (right) the branching ratio as a function of pseudoscalar mass m_a . The green and yellow bands represent 68 and 98% confidence intervals, respectively, around the median for expected and observed distribution of limits.

5.10 Summary

The first search results for new physics in the extended Higgs sector in signatures expected from the decay of Higgs boson to electroweak Z boson and a light pseudoscalar a boson has been presented where a Z boson is expected to decay into bottom-antibottom ($b\bar{b}$) quark pair and a a boson into muon-antimuon ($\mu^-\mu^+$) lepton pair. The search used data collected by the CMS experiment at center-of-mass energy 13 TeV corresponding to an integrated luminosity of 41.5 fb^{-1} during the year 2017. The decay channel is extremely motivated in many BSM models and is expected to provide better sensitivity compared to other decay modes with either $4b$ quark jets or 4 leptons in the final state. No excess of events is found over the expected SM background. The upper limits are set on $\sigma_h \times \mathcal{B}(h \rightarrow Za \rightarrow b\bar{b}\mu^-\mu^+)$ as well as on the branching fraction of the Higgs boson decay. The limits on the branching fraction are determined to be $(0.3 - 2.3) \times 10^{-3}$, which can be compared with the expected value $(1.0 - 1.2) \times 10^{-3}$, assuming particular scenarios of two-Higgs-doublet-models augmented with a scalar singlet. The limits are stringent for the decay channel $h \rightarrow Za \rightarrow b\bar{b}\mu^-\mu^+$ in the pseudoscalar mass range $11 < m_a < 34 \text{ GeV}$ and are the first such results at the LHC so far.

BIBLIOGRAPHY

- [1] F. Englert et al., “[Broken symmetry and the mass of gauge vector mesons](#)”, Phys. Rev. Lett. 13 (1964) 321.
- [2] P. W. Higgs, “[Broken symmetries, massless particles and gauge fields](#)”, Phys. Lett. 12 (1964) 132.
- [3] P. W. Higgs, “[Broken symmetries and the masses of gauge bosons](#)”, Phys. Rev. Lett. 13 (1964) 508.
- [4] G. S. Guralnik et al., “[Global conservation laws and massless particles](#)”, Phys. Rev. Lett. 13 (1964) 585.
- [5] P. W. Higgs, “[Spontaneous symmetry breakdown without massless bosons](#)”, Phys. Rev. 145 (1966) 1156.
- [6] T. W. B. Kibble, “[Symmetry Breaking in Non-Abelian Gauge Theories](#)”, Phys. Rev. 155 (1967) 1554.
- [7] ATLAS Collaboration, “[Observation of a new particle in the search for the Standard Model Higgs boson with the ATLAS detector at the LHC](#)”, Phys. Lett. B 716 (2012).
- [8] CMS Collaboration, “[Observation of a new boson at a mass of 125 GeV with the CMS experiment at the LHC](#)”, Phys. Lett. B 716 (2012).
- [9] CMS Collaboration, “[Observation of a new boson with mass near 125 GeV in pp collisions at \$\sqrt{s} = 7\$ and 8 TeV](#)”, JHEP 06 (2013) 081.
- [10] ATLAS and CMS Collaborations, “[Measurements of the Higgs boson production and decay rates and constraints on its couplings from a combined ATLAS and CMS analysis of the LHC pp collision data at \$\sqrt{s} = 7\$ and 8 TeV](#)”, JHEP 08 (2016) 045.
- [11] ATLAS and CMS Collaborations, “[Combined measurement of the Higgs boson mass in pp collisions at \$\sqrt{s} = 7\$ and 8 TeV with the ATLAS and CMS experiments](#)”, Phys. Rev. Lett. 114 (2015) 191803.
- [12] R. Dermisek et al., “[Escaping the large fine tuning and little hierarchy problems in the next to minimal supersymmetric model and \$h \rightarrow aa\$ decays](#)”, Phys. Rev. Lett. 95 (2005) 041801.

- [13] R. Dermisek et al., “[The NMSSM close to the R-symmetry limit and naturalness in \$h \rightarrow aa\$ decays for \$m_a < 2m_b\$](#) ”, Phys. Rev. D 75 (2007) 075019.
- [14] S. Chang et al., “[Nonstandard Higgs boson decays](#)”, Ann. Rev. Nucl. Part. Sci. 58 (2008) 75.
- [15] D. Curtin et al., “[Exotic decays of the 125 GeV Higgs boson](#)”, Phys. Rev. D 90 (2014) 075004.
- [16] D. Curtin et al., “[Uncovering light scalars with exotic Higgs decays to \$b\bar{b} \mu^+ \mu^-\$](#) ”, JHEP 06 (2015) 025.
- [17] CMS Collaboration, “[Search for neutral mssm higgs bosons decaying to a pair of tau leptons in pp collisions](#)”, JHEP 10 (2014) 160.
- [18] CMS Collaboration, “[Search for neutral MSSM Higgs bosons decaying into a pair of bottom quarks](#)”, JHEP 11 (2015) 071.
- [19] CMS Collaboration, “[Search for neutral MSSM Higgs bosons decaying to \$\mu^+ \mu^-\$ in pp collisions at \$\sqrt{s} = 7\$ and 8 TeV](#)”, Phys. Lett. B 752 (2016) 221.
- [20] CMS Collaboration, “[Search for a charged Higgs boson in pp collisions at \$\sqrt{s} = 8\$ TeV](#)”, JHEP 11 (2015) 018.
- [21] CMS Collaboration, “[Search for Higgs boson pair production in events with two bottom quarks and two tau leptons in proton-proton collisions at \$\sqrt{s} = 13\$ TeV](#)”, Phys. Lett. B 778 (2018) 101-117.
- [22] CMS Collaboration, “[Searches for a heavy scalar boson H decaying to a pair of 125 GeV Higgs bosons hh or for a heavy pseudoscalar boson A decaying to Zh, in the final states with \$h \rightarrow \tau\tau\$](#) ”, Phys. Lett. B 755 (2016) 217.
- [23] S. Heinemeyer et al., “[Interpreting the LHC Higgs search results in the MSSM](#)”, Phys. Lett. B 710 (2012) 201.
- [24] G. C. Branco et al., “[Theory and phenomenology of two-Higgs-doublet models](#)”, Phys. Rep. 516 (2012) 1.
- [25] J. Alwall et al., “[The automated computation of tree-level and next-to-leading order differential cross sections, and their matching to parton shower simulations](#)”, JHEP 07 (2014) 079.
- [26] NNPDF Collaboration et al., “[Parton distributions from high-precision collider data](#)”, Eur. Phys. J. C 77 (2017) 663.
- [27] Y. Li et al., “[Combining QCD and electroweak corrections to dilepton production in FEWZ](#)”, Phys. Rev. D 86 (2012) 094034.

- [28] E. Re, “[Single-top Wt-channel production matched with parton showers using the POWHEG method](#)”, Eur. Phys. J. C 71 (2011) 1547.
- [29] S. Alioli et al., “[A general framework for implementing NLO calculations in shower Monte Carlo programs](#)”, JHEP 06 (2010) 043.
- [30] S. Alioli et al., “[NLO single-top production matched with shower in POWHEG: s- and t-channel contributions](#)”, Phys. Rep. 516 (2012) 1.
- [31] S. Frixione et al., “[Matching NLO QCD computations with parton shower simulations: the POWHEG method](#)”, JHEP 09 (2009) 111.
- [32] NNPDF Collaboration, “[Parton distributions for the LHC Run II](#)”, Comput. Phys. Commun. 191 (2015) 159.
- [33] T. Sjostrand et al., “[An introduction to PYTHIA 8.2](#)”, Phys. Rep. 516 (2012) 1.
- [34] P. Skands et al., “[Tuning PYTHIA 8.1: the Monash 2013 tune](#)”, Eur. Phys. J. C 74 (2014) 3024.
- [35] CMS Collaboration, “[Event generator tunes obtained from underlying event and multi-parton scattering measurements](#)”, Eur. Phys. J. C 76 (2016) 155.
- [36] GEANT4 Collaboration, “[GEANT4-a simulation toolkit](#)”, Nucl. Inst. Meth. A 506 (2003) 250.
- [37] CMS Collaboration, “[CMS luminosity measurements for the 2016 data taking period](#)”, CMS Physics Analysis Summary CMS-PAS-LUM-17-001, 2017.
- [38] CMS Collaboration, “[Particle-flow reconstruction and global event description with the CMS detector](#)”, 12 JINST (2017) P10003.
- [39] M. Cacciari et al., “[The anti- \$k_t\$ jet clustering algorithm](#)”, JHEP 04 (2008) 063.
- [40] M. Cacciari et al., “[FastJet user manual](#)”, Eur. Phys. J. C 72 (2012) 1896.
- [41] CMS Collaboration, “[Determination of jet energy calibration and transverse momentum resolution in CMS](#)”, JINST 6 (2011) 11002.
- [42] CMS Collaboration, “[Identification of heavy-flavour jets with the CMS detector in pp collisions at 13 TeV](#)”, 13 JINST (2018) P05011.
- [43] CMS Collaboration, “[Search for a standard model-like Higgs boson in the \$\mu^+\mu^-\$ and \$e^+e^-\$ decay channels at the LHC](#)”, Phys. Lett. B744 (2015) 184-207.
- [44] CMS Collaboration, “[Performance of Electron Reconstruction and Selection with the CMS Detector in Proton-Proton Collisions at \$\sqrt{s} = 8\$ TeV](#)”, 2015 JINST 10 P06005.

- [45] CMS Collaboration, “[Jet algorithms performance in 13 TeV data](#)”, CMS Physics Analysis Summary CMS-PAS-JME-16-003, 2017.
- [46] P. Dauncey et al., “[Handling uncertainties in background shapes: the discrete profiling method](#)”, (2015) JINST 10 P04015.
- [47] CMS Collaboration, “[Observation of the diphoton decay of the Higgs boson and measurement of its properties](#)”, Eur. Phys. J. C74 (2014), no. 10, 3076.
- [48] ATLAS and CMS Collaborations, “[Combined Measurement of the Higgs Boson Mass in pp Collisions at \$\sqrt{s} = 7\$ and 8 TeV with the ATLAS and CMS Experiments](#)”, Phys. Rev. Lett. 114 (2015) 191803.
- [49] D. de Florian et al., “[Handbook of LHC Higgs cross sections: 4. Deciphering the nature of the Higgs sector](#)”, CERN Report CERN-2017-002-M, 2016.
- [50] ATLAS Collaboration, “[Measurement of the inelastic proton-proton cross section at \$\sqrt{s} = 13\$ TeV with the ATLAS detector at the LHC](#)”, Phys. Rev. Lett. 117 (2016) 182002.
- [51] CMS Collaboration, “[Measurements of inclusive W and Z cross sections in pp collisions at \$\sqrt{s} = 7\$ TeV](#)”, Phys. Rev. Lett. 117 (2016) 182002.
- [52] CMS Collaboration, “[CMS luminosity measurement for the 2017 data-taking period at \$\sqrt{s} = 13\$ TeV](#)”, CMS Physics Analysis Summary CMS-PAS-LUM-17-004, 2017.
- [53] J. Butterworth et al., “[PDF4LHC recommendations for LHC Run II](#)”, J. Phys. G 43 (2016) 023001.
- [54] G. Cowan et al., “[Asymptotic formulae for likelihood-based tests of new physics](#)”, Eur. Phys. J. C71 (2011) 1554.
- [55] CMS Collaboration et al., “[Determination of jet energy calibration and transverse momentum resolution in CMS](#)”, JINST 6 (2011) P11002.
- [56] CMS Collaboration et al., “[Performance of the CMS muon detector and muon reconstruction with proton-proton collisions at \$\sqrt{s} = 13\$ TeV](#)”, JINST 13 (2018) P06015.

Search for exotic Higgs boson decay in $h \rightarrow aa \rightarrow b\bar{b}\mu^-\mu^+$

You cannot prove the theory with considerable experiments but one experiment is enough to deny all theories.

— Albert Einstein

A search for an exotic decay of a Higgs boson to a pair of light pseudoscalar bosons (aa), where one of the bosons decays to a muon-antimuon pair ($a \rightarrow \mu^-\mu^+$) and the other decays to bottom-antibottom quark pair ($a \rightarrow b\bar{b}$) is presented. The search is based on Higgs models with extended scalar sectors. Masses of light bosons between 20 and 62.5 GeV are probed. The results are based on the data collected by the CMS experiment during the year 2017 in proton-proton collisions at the center-of-mass energy of 13 TeV and correspond to an integrated luminosity of 41.5 fb^{-1} .

6.1 Introduction

Studies of the recently discovered particle h with a mass of 125 GeV and spin-0 [1–3] appear to be consistent with the properties of the SM Higgs boson [4], and hence constrain severely SM extensions that include scalar sectors [5–7]. Several well-motivated models predict decays of the Higgs boson to BSM particles [8]. Without making presumptions about the h couplings to vector bosons, leptons, and quarks, the CMS and ATLAS collaborations exclude at a 95% confidence level (CL) branching fractions of the Higgs boson to BSM particles ($\mathcal{B}(h \rightarrow \text{BSM})$) greater than 52% and 49%, respectively [4, 9]. By combining the results obtained by the CMS and ATLAS experiments, branching fractions as low as 34% are excluded at 95% CL [4, 9]. These experiments are expected to constrain branching fractions to new particles beyond 5-10% level using indirect measurements [10, 14, 15]. Therefore, it is very interesting to explore the possibility of decays of the SM-like Higgs boson to lighter scalars or pseudoscalars [8, 16–18].

The width of the SM Higgs boson is extremely narrow relative to its mass because of its remarkably small Yukawa couplings to the SM fermions to which it can decay. This implies that any BSM final state is expected to have a substantial partial width and non-negligible branching fraction compared to decays to SM particles [8]. Many BSM models that provide such decay channels include the ones in which the Higgs boson serves as a gateway

to hidden-sector particles (e.g., dark matter) that can couple to SM fermions and gauge bosons [25]. Other models include extended scalar sectors such as two-Higgs-doublet models (2HDM) [26, 29], Next-to-Minimal Supersymmetric Model (NMSSM) [30, 31], or models in which a singlet Higgs field is added to a double sector SM. The NMSSM is exceptionally well-motivated as it can provide a contribution to electroweak baryogenesis [32, 33] and also solves the μ -problem associated with supersymmetry breaking. These models (NMSSM and 2HDM) may contain pseudoscalar particle ‘ a ’ having a large $h \rightarrow aa$ branching fraction. In NMSSM, there are two light pseudoscalar Higgs bosons, a_1 and a_2 . Constraints from the R symmetries and Peccei-Quinn [35, 36] imply that the lighter a_1 is likely to have a smaller mass than that of the h boson [33], and also, being typically a singlet, suppression of $\mathcal{B}(h \rightarrow a_1 a_2)$ to a level compatible with observation is a natural possibility.

	Type-1	Type-2	Type-3 [†]	Type-4 [‡]
Up-type quarks	Φ_2	Φ_2	Φ_2	Φ_2
Down-type quarks	Φ_2	Φ_1	Φ_2	Φ_1
Charged leptons	Φ_2	Φ_1	Φ_1	Φ_2

Table 6.1: Coupling of different types of fermions to doublets in different types of 2HDM without FCNC at the lowest order.

[†]lepton specific

[‡]flipped

The Minimal Supersymmetric Model (MSSM) has a single pseudoscalar A , but the construction of the Higgs potential is such that mass has a lower bound of 95 GeV when the scalar is identified as SM-like h with a mass close to 125 GeV as implied by the LHC data [38]. The decay phenomenology of the the observed SM-like Higgs boson to a pair of light boson is detailed in references [8, 47–50] in the context of NMSSM-like, in [8, 39–46] for 2HDM, and in for 2HDM [8, 51, 52] for the general case of adding a singlet field to a 2HDM prescription.

	Type-1	Type-2	Type-3 [†]	Type-4 [‡]
Up-type quarks	$\cot\beta$	$\cot\beta$	$\cot\beta$	$\cot\beta$
Up-type quarks	$-\cot\beta$	$\tan\beta$	$-\cot\beta$	$\tan\beta$
Charged leptons	$-\cot\beta$	$\tan\beta$	$\tan\beta$	$-\cot\beta$

Table 6.2: The ratio of the Yukawa couplings of the 2HDM pseudoscalar a boson to those of the SM Higgs boson h , in the four types of 2HDM without FCNC at lowest order [11].

[†]lepton-specific

[‡]flipped

The 2HDM has two Higgs doublet fields, Φ_1 and Φ_2 , which after symmetry breaking leads to five physical states. One of the free parameters is mass of the a boson but if $m_a < h/2$, fine-tuning of the 2HDM potential is needed to have the branching $\mathcal{B}(h \rightarrow aa)$ consistent with the LHC data. The other free parameter is the $\tan\beta$, the ratio between the vacuum expectation values of the doublets expressed as $\tan\beta = v_2/v_1$. The lightest scalar is compatible with the properties of already discovered SM-like boson in the decoupling limit¹,

¹The limit where all the other scalars have large masses.

and is also in the alignment limit² [53]. Approximate alignment, a sufficient condition for consistency with the LHC data is plausible for a substantial portion of parameter space [53], particularly when the a boson has adequately small mass to make $h \rightarrow aa$ decays possible.

There are four types of 2HDM at lowest order without flavor-changing neutral currents (FCNC) which can be delineated through the coupling of each fermion to the doublet (Table 6.1). The Yukawa couplings of the 2HDM pseudoscalar a boson relative to those of the SM Higgs boson h are functions of the type of 2HDM and of $\tan\beta$, and are presented in Table 6.2. Type-1 and type-2 models are the commonly considered ones, and the latter is required in supersymmetric models. The leptons and down-type quarks have the same couplings in these two models. In type-3 2HDM, all leptons couple to Φ_1 and all quarks couple to Φ_2 such that all decays of a dominate.

The 2HDM augmented with a complex $SU(2)_L$ singlet field S is termed as 2HDM+S, and include the NMSSM as a special case. If singlet S mixes weakly with the doublets, one of the CP-even scalars can have SM-like properties. The extension with a singlet S leads to an additional CP-odd scalar and a CP-even scalar. The two CP-odd scalars a_1 and a_2 , and three CP-even scalars h_1 , h_2 , and h_3 result after mixing among the spin-0 states. Among the CP-even scalars, one can be identified as the observed SM Higgs boson-like state, h . The branching fractions of the h to a pair of CP-odd or CP-even bosons can be sizeable leading to a variety of possible exotic decays of h . In the 2HDM augmented with an extra singlet, the ratio of the decay width of a pseudoscalar boson to different flavors of leptons depends only upon the masses of these leptons. In particular, for a pseudoscalar boson of mass m_a decaying into muons and τ leptons, decay width relation [8, 54] can be written as

$$\frac{\Gamma(a \rightarrow \mu^- \mu^+)}{\Gamma(a \rightarrow \tau^- \tau^+)} = \frac{m_\mu^2 \sqrt{1 - (2m_\mu/m_a)^2}}{m_\tau^2 \sqrt{1 - (2m_\tau/m_a)^2}} \quad (6.1)$$

In general, such a relationship can also be written for muons and electrons. In models where a boson decays to leptons only, its branching fraction to τ leptons is greater than 99% for a boson masses above 5 GeV. This approximation is useful for pseudoscalar masses below twice the mass of the bottom quarks, or 2HDM type-3, assuming loop-induced decays such a $a \rightarrow gg$ are ostracized. In type-1 and type-2, and their extensions, a similar relation between the partial decay widths of the pseudoscalar boson to down-type quarks and leptons exists [8, 54], and in particular, for muons and b quarks, it can be written as

$$\frac{\Gamma(a \rightarrow \mu^- \mu^+)}{\Gamma(a \rightarrow b \bar{b})} = \frac{m_\mu^2 \sqrt{1 - (2m_\mu/m_a)^2}}{3m_b^2 \sqrt{1 - (2m_b/m_a)^2} (1 + QCD \text{ corrections})} \quad (6.2)$$

The factor of three in the denominator is due to the color quantum of the b quarks. The perturbative quantum chromodynamics (QCD) corrections are approximate 20% [8]. In models of type-3 or type-4, the ratio of the partial decay widths has a dependence on $\tan\beta$.

²The limit in which mass eigenstate of neutral Higgs boson is aligned approximately with the direction of the vacuum expectation values for the scalar field.

6.2 Review of $h \rightarrow aa$ searches

The important $h \rightarrow aa$ decays to following final states have been analyzed at 8 TeV proton-proton collisions datasets recorded by the CMS experiment during Run-I:

1. $h \rightarrow aa \rightarrow 4\tau$
2. $h \rightarrow aa \rightarrow 4\mu$
3. $h \rightarrow aa \rightarrow 2\mu 2\tau$
4. $h \rightarrow aa \rightarrow 2\mu 2b$

where, μ and τ represents muon and tau leptons, respectively, and b a bottom quark. These channels consider the production of SM-like Higgs boson and its decay to a pair of light mass a bosons with a decaying to different final states. For notational simplicity, a represents a light scalar or a pseudoscalar. Also, the channels consider masses of decay products large enough that they are well separated from each other. The results of these searches in Run-I are interpreted in the context of various 2HDM+S models. Earlier, D0 collaboration at the Tevatron published results for $h \rightarrow aa \rightarrow 4\mu$ and $h \rightarrow aa \rightarrow 2\mu 2\tau$ searches for pseudoscalar masses m_a between 3.5 and 19 GeV [57]. The ATLAS collaboration reported a search for $h \rightarrow aa \rightarrow 2\mu 2\tau$ decays with m_a between 3.7 and 50 GeV [57]. additionally, CMS collaboration performed searches for the production of light pseudoscalar that decay to pairs of muons in the mass range between 5.5 and 14 GeV [59] and to pairs of τ leptons in the mass range between 25 and 80 GeV [60].

6.2.1 4τ final state

In specific 2HDM models and regions of the phase space, the branching fraction of the pseudoscalar boson to τ leptons is expected to be large. The Run-I search for $h \rightarrow aa \rightarrow 4\tau$ decay considered 4τ final state arising from pseudoscalar boson a with the Higgs boson production via gluon fusion (ggF) in association with a W (Wh) or Z (Zh) boson or via vector boson fusion (VBF), light bosons in the mass range 5-15 GeV were probed. A type-2 2HDM model in which pseudoscalar branching fraction to τ leptons is dominant was considered with a mass of a boson of 9 GeV as a benchmark model to illustrate the performance of the analysis. The decay products tend to overlap due to the large Lorentz boost of the boson at light masses. A special boosted $\tau\tau$ pair reconstruction technique was used to maximize the sensitivity to overlapping τ leptons. Based on the p_T^{miss} and the transverse mass (m_T) formed from a high- p_T muon, the analysis was performed in two search regions. The two regions were exercised to differentiate between the Wh production mode and other modes such as ggF without significant \cancel{E}_T . Search considered the events with a single muon trigger that requires the presence of an isolated muon with $p_T > 24$ GeV and $|\eta| < 2.1$. The search specifically targeted the event topology with at least one boosted decay in the boosted $\tau\tau$ pair was ruled out. Isolated high p_T muon triggering the event were declared as “trigger muon” candidates μ_{trg} and the “ $\tau_\mu\tau_X$ ” object, intending to reconstruct the decay of the boosted $\tau\tau$ pair. Therefore, the search considered two classes of signal events. The one in which the Higgs boson decays as $h \rightarrow a(\rightarrow \tau_\mu\tau_X)$ and its production considers gluon fusion (ggF) or vector boson fusion (VBF). The τ_μ from the decay of one a

having a high p_T and is well separated from the τ_X arising from the same decay, satisfied the trigger muon criteria. The other reconstructed $\tau\tau$ pair was considered as a $\tau_\mu\tau_X$ object. The other class of signal events considered the Higgs boson decay as $h \rightarrow a(\rightarrow \tau_\mu\mu_X)a(\rightarrow \tau_X\tau_X)$ with the production mechanism as associated with aZ or aW boson that finally decays to isolated muons. The muon from the Z or W decays is required to pass the trigger criteria, one of the $\tau\tau$ pairs was reconstructed as $\tau_\mu\tau_X$ object, and no requirement was applied to another $\tau\tau$ pair. Further details are in reference [11].

SM production cross sections were taken for ggF , Wh , and VBF processes [63] and the number of events in the signal window were observed to be compatible with the SM background prediction. Upper limits were calculated using the CLs technique in which the test statistic is a profile likelihood ratio [64–66, 68] and the results have been interpreted as upper limits on the production of $h \rightarrow aa$ with respect to SM Higgs boson production scaled by $\mathcal{B}(h \rightarrow aa) \mathcal{B}^2(a \rightarrow \tau^-\tau^+)$.

6.2.2 4μ final state

The search for the pair of new light bosons ‘ aa ’, each decaying to a pair of isolated, oppositely charged muons has been previously performed [19]. Many new physics scenarios such as the NMSSM [20] and the models with hidden sectors [21, 22, 24] predict such a decay topology. More recent results can be found in the reference [23] and the search corresponds to a data sample recorded by the CMS detector at an integrated luminosity of 20 fb^{-1} in proton-proton collisions at center-of-mass energy equal to 8 TeV. The masses of light bosons considered are between $2m_\mu < m_a < 2m_\tau$. The analysis used a dataset four times larger than the earlier study [19]. Compared to the previous search, new approaches have been employed to improve the sensitivity to signatures with the intermediate light mass bosons traversing a non-negligible distance before decaying into muons. The data used has been collected using an online trigger selecting events containing at least two muon candidates with p_T of leading and subleading muons greater than 17 and 8 GeV, respectively. Final events have been selected by requiring at least four offline muon candidates to form two oppositely charged pairs within $|\eta| < 2.4$. Additionally, one of the muons was required to have $p_T > 17$ GeV and $|\eta| < 0.9$, to ensure the trigger efficiency is high and independent of the event topology, including effects associated with the overlap of nearby muon trajectories. For the events, invariant masses of the reconstructed dimuons were required to be compatible within the resolution of the detector. The dimuons were needed to be isolated from other event activity using the isolation criteria parameter³ $I_{sum} < 2$ GeV to suppress the background events from the decay of heavy flavor quarks. The I_{sum} selection criteria suppress the contamination from heavy flavor quarks such as $b\bar{b}$ production by about a factor of 40 GeV while rejecting less than 20% of events with the signal topology.

The search reported no excess of events in the data relative to the expected SM background. The results were obtained in the benchmark scenarios of NMSSM and dark SUSY

³The isolation parameter I_{sum} is calculated as the scalar sum of the p_T of charged tracks with $p_T > 0.5$ GeV within a jet cone of size $\Delta R = 0.4$ around the dimuon momentum vector, excluding the muon candidate tracks.

and interpreted within a broad range of physics models that predict the same type of signature. The model-independent upper limits on the product of the cross section and branching fraction have been set.

6.2.3 $2\mu 2\tau$ final state

Different final states were studied in the $h \rightarrow aa \rightarrow 2\mu 2\tau$ decay channel [11] depending on whether the τ leptons decay to hadrons (τ_h), electrons (τ_e) or muons (τ_μ). These include $\mu^+\mu^-\tau_h^+\tau_h^-$, $\mu^+\mu^-\tau_e^+\tau_e^-$, $\mu^+\mu^-\tau_\mu^+\tau_\mu^-$, $\mu^+\mu^-\tau_h^+\tau_e^-$ and $\mu^+\mu^-\tau_e^+\tau_\mu^-$. The particular final state $\mu^+\mu^-\tau_\mu^+\tau_\mu^-$ was not considered because of the difficulty in correctly identifying the reconstructed muons either τ decay product or as a direct pseudoscalar which finally results decline in sensitivity. An unbinned likelihood fit was performed to extract the results by considering $m_{\mu\mu}$ as the observable with 2% dimuon mass resolution for the muons originating promptly from one of the a bosons. Light boson masses between 15 and 62.5 GeV were probed. The 15 GeV lower bound is the minimum mass that ensures a reasonable signal efficiency with the given selection criteria. Below this mass efficiency decreases drastically as the lepton pairs are boosted and need to be studied using different selection techniques.

The events were selected using a double muon trigger with leading and subleading muon thresholds 17 and 8 GeV, and for the offline case as 18 and 9 GeV, respectively. The dimuon pair from the $a \rightarrow \mu^-\mu^+$ decay has been reconstructed with two isolated and opposite charged muons within $|\eta| < 2.4$. The final states $\mu^+\mu^-\tau_e^+\tau_h^-$, $\mu^+\mu^-\tau_h^+\tau_h^-$ and $\mu^+\mu^-\tau_e^+\tau^-$ having only two muons, p_T thresholds of 18 and 9 GeV were considered to match the trigger requirements, and in case of more than two muons in the final state, the highest- p_T muon was considered as arising from the prompt decay of the light boson. The muon was paired with another oppositely charged highest- p_T muon. The other muons were supposed to result from leptonic decays of the τ lepton. The $\tau\tau$ pair has been reconstructed from a combination of oppositely charged identified and isolated muons, electrons, or τ_h depending on the final state.

The muons were considered within $|\eta| < 2.4$, the electrons within $|\eta| < 2.5$, and the τ_h candidates within $|\eta| < 2.3$. The selection has high signal efficiency since the four-lepton invariant mass in $\mu^+\mu^-\tau_e^+\tau_e^-$ events is significantly decreased due to the presence of neutrinos in the decay of τ lepton. The separation ΔR from all the four reconstructed objects was required to be at least greater than 0.4. To reduce the contribution from top quark backgrounds, events containing at least one jet with tagging efficiency of about 50% for genuine b jets, satisfying b -tagging requirement allowing 0.1% of the light quarks jets to pass, were discarded. Single events containing other isolated muons or electrons in addition to the selected objects were rejected to prevent contributing to different final states. The normalized mass differences between dimuon and di- τ systems were required to be small ($|m_{\mu\mu} - m_{\tau\tau}| < 0.8$) and the invariant mass of the $\mu\mu\tau\tau$ system was demanded to be close to the Higgs boson mass ($|m_{\mu\mu\tau\tau} - h| < 25$ GeV) to reduce the contribution of the backgrounds to the signal region.

The maximum likelihood algorithm was used to reconstruct $\tau\tau$ and $m_{\tau\tau}$ masses, as well as E_T [62]. This method gives a resolution of about 10% and 20% for the four-lepton mass

$m_{\mu\mu\tau\tau}$ and $m_{\tau\tau}$, respectively. Dimuon invariant mass between 14 and 66 GeV was considered in this particular analysis.

Considering the production mechanisms ggF , VBF , Zh , Wh , and $t\bar{t}h$, the upper limits on the decay $h \rightarrow aa$ relative to the SM Higgs boson production scaled by $\mathcal{B}(a \rightarrow \tau^+\tau^-)\mathcal{B}(a \rightarrow \mu^+\mu^-)$, have been set at 95% CL by performing unbinned maximum likelihood fit to data taking into account the the yield and shape systematic uncertainties. The observed events in the number of final states studied are within two standard deviations of global significance.

6.2.4 $2\mu 2b$ final state

The search for a light pseudoscalar a in $h \rightarrow aa \rightarrow 2\mu 2b$ ⁴ decays was restricted to m_a between 25 and 62.5 GeV [13]. The upper bound on m_a was imposed by the kinematical constraint of Higgs boson mass $m_h = 125$ GeV and the lower bound was chosen due to the overlap between the two muons or the two b jets arising from an increased boost of the pseudoscalar [61], and below this value, there is a loss of sensitivity. A slightly wider pseudoscalar mass range⁵ was considered for the selection, background modeling, and the optimization intending at maximum expected signal significance. In particular, it ensures a good description of the background distribution over the search region.

The events were selected based on the presence of a pair of muons with $p_T > 17$ and 8 GeV. For the offline selection and depending upon the optimization, the p_T thresholds for leading and subleading muons were increased to 24 and 9 GeV, respectively. The muon candidates were required to be isolated with opposite electric charges. If more than one muon was found in an event with the same sign (charge), the one with the highest p_T was considered. Additionally, at least two jets within $|\eta| < 2.4$ and with $p_T > 15$ GeV were required to satisfy b -tagging requirements that allow less than 1% of the light quark jets to pass for an efficiency of 65% for genuine b jets. Also, the only events with the $|m_{\mu\mu bb} - 125| < 25$ GeV were considered.

The analysis reported no significant excess of events over the predicted SM background. Upper limits at 95% CL using asymptotic CLs method have been set on the Higgs boson production in the decay of $h \rightarrow aa$ relative to the SM Higgs boson ggF production mode, scaled by $\mathcal{B}(a \rightarrow b\bar{b})\mathcal{B}(a \rightarrow \mu^-\mu^+)$.

6.2.5 Interpretation

The results of the searches discussed (from Section 6.2.1 to Section 6.2.4) have been interpreted within the context of 2HDM+S. Additionally, the interpretations include the analysis $h \rightarrow aa \rightarrow 4\mu$ within the mass range between 0.25 and 3.55 GeV [55], and $h \rightarrow aa \rightarrow 4\tau$ between 4 and 8 GeV with different boosted τ lepton reconstruction techniques [56].

The branching fractions of the new light bosons to SM particles depend on the model type and $\tan\beta$ of the 2HDM+S. In type-1, all the fermionic couplings have the same scaling with respect to the SM, whereas, in type-2 which is NMSSM-like, they are enhanced for down-type fermions for $\tan\beta > 1$ and suppressed for $\tan\beta < 1$. In type-3 which is lepton

⁴The channel is written as $h \rightarrow aa \rightarrow b\bar{b}\mu^-\mu^+$ from Section 6.3 onwards.

⁵The only events with an invariant mass $m_{\mu\mu}$ within the range 20 – 70 GeV were considered.

6.2. REVIEW OF $H \rightarrow AA$ SEARCHES

Model		$m_a \in [1, 3.5]$ GeV	$m_a \in [5, 15]$ GeV	$m_a \in [20, 62.5]$ GeV
Type-1	$\mathcal{B}(a \rightarrow \mu^- \mu^+)$	$4.6 \times 10^{-3} - 44.0 \times 10^{-2}$	$2.1 \times 10^{-4} - 1.8 \times 10^{-3}$	$2.0 \times 10^{-4} - 2.2 \times 10^{-4}$
	$\mathcal{B}(a \rightarrow \tau^- \tau^+)$	0	$5.7 \times 10^{-2} - 3.6 \times 10^{-1}$	$5.5 \times 10^{-2} - 6.3 \times 10^{-2}$
	$\mathcal{B}(a \rightarrow b\bar{b})$	0	—	$8.3 \times 10^{-1} - 8.8 \times 10^{-1}$
Type-2 $\tan\beta = 2$	$\mathcal{B}(a \rightarrow \mu^- \mu^+)$	$2.5 \times 10^{-2} - 3.8 \times 10^{-2}$	$2.2 \times 10^{-4} - 4.0 \times 10^{-3}$	$2.1 \times 10^{-4} - 2.5 \times 10^{-4}$
	$\mathcal{B}(a \rightarrow \tau^- \tau^+)$	0	$6.0 \times 10^{-2} - 7.9 \times 10^{-1}$	$5.8 \times 10^{-2} - 7.0 \times 10^{-2}$
	$\mathcal{B}(a \rightarrow b\bar{b})$	0	—	$9.2 \times 10^{-1} - 9.3 \times 10^{-1}$
Type-3 $\tan\beta = 5$	$\mathcal{B}(a \rightarrow \mu^- \mu^+)$	$7.4 \times 10^{-1} - 9.6 \times 10^{-1}$	$3.5 \times 10^{-3} - 5.0 \times 10^{-3}$	$3.4 \times 10^{-3} - 3.5 \times 10^{-3}$
	$\mathcal{B}(a \rightarrow \tau^- \tau^+)$	0	$9.1 \times 10^{-1} - 9.9 \times 10^{-1}$	9.7×10^{-1}
	$\mathcal{B}(a \rightarrow b\bar{b})$	0	—	$2.0 \times 10^{-2} - 2.5 \times 10^{-2}$
Type-4 $\tan\beta = 0.5$	$\mathcal{B}(a \rightarrow \mu^- \mu^+)$	$4.5 \times 10^{-3} - 1.4 \times 10^{-1}$	$1.2 \times 10^{-3} - 1.8 \times 10^{-3}$	$1.1 \times 10^{-3} - 1.2 \times 10^{-3}$
	$\mathcal{B}(a \rightarrow \tau^- \tau^+)$	0	$3.2 \times 10^{-1} - 3.5 \times 10^{-1}$	$3.0 \times 10^{-1} - 3.3 \times 10^{-1}$
	$\mathcal{B}(a \rightarrow b\bar{b})$	0	—	$2.5 \times 10^{-1} - 3.2 \times 10^{-1}$

Table 6.3: Branching fractions [11], as a function of the mass of the pseudoscalar boson a to b quarks, τ leptons, and muons in the four different scenarios of 2HDM+S considered in Figure 6.1.

specific as the decays to leptons are enhanced for $\tan\beta > 1$ for the decays to quarks, and in type-4, which is flipped with respect to type-1 as the decays to up-type quarks and leptons are enhanced for $\tan\beta < 1$.

The value of $\mathcal{B}(a \rightarrow \mu^+ \mu^-)$ depends on the mass of the pseudoscalar boson, on the type of 2HDM+S, and on $\tan\beta$. Also, the $\mathcal{B}(a \rightarrow \tau^+ \tau^-)$ (and $\mathcal{B}(a \rightarrow b\bar{b})$ in type-1 and type-2) is proportional to $\mathcal{B}(a \rightarrow \mu^+ \mu^-)$ (Equations 6.1 and 6.2) and, therefore, after applying the assumption, the results of all analyses have been expressed as exclusion limits on $\frac{\sigma(h)}{\sigma_{SM}} \mathcal{B}(h \rightarrow aa) \mathcal{B}(a \rightarrow \mu^+ \mu^-)$. Statistically, no significant excess of events is reported in data with respect to the predicted SM for any of the above analyses.

The sensitivity of the search channel $h \rightarrow aa \rightarrow 2\mu 2b$ is higher than the search channel $h \rightarrow aa \rightarrow 2\mu 2\tau$ by order of magnitude in type-1 and type-2 2HDM+S hypothesis. On the other hand, $h \rightarrow aa \rightarrow 4\tau$ search channels have comparable sensitivity in different mass ranges. The values of the branching fractions for a pseudoscalar boson to SM particles can be computed precisely using the prescriptions in references [8, 54], except for pseudoscalar boson masses less than 1 GeV due to large QCD uncertainties in the hadronic final state [8], and for mass ranges between 3 and 5 GeV and 9 and 11 GeV (approximately) because of decays to quarkonia. The branching fractions have been used to interpret the results in the different 2HDM+S scenarios and are given in Table 6.3.

Figure 6.1 (top left) shows the 95% CL in $\frac{\sigma(h)}{\sigma_{SM}} \mathcal{B}(h \rightarrow aa)$ in type-1 2HDM+S, with no $\tan\beta$ dependence. Figure 6.1 (top right) shows corresponding limits in type-2 with $\tan\beta = 2$ and due to the enhancement of the couplings to leptons in this scenerio, the sensitivity of the $h \rightarrow aa \rightarrow 4\tau$ analysis is improved for $m_a < 2m_b$. The sensitivity of search channels $h \rightarrow aa \rightarrow 4\tau$ and $h \rightarrow aa \rightarrow 2\mu 2\tau$ for $m_a > 2m_b$ is very low in type-1 and type-2 scenerios with $\tan\beta = 2$, and decays to b quarks dominate over decays to muons and τ leptons. The results in type-3 with $\tan\beta = 5$ are depicted in Figure 6.1 (bottom left); this scenerio provides high sensivity for the various searches because of the enhancement of the couplings to leptons over quarks. Finally, the limits obtained in type-4 with $\tan\beta = 0.5$ are shown in Figure 6.1 (bottom right); the choice of $\tan\beta < 1$ ensures large couplings to leptons. The grey shaded areas in these Figures are the regions where theoretical predictions are not reliable for the branching fractions of the pseudoscalar boson to SM particles. The exclusion limits in these regions are obtained by model-independent limit calculations by extrapolating certain mass points to intermediate masses using polynomial fit, before being divided by the square

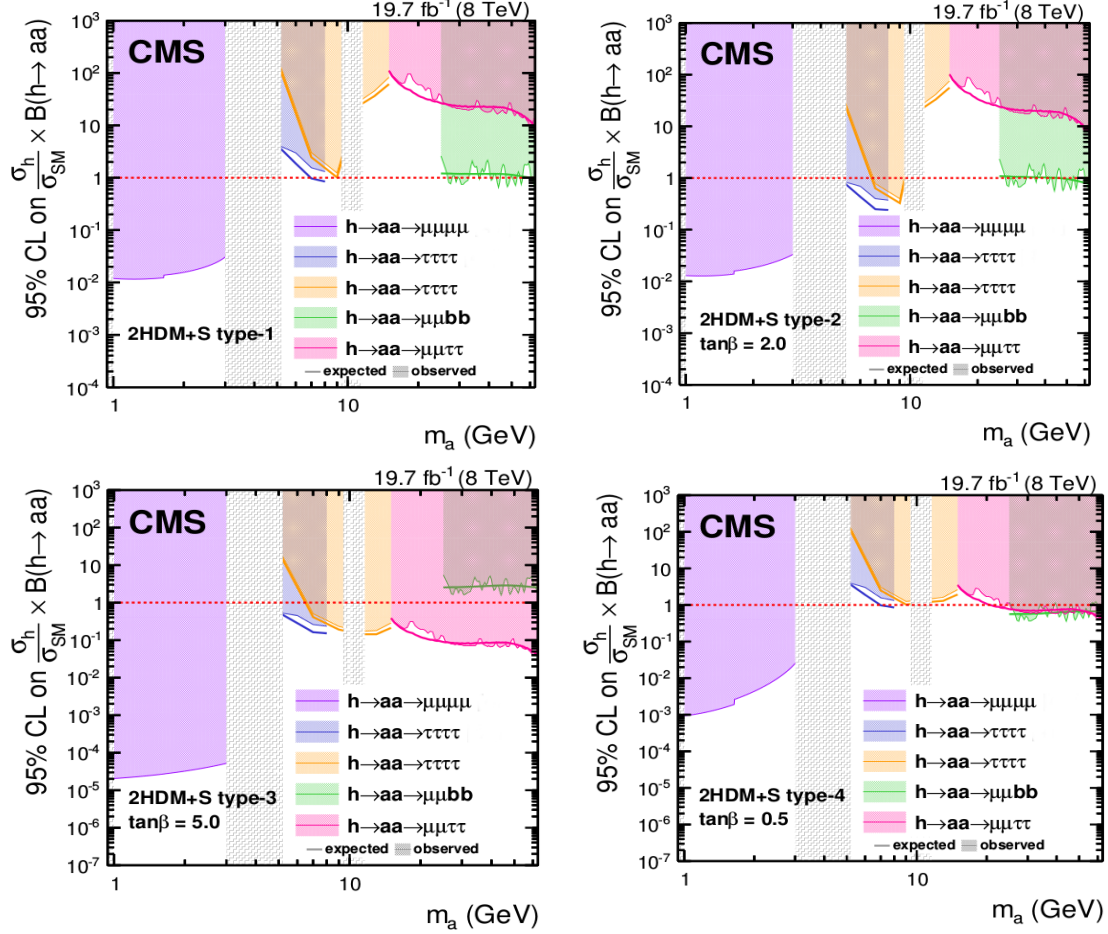


Figure 6.1: Expected and observed 95% CL limits on $\frac{\sigma(h)}{\sigma_{SM}} \mathcal{B}(h \rightarrow aa)$ as a function of the mass of the light boson in 2HDM+S: (top left) type-1, (top right) type-2 with $\tan\beta = 2$, (bottom left) type-3 with $\tan\beta = 5$, and (bottom right) type-4 with $\tan\beta = 0.5$ [11].

$\mathcal{B}(a \rightarrow \mu^- \mu^+)$. The computation of the running of coupling constant at the renormalization scale equal to m_a and the variation in the number of active flavors in the QCD corrections results in enhancement in the decay width of pseudoscalar boson to gluons, and the variation of the limit at around $m_a = 1.5$ GeV (Figure 6.1).

The ratio of the branching fractions of the pseudoscalar boson to b quarks and τ leptons depends on $\tan\beta$ and therefore, the search studies $h \rightarrow aa \rightarrow 2\mu 2b$ and $h \rightarrow aa \rightarrow 2\mu 2\tau$ are alike over the $\tan\beta$ spectrum in type-3 and type-4 scenarios of 2HDM+S. The final states $2\mu 2b$ and $2\mu 2\tau$ are more sensitive in type-3 for $\tan\beta \leq 2.2$ and in type-4 for type-4 for $\tan\beta \geq 0.8$, respectively. The best limits on $\frac{\sigma(h)}{\sigma_{SM}} \mathcal{B}(h \rightarrow aa)$ are obtained in type-3 2HDM+S with large value of $\tan\beta$ for the $h \rightarrow aa \rightarrow 2\mu 2\tau$ and $h \rightarrow aa \rightarrow 4\tau$ analyses. Upper limits as low as 4% for the $h \rightarrow aa \rightarrow 2\mu 2\tau$ and 17% for the $h \rightarrow aa \rightarrow 4\tau$ analyses can be set at 95% CL for $\tan\beta = 5$. The best limit for the $h \rightarrow aa \rightarrow 2\mu 2b$ analysis is obtained in type-3

2HDM+S with $\tan\beta = 2$ and is 16%. The upper limit of 34% on branching fraction of the Higgs boson to BSM has been set by measurements from the combination of 8 TeV center-of-mass energy data collected by the CMS and ATLAS experiments at the LHC. Limits improve the sensitivity to the particular scenarios of 2HDM+S models. Assuming SM production of Higgs boson with mass equal to 125 GeV, upper limits at 95% CL on $\frac{\sigma(h)}{\sigma_{SM}} \mathcal{B}(h \rightarrow aa)$, as low as 4, 16, and 17% have been determined for the $h \rightarrow aa \rightarrow 2\mu 2\tau$, $h \rightarrow aa 2\mu 2b$, and $h \rightarrow aa \rightarrow 4\tau$ analyses, respectively.

6.3 Present analysis

Current analysis studies a search for a new light boson by considering the exotic decay of 125 GeV Higgs boson into the pair of light pseudoscalar a boson's in the decay channel $h \rightarrow aa \rightarrow b\bar{b}\mu^-\mu^+$. The Feynman diagram of such a decay channel is shown in Figure 6.2, where a pair of gluons fuses to form h , which then decays into a pair of light pseudoscalar bosons a . The new bosons further decay to a pair of bottom quarks and a pair of muons.

Since one side of the $h \rightarrow aa$ decay ($a \rightarrow \mu^-\mu^+$) is estimated better than 2% mass resolution for prompt muon decays compared to other side of the decay ($a \rightarrow b\bar{b}$), therefore, search for a narrow resonance over the dimuon mass $m_{\mu^-\mu^+}$ spectra is considered. The upper bound on $m_{\mu^-\mu^+}$ is determined by the assumption that the 125 GeV Higgs boson decays into two on-shell particles of identical masses, while the lower bound is motivated by the kinematics of the pseudoscalar a boson decays. For lower mass values of a (typically $m_a < 20$ GeV), most of the signal jets fall below the reconstruction threshold and tend to merge geometrically in the detector so that the sensitivity largely decreases below $m_a < 20$ GeV (Figure 6.3). Therefore, the sensitive region of the search mass range of $20 \leq m_a \leq 62.5$ GeV is considered. The analysis is performed using the proton-proton collision dataset corresponding to an integrated luminosity of 41.5 fb^{-1} recorded by the CMS during the year 2017.

The search strategy for the current analysis is slightly different and is highly improved compared to previous searches. In addition to gluon-gluon fusion (ggF) production mechanisms at NNNLO with the production cross section of 48.58 ± 1.89 pb, vector boson fusion (VBF) production process with the cross section of 3.93 ± 0.08 pb at NNLO is considered. Event categorization as discussed in the latter part of Section 6.4 is employed to enhance the sensitivity. Further, a new tagger, DeepCSV, introduced in Chapter 5 is employed.

Though, the signal selection is optimized for the $h \rightarrow aa \rightarrow b\bar{b}\mu^-\mu^+$ process but the contribution to the current final state from the decays of $h \rightarrow aa \rightarrow \mu^-\mu^+\tau^-\tau^+$ is also possible if the hadronically decaying τ leptons are misidentified as b quark jets. Similarly, the contribution from $h \rightarrow aa \rightarrow b\bar{b}\tau^-\tau^+$ is also expected. Therefore, contamination from $\mu^-\mu^+\tau^-\tau^+$ final states and $b\bar{b}\tau^-\tau^+$ to current final state is also studied.

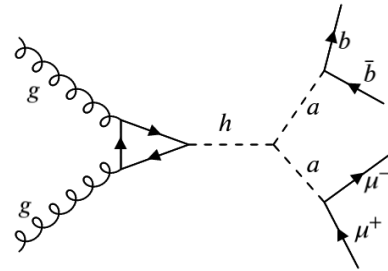


Figure 6.2: Feynman diagram for signal topology $h \rightarrow aa \rightarrow b\bar{b}\mu^-\mu^+$.

The branching fractions of 10% is assumed for $h \rightarrow aa$ decay as a benchmark whereas its value for a to SM particles depend on the 2HDM+S model type, $\tan\beta$ ⁶ and on the pseudoscalar mass m_a . The $\tan\beta$ parameter is considered to be 2, implying $2\mathcal{B}(a \rightarrow b\bar{b})\mathcal{B}(a \rightarrow \mu^-\mu^+) = 1.7 \times 10^{-3}$ for $m_a = 30$ GeV in type-3 2HDM+S. With the set of parameters under consideration and with mass range $20 \leq m_a \leq 62.5$ GeV, no strong dependance on m_a is expected for $\mathcal{B}(a \rightarrow \mu^-\mu^+)$ and $\mathcal{B}(a \rightarrow b\bar{b})$. The cross section times branching fraction is, therefore, approximated to be 8 fb for all the m_a values considered in the analysis.

6.4 Simulated samples

The signal samples with a mass from 15 to 60 GeV in steps of 5 GeV are generated for $h \rightarrow aa \rightarrow b\bar{b}\mu^-\mu^+$ at the leading order by importing NMSSMHET model [69] into Monte Carlo (MC) event generator MADGRAPH5_aMC@NLO [71] in gluon-gluon fusion (ggF) process. Signal samples with mass of pseudoscalar boson equal to 20, 30, 40, 50, and 60 GeV are also generated using vector boson fusion (VBF) process. In each case, the NNPDF31_lo_as_0130 and NNPDF31_nlo_hessian_pdfas [72] parton distribution functions (PDFs) are used for LO and NLO simulations, respectively. Further, $h \rightarrow aa \rightarrow b\bar{b}\tau^-\tau^+$ and $h \rightarrow aa \rightarrow \mu^-\mu^+\tau^-\tau^+$ signal samples are also generated to study their contribution in current signal process. The background process Drell-Yan ($Z/\gamma^* \rightarrow ll$) + jets is generated with MADGRAPH5_aMC@NLO at LO and the cross section is computed using FEWZ 3.1 [73] at NNLO. The top-antitop ($t\bar{t}$) and single top quark background processes are produced with POWHEG 2.0 [74–77] at NLO. Background contributions from diboson (WW , WZ , ZZ) are generated at NLO with the same algorithm and settings as that of Z/γ^* samples with the only exception being WW which is generated at LO. The LO NNPDF3.0 is used as a set of parton distribution functions (PDFs) for LO samples and NLO NNPDF3.0 for NLO samples [78]. PYTHIA 8.212 [79] with tune CUET8M1 [80, 81] is used for the modelling of the parton showering and fragmentation for all the samples with full CMS detector simulations [82]. The Z/γ^* production in association with additional b jets and $t\bar{t}$ are observed to be dominant backgrounds in the dimuon final state. Minimum bias events are generated and added to the simulated samples to account the effect of additional interactions per bunch crossing. These additional interactions are reweighted in a way to have the same pileup distribution as that of data [83].

6.5 Event selection and optimization

The event reconstruction relies on the particle-flow (PF) algorithm [84], which uses the information from the CMS sub-detectors such as tracker, calorimeters, and muon systems to identify charged and neutral hadrons, photons, electrons, muons, etc. emerging from proton-proton (pp) collisions in an event. Details about muon and jet reconstruction⁷ can be found in the references [85, 86, 89].

⁶ $\tan\beta$ is defined as the ratio between the vacuum expectations of the second to first doublets.

⁷Jets are reconstructed from PF objects using a distance parameter of 0.4 and are required to be separated from the selected muons by $\Delta R \geq 0.5$.

Events are selected at trigger level with two isolated muons having p_T greater than 17 GeV and 8 GeV, and two jets with $p_T > 15$ GeV. All the four objects are required to be within $|\eta| < 2.4$ region of the detector. The mass of the dimuon system is considered to be within 20 and 70 GeV. The range is wider than the search interval 20 and 62.5 GeV to allow for the full coverage at the boundaries during optimization. The jets with a given discriminant are required to pass the different working points of the DeepCSV algorithm.

The simulated samples are used for optimization purposes, while as the actual background contribution from various processes to the selected signal sample is directly extracted from data with no reference to simulation. The optimization is performed using the variable $S/\sqrt{S + (\Delta B)^2}$, where S represents the signal and ΔB is the statistical uncertainty on the background for each simulated mass point. The optimal cuts of 20 and 9 GeV are obtained on p_T of leading and sub-leading muons, respectively. Similarly, optimal cuts of 20 and 15 GeV are obtained for jet p_T , respectively. The details about the optimization procedure have already been provided in Chapter 5.

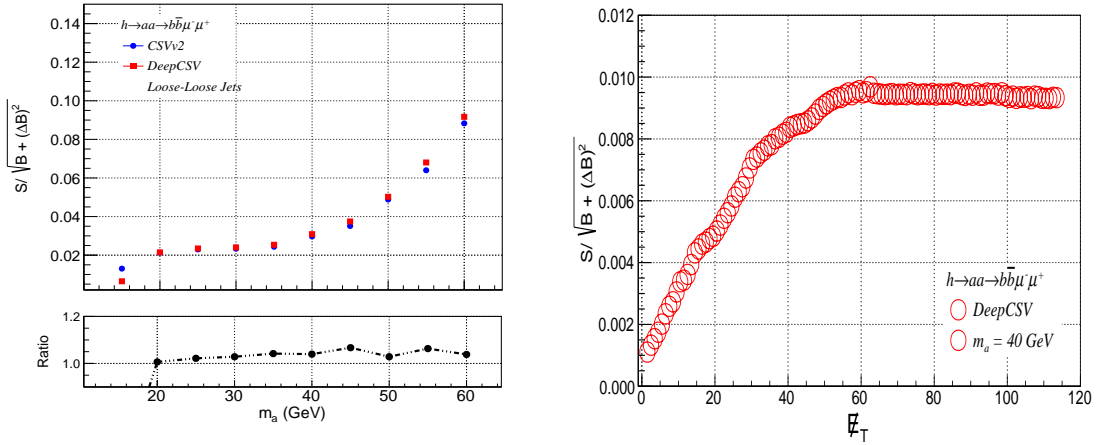


Figure 6.3: (left) The significance as a function of m_a for DeepCSV and CSVv2 taggers, and (right) the significance as a function of missing transverse energy (E_T).

A DeepCSV and CSVv2 algorithms⁸ are used to identify jets that are likely to originate from bottom (b) quarks [87]. The algorithms use track-based lifetime information together with the secondary vertices inside the jet cone to provide a multivariate discriminator for the identification of b jet [87]. Working points “tight (T)”, “medium (M)”, and “loose (L)” are defined and correspond to thresholds on the discriminator of a given tagger for which the misidentification probability is around 0.1%, 1%, and 10%, respectively, for the jets originating from gluons and light quarks.

Oppositely charged and isolated muons with a relative isolation and a separation of less than 15% and ΔR greater than 0.4, respectively, are selected within the pseudo-rapidity region of $|\eta| < 2.4$ to reject events with muons from non-prompt decays [88]. The leading b tagged jet pair with p_T greater than 20 GeV and 15 GeV, respectively, in a given event is

⁸The CSVv2 algorithm is employed only for comparison purposes and is not used for the interpretation of the final results.

identified as one a ($a \rightarrow b\bar{b}$) candidate and the leading muon pair within the invariant mass window between 20 GeV and 70 GeV is identified as another a ($a \rightarrow \mu^-\mu^+$) candidate. The mass window of $100 < m_{b\bar{b}\mu^-\mu^+} < 250$ GeV is used to construct the Higgs candidate.

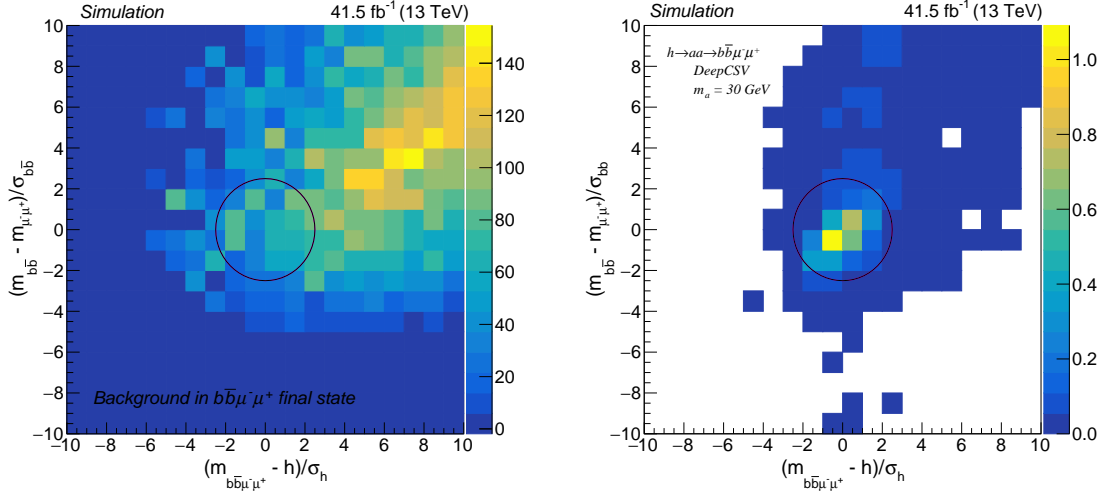


Figure 6.4: (left) The distribution of $\chi_{b\bar{b}}$ versus χ_h as defined in equation 6.3 for simulated background processes and (right) the signal process with $m_a = 30$ GeV. The contours encircle the area with $\chi^2 < 5$. The scale on the right side of each plot represents the expected yields at 41.5 fb^{-1} .

Exploiting the symmetry of $h \rightarrow aa$ decays and assuming muons and b quark jets are the decay products of the pseudoscalar a bosons, it is expected that $m_{\mu^-\mu^+} \approx m_{b\bar{b}} \approx m_a$ and $m_{\mu^-\mu^+b\bar{b}} \approx m_h \approx 125$ GeV in signal events. Under this hypothesis, a new variable χ^2 is defined as

$$\chi^2 = \chi_{b\bar{b}}^2 + \chi_h^2 \quad (6.3)$$

where

$$\chi_{b\bar{b}} = \frac{(m_{b\bar{b}} - m_{\mu^-\mu^+})}{\sigma_{b\bar{b}}} \quad \text{and} \quad \chi_h = \frac{(m_{b\bar{b}\mu^-\mu^+} - m_h)}{\sigma_h} \quad (6.4)$$

The variables, $\sigma_{b\bar{b}}$ and σ_h are the mass resolutions derived from simulation for the di- b -quark jet system and the Higgs boson candidate, respectively. The mass resolutions of the di- b -quark jet system and $m_{\mu^-\mu^+}$ are evaluated on event-by-event basis and increases linearly with m_a . The χ^2 components, $\chi_{b\bar{b}}^2$ and χ_h^2 are shown in 2D histograms for the signal sample with $m_a = 40$ GeV, and backgrounds (Figure 6.4) as described in Chapter 5. More than 95% background events with invariant mass of dimuon system $m_{\mu^-\mu^+}$ lying in the interval $\{20, 70\}$ GeV are rejected by considering a χ^2 contour of radius less than 5 with a signal acceptance efficiency of up to $\approx 65\%$.

The various permutations are formed depending on whether or not the final jet pair passes discriminator thresholds. The Tight-Loose (TL) and Tight isolation-Medium ID [97] working point combination for jets and muons are considered, respectively.

An event categorization technique is exercised to enhance sensitivity. Various categorization schemes are worked, and the one appearing in the highest expected significance is

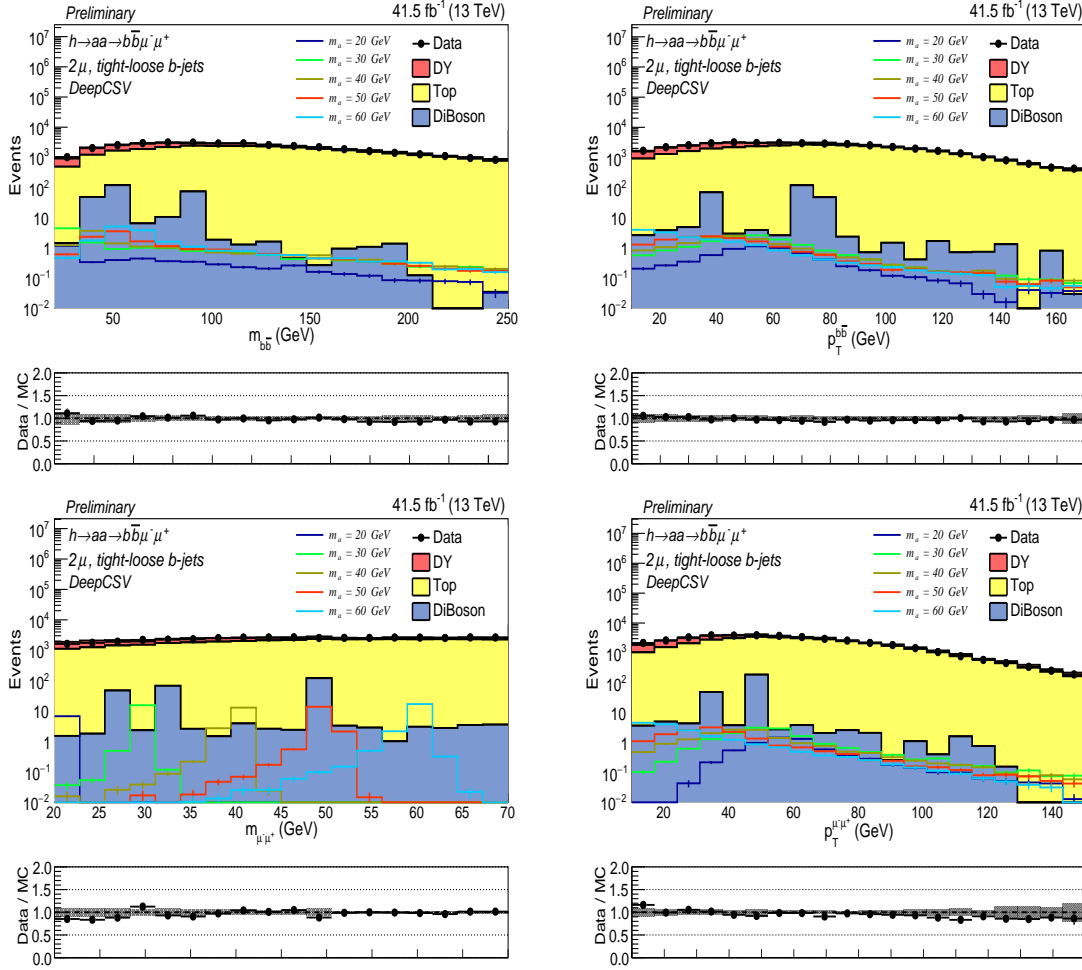


Figure 6.5: The reconstructed pseudo-scalar a boson from pair of b tagged jets: (top left) mass and (top right) its momentum; and the reconstructed pseudo scalar a from pair of muons: (bottom left) mass and (bottom right) its momentum.

preferred. The data in a side-band region are utilized to determine the categorization that is most sensitive. The sideband region is formed using the criteria $5 < \chi^2 < 17$ in addition to the selection as that for the signal region. The correlations between $m_{\mu-\mu^+}$ and χ^2 , and the variables utilized for categorization for simulated background samples are found to be very small. The soundest sensitivity is found with categorization when one b jet passes tight and the second passes loose requirements of the b -tagging discriminator threshold. The latter category is referred to as inclusive TL. The tight-tight (TT) category, the subset of the TL category, comprises events with both jets passing the tight requirements of the b jet identification algorithm. Another subset category of TL is the TM where one jet passes tight conditions and the other passes the medium b -tagging requirements but fails the tight conditions. The surviving events with the loose b -tagged jet failing the medium requirements of the b jet identification algorithm refer to the exclusive tight-loose (TL) category. On average, 35.21% of signal events pass the TL (exclusive) criteria, 23.14% pass TM, and 14.59% belong to the TT category.

Further, the events are selected based on the missing transverse energy \cancel{E}_T . Since the contribution from neutrinos from semileptonic decays in b jets is very small, therefore, the imbalance in the transverse momentum \vec{p}_T in signal events is not expected to be large. After optimization (Figure 6.3), the events are required to have missing transverse energy of $\cancel{E}_T < 60$ GeV.

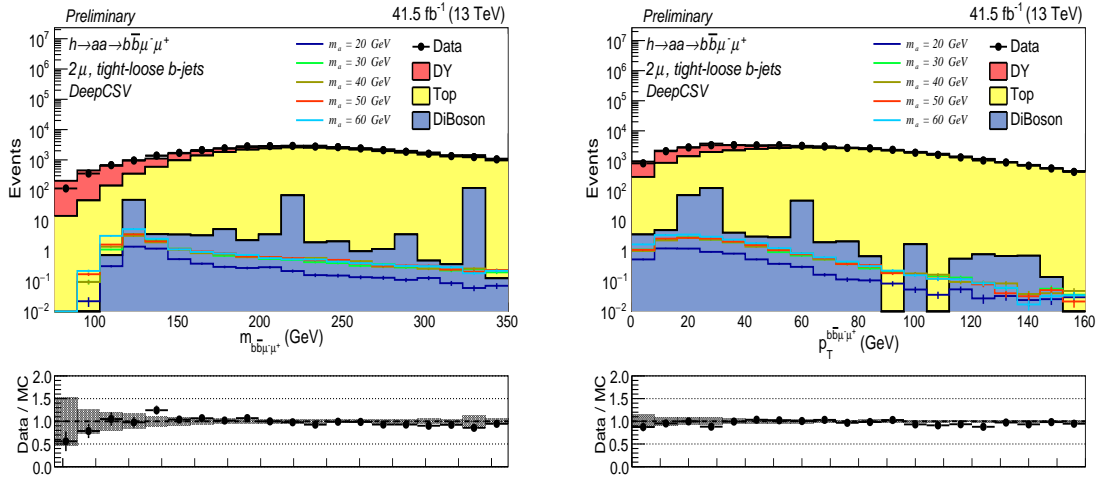


Figure 6.6: The reconstructed: (left) mass and (right) momentum of the Higgs boson from four object ($b\bar{b}\mu^-\mu^+$) system).

Figure 6.5 shows distributions in simulation and data for events passing the selection requirements except those of \cancel{E}_T and χ^2 . The expected number of simulated events are normalised to the integrated luminosity of 41.5 fb^{-1} . Data and simulations are compared for the p_T of the di-b-jet system and the dimuon system. Figure 6.6 illustrates the distribution of the invariant mass $m_{b\bar{b}\mu^-\mu^+}$ and the transverse momentum $p_T^{b\bar{b}\mu^-\mu^+}$ of the four-body system using the selected jets and muons. Within the statistical uncertainties, the distributions for simulated events follow a reasonable agreement with data. The event yields in simulation and data are also in a reasonable agreement and is presented in Table 6.4. The background from top quark ($t\bar{t}$) is dominant, contributing $\approx 75\%$, Drell-Yan is sub-dominant and is contributing $\approx 25\%$. The event yields for $h \rightarrow aa \rightarrow b\bar{b}\mu^-\mu^+$ for VBF process is presented in Table 6.5. Further, yields for the processes $h \rightarrow aa \rightarrow \mu^-\mu^+\tau^-\tau^+$ and $h \rightarrow aa \rightarrow b\bar{b}\tau^-\tau^+$ when ggF process is considered is also presented in the same Table. It is found that VBF contribution to $h \rightarrow aa \rightarrow b\bar{b}\mu^-\mu^+$ process is not significant and hence is not included. On the similar lines, it is found that contribution to $b\bar{b}\mu^-\mu^+$ final state from the final states $\mu^-\mu^+\tau^-\tau^+$ and $b\bar{b}\tau^-\tau^+$ is also not very significant and hence is not included in the interpretation of the final results.

6.5. EVENT SELECTION AND OPTIMIZATION

Process	Yield \pm Error	Signal [†] (GeV)	Yield \pm Error
Top	35088.89 ± 49.36	$m_a = 20$	16.21 ± 0.20
Drell-Yan	8795.06 ± 368.99	$m_a = 30$	16.32 ± 0.22
Diboson	274.40 ± 142.80	$m_a = 40$	16.17 ± 0.21
Total	44158.35 ± 398.72	$m_a = 50$	16.92 ± 0.22
Data	42855.00 ± 207.01	$m_a = 60$	20.41 ± 0.23

Table 6.4: Event yields obtained for simulated processes and data after selecting two muons and two b jets (tight-loose). The expected number of simulated events are normalized to $\mathcal{L} = 41.5 \text{ fb}^{-1}$.

([†]) is for $b\bar{b}\mu^-\mu^+$ final state when only ggF is considered.

Signal* (GeV)	Yield \pm Error	Signal [†] (GeV)	Yield \pm Error	Signal [‡]	Yield \pm Error
$m_a = 20$	1.62 ± 0.02	$m_a = 20$	0.35 ± 0.04	$m_a = 20$	0.00 ± 0.00
$m_a = 30$	1.65 ± 0.02				
$m_a = 40$	1.75 ± 0.02	$m_a = 40$	0.66 ± 0.05	$m_a = 40$	0.02 ± 0.01
$m_a = 50$	1.67 ± 0.02				
$m_a = 60$	1.76 ± 0.02	$m_a = 60$	0.71 ± 0.05	$m_a = 60$	0.03 ± 0.01

Table 6.5: Event yields obtained for simulated processes in TL category.

(*) is for $b\bar{b}\mu^-\mu^+$ final state when only VBF is considered,

([†]) is for $\mu^-\mu^+\tau^-\tau^+$ final state when only ggF is considered, and

([‡]) is for $b\bar{b}\tau^-\tau^+$ final state when only ggF is considered.

Process	Yield \pm Error	Signal [†] (GeV)	Yield \pm Error
Top	111.67 ± 2.53	$m_a = 20$	5.81 ± 0.12
Drell-Yan	481.55 ± 109.47	$m_a = 30$	6.10 ± 0.14
Diboson	3.51 ± 0.79	$m_a = 40$	6.51 ± 0.12
Total	596.73 ± 74.05	$m_a = 50$	7.82 ± 0.13
Data	642.00 ± 25.92	$m_a = 60$	8.73 ± 0.15

Table 6.6: Event yields obtained after applying final cuts for simulated processes and data in tight-loose (TL) category. The expected number of simulated events are normalized to $\mathcal{L} = 41.5 \text{ fb}^{-1}$.

([†]) is for $b\bar{b}\mu^-\mu^+$ final state when only ggF is considered.

Signal* (GeV)	Yield \pm Error	Signal [†] (GeV)	Yield \pm Error	Signal [‡]	Yield \pm Error
$m_a = 20$	0.14 ± 0.01	$m_a = 20$	0.02 ± 0.01	$m_a = 20$	0.00 ± 0.00
$m_a = 30$	0.15 ± 0.01				
$m_a = 40$	0.17 ± 0.01	$m_a = 40$	0.04 ± 0.01	$m_a = 40$	0.00 ± 0.00
$m_a = 50$	0.17 ± 0.01				
$m_a = 60$	0.20 ± 0.01	$m_a = 60$	0.05 ± 0.01	$m_a = 60$	0.00 ± 0.00

Table 6.7: Event yields obtained for simulated processes in TL category after applying final cuts.

(*) is for $b\bar{b}\mu^-\mu^+$ final state when only VBF is considered,

([†]) is for $\mu^-\mu^+\tau^-\tau^+$ final state when only ggF is considered, and

([‡]) is for $b\bar{b}\tau^-\tau^+$ final state when only ggF is considered.

6.6 Signal and background models

The signal samples are simulated for various mass points as described in Section 6.4. The search is conducted using an unbinned fit to the reconstructed dimuon mass $m_{\mu^-\mu^+}$ distribution in data, simultaneously in the TL, TM and TT categories and the results are extracted. The dimuon mass distributions for the simulated $h \rightarrow aa \rightarrow b\bar{b}\mu^-\mu^+$ signal events passing all selection criteria are parameterized with the combination of Voigtion (V) and double-sided Crystall Ball (CB) functions as

$$S(m_{\mu^-\mu^+} | f, p_V, p_{CB}) \equiv f \cdot V(m_{\mu^-\mu^+} | p_V) + (1 - f) \cdot CB(m_{\mu^-\mu^+} | p_{CB}) \quad (6.5)$$

where p_V corresponds to set of parameters for Voigtion with its relative contribution f , and p_{CB} is the parameter set for the Crystal ball function. The constructed model is shown in Figure 6.7.

The Voigtion profile function is a convolution of Gaussian and Lorentz profiles. The CB function, on the other hand, has a Gaussian core with a power-law low-end tail below a certain threshold, α . The mean and width of the CB profile are assumed to be proportional to m_a . Figure 6.8 shows simulated signal distributions together with fitted functions where the constructed model obtains a reasonable signal description.

In the signal model $S(m_{\mu^-\mu^+} | f, p_V, p_{CB})$, there is a possibility of correlations amongst the various parameters f , p_V and p_{CB} etc., which could change with m_a . To account for such correlations and preserve the mass dependencies, the number of parameters of the signal model are reduced to three free parameters; one is a perturbation to the mass of the hypothetical signal, $\tilde{m}_a = m_a + \epsilon_{m_a}$, and the other two, a_1 and b_1 , are used to linearly model the resolutions, σ and σ_{CB} , with mass. A fit to all signal hypotheses is performed to establish the 3-parameter model as well as to extract the initial values of the fixed and free parameters. With this parameterization, it is possible to interpolate the signal shape into regions for which the simulated samples are not available.

The associated uncertainties with the selective choice of a background model are treated in the same way as other uncertainties having nuisance parameters in the fit. The likelihood function for the signal-plus-background fit has the structure

$$\mathcal{L}(\text{data} | s(p, m_{\mu^-\mu^+}) + b(m_{\mu^-\mu^+})) \quad (6.6)$$

where $s(p, m_{\mu^-\mu^+})$ is the parametric signal shape with a set of parameters represented by p , and $b(m_{\mu^-\mu^+})$ is the background model.

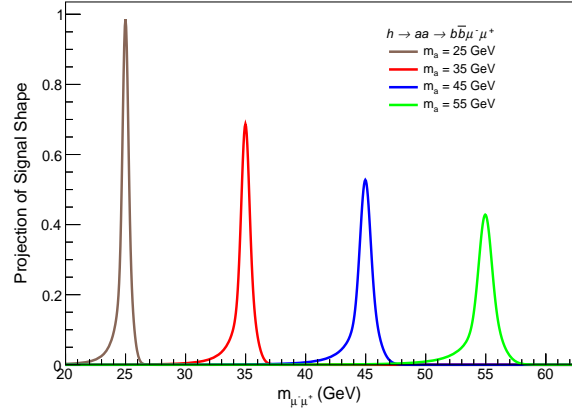


Figure 6.7: The projected signal shape (dimuon invariant mass distribution) using the model presented in Equation 6.5. The shapes are normalized to unit area.

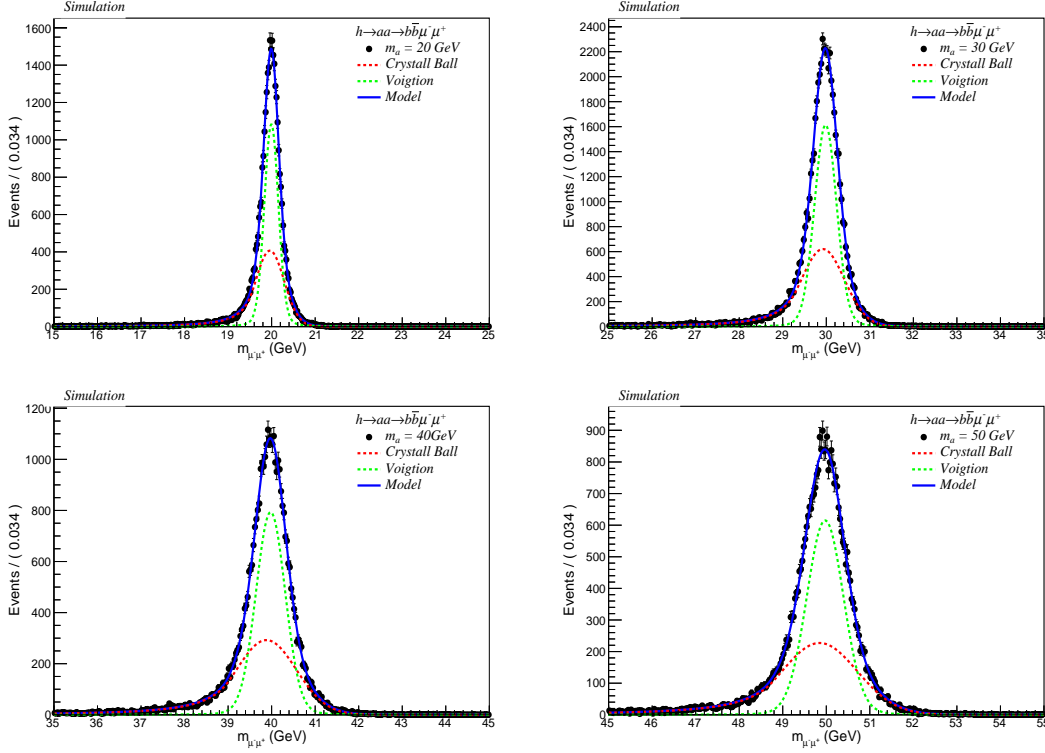


Figure 6.8: Results of the signal model $S(m_{\mu^-\mu^+} | f, p_V, p_{CB})$, fitted independently to $m_{\mu^-\mu^+}$ distributions for $m_a = 20, 30, 40$ and 50 GeV. Dotted lines in each distribution are the Crystal-ball and Voigtion components, and the solid line is the constructed model.

The shape for the background in different categories like TL, TM, and TT is independently modeled with a set of analytical functions by employing the discrete profiling method [90–92]. The approach treats background shape as a discrete nuisance parameter in the fit for which the best value can vary as the trial value of the parameter of interest ($m_{\mu^-\mu^+}$) varies. Therefore, input models starting with the lowest number of parameters are provided to the profiling method by modeling background data with different parametrization of polynomials. These include Polynomials ($P_n(x)$), Inverse Polynomials ($1/P_n(x)$), Chebychev, and Bernstein functions and the degree of models in each category are determined by F -test to avoid the overfitting of the data as discussed in Chapter 5. Figure 6.9 and Figure 6.10 shows the $m_{\mu^-\mu^+}$ distribution in the data of all event categories together with the best fits for the background model. The input background functions are tried in the minimization of the negative logarithm of the likelihood. The free parameters in the background model are accounted for by adding a penalty term. The likelihood ratio for the penalized likelihood function is written as

$$-2 \ln \frac{\tilde{\mathcal{L}}(\text{data} | \kappa, \hat{\theta}_\kappa, \hat{b}_\kappa)}{\tilde{\mathcal{L}}(\text{data} | \hat{\kappa}, \hat{\theta}, \hat{b})} \quad (6.7)$$

where κ is the measured quantity. The numerator is the maximum penalized likelihood for a given κ , at the best-fit values of nuisance parameters, $\hat{\theta}_\kappa$ and \hat{b}_κ . The denominator is the global maximum for $\tilde{\mathcal{L}}$ achieved at $\kappa = \hat{\kappa}$, $\theta = \hat{\theta}$ and $b = \hat{b}$. A confidence interval on κ is

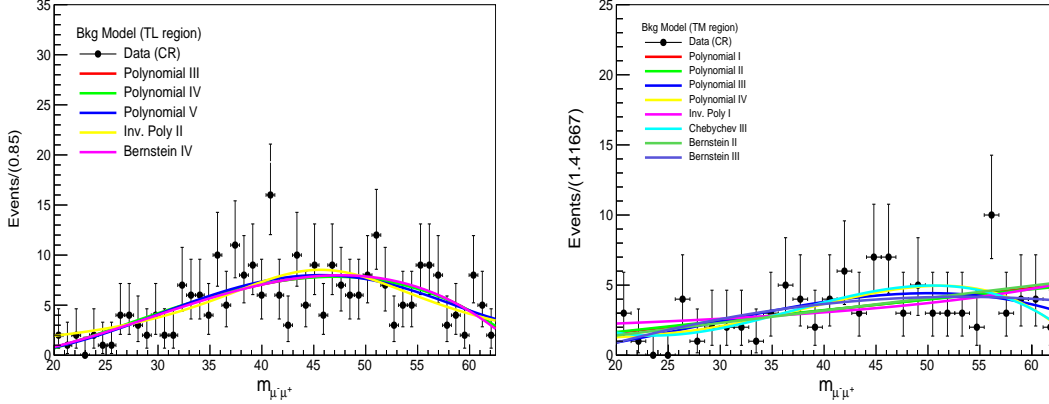


Figure 6.9: The best fits to background model under background-only hypothesis for the (left) TL category (data fitted with different polynomial functions), (right) TM category (data fitted with different polynomial functions).

obtained with the background function maximizing $\tilde{\mathcal{L}}$ for any value of κ . This interval is always wider than those evaluated with the fixed functional form from the global best-fit, $b = \hat{b}$ [91].

6.7 Systematic uncertainties

Various factors contribute to the uncertainties that include experimental ones on the selection and measurement of the reconstructed objects as well as theoretical ones on the signal and background process derived from MC simulation. The upper limit on $\mathcal{B}(h \rightarrow aa \rightarrow b\bar{b}\mu^-\mu^+)$ is evaluated by setting the Higgs boson production cross section to SM prediction and assigning an uncertainty of 3.6%, accounting PDF and α_s uncertainties on the ggF and VBF production cross sections [61].

An uncertainty of 2.3% is attributed to the integrated luminosity of the 13 TeV data collected by CMS during the year 2017 [83, 95].

By varying the total inelastic cross section by a factor of $\pm 4.6\%$, the uncertainty on the number of pileup interactions per event is determined [93]. The simulation-to-data correction factors for the selection and trigger efficiencies and muon reconstruction are estimated by using the ‘tag-and-probe’ method [94] in data and Drell-Yan simulated samples. The pileup dependence of the correction factors is also included in the uncertainties. For the jet energy scale (JES), the variations are made according to the p_T and η dependent uncertainties which are then propagated to the p_T^{miss} of the event. The smearing corrections are varied within their uncertainties for the jet energy resolution (JER) [84]. The simulations-to-data corrections uncertainty sources that affect the b tagging discriminator distribution are the

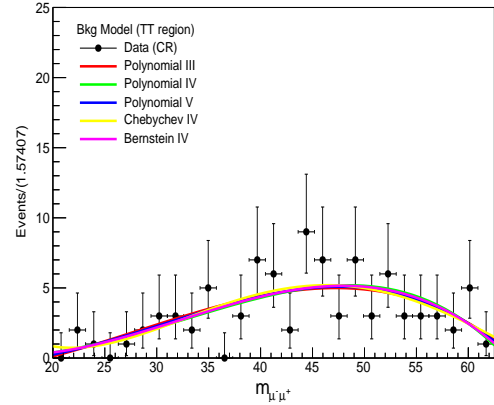


Figure 6.10: The best fits to background model to the data under background-only hypothesis for TT category.

statistical fluctuations in data and MC, JES, the contaminations from heavy flavor (HF) jets in the light-flavor jet sample, and the contamination from light flavor (LF) jets in the b jet sample. The contributions due to light-flavor jet contamination and JES in b -jet samples are found to be dominant [87].

Finally, uncertainties resulting due to the limited understanding of the PDFs [96] are also taken into account. The latter have a negligible effect on the signal shape and their effects on the yield are considered by introducing nuisance parameters with log-normal distributions into the fit.

6.8 Results

The expected SM background in each of the analysis regions for $m_{\mu^-\mu^+}$ is determined by a profile likelihood fit to the data. The signal yield for masses for which no events are simulated is obtained by interpolating the acceptance times efficiency with spline functions between available simulated mass points. Since the current analysis yields no significant deviation from the predicted background in the signal region, therefore, upper limits on signal yields are set.

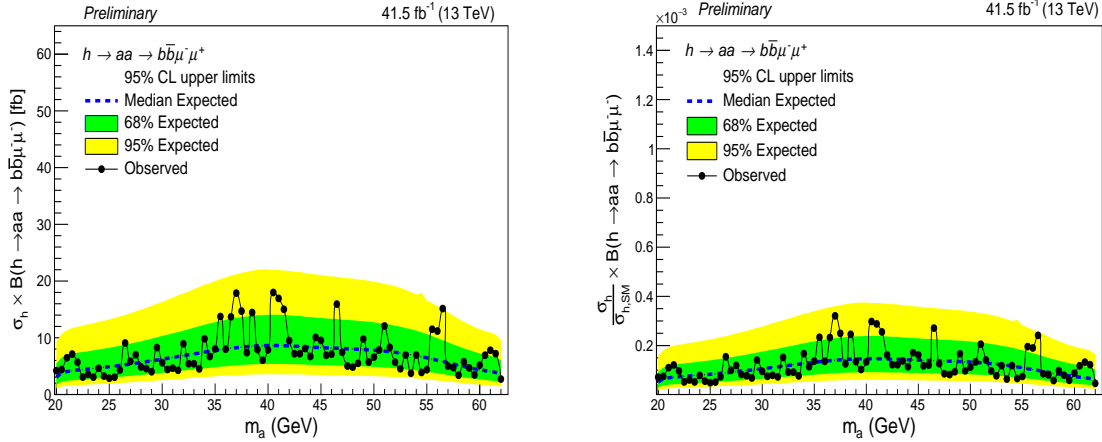


Figure 6.11: Observed and expected upper limits at 95% CL on the (left) Higgs boson production times branching fraction ($\mathcal{B}(h \rightarrow aa \rightarrow b\bar{b}\mu^-\mu^+)$) and (right) the branching ratio as a function of pseudoscalar mass m_a . The green and yellow bands represent 68 and 95% confidence intervals around the median, respectively, for expected and observed distribution of limits.

The upper limits at 95% CL on $\sigma_h \times \mathcal{B}(h \rightarrow aa \rightarrow b\bar{b}\mu^-\mu^+)$ is obtained using the CLs criterion [66, 67] and an asymptotic approximation to the distribution of the profiled likelihood ratio test statistic [65]. By assuming the SM production cross section for the Higgs boson, an upper limit is put on branching fraction $\mathcal{B}(h \rightarrow aa \rightarrow b\bar{b}\mu^-\mu^+)$ within the theoretical uncertainties. Limits are evaluated as a function of pseudoscalar mass m_a . The expected and observed limits are illustrated in Figure 6.11 for both cases. Over the entire mass range considered, the dominant systematic uncertainties are mostly associated with the b jet identification. The b -tagging uncertainties largely arise from light flavor (LF) contamination and jet energy scale (JES).

The observed limits on $\mathcal{B}(h \rightarrow aa \rightarrow b\bar{b}\mu^-\mu^+)$ are $(0.5-4) \times 10^{-4}$ for the mass range 20 to 62.5 GeV, while the expected limits are $(0.6-1) \times 10^{-4}$. The Run-I CMS search [11] at 95% CL led an observed upper limits of $(2-9) \times 10^{-4}$ at 95% CL for ggF Higgs boson production mode in the mass range $25 \leq m_a \leq 62.5$ GeV and expected limits on the branching fractions of $(4-6) \times 10^{-4}$. The ggF Higgs boson production cross section at 13 TeV has increased by a factor of about 2.3 compared to 8 TeV and the production cross section of dominant backgrounds, Drell-Yan and $t\bar{t}$ has increased by a factor of 1.6 and 3.4, respectively. Despite relative rise in backgrounds, better sensitivity is obtained using revised and much improved analysis techniques in the current work.

6.9 Conclusions

A search for the exotic Higgs boson decay to a pair of new pseudoscalar spin-zero bosons in the decay channel $h \rightarrow aa \rightarrow b\bar{b}\mu^-\mu^+$ has been performed. The search is profoundly motivated by the Next-to-Minimal Supersymmetric Model (NMSSM) and models like two-Higgs-doublet augmented with a scalar singlet (2HDM+S). The search for a narrow dimuon resonance has been conducted using a sample of proton-proton collisions data accumulated by the CMS during the year 2017 at 13 TeV center-of-mass energy and corresponds to an integrated luminosity of 41.5 fb^{-1} . In addition to the gluon-gluon fusion (ggF) production mechanism, vector boson fusion (VBF) production process has been included. Apart from employing a new tagger, DeepCSV, new optimization techniques involving event categorization has been employed to enhance the search sensitivity. Contributions to the current final state due to hadronically decaying τ leptons being misidentified as b quark jets from the decays $h \rightarrow aa \rightarrow \mu^-\mu^+\tau^-\tau^+$ and $h \rightarrow aa \rightarrow b\bar{b}\tau^-\tau^+$ have also been modelled. Statistically, no significant excess of events is found in data with respect to the standard model (SM) background prediction. Assuming the SM prediction of σ_h , the results are presented in the form of upper limits at 95% confidence level on the Higgs boson production cross section times branching fraction, $\sigma_h \times \mathcal{B}(h \rightarrow aa \rightarrow b\bar{b}\mu^-\mu^+)$, as well as on the Higgs boson branching fraction.

The CMS reported results on branching fraction based on 2016 data that correspond to 35.9 fb^{-1} integrated luminosity in the mass range of $20 \leq m_a \leq 62.5$ GeV. The limits are $(1-1.6) \times 10^{-4}$, which are improved by a factor of 1.4–1.8 with respect to Run-I results obtained in the mass range $25 \leq m_a \leq 62.5$ GeV [11]. Therefore, expected upper limits on the branching fraction show an improvement by a factor of nearly 2. On the other hand, the limits on the branching fraction as performed by ATLAS based on the 2016 data range between 2×10^{-4} and 10^{-3} [12] which are 20% less sensitive compared to the CMS results.

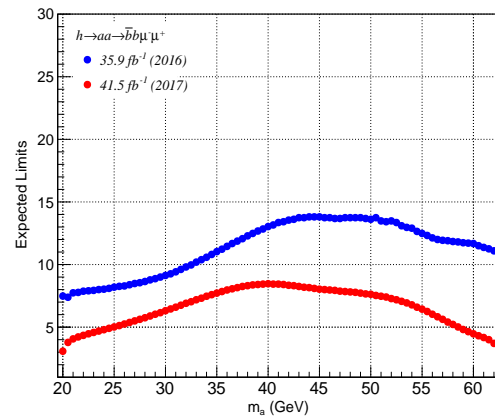


Figure 6.12: The comparison of the expected upper limits at 95% CL on the Higgs boson production cross section times branching fraction for the analysis based on 2016 and 2017 data corresponding to 35.9 fb^{-1} and 41.5 fb^{-1} , respectively.

6.9. CONCLUSIONS

The current results on the cross section are compared with the recent results published by CMS and are presented in Figure 6.12. The current limits on the branching fraction are $(0.6 - 1) \times 10^{-4}$ in the mass range of $20 \leq m_a \leq 62.5$ GeV and appear to be highly improved with respect to the previous CMS and ATLAS searches. The reason for such an improvement could be due to the use of the new b -tagging algorithm “DeepCSV” and employing improved analysis techniques such as event categorization compared to the previous searches.

BIBLIOGRAPHY

- [1] ATLAS collaboration, “[Observation of a new particle in the search for the Standard Model Higgs boson with the ATLAS detector at the LHC](#)”, Phys. Lett. B 716 (2012) 1.
- [2] CMS collaboration, “[Observation of a new boson at a mass of 125 GeV with the CMS experiment at the LHC](#)”, Phys. Lett. B 716 (2012) 30.
- [3] CMS collaboration, “[Observation of a new boson with mass near 125 GeV in pp collisions at \$\sqrt{s} = 7\$ and 8 TeV](#)”, JHEP 06 (2013) 081.
- [4] ATLAS and CMS collaboration, “[Measurements of the Higgs boson production and decay rates and constraints on its couplings from a combined ATLAS and CMS analysis of the LHC pp collision data at \$\sqrt{s} = 7\$ and 8 TeV](#)”, JHEP 06 (2013) 081.
- [5] CMS collaboration, “[Precise determination of the mass of the Higgs boson and tests of compatibility of its couplings with the standard model predictions using proton collisions at 7 and 8 TeV](#)”, Eur. Phys. J. C 75 (2015) 212.
- [6] ATLAS collaboration, “[Precise determination of the mass of the Higgs boson and tests of compatibility of its couplings with the standard model predictions using proton collisions at 7 and 8 TeV](#)”, Eur. Phys. J. C 75 (2015) 212.
- [7] ATLAS collaboration, “[Constraints on new phenomena via Higgs boson couplings and invisible decays with the ATLAS detector](#)”, JHEP 11 (2015) 206.
- [8] D. Curtin et al., “[Exotic decays of the 125 GeV Higgs boson](#)”, Phys. Rev. D 90 (2014) 075004.
- [9] ATLAS and CMS collaborations, “[Combined measurement of the Higgs boson mass in pp collisions at \$\sqrt{s} = 7\$ and 8 TeV with the ATLAS and CMS experiments](#)”, Phys. Rev. Lett. 114 (2015) 191803.
- [10] M.E. Peskin, “[Comparison of LHC and ILC capabilities for Higgs boson coupling measurements](#)”, [arXiv:1207.2516](#).
- [11] CMS collaboration, “[Search for light bosons in decays of the 125 GeV Higgs boson in proton-proton collisions at \$\sqrt{s} = 8\$ TeV](#)”, JHEP 10 (2017) 076.

- [12] ATLAS Collaboration, “Search for Higgs boson decays into a pair of light bosons in the $b\bar{b}\mu\mu$ final state in pp collision at $\sqrt{s} = 13$ TeV with the ATLAS detector”, Submitted to Phys. Lett. B.
- [13] CMS collaboration, “Search for exotic decays of the Higgs boson to a pair of new light bosons with two muon and two b jets in final states”, CMS PAS HIG-14-041 (2014).
- [14] CMS collaboration, “Projected performance of an upgraded CMS detector at the LHC and HL-LHC: contribution to the Snowmass process”, arXiv:1307.7135.
- [15] ATLAS collaboration, “Physics at a high-luminosity LHC with ATLAS”, arXiv:1307.7292.
- [16] R. Dermisek et al., “R. Dermisek and J.F. Gunion, Escaping the large fine tuning and little hierarchy problems in the next to minimal supersymmetric model and $h \rightarrow aa$ decays”, Phys. Rev. Lett. 95 (2005) 041801.
- [17] R. Dermisek et al., “The NMSSM close to the R-symmetry limit and naturalness in $h \rightarrow aa$ decays for $m_a < 2m_b$ ”, Phys. Rev. D 75 (2007) 075019.
- [18] S. Chang et al., “Nonstandard Higgs boson decays”, Ann. Rev. Nucl. Part. Sci. 58 (2008) 75.
- [19] CMS Collaboration, “Search for a non-standard-model Higgs boson decaying to a pair of new light bosons in four-muon final states”, Phys. Lett. B 726 (2013) 564.
- [20] U. Ellwanger et al., “Phenomenology of supersymmetric models with a singlet”, Nucl. Phys. B 492 (1997) 21.
- [21] N. Arkani-Hamed, “A theory of dark matter”, Phys. Rev. D 79 (2009) 015014.
- [22] M. Baumgart et al., “Non-abelian dark sectors and their collider signatures”, JHEP 04 (2009) 014.
- [23] CMS Collaboration, “A search for pair production of new light bosons decaying into muons”, Phys. Lett. B 752 (2016) 146.
- [24] A. Falkowski et al., “Hidden Higgs decaying to lepton jets”, JHEP 05 (2010) 077.
- [25] C. Englert et al., “Exploring the Higgs portal”, Phys. Lett. B 703 (2011) 298.
- [26] T.D. Lee, “A theory of spontaneous T violation”, Phys. Rev. D 8 (1973) 1226.
- [27] N.G. Deshpande et al., “Pattern of symmetry breaking with two Higgs doublets”, Phys. Rev. D 18 (1978) 2574.
- [28] H.E. Haber et al., “The fermion mass scale and possible effects of Higgs bosons on experimental observables”, Nucl. Phys. B 161 (1979) 493.

- [29] G.C. Branco et al., “[The fermion mass scale and possible effects of Higgs bosons on experimental observables](#)”, Phys. Rept. 516 (2012) 1.
- [30] P. Fayet, “[Supergauge invariant extension of the Higgs mechanism and a model for the electron and its neutrino](#)”, Nucl. Phys. B 90 (1975) 104.
- [31] P. Fayet, “[Spontaneously broken supersymmetric theories of weak, electromagnetic and strong interactions](#)”, Phys. Lett. B 69 (1977) 489.
- [32] J.E. Kim et al., “[The \$\mu\$ -problem and the strong CP problem](#)”, Phys. Lett. B 138 (1984) 150.
- [33] U. Ellwanger et al., “[The next-to-minimal supersymmetric Standard Model](#)”, Phys. Rept. 496 (2010) 1.
- [34] J. Bernon et al., “[Light Higgs bosons in two-Higgs-doublet models](#)”, Phys. Rev. D 91 (2015) 075019.
- [35] R.D. Peccei et al., “[CP conservation in the presence of instantons](#)”, Phys. Rev. Lett. 38 (1977) 1440.
- [36] R.D. Peccei et al., “[Constraints imposed by CP conservation in the presence of instantons](#)”, Phys. Rev. D 16 (1977) 1791.
- [37] P. Fayet, “[Supersymmetry and weak, electromagnetic and strong interactions](#)”, Phys. Lett. B 64 (1976) 159.
- [38] S. Heinemeyer et al., “[Interpreting the LHC Higgs search results in the MSSM](#)”, Phys. Lett. B 710 (2012) 201.
- [39] A. Celis et al., “[LHC constraints on two-Higgs doublet models](#)”, JHEP 07 (2013) 053.
- [40] B. Grinstein et al., “[Carving out parameter space in type-II two Higgs doublets model](#)”, JHEP 06 (2013) 094.
- [41] B. Coleppa et al., “[Constraining type-II 2HDM in light of LHC Higgs searches](#)”, JHEP 01 (2014) 161.
- [42] C.-Y. et al., “[Heavy Higgs searches and constraints on two Higgs doublet models](#)”, Phys. Rev. D 88 (2013) 015018.
- [43] N. Craig et al., “[Searching for signs of the second Higgs doublet](#)”, arXiv:1305.2424.
- [44] L. Wang et al., “[Status of the aligned two-Higgs-doublet model confronted with the Higgs data](#)”, JHEP 04 (2014) 128.
- [45] J. Baglio et al., “[Benchmarks for Higgs pair production and heavy Higgs boson searches in the two-Higgs-doublet model of type II](#)”, Phys. Rev. D 90 (2014) 015008.

- [46] B. Dumont et al., “[Constraints on and future prospects for two-Higgs-doublet models in light of the LHC Higgs signal](#)”, Phys. Rev. D 90 (2014) 035021.
- [47] S.F. King et al., “[Natural NMSSM Higgs bosons](#)”, Nucl. Phys. B 870 (2013) 323.
- [48] J. Cao et al., “[A light Higgs scalar in the NMSSM confronted with the latest LHC Higgs data](#)”, JHEP 11 (2013) 018.
- [49] N.D. Christensen et al., “[Low-mass Higgs bosons in the NMSSM and their LHC implications](#)”, JHEP 08 (2013) 019.
- [50] D.G. Cerdeno et al., “[Probing the two light Higgs scenario in the NMSSM with a low-mass pseudoscalar](#)”, JHEP 06 (2013) 031.
- [51] G. Chalons et al., “[Analysis of the Higgs potentials for two doublets and a singlet](#)”, Phys. Rev. D 86 (2012) 115024.
- [52] A. Ahriche et al., “[Higgs phenomenology in the two-singlet model](#)”, JHEP 02 (2014) 042.
- [53] J. Bernon et al., “[Scrutinizing the alignment limit in two-Higgs-doublet models: \$m_h = 125\$ GeV](#)”, Phys. Rev. D 92 (2015) 075004.
- [54] A. Djouadi et al., “[The anatomy of electro-weak symmetry breaking. I: the Higgs boson in the standard model](#)”, Phys. Rept. 457 (2008) 1.
- [55] CMS collaboration, “[A search for pair production of new light bosons decaying into muons](#)”, Phys. Lett. B 752 (2016) 146.
- [56] CMS collaboration, “[Search for a very light NMSSM Higgs boson produced in decays of the 125 GeV scalar boson and decaying into \$\tau\$ leptons in pp collisions at \$\sqrt{s} = 8\$ TeV](#)”, JHEP 01 (2016) 079.
- [57] D0 collaboration, “[Search for NMSSM Higgs bosons in the \$h \rightarrow aa \rightarrow \mu\mu\mu\mu, \mu\mu\tau\tau\$ channels using \$p\bar{p}\$ collisions at \$\sqrt{s} = 1.96\$ TeV](#)”, Phys. Rev. Lett. 103 (2009) 061801.
- [58] ATLAS collaboration, “[Search for Higgs bosons decaying to \$aa\$ in the \$\mu\mu\tau\tau\$ final state in pp collisions at \$\sqrt{s} = 8\$ TeV with the ATLAS experiment](#)”, Phys. Rev. D 92 (2015) 052002.
- [59] CMS collaboration, “[Search for a light pseudoscalar Higgs boson in the dimuon decay channel in pp collisions at \$\sqrt{s} = 7\$ TeV](#)”, Phys. Rev. Lett. 109 (2012) 121801.
- [60] CMS collaboration, “[Search for a low-mass pseudoscalar Higgs boson produced in association with a \$b\bar{b}\$ pair in pp collisions at \$\sqrt{s} = 8\$ TeV](#)”, Phys. Lett. B 758 (2016) 296.

- [61] LHC Higgs Cross section Working Group collaboration, “[Handbook of LHC Higgs Cross sections: 3. Higgs Properties](#)”, [arXiv:1307.1347](#).
- [62] L. Bianchini et al., “[Reconstruction of the Higgs mass in \$H \rightarrow \tau\tau\$ events by dynamical likelihood techniques](#)”, J. Phys. Conf. Ser. 513 (2014) 022035.
- [63] LHC Higgs Cross section Working Group collaboration, “[Handbook of LHC Higgs Cross sections: 3. Higgs Properties](#)”, [arXiv:1307.1347](#).
- [64] ATLAS and CMS collaborations and The LHC Higgs Combination Group, “[Procedure for the LHC Higgs boson search combination in Summer 2011](#)”, CMS-NOTE-2011-005 (2011).
- [65] G. Cowan et al., “[Asymptotic formulae for likelihood-based tests of new physics](#)”, Eur. Phys. J. C 71 (2011) 1554.
- [66] T. Junk et al., “[Confidence level computation for combining searches with small statistics](#)”, Nucl. Inst. Meth. A 434 (1999) 435.
- [67] A. L. Read, “[Presentation of search results: the CLs technique](#)”, J. Phys. G 28 (2002) 2693.
- [68] DELPHI collaboration, “[A search for heavy stable charged and long-lived squarks and sleptons in \$e^+e^-\$ collisions at energies from 130 to 183 GeV](#)”, CERN-OPEN-2000-005 (2008).
- [69] D. Curtin et al., “[Exotic decays of the 125 GeV Higgs boson](#)”, Phys. Rev. D 90 (2014) 075004.
- [70] D. Curtin et al., “[Uncovering light scalars with exotic Higgs decays to \$b\bar{b} \mu^+ \mu^-\$](#) ”, JHEP 06 (2015) 025.
- [71] J. Alwall et al., “[The automated computation of tree-level and next-to-leading order differential cross sections, and their matching to parton shower simulations](#)”, JHEP 07 (2014) 079.
- [72] NNPDF Collaboration et al., “[Parton distributions from high-precision collider data](#)”, Eur. Phys. J. C 77 (2017) 663.
- [73] Y. Li et al., “[Combining QCD and electroweak corrections to dilepton production in FEWZ](#)”, Phys. Rev. D 86 (2012) 094034.
- [74] E. Re, “[Single-top Wt-channel production matched with parton showers using the POWHEG method](#)”, Eur. Phys. J. C 71 (2011) 1547.
- [75] S. Alioli et al., “[A general framework for implementing NLO calculations in shower Monte Carlo programs](#)”, JHEP 06 (2010) 043.

- [76] S. Alioli et al., “[NLO single-top production matched with shower in POWHEG: s- and t-channel contributions](#)”, Phys. Rep. 516 (2012) 1.
- [77] S. Frixione et al., “[Matching NLO QCD computations with parton shower simulations: the POWHEG method](#)”, JHEP 09 (2009) 111.
- [78] NNPDF Collaboration, “[Parton distributions for the LHC Run II](#)”, Comput. Phys. Commun. 191 (2015) 159.
- [79] T. Sjostrand et al., “[An introduction to PYTHIA 8.2](#)”, Phys. Rep. 516 (2012) 1.
- [80] P. Skands et al., “[Tuning PYTHIA 8.1: the Monash 2013 tune](#)”, Eur. Phys. J. C 74 (2014) 3024.
- [81] CMS Collaboration, “[Event generator tunes obtained from underlying event and multi-parton scattering measurements](#)”, Eur. Phys. J. C 76 (2016) 155.
- [82] GEANT4 Collaboration, “[GEANT4-a simulation toolkit](#)”, Nucl. Inst. Meth. A 506 (2003) 250.
- [83] CMS Collaboration, “[CMS luminosity measurements for the 2016 data taking period](#)”, CMS Physics Analysis Summary CMS-PAS-LUM-17-001, 2017.
- [84] CMS Collaboration, “[Particle-flow reconstruction and global event description with the CMS detector](#)”, 12 JINST (2017) P10003.
- [85] M. Cacciari et al., “[The anti- \$k_t\$ jet clustering algorithm](#)”, JHEP 04 (2008) 063.
- [86] M. Cacciari et al., “[FastJet user manual](#)”, Eur. Phys. J. C 72 (2012) 1896.
- [87] CMS Collaboration, “[Identification of heavy-flavour jets with the CMS detector in pp collisions at 13 TeV](#)”, 13 JINST (2018) P05011.
- [88] CMS Collaboration, “[Search for a standard model-like Higgs boson in the \$\mu^+\mu^-\$ and \$e^+e^-\$ decay channels at the LHC](#)”, Phys. Lett. B744 (2015) 184-207.
- [89] CMS Collaboration, “[Performance of Electron Reconstruction and Selection with the CMS Detector in Proton-Proton Collisions at \$\sqrt{s} = 8\$ TeV](#)”, 2015 JINST 10 P06005.
- [90] CMS Collaboration, “[Jet algorithms performance in 13 TeV data](#)”, CMS Physics Analysis Summary CMS-PAS-JME-16-003, 2017.
- [91] P. Dauncey et al., “[Handling uncertainties in background shapes: the discrete profiling method](#)”, (2015) JINST 10 P04015.
- [92] CMS Collaboration, “[Observation of the diphoton decay of the Higgs boson and measurement of its properties](#)”, Eur. Phys. J. C74 (2014), no. 10, 3076.

- [93] CMS Collaboration, “[Measurement of the inelastic proton-proton cross section at \$\sqrt{s} = 13\$ TeV](#)”, JHEP 07 (2018) 161.
- [94] CMS Collaboration, “[Measurements of inclusive W and Z cross sections in pp collisions at \$\sqrt{s} = 7\$ TeV](#)”, Phys. Rev. Lett. 117 (2016) 182002.
- [95] CMS Collaboration, “[CMS luminosity measurement for the 2017 data-taking period at \$\sqrt{s} = 13\$ TeV](#)”, CMS Physics Analysis Summary CMS-PAS-LUM-17-004, 2017.
- [96] J. Butterworth et al., “[PDF4LHC recommendations for LHC Run II](#)”, J. Phys. G 43 (2016) 023001.
- [97] CMS Collaboration et al., “[Performance of the CMS muon detector and muon reconstruction with proton-proton collisions at \$\sqrt{s} = 13\$ TeV](#)”, JINST 13 (2018) P06015.
- [98] CMS Collaboration, “[Search for exotic Higgs boson decays into \$b\bar{b}\mu^-\mu^+\$ final state](#)”, CMS publication with full Run-II dataset in progress.

Epilogue

*Where is the life we have lost in living?
Where is the wisdom we have lost in knowledge?
Where is the knowledge we have lost in information?*

— T. S. Eliot

7.1 Summary and conclusion

The present thesis is based upon extensive work on three aspects: R&D on Gas Electron Multiplier (GEM) detectors, Phase-II upgrade of the Compact Muon Solenoid (CMS) experiment at the Large Hadron Collider (LHC), and physics data analysis. The R&D on GEM detectors includes important studies in the context of the CMS muon upgrade using GEM technology. The part of the R&D work on GEM foils has been performed in collaboration with the Indian industry for their possible usage in scientific and other industrial applications. The Phase-II work includes the development of large size GEM detectors for the forward muon endcap of the CMS experiment and the physics analysis includes a search for a new light boson in the exotic decays of Higgs boson in the $b\bar{b}\mu^-\mu^+$ final state.

The Standard Model (SM) framework of particle physics describes a basic architecture for electromagnetic, strong, and weak interactions. Despite its enormous successful implications, the model has various limitations as it does not answer satisfactorily questions like matter-antimatter asymmetry, hierarchy problem, nature of dark matter, etc. Therefore, theoretical solutions are provided by many extensions of SM such as two-Higgs-doublet model augmented with a scalar singlet (2HDM+S), Next-to-Minimal Supersymmetric Standard Model (NMSSM), etc.

One of the vital questions, how elementary particles gain their masses is explained in the SM via the Brout-Englert-Higgs (BEH) mechanism. According to the BEH mechanism, all massive particles acquire their mass through interaction with the Higgs field. The existence of such a field could be proven through the experimental detection of the Higgs boson associated with the Higgs field. A similar particle with a mass of 125 GeV and featuring properties as that of the SM Higgs boson, was reported by the ATLAS and CMS collaborations in 2012. With the current precision, the measurements of the couplings and properties of this newly discovered particle show compatibility with the SM within the experimental uncertainties.

However, the existence of BSM exotic decays of the Higgs boson to lighter scalar/pseudoscalar particles which might have eluded our detections so far are not yet excluded. Therefore, the current work has been carried out to explore the possibilities of such BSM decays. The search includes the exotic decay of already discovered 125 GeV boson into new light bosons which subsequently decay into $b\bar{b}\mu^-\mu^+$ final state. The 2HDM+S and NMSSM models have been used for benchmarking the performance of the search.

The current thesis documents the analysis results that are based on data accumulated by the CMS during the year 2017 at 13 TeV center-of-mass energy and correspond to an integrated luminosity of 41.5 fb^{-1} . The analysis is performed by simulating private signal samples after following CMS official recipe at the leading order in gluon-gluon fusion (ggF) and vector boson fusion (VBF) processes. After validating signal samples, optimizations are performed. The event categorization technique is exercised to enhance sensitivity and various schemes are worked, and the one appearing in the highest expected significance has been preferred. The dimuon mass distributions for the simulated signal events passing all selection criteria are parameterized with the combination of Voigtion and double-sided Crystal Ball functions. The shape for the background is independently modeled with a set of analytical functions by employing the discrete profiling method that treats background shape as a discrete nuisance parameter in the fit for which the best value can vary as the trial value of the parameter of interest varies. The background contribution from various processes to the selected signal sample is directly extracted from data and the search results are extracted from the unbinned fit to the reconstructed dimuon mass distribution. Various factors contributing to the uncertainties that include experimental ones on the selection and measurement of the reconstructed objects, as well as theoretical ones on the signal and background process derived from MC simulation are taken into account. The upper limits are evaluated by setting the Higgs boson production cross section to SM prediction and by assigning various uncertainties to account PDF and other uncertainties on the ggF and VBF production cross sections.

The results have been obtained for two decay channels. In the first case, the first search results for new physics in the extended Higgs sector in signatures expected from the decay of Higgs boson to electroweak Z boson and a light pseudoscalar a boson has been presented where a Z boson is expected to decay into bottom-antibottom ($b\bar{b}$) quark pair and a boson into muon-antimuon ($\mu^-\mu^+$) lepton pair. The decay channel is extremely motivated in many BSM models, for example, in 2HDM+S, and is expected to provide better sensitivity. The search used data collected by the CMS experiment at center-of-mass energy 13 TeV corresponding to an integrated luminosity of 41.5 fb^{-1} during the year 2017. No excess of events is found over the expected SM background. The upper limits are set on $\sigma_h \times \mathcal{B}(h \rightarrow Za \rightarrow b\bar{b}\mu^-\mu^+)$ as well as on the branching fraction of the Higgs boson decay. The limits on the branching fraction are determined to be $(0.3 - 2.3) \times 10^{-3}$, which can be compared with the expected value $(1.0 - 1.2) \times 10^{-3}$, assuming particular scenarios of two-Higgs-doublet-models augmented with a scalar singlet. The limits are stringent for the decay channel $h \rightarrow Za \rightarrow b\bar{b}\mu^-\mu^+$ in the pseudoscalar mass range $11 < m_a < 34\text{ GeV}$ and are the first such results at the LHC so far.

In the second case, a search for the exotic Higgs boson decay to a pair of new pseudoscalar spin-zero bosons in the decay channel $h \rightarrow aa \rightarrow b\bar{b}\mu^-\mu^+$ has been performed. The search is profoundly motivated by the Next-to-Minimal Supersymmetric Model (NMSSM) and models like two-Higgs-doublet augmented with a scalar singlet (2HDM+S). The search for a narrow dimuon resonance has been conducted using a sample of proton-proton collisions data accumulated by the CMS during the year 2017 at 13 TeV center-of-mass energy and corresponds to an integrated luminosity of 41.5 fb^{-1} . In addition to the gluon-gluon fusion (ggF) production mechanism, vector boson fusion (VBF) production process has been included. Apart from employing a new tagger, DeepCSV, new optimization techniques involving event categorization has been employed to enhance the search sensitivity. Contributions to the current final state due to hadronically decaying τ leptons being misidentified as b quark jets from the decays $h \rightarrow aa \rightarrow \mu^-\mu^+\tau^-\tau^+$ and $h \rightarrow aa \rightarrow b\bar{b}\tau^-\tau^+$ have also been modelled. Statistically, no significant excess of events is found in data with respect to the standard model (SM) background prediction. Assuming the SM prediction of σ_h , the results are presented in the form of upper limits at 95% confidence level on the Higgs boson production cross section times branching fraction, $\sigma_h \times \mathcal{B}(h \rightarrow aa \rightarrow b\bar{b}\mu^-\mu^+)$, as well as on the Higgs boson branching fraction.

The CMS reported results on the branching fraction of the current channel based on 2016 data that correspond to 35.9 fb^{-1} integrated luminosity in the mass range of $20 \leq m_a \leq 62.5 \text{ GeV}$. The limits are $(1 - 1.6) \times 10^{-4}$, which are improved by a factor of $1.4 - 1.8$ with respect to Run-I results obtained in the mass range $25 \leq m_a \leq 62.5 \text{ GeV}$. The expected upper limits on the branching fraction show an improvement by a factor of nearly 2. On the other hand, the limits on the branching fraction as performed by ATLAS based on the 2016 data range between 2×10^{-4} and 10^{-3} which are 20% less sensitive compared to the CMS results.

The results obtained in the current work on the cross section are compared with the recent results published by CMS on the 2016 data. The obtained limits on the branching fraction are $(0.6 - 1) \times 10^{-4}$ in the mass range of $20 \leq m_a \leq 62.5 \text{ GeV}$ and appear to be highly improved with respect to the previous CMS and ATLAS searches. The reason for such an improvement could be due to the use of the new b -tagging algorithm “DeepCSV” and the use of improved analysis techniques such as event categorization compared to the previous searches.

Since a successful physics program can only be achieved with sufficient understanding and optimization of the detector performance, therefore part of the work has been considered on the detector R&D and muon endcap upgrade of the CMS experiment. The Run-II of the LHC at 13 TeV proton-proton collisions ended in November 2018 with a total of over 165 fb^{-1} accumulated integrated luminosity. After the second Long Shutdown (LS2)¹, the energy should reach a planned value of 14 TeV with a steady increase in the instantaneous luminosity over the years to $2 \times 10^{34} \text{ cm}^{-2} \text{ s}^{-1}$ near the end of Phase-I. The Phase-II of the LHC starting after 2026 will deliver even higher luminosities of the order of $7 \times 10^{34} \text{ cm}^{-2} \text{ s}^{-1}$. The corresponding increase in particle rates pushes the present CMS detection and

¹Already underway and going to last until December 2020.

trigger capabilities to their limits and imposes the need for an upgrade in many subsystems to ensure reliable operation at high rates and luminosity. The high particle rates during HL-LHC strongly affects the muon system of the CMS, and therefore, part of the work considered in this thesis has been dedicated to the muon endcap upgrade of the CMS detector. This, in turn, will be very important in the future for all the analysis having muons in the final state. In particular, the analysis considered in the current work was chosen to have muons in the final state so that work finds a natural relevance to be the part of ongoing muon upgrade and the results obtained as a part of the analysis can be compared in the future in terms of significance after the upgrade which considers the usage of Gas Electron Multiplier (GEM) technology.

Currently, the forward endcap high- $|\eta|$ region $1.6 < |\eta| < 2.2$ of the CMS remains uninstrumented. The part of the work presented in this thesis aims at covering this region of the muon endcap with large-size GEM chambers. These detectors can operate under high rates with excellent performance and are considered ideal for the high luminosity phase of the LHC. Such chambers offer enhanced tracking and triggering capabilities for the muon system and are suited for stable and long-term operation in the high rate environments such as the HL-LHC.

As part of the High Luminosity LHC project, the CMS collaboration approved the use of GEM technology to extend its muon system coverage in the forward region. The GE1/1 project was in R&D phase, the fourth generation prototypes of GE1/1 chambers were about to assemble, and the major perspectives of the project were not yet established when the current work started in 2014. The work contributed to the success of the CMS GEM GE1/1 project in terms of design layout, assembly and construction, and validation of several full-size GE1/1 chambers. To elaborate a bit more, the CMS GE1/1 chambers are constructed using a novel mechanical stretching technique that has been presented in the current thesis. The technique requires no spacers inside the active area and no gluing during detector assembly and reduces the chamber construction time from several days to only a few hours. In the first step, ten chambers were produced with the current assembly technique and installed inside the CMS experiment during the 2017 Extended Year End Technical Stop (EYETS). These chambers are providing the first operational experience with GEM detectors inside the CMS cavern. Further, a total of 144 new full-size GE1/1 chambers have been produced using this technique. All these chambers needed for the CMS high eta upgrade have been validated successfully after subjecting them to a series of quality control (QC) tests.

Apart from the assembly and construction, the work contributed to the R&D, quality control (QC), and performance measurements of GE1/1 chambers evaluated during various beam tests at CERN Super Proton Synchrotron (SPS). The QC measurements consist of optical inspection and leakage current measurements of the GEM foils, gas leakage tests of the GE1/1 chambers, gain and its uniformity measurements, etc., and it is very difficult to include all the results in the current thesis.

During the process of R&D, different GE1/1 generations have been tested for gain, efficiency, spatial and time resolutions, and discharge probability for the gas composition Ar/CO₂ and Ar/CO₂/CF₄. Measurements show that the detector can be operated smoothly up

to a gain of about 10^5 with a discharge probability of less than 10^{-11} under CMS operating conditions which are being considered safe during HL-LHC and the results are very important for the CMS. The studies performed to understand the rate capability demonstrated that the GE1/1 chambers do not show any decrease in gain up to 10^6 Hz/mm², the result is again very important since the maximum flux in the CMS end-caps is expected to be nearly 100 Hz/mm² (10 kHz/cm²), therefore, the chambers can tolerate such high particle rates without any loss in performance. Further, the performance of the chambers in beam tests show an efficiency of 98% or better obtained across the active area, and time resolution close to 5 ns. The results have been obtained for different gas compositions such as Ar/CO₂ and Ar/CO₂/CF₄ with different mixtures and the performance of the chamber have been compared. The results show that better performances are obtained by adding CF₄ to Ar/CO₂, especially the timing performance with a reduced discharge probability. However, since the CF₄ is a potential global warming gas and the CMS has followed not to continue working with the CF₄ gas mixtures.

To characterize the performance of a GE1/1 chamber for any drift voltage, the data for gain, discharge probability, efficiency, and time resolution are fit with parametric equations. The fits provide a good description of the data and allow interpolation to any desired value of drift voltage. Interpolated data points are obtained for the measured quantities for different gas compositions and the ‘CMS Region’, has been defined which corresponds to the operational regime of GE1/1 chambers for the CMS experiment.

Furthermore, GE1/1 chambers use large-size GEM foils which are produced using a single-mask production technique. This technique introduces geometrical asymmetries in the shapes of holes and is expected to affect the operation of the GEM detectors conceived from these foils. Therefore, the characterizations of such foils have been performed in detail. In particular, gas gain, energy resolution and its uniformity, charging-up behavior, rate capability, and discharge probability have been studied. The measurements were performed as per the interests of the CMS GEM upgrade project and are valid in general. Though a 10 cm × 10 cm detector has been employed for the measurement purposes but results are acceptable for GE1/1 chambers as the behavior of the detector is determined by the local phenomena governed by the hole structures within the GEM foils which is independent of the size of the foils for the given production technology. From the results, it was concluded that the hole asymmetry strongly affects the properties of the detector, and accordingly, optimized configurations were provided, some of which CMS were already following without much understanding.

The other part of the R&D study considered the production and qualification of Indian GEM foils. Being the main distributor of small as well as large size GEM foils, it is quite difficult for CERN to meet the growing demands of GEM foils. Therefore, to meet the future requisites, a significant development took place involving the production of the first successful commercial double-mask Indian GEM foils under the transfer of technology (TOT) agreement between CERN and Micropack, a Bengaluru based Indian industry. The desired quality control assessment that included optical and leakage current measurements have been performed, and the foils were declared fit for research and other industrial applications.

This, in turn, will have an enormous impact in terms of cost and technological availability on the upcoming high energy physics experiments (like Compressed Baryonic Matter (CBM), Germany) which are going to use GEM technology. The Micropack has also produced larger size foils and the quality control tests on the constructed large size detector from such foils are currently underway at CERN's Gamma Irradiation Facility (GIF++). Indian CMS groups are planning to use these foils in the next CMS GEM (GE2/1) upgrade.

The end of the year 2018 has accomplished the successful production and validation of 144 GE1/1 full-size chambers which are going to be installed in positive and negative endcaps of the CMS experiment. The current work contributed to QC testing and resulted in the validation of several GE1/1 chambers at CERN. Specifically, out of 144 GE1/1 full-size chambers, sixteen chambers were fully assembled in India (eight in Delhi University). All these sixteen detectors were validated at Delhi University after performing a series of quality control (QC) tests such as optical inspection of GEM foils, leakage current and spurious count measurements, gas leak tests, gain and response uniformity measurements, and were finally shipped to CERN in December-2018. The CMS experiment is currently available for their planned upgrade installation. Even after the integration and commissioning of the GE1/1 chambers with the CMS, there are still open studies to contribute to the next CMS GEM-based project, 'GE2/1'. The GE2/1 chamber and its front end electronics are presently under the R&D phase. The low and high voltage powering design systems are still under discussion. The readout electronics VFAT3 chip is in the improvement phase. Such chambers will be installed in the CMS during the third Long Shutdown (LS3) currently scheduled during the period 2024-2025. The introduction of such technology into the CMS will increase the acceptance and the efficiency of reconstruction of muons that would be crucial in the future for the broad spectrum of physics processes whose signatures are characterized by the presence of muons in the final state.

Concluding remarks—the first thing expected from the CERN LHC was a Higgs boson and a similar particle was discovered in 2012 leading the 2013 Nobel Prize in Physics to Peter Higgs and Francois Englert. Now we are very curious because there are little known things about the Higgs except for some interaction signs. There could be more than one Higgs, several Higgs, or a composite Higgs. As the current thesis attempted to look for such particles and reported null results, I wish the work could have come up with a set of entirely new particles that did not look in any way like the particles that all of us expect today. It would have been really interesting to figure out how to interpret those results. Further, with the ongoing LHC upgrade to which current work contributed enormously, I wish the journey of new discoveries to continue at CERN that could give us clues about the new physics, and help in solving the mysteries that the Standard Model (SM) leaves open. Therefore, I conclude this thesis with the quote² of late astronomer, Carl Sagan, “Somewhere, something incredible is waiting to be known”, hoping some new puzzles are waiting to be discovered at CERN.

²Quote is sometimes also credited to the reporter Sharon Begley.

TABLES

A.1 GE1/1 operating conditions for Ar/CO₂ gas

Ar/CO ₂ (70/30)					
Drift Voltage (V)	Gain	Efficiency	Resolution (ns)	Rate Capability (kHz/cm ²)	Discharge Probability
2900	1.02×10^2	0.54	17.42	10^5	2.36×10^{-17}
3000	2.17×10^2	0.84	14.54	10^5	8.68×10^{-17}
3100	4.60×10^2	0.95	12.04	10^5	3.18×10^{-16}
3200	9.74×10^2	0.97	9.912	10^5	1.16×10^{-15}
3300	2.06×10^3	0.98	8.109	10^5	4.28×10^{-15}
3400	4.36×10^3	0.98	6.60	10^5	1.57×10^{-14}
3500	9.24×10^3	0.98	5.35	10^5	5.77×10^{-14}
3600	1.95×10^4	0.98	4.32	10^5	2.11×10^{-13}
3700	4.14×10^4	0.98	3.48	10^5	7.77×10^{-13}
3800	8.76×10^4	0.98	2.80	10^5	2.85×10^{-12}
3900	1.85×10^5	0.98	2.25	10^5	1.00×10^{-11}
4000	3.93×10^5	0.98	1.80	10^5	3.84×10^{-11}
4100	8.31×10^5	0.98	1.44	10^5	1.40×10^{-10}

Table A.1: The gain, efficiency, rate capability and discharge probability as a function of drift voltage for GE1/1 chambers corresponding to Ar/CO₂ gas. The green region are the recommended working points while as light gray is under efficient region. The red region is merely an extrapolation and should be strongly avoided because of steep rise in discharge probability.

A.2 GE1/1 operating conditions for Ar/CO₂/CF₄ gas

Ar/CO ₂ /CF ₄ (45/15/40)					
Drift Voltage (V)	Gain	Efficiency	Resolution (ns)	Rate Capability (kHz/cm ²)	Discharge Probability
2900	0.62×10^1	0.00	24.67	10^5	3.87×10^{-19}
3000	1.22×10^1	0.00	22.48	10^5	9.52×10^{-19}
3100	2.41×10^1	0.00	20.21	10^5	2.34×10^{-18}
3200	4.76×10^1	0.00	17.93	10^5	5.76×10^{-18}
3300	9.41×10^1	0.01	15.69	10^5	1.41×10^{-17}
3400	1.85×10^2	0.11	13.55	10^5	3.48×10^{-17}
3500	3.66×10^2	0.48	11.56	10^5	8.57×10^{-17}
3600	7.23×10^2	0.86	9.75	10^5	2.10×10^{-16}
3700	1.42×10^3	0.97	8.14	10^5	5.18×10^{-16}
3800	2.82×10^3	0.98	6.73	10^5	1.27×10^{-15}
3900	5.56×10^4	0.98	5.53	10^5	3.13×10^{-15}
4000	1.09×10^4	0.98	5.51	10^5	7.71×10^{-15}
4100	2.16×10^4	0.98	3.66	10^5	1.89×10^{-14}

Table A.2: The gain, efficiency, rate capability and discharge probability as a function of drift voltage for GE1/1 chambers corresponding to Ar/CO₂/CF₄ gas. The green region are the recommended working points while as light gray is under efficient region. The red region is merely an extrapolation and should be strongly avoided because of steep rise in discharge probability.